Departamento de Física Teórica
Facultad de Ciencias
Universidad Autónoma de Madrid

Primordial magnetic fields from preheating at the electroweak scale

Memoria de Tesis realizada por
D. Andrés Díaz-Gil Díaz-Tendero,
presentada ante el Departamento de Física Teórica
de la Universidad Autónoma de Madrid
para optar al grado de Doctor en Ciencias (Físicas)

Trabajo dirigido por
Dr. Dña. Margarita García Pérez
y co-dirigido por
Dr. D. Antonio González-Arroyo España

Madrid, Enero de 2009

The present thesis is based on the following publications:

- A. Díaz-Gil, J. García-Bellido, M. García Perez and A. González-Arroyo, "Primordial magnetic fields from preheating at the electroweak scale," JHEP **0807** (2008) 043.
- A. Díaz-Gil, J. García-Bellido, M. García Pérez and A. González-Arroyo, "Magnetic field production during preheating at the electroweak scale," Phys. Rev. Lett. **100** (2008) 241301.
- A. Díaz-Gil, J. García-Bellido, M. García Pérez, A. González-Arroyo, "Primordial magnetic fields at preheating," in proceedings of *Lattice 2005 conference*, PoS(LAT2005) 242.
- A. Díaz-Gil, J. García-Bellido, M. García Pérez, A. González-Arroyo, "Magnetic field production after inflation," in proceedings of *Lattice 2007 conference*, PoS(LAT2007) 052.

Contents

1 Introducción y Resumen. **9**

2 Introduction and Outline. **13**

3 Large Scale Magnetic Fields. **17**
3.1 Observations of large scale magnetic fields. 18
3.1.1 Zeeman splitting 18
3.1.2 Synchrotron emission. 19
3.1.3 Faraday rotation. 20
3.2 UHECR and the Future of LSMF measurements. 21
3.3 Origin and evolution. 22
3.4 The Hypothesis. 27

4 Inflation and CEW **29**
4.1 Cosmological Evolution. 29
4.2 The inflationary paradigm. 31
4.3 Hybrid inflation. 37
4.4 The breaking of the EW symmetry. 38
4.5 Tachyonic preheating. 40

5 Lattice gauge theories. A review. **43**
5.1 The Lattice set-up. 43
5.2 Gauge fields 48
5.3 The way to improvement. 53
5.3.1 Improving the lattice. 54
5.3.2 The improved derivatives. 54
5.3.3 Gauge Improvement: The Clover. 56

6 Methodology. **59**
6.1 The classical approximation. 59

6.1.1 Linear quantum evolution 61
6.2 The initial condition. 68
6.3 The lattice approach. 73
6.3.1 The Electromagnetic field. 76
6.4 Model and Lattice parameters. 77
6.4.1 Model parameters. 77
6.4.2 Lattice parameters. 79

7 Helicity and MHD **85**
7.1 The Magnetohydrodynamics Equations. 87
7.1.1 The Ideal MHD. 90
7.1.2 Resistive MHD. 92
7.2 The role of the helicity in the MHD scenario. 95
7.2.1 Helicity in the ideal MHD limit. 97
7.2.2 Helicity in the resistive MHD. 98
7.3 Helicity in the LSMF evolution 100
7.4 Generation of helical magnetic fields 104

8 Generation. **107**
8.1 Initial Magnetic fields 108
8.2 The symmetry breaking period 119
8.3 Charge and current. 128

9 Late time evolution. **137**
9.1 Late time evolution. 137
9.2 Helicity, charge and energy 138
9.3 Kinetic turbulence. 142
9.4 The Influence of the Inflaton. 145
9.5 Magnetic seeds. 146
9.6 Electromagnetic field spectrum. 150
9.6.1 Electromagnetic radiation. 151
9.7 The Helical length. 158

10 Dependence on parameters. **161**
10.1 Lattice and finite volume artifacts 161
10.2 The Higgs to W boson mass ratio 165

11 Conclusiones y trabajo futuro. **171**
11.1 Conclusiones. 171
11.2 Trabajo futuro. 176

12 Conclusions and future work. **179**
12.1 Conclusions 179
12.2 Future Work. 183

13 Agradecimientos. **187**

14 Acknowledgments. **189**

A The Lattice Equations of Motion **191**

B Maxwell equations **197**
B.1 The transverse and longitudinal components 200

C Thermal radiation **203**

D Gaussian Random fields **207**

Chapter 1

Introducción y Resumen.

Han pasado más de sesenta años dese que Alfvén, en 1943, mostrara que los campos magnéticos podrían preservarse durante mucho tiempo en plasmas con una gran conductividad. Este fue el punto de inicio para uno de los problemas que, a dia de hoy, representan uno de los más intrigantes misterios sin resolver en la astrofísica y la cosmología modernas. Este problema es el origen de los campos magnéticos de gran escala. Estos campos magnéticos son observados en el Universo y, sin motivo aparente, están presentes en objetos muy diferentes entre sí, como son las galaxias o los clústeres.

Aunque aún sin determinar, se sospecha que el origen de estos campos está en el Universo primordial. Esto es debido a alguna de las características que presentan, como es su ubicuidad y su similitud en diferentes galaxias y clústeres, todos con intensidades en el rango de los μG. Durante mucho tiempo se ha especulado con diversos mecanismos para la generación de estos campos. Entre éstos, se han contemplado algunos que proponen que su origen, está situado en alguna de las transiciones de fase que podrían haberse desarrollado a lo largo de la evolución del Universo. Concretamente, las más extendidas discusiones en este sentido, son las que usan la transición QCD y la transición de fase electrodébil como escenarios para la producción de dichos campos.

El presente trabajo puede situarse dentro de estos últimos. El objetivo de la presente tesis, es el de arrojar un poco más de luz sobre este incierto origen, mediante una nueva aproximación al problema en la transición de fase electrodébil. Es sin embargo, que este estudio parte de un enfoque ligeramente nuevo. No sólo porque el escenario propuesto es la época de "preheating" taquiónico en la transición electrodébil, que ha sido poco estudiado en el contexto de los campos magnéticos de gran escala [84], sino que por primera

vez, se va a seguir la evolución detallada del sistema completo, desde el final de inflación, a través de la ruptura espontánea de simetría, y a tiempos muy alejados en el subsiguiente periodo de "reheating". Esto incluye la introducción y estudio del grupo gauge completo $SU(2) \times U(1)$, junto al modelo hibrído Higgs-Inflatón.

Como se ha dicho, el estudio de la evolución del sistema pasa por la etapa altamente no lineal y no perturbativa de la transición de fase. Para realizar esta detallada evolución, ha sido necesario el uso de la aproximación clásica. Esta aproximación ha proporcionado el marco adecuado para el uso de una evolución númerica del sistema. Este tratamiento númerico lleva a su vez involucrado el uso de ciertas herramientas, tomadas prestadas de las teorías gauge en la lattice, que han provisto lo necesario para el seguimiento de la fenomenología del sistema a lo largo de la complicada evolución.

Adelantándonos a las conclusiones, en la presente tesis se han conseguido objetivos muy notables. Entre ellos se ha mostrado la existencia de un mecanismo para la generación de campos magnéticos en las etapas tempranas de la evolución. Los campos magnéticos creados han presentado una tendencia a desarrollar una longitud de correlacion larga, así como una componente helical no trivial. Se han encontrado también ciertas evidencias de cascada inversa en el sistema magnético. Paralelamente a los conceptos extrictamente relacionados con campos magnéticos, se han encontrado también una gran cantidad de fenómenos interesantes relacionados con la cargas y corrientes del sistema.

La comprensión de los fenómenos que ocurren en la evolución ha demostrado ser una especie de tarea multidisciplinar. Para el desarrollo de esta tesis, y como puede apreciarse en la bibliografía usada, se han visto involucrados conceptos de astrofísica, cosmología, teorías gauge en la lattice y física de plasmas. Es por esto que la presente tesis se estructura de la siguiente manera:

Primero se presentan unos breves cápitulos introductorios en los que se definen y discuten los conceptos necesarios para el desarrollo de este trabajo. En el capítulo 3, se resumen en general, algunas de las observaciones y aspectos más importantes sobre los campos magnéticos de gran escala. Es también donde se expone la hipótesis principal de este trabajo. Después, en el capítulo 4, se presenta un breve resumen sobre inflación, y se introduce el modelo particular de inflación híbrida elegido. En el capítulo 5, los conceptos lattice y las herramientas usadas en esta tesis son expuestos. El capítulo 6 es un capítulo central. Está dedicado a la metodología particular utilizada en este estudio. Esta metodología abarca desde el uso y justificación de la

aproximación clásica, hasta la descripción de la evolución númerica, pasando por la elección de los parámetros libres en la teoría. También incluida en la metodología está la definición de los campos electromagnéticos usada. Posteriormente, en el capítulo 7, se introducen ciertos conceptos que se usan frecuentemente en la física de plasmas. Este capítulo dedica una amplia discusión al concepto de la helicidad y su papel en la evolución de los campos magnéticos. Los dos siguientes capítulos, 8 y 9, presentan el análisis de los resultados de la evolución. Ésta está dividida en dos partes que se corresponden con cada capítulo. El capítulo 8 está dedicado a los primeros pasos de la evolución y las inmediaciones de la ruptura de simetría, mientras que el capítulo 9 presenta la posterior evolución del sistema. El comportamiento de los observables con la elección de los parámetros, tanto lattice como físicos, es investigado en el capítulo 10. Los capítulos 11 y 12 presentan las conclusiones y el trabajo futuro, tanto en Español como en Inglés. Por último, los apéndices se organizan de la siguiente forma: Los apéndices A y B, atienden a las tecnicidades de la discretización lattice. El apéndice C está dedicado a la distribución térmica de campo magnético, y por último el apéndice D muestra algunas tecnicidades sobre los campos aleatorios gaussianos.

Chapter 2

Introduction and Outline.

It has been more than sixty years since Alfvén, in 1943, showed that the magnetic fields in highly conducting plasmas could be preserved for a long time. This work was the starting point for what became one of the most intriguing problems in modern astrophysics and cosmology. This is the origin of the large scale or cosmological magnetic fields (LSMF). They are observed in the Universe and are present in a diversity of objects, which range from galaxy to cluster or even supercluster scales. There is no satisfactory explanation for the origin of such a fields.

Although this point is also undetermined, it is believed that the origin of the LSMF is in the primordial Universe. Several of their properties suggest that fact, as are their ubiquity and their similarity between very different cosmological objects. This similarity is the order μG strength. It has been speculated for a long time with several generation mechanism candidates. Within them, there were some which proposed that the generation mechanisms may be related with some of the phase transitions that could be performed along the evolution of the Universe. More precisely, the most interesting mechanisms use both QCD and EW phase transitions as magnetic field generation scenarios.

The present work can be placed inside these last. The objective of the present thesis, is to give a new insight to the LSMF uncertain origin, using a slightly new approach to the problem in the scenario of a EW phase transition. Our proposal is a bit different, because uses the preheating epoch at the EW phase transition, which represents a scenario only slightly studied in the context of the LSMF [84], and also since we follow, for the first time, the detailed evolution of the whole system, from the end of inflation, through the spontaneous symmetry breaking, until further times in the evolution,

within the subsequent reheating period. This gives involved the introduction and study of the whole $SU(2) \times U(1)$ gauge group, together with the Higgs-Inflaton hybrid model.

As mentioned, the study of the evolution of the system goes through the highly non-lineal and non-perturbative phase transition. To track the detailed evolution along this phase, it has been necessary to use the classical approximation. This approximation provided the necessary ingredients for a numerical evolution of the system. The numerical treatment involves the use of tools, which in our case have been taken from the lattice gauge theory, which have been proved to be useful for the study of the system phenomenology along the complicated dynamics.

In advance of the conclusions, the present thesis has achieved some remarkable objectives. Within them, it has been shown the presence of a magnetic field generation mechanism, active in the early stages of the evolution. The magnetic fields so generated, have shown to posses a large correlation length, and a non trivial helicity. It has been also found certain evidences of an inverse cascade in the magnetic system. In parallel with the explicitly magnetic related issues, we found that the system of charge and currents presents also a very interesting phenomenology.

The study of the system evolution has shown to be quite a multidisciplinary task. Hence, several concepts coming from different areas are been used in the development of this thesis. They come from astrophysics, cosmology, gauge field theories and plasma physics as can be seen in the bibliography. For that reason the present thesis is structured as follows:

First some introductory brief chapters are presented. In them, some concepts used in the development of this work are reviewed. Chapter 3 is a general summary of the observation and most important aspects of the LSMF. In it is also introduced our main hypothesis. Later, in chapter 4, a brief summary about inflation is presented, focusing in the particular hybrid inflation model used. Chapter 5 is devoted to the introduction of the lattice gauge theories and the tools useful for the present work. Chapter 6 is a central one. In it, it is discussed the used methodology, which goes from the use and justification of the classical approximation, to the description of the numerical evolution, including the discussion about the choice of the free parameters in the theory. Also included in the methodology, is the electromagnetic field definition. After that, in chapter 7, the concept of helicity is discussed, as well as its role in the magnetic field evolution. The two following chapters, 8 and 9, present the analysis of our evolution results. The evolution is divided in two parts, corresponding with each chapter. Chapter

8 is devoted to the first stages of the evolution, and the neighborhood of the spontaneous symmetry breaking region. Chapter 9 presents the following evolution of the system. The behavior of the observables with the choice of the parameters, both lattice and physical, is studied in chapter 10. Chapters 11 and 12 present the conclusions and future work, in Spanish and English respectively. Finally, the appendix are organized as follows: Appendix A and B are devoted to the discussion of the technicalities of the lattice discretization. Appendix C is devoted to the study of the thermal magnetic distribution, and finally appendix D shows some technicalities related with the Gaussian random fields.

Chapter 3

Large Scale Magnetic Fields.

The origin of the observed large scale magnetic fields (LSMF) is one of the remaining mysteries in relativistic astrophysics and cosmology (for reviews see the list of references [17]-[34]). They have been found on the scale of galaxies and clusters of galaxies with a magnitude of order the microgauss. There is even some evidence of their existence on the scale of superclusters. Summarizing the measured LSMF values on all scales L :

- galaxies: $B \simeq 50\ \mu$G at $L < 1$ kpc; $B \simeq 5 - 10\ \mu$G at $L \sim 10$ kpc.
- clusters: $B \simeq 1\ \mu$G at $L \sim 1$ Mpc.
- superclusters: $B < 10^{-2} - 10^{-3}\ \mu$G at $L \sim 1 - 50$ Mpc.
- CMB: $B < 10^{-3} - 10^{-5}\ \mu$G at $L > 100$ Mpc.
- Primordial nucleosynthesis: $B < 10^{11}$ G at $T = 10^{9}$ K.

where the last bound (BBN) comes from the modification, that such a background, would imply for the expansion rate of the universe at primordial nucleosynthesis. This would change the observed Helium abundance.

Magnetic fields play an important role in the evolution of the primordial plasma in the early universe (possibly also in cosmic phase transitions), in the propagation of cosmic rays in our galaxy, as well as in clusters of galaxies. They may influence galaxy formation and large scale structures, and they may generate a stochastic background of gravitational waves, which is particularly intriguing.

Although several attempts have been performed during years, there is no candidate for a generation mechanism, which explains both a magnitude and a correlation length according with the observations.

In what follows we will briefly review some generalities about the most commonly used techniques for the detection of both galactic and extragalactic fields. For a review on observational results see [36].

3.1 Observations of large scale magnetic fields.

In this section we will follow closely the discussion in reference [29]. A complete review can be also found in [28].

The experiments measuring the large scale magnetic fields are based on three main effects. They all produce indirect measures of both the magnitude and correlation length of those magnetic fields. They however, attend to different characteristics of the fields. For this reason it is convenient to describe the magnetic field of an object, as composed by two different phenomenologically relevant components:

$$B = \bar{B} + \delta B$$

where $\bar{B}$ is the background homogeneous component of the field and δB is the non-uniform component. Also, it is useful for some techniques to separate the magnetic field in B_L and B_T. These are respectively the magnetic field projection along the line of sight and the component transverse to this line. There are measurements that are sensitive to each of them, as we will see below.

3.1.1 Zeeman splitting

The well known Zeeman splitting phenomenon, consists in the breakdown of the degeneracy of the energy levels in the atom of Hydrogen in the presence of a background magnetic field. This magnetic field produces a splitting in the levels that is given by:

$$\Delta\nu = \frac{e\bar{B}_L}{2\pi m_e}$$

where $\bar{B}_L$ is the homogeneous component of the magnetic field along the line of sight. The Zeeman splitting is the most direct method to obtain the magnetic field magnitude. Once the splitting is measured $\bar{B}_L$ can be obtained without further assumptions. It provided the first observations of extraterrestrial magnetic fields, obtained by Hale (1908).

This splitting affects the observed spectral lines, producing a shift in the 21-cm neutral Hydrogen line. The measurement of this splitting in the

hydrogen in the interstellar medium could provide a determination of the magnetic field present in it. In a background magnetic field of order μG in this medium, the splitting produced in the 21-cm line would be $\Delta\nu \sim 3Hz$. This makes the line to appear as two separated lines. However this splitting is too small compared with the Doppler effect. Atoms in the interstellar medium are in thermal motion which produces, by Doppler effect, a broadening of the spectral lines. The broadening is given by:

$$\Delta\nu_D \sim \left(\frac{v_{th}}{c}\right)\nu$$

where v_{th} is the thermal velocity. In the interstellar medium the amount of Doppler broadening is $\Delta\nu_D \sim 30kHz$, much larger than the Zeeman splitting. For that reason, as far as we know, there are no confirmed detections of Zeeman splitting in systems beyond the galaxy. Within it however, some measurements of this splitting have been found in regions with low temperature and high magnetic field, like in star forming regions near the Galactic center, water and OH masers, and CN and CH regions. All these observations range in the mG interval. These observations are regarded to be local, since the mentioned molecules are much less common than neutral Hydrogen in the interstellar medium, but they are useful to understand the local nature of the galactic magnetic field.

3.1.2 Synchrotron emission.

The synchrotron emission is the radiation produced by the relativistic electrons moving in spirals along the magnetic field lines. It provided the first observation of large scale magnetic field fields in external galaxies. The synchrotron radiation is an important measurement because it contains both indicators of magnetic strength and, attending to the polarization of the emitted radiation, information about the field structure and uniformity. The quantity of interest is the emissivity, i.e. the energy emitted per unit volume, per unit time, per unit frequency and per unit solid angle. It depends on the total transverse component of the field in the form:

$$W(B_T, \nu) = W_0 n_0 B_T^{(1+\alpha)/2} \nu^{(1-\alpha)/2}$$

W_0 is a constant depending on the spectral index α, which is also involved in the relativistic electron number density distribution:

$$n_e = n_0 E^{-\alpha}$$

The measurement procedure is more indirect than the one coming from the Zeeman effect. It is performed by specifying the electron density distribution of the source. It is a model dependent quantity that is difficult to determine. Sometimes [88] it is estimated by using equipartition, but this is not applicable in all cases. The averaged values observed in galaxies by means of this effect range in the μG interval.

3.1.3 Faraday rotation.

Polarized electromagnetic waves, propagating through a region with both magnetic field and free electrons, experience a rotation of the polarization plane with time as they advance through the region. This effect is particularly interesting from the observational point of view, when a polarized radio wave passes through a region filled with a plasma with a magnetic field. The Faraday effect predicts an amount of rotation of the plane of polarization given by the angle:

$$\phi - \phi_0 = \frac{e^3\lambda^2}{2\pi m_e^2 c^4}\int_0^{l_s} n_e(l)B_L(l)dl$$

where l_s is the length of the path in the cited region, λ is the wavelength of the radiation, ϕ_0 is the initial polarization angle, and $n_e(l)$ is the thermal electron density along the line of sight. This angle difference is usually given in terms of the rotation measure (RM):

$$\phi - \phi_0 = \mathrm{RM}\lambda^2$$

RM is approximately expressed as:

$$\mathrm{RM} \sim 811.9\int_0^{l_s}\Big(\frac{n_e}{cm^3}\Big)\Big(\frac{B_L}{\mu G}\Big)d\Big(\frac{l}{kpc}\Big)$$

The λ dependence of the rotation angle is useful to determine the value for $\bar{B}_L$. In general the polarization angle must be measured at three or more wavelengths in order to determine the RM accurately and remove the $\phi = \phi \pm n\pi$ degeneracy. As in the synchrotron radiation case, the column density of electrons has to be determined in someway. One technique has showed to be especially useful. It is the study of the delay of different radio pulses coming from pulsars [89]. This allows a very accurate description for our galaxy and external galaxies LSMF. However, in general clusters, it has been very difficult to determine the column density of electrons. Nevertheless, observations have been extracted from a sample of clusters, composed

by some regular Abell clusters, with one or two radio sources inside [90]. Their electron density was determined by the x-ray sky survey ROSAT [91], and their RM was obtained by the VLA radio-telescope. All they showed a large scale magnetic field with an order μG strength, that could not be associated to galaxies [90].

As a summary we can say, that the experimental measurements showed in the previous section come from these effects. More concretely, the galactic measurements can be divided in results for the Milky Way, where the three effects exposed above can be used, and other galaxies, where the measurements come basically from synchrotron emission and Faraday rotation. Zeeman splitting is useless in that case because of the Doppler effect described above. In the case of the cluster and supercluster measurements, the only effect available is the Faraday rotation. This together with the fact that there are not many clusters with the appropriate sources to be measured, makes the cluster measurements a bit less confident.

3.2 UHECR and the Future of LSMF measurements.

Apart from the previously discussed measurements, a new and promising way for the experimental study of the LSMF, has being developed during the last years. It is the possibility that the study of the cosmic rays can be used to extract information of the magnetic fields they travel through. Without the aim of being exhaustive, I would like to review the main concepts of the issue and the future possibilities.

There is a concept that, as will be discussed in following chapters, has crucial importance in the evolution of any magnetic field, specially for the LSMF, and it is then desirable to measure. It is the magnetic helicity (see chapter 7). The magnetic helicity can be measured by means of different mechanisms, as the analysis of the polarization of the synchrotron radiation. But its determination always involves additional information about the system. In situations with few or null additional information it is difficult to measure. For example, in the case of magnetic fields detected only by Faraday rotation (as is the magnetic field present in clusters) is impossible to measure the helicity, since the Faraday effect is insensitive to it. The measurement of the helicity in such cases is a challenging problem. However [67] proposed that measurements of the helicity could be performed through the

study of the bending of the trajectories of the cosmic rays. This promising proposal, had to face a big problem. To know the bending of a trajectory it is necessary to know the origin of the cosmic ray. Unfortunately the by far majority of the cosmic rays that arrive to Earth are of the type LECR (Low energy cosmic rays). These rays have not enough energy to maintain an approximately straight trajectory, and are strongly deflected by the magnetic fields they are passing. It is then impossible to know their origin, and representing a problem for the proposal of [67][1]. However, at present this problem could be solved.

Although much less frequent than the LECR, there exist another kind of cosmic rays, the Ultra High Energy Cosmic Rays (UHECR). They have energies above $40EeV$ ($1EeV = 10^{18}eV$). They are so energetic that maintain their straight trajectory, being possible to determine their source. For their detection and study the Pierre Auger Observatory[2] (PAO) was created. Recentely, the PAO collaboration [46] announced the conclusion that the origin of these UHECR is linked to Active Galactic Nuclei (AGN) of nearby galaxies, giving a catalog of hundreds of sources for these rays. This result opens the possibility for measurements similar to the ones proposed in [67].

Furthermore, apart of the information about helicity, these UHECR could be used to confirm the measurements of LSMF in clusters, since the found sources are outside of our galaxy. As an example, reference [47] claims that no sources for cosmic rays will be found further away than $\sim$ 100Mpc, if it is true that there exists a magnetic field with an intensity of at least $\sim$ 100nG, which surrounds the sources over distances of several Mpc, as is the expected case if the sources lie within a cluster.

These facts ensures a promising future for the observations of the LSMF.

3.3 Origin and evolution.

As discussed in our papers [118], [121], the main difficulty in understanding the origin of magnetic fields is not in their amplitude (i.e. magnitude) but in its correlation scale, from galaxies to clusters to superclusters. The microgauss order of magnitude of present galactic MF could be explained easily from an amplification via a dynamo mechanism initiated by a tiny seed, with

[1] In the paper, they claim that without knowing the sources, it is possible to use their proposal if there is some knowledge of the distribution of sources, but they do not explore this possibility in detail.

[2] www.auger.org

$B \sim 10^{-23} - 10^{-30}$ G (when taking into account gravitational collapse in a flat ΛCDM model). The explanation of the scale of the magnetic seed in this case is rather straightforward. The dynamo mechanism is an exponential mechanism which makes the MF amplitude increase a factor e at every turn of the object (typically a galaxy) with free charge and thus large electrical conductivity. Since the typical galaxy has made around 30 turns in their lifetime, the growth factor is $e^{30} = 10^{13}$. Since we observe microgauss, we just need a seed $B_{\rm seed} \sim 10^{-19}$ G over a scale of 30 kpc. This is the MF *after* gravitational collapse. Typically a galaxy forms by gravitational collapse of a lump of matter the size of about a Mpc with density of order the critical density, and ends collapsing to a size of order 30 kpc and density $\rho_{\rm gal} \sim 10^6 \rho_c$. By flux conservation, the gravitational collapse amplification gives an extra factor

$$(\rho_{\rm gal}/\rho_c)^{2/3} \sim 10^4 \,,$$

which gives a seed $B_{\rm seed} \sim 10^{-23}$ G over a scale of 1 Mpc. This calculation was done assuming matter domination. If we consider a ΛCDM universe, then gravitational collapse amplification is greater and the seed can start with $B_{\rm seed} \sim 10^{-30}$ G over a scale of 1 Mpc. This is the *minimal* value required for a typical galaxy.

The microgauss amplitude at cluster scales is more difficult to explain via a dynamo mechanism because it did not have as much time since its formation to build up from such a tiny seed, and the order of fractions of microgauss amplitude at supercluster scales is simply impossible to explain by dynamo mechanisms or gravitational collapse. In any case, even in the presence of dynamo amplification, an initial magnetic seed is required which is not provided by the dynamo mechanism itself. Theoretical models trying to account for the origin of the primordial seeds can be classified in two groups:

- Astrophysical: Biermann battery in intergalactic shocks, stellar magnetic winds (like in our Sun), supernova explosions, galactic outflows in the inter-galactic medium (IGM), quasar outflows of magnetized plasma into the intra-cluster medium (ICM), see Refs. [25, 28, 32], and a recently suggested proposal in conjunction with high energy cosmic rays [37].

- Cosmological: Early universe phase transitions [38]-[62], magnetic helicity together with the baryon asymmetry of the universe (BAU) at the

electroweak (EW) transition [68]-[75], via hypercharge and hypermagnetic field generation before EW transition [76, 77], from second order cosmological perturbations from inflation [78]-[101], from preheating after inflation [102]-[105], etc.

Moreover, MF have also been observed in quasars at redshift $z \sim 2$, again with a magnitude of order the microgauss. This indicates not only ubiquity but also invariance (within an order of magnitude) with time. Such features cry for a cosmological, rather than astrophysical, origin of MF. Could it be that some yet unknown mechanism directly generated microgauss MF on all scales? The first reaction is to ask about the dynamo mechanism in galaxies, would it not amplify this microgauss MF to even larger amplitudes, as can be seen in neutron stars, and even our Sun? The surprising answer is no, because a few microgauss is the *maximum* magnetic field possible on galactic scales, due to the existence of relativistic cosmic rays and ionized gas moving at large speeds. If one computes the total energy density in cosmic rays (integrating the measured flux spectrum over all energies), one finds

$$\frac{1}{2}\rho_{\rm CR}v^2/c^2 = 0.5 \text{ eV/cm}^3\,,$$

and a similar number for the energy density in the ionized gas moving with rotation speeds of order 200 km/s,

$$\frac{1}{2}\rho_{\rm gas}v^2/c^2 = 0.3 \text{ eV/cm}^3\,.$$

If we assume that magnetic fields are in equilibrium, due to their interaction with the cosmic rays and the gas, and furthermore we suppose equipartition, then their energy density (using 1 G $= 1.95 \times 10^{-20}$ GeV^2) becomes

$$\rho_{\rm B} = B^2/2 = 0.5 \text{ eV/cm}^3 = (2.5\ \mu\text{G})^2\,,$$

which corresponds to a few microgauss, in surprising agreement with observations. Some people suggest that this argument may also explain the cluster MF value.

The ubiquity of MF with similar amplitude on all scales reminds us of the issue of Helium abundance in the universe. Early measurements in the fourties indicated that the Helium mass fraction to Hydrogen in the Universe was about a quarter, very nearly *everywhere*. This observation was correctly interpreted by Gamow and collaborators as indicating a primordial origin. Simple order of magnitude computation of nuclear interaction rates

(mainly those of deuterium, a necessary step in the reactions from H to He) and comparison with the rate of expansion in the early universe at temperatures of order the nuclear transitions (i.e. MeV), together with the then largely unknown neutron decay rate, suggested that the present abundance of Helium could have been produced from Hydrogen in the early universe and thus be present everywhere. The other light elements seemed to require further synthesis in stars and thus depended on location, but the Helium was ubiquitous because it was there from the very beginning.

Something similar may have happened with magnetic fields, if they were generated in the early universe by some unknown mechanism and then redshifted until today. The question is what is the typical energy density which today gives the order microgauss fields? These fields (if homogeneous) redshift as radiation, i.e. $\rho_{\rm B}(a) = \rho_{\rm B}({\rm today})(a_0/a)^4$. Like with Helium, we have to ask what was the energy scale of interactions responsible for the generation of primordial magnetic fields? Photons are massless so in principle any scale, as long as there are charged particles, is sufficient to generate magnetic fields, and this is the reason why there is still so much debate as to their origin. However, was the universe always permeated with electromagnetic waves? The answer is no, the electromagnetic interaction as we know it came into being at a very precise time, when the electroweak (EW) force broke into the weak interactions plus electromagnetism. Before we could not talk about photons and magnetic fields. This occurred when the typical energy (or temperature) in the universe was around $T_{\rm EW} \sim 100$ GeV. If we construct an energy density with this scale we get $\rho_{\rm EW} \sim 10^8$ GeV^4. At that time the universe was (or became) radiation dominated. If we now redshift this MF energy density until today ($T_0 = 2.725$ K) we get

$$\rho_{\rm B}({\rm today}) = (T_0/T_{\rm EW})^4 \rho_{\rm EW} \sim 3.04 \times 10^{-53}\ {\rm GeV}^4 = 0.4\ {\rm eV/cm}^3$$

which is *precisely* the order of magnitude of the present MF energy density.[3] This would be enough to explain the cluster and supercluster values, and would perhaps require a mild dynamo mechanism to grow to galactic values (if the fraction of energy stored in the magnetic field $f \ll 1$). The question is whether this is just a coincidence or it is hinting directly at its origin.[4] While other mechanisms require a seed with an arbitrary scale (typically

[3] We could be even more conservative and suppose that the fraction of magnetic field energy density to radiation at the time of the EW transition was given by $f = \rho_{\rm B}/\rho_{\rm rad} < 1$. In this case, the present MF magnitude would be $B_0 \sim 5\, f^{1/2}\ \mu$G.

[4] Some authors suppose that the generation occurred *earlier* in the form of hypermagnetic fields and was then converted into ordinary magnetic fields at the EW scale [77].

$B \sim 10^{-23}$ G, so that today we observe microgauss MF on galactic scales via the dynamo mechanism), there is no physical reason behind this scale. On the other hand, the EW scale is a *natural* scale for the generation on magnetic fields since it is the scale at which electromagnetism arises for the first time as a fundamental interaction.

Whether this is sufficient reason to assign the EW energy scale to the origin of magnetic fields is another issue. In particular, it is not clear how to obtain the large correlation length of magnetic fields observed at galactic and cluster scales. Any physical mechanism that creates magnetic fields must be necessarily causal, but at high temperatures in the early universe there is also a natural coherence scale given by the particle horizon. At the electroweak scale the physical horizon is 10^{-10} light-seconds ($\sim$ 3 cm), which today corresponds to a co-moving scale of 0.3 Mpc ($\sim$ 1 AU), clearly insufficient when compared even with the irregular (turbulent) component of the galactic magnetic field ($L \sim$ 100 pc), not to mention the regular (uniform) component, which has correlations $L \sim$ 10 kpc. It thus seems impossible to explain the coherent magnetic fields observed on galaxy clusters and supercluster scales (of order 10 Mpc) with intensities of order μG to nG.

There is however a second coincidence, which makes things even more intriguing. If we assume that the plasma after the electroweak transition is sufficiently turbulent to maintain magnetic fields of the largest possible coherence scales via inverse cascade [45]-[62], then we could reach cosmological scales today. Let us follow the argument. The largest coherence scale at the electroweak transition is the physical horizon, of order 3 cm. If a strong inverse cascade is active, then the coherence length of the magnetic fields will grow as fast as the horizon (it cannot grow faster). This means that it grows like the scale factor *squared* during the radiation dominated era. This ideal situation could only last while there is a plasma and thus it is bound to stop acting at photon decoupling, when the universe becomes neutral. Since then, the correlation length can only grow with the expansion of the universe, as the scale factor. If we take this effect into account from the electroweak scale until today we find, using the adiabatic expansion relation $T \propto a^{-1}$,

$$\xi_0 = \xi_{\rm EW} \left(\frac{a_{\rm dec}}{a_{\rm EW}}\right)^2 \frac{a_0}{a_{\rm dec}} = 3\,{\rm cm} \left(\frac{T_{\rm EW}}{T_{\rm eq}}\right)^2 \frac{T_{\rm eq}}{T_0} \sim 6 \times 10^{25}\,{\rm cm} = 20\ {\rm Mpc}\,, \tag{3.1}$$

where we have made the approximation that equality and decoupling occurred more or less simultaneously (a careful computation gives only a minor correction). The surprising thing is that this simple calculation gives

precisely the order of magnitude for the largest correlation length of cosmic MF ever observed (i.e. cluster scales). If the agreement in the magnitude of the primordial MF seed seemed peculiar, the fact that an inverse cascade could also be responsible for the observed correlation length becomes a surprising coincidence, probably hinting at an underlying mechanism. It is therefore worthwhile exploring the conditions that could have taken place at the electroweak transition which could give rise to a significant fraction of energy density in magnetic fields, and be responsible for a sustained period of inverse cascade until photon decoupling. It has been shown in Refs. [57]-[62] that one important ingredient is the generation of magnetic fields with a non trivial helical component, which guarantees an optimal amplification of the magnetic correlation length through inverse cascade. A very good account of the large number of works investigating these issues, with a complete list of references is given in Ref. [25] (see also [43]-[77]).

3.4 The Hypothesis.

In the previous section, we have presented several arguments in favour of placing the generation of the LSMF at the EW transition. This is the basic hypothesis underlying the work developed in this thesis. More specifically, our proposal can be expressed as follows:

- The large scale magnetic fields were generated during the EW symmetry breaking period.
- We assume that this breaking takes place in the context of a preheating scenario at the end of inflation, providing a cold EW phase transition.
- It is precisely in this preheating epoch, which is highly non-perturbative and out of equilibrium, where we place the generation mechanism for the magnetic fields.
- After the generation, these fields persist and there exists some mechanism providing an enhancement of the magnetic field correlation length.

In what follows, we will give support to these statements. We can say that to achieve these results, two essential items have been required: First, a model combining inflation and EW symmetry breaking. This is described in chapter 4. Second, a way to study the non-perturbative, out of equilibrium preheating epoch and the complicated dynamics taking place afterwards.

This is provided by the use of lattice techniques, exposed in general in chapter 5, together with the classical approximation. These conform what we call the methodology, further discussed in chapter 6.

We will also need to address the issue of the creation and persistence of the magnetic fields, and the enhancement of their correlation length. As we will see in all of them, the concept of helicity will play a crucial role. For that reason we dedicate a chapter to the helicity related issues. This is chapter 7. We take as a reference for the discussion presented in that chapter, the literature about helicity in the context of magnetohydrodynamics and turbulence. We also review in that chapter, what we think is the magnetic generation mechanism present in our system, as will be manifest in chapter 8. The analysis of the actual persistence and growth of the correlation length in our system will be presented in chapter 9.

Chapter 4

Inflation and Cold electroweak transition.

The scenario we will be considering is that of preheating after a period of hybrid inflation which ends at the EW scale. This was first introduced in Ref. [108] to provide a new mechanism for the generation of baryon asymmetry in the Universe (BAU). It has been extensively studied since then both in connection with BAU [108]-[116] and in relation with the production of gravitational waves [117]. In the present thesis we include for the first time the Hypercharge field in order to study the generation of electromagnetic fields during preheating. In this chapter we will briefly review the basics of the inflationary paradigm, especially those aspects referring to Hybrid inflation, we introduce the model and describe the first stages of evolution after inflation ends which provide the initial conditions for the non-linear approach addressed in chapter 6.

4.1 Cosmological Evolution.

The study presented in this thesis relies on a particular scenario in a very particular epoch in the evolution of the Universe. This scenario is placed at the electroweak phase transition. For those non-familiar with the cosmological terminology and in order to place the reader in context, in this section I briefly present a time line evolution of the Universe, from the electroweak epoch until nowadays, and locate on it some of the most important events that have taken place.

We take as starting point the electroweak phase transition, at a scale of around 100GeV. According to the Standard Model physics, the scalar Higgs

field acquires a non vanishing vacuum expectation value, breaking the gauge group symmetry $SU(2) \times U(1)$ into a $U(1)_{em}$ remnant. This implied the onset of the electromagnetic force as an independent force. At this time the causal horizon had an extension of approximately 3cm.

The next important event in the evolution of the Universe, is the QCD phase transition, at a temperature around $T_{QCD} \sim 170$MeV. It is in this transition where the free quarks and gluons get confined into hadrons.

At a temperature of around $T \sim 1$MeV neutrino decoupling takes place. Previously, the neutrinos were in thermal equilibrium with the primordial plasma. This equilibrium, however, can only be maintained while the interactions are frequent enough. Due to the expansion of the Universe, at this epoch these primordial neutrinos stop to interact with the rest of the matter, preserving a thermal distribution at the temperature of the moment.

Almost at the same epoch, nucleosynthesis took place. In this epoch the first light nuclei appeared in the Universe from the free hadrons. Its scale is again ~ 1MeV which is the typical binding energy of a nucleus.

Before nucleosynthesis, the Universe has been dominated by relativistic particles with high energy. That means that the energy density of the Universe diluted with the scale factor as $\rho \propto a^{-4}$. Long time after nucleosynthesis, as the Universe was expanding and cooling down, the matter stopped to behave like a relativistic fluid, changing the evolution of the energy density into a matter dominated era, in which $\rho \propto a^{-3}$.

Following with its expansion, the Universe reached a temperature of $\sim$ 1eV. This temperature represents an energy below the binding energy of an atom, so neutral atoms started to appear. This produced the photons to interact rarely with matter and propagate freely. The light emitted at photon decoupling produced a signal observed today as the Cosmic Microwave Background. It shows that the Universe at that stage was not completely homogeneous. These inhomogeneities conformed as the Universe evolved, the seeds for galaxies and stars, and the structure of the Universe nowadays.

This expanding evolution gives at present a temperature of $\sim 2.7\,K$, thousands of millions of years later. At our time, we are again in a transition epoch. The Universe is going from the matter dominated era to a vacuum dominated era. This statement comes from the interpretation of the observations as the existence of a non-zero cosmological constant.

4.2 The inflationary paradigm.

In this section some essentials of the inflationary paradigm are reviewed.

Inflation was proposed with the aim to solve several problems arising in the very early Universe, as was the flatness, homogeneity, monopole and causality problems in the standard Big Bang theory [1] $\sim$ [4]. It also explains the presence and size of anisotropies in the Cosmic Microwave Background (CMB). What characterizes the Inflationary period is that the Universe experiences an accelerated expansion. Some generalities of the inflationary process can be described before going to concrete models. In an isotropic homogeneous Universe the metric is described by:

$$ds^2 = dt^2 - a^2(t)[\frac{dr^2}{1-Kr^2} + r^2(d\theta^2 + sin^2\theta d\phi^2)], \tag{4.1}$$

where K is the usual parameter that depends on the geometry of the Universe, being $K = 0$ for a flat Universe and $K = \pm 1$ for an positive/negative curvature Universe. The variable $a(t)$ is the spatial radius of the Universe in terms of which the Hubble parameter is defined as:

$$H(t) = \frac{\dot{a}(t)}{a(t)}. \tag{4.2}$$

Considering that the Universe at some early epoch was filled with an homogeneous isotropic fluid, the Einstein equations with the metric (4.1) are:

$$\begin{aligned} \left(\frac{\dot{a}}{a}\right)^2 + \frac{K}{a^2} &= \frac{8\pi}{3M_P^2}\rho, \\ \frac{\ddot{a}}{a} &= -\frac{4\pi}{3M_P^2}(\rho + 3p), \end{aligned} \tag{4.3}$$

where it is used the fact that for a homogeneous, isotropic fluid, the comoving energy momentum tensor is diagonal:

$$T^\mu_\nu = \mathrm{diag}(\rho, p, p, p) \tag{4.4}$$

where ρ and p are the energy density and pressure of the fluid. These equations can be solved in certain situations, if we make use of the equation of state:

$$p = \omega\rho \tag{4.5}$$

where ω is a constant with known values for several cases. The equations can be solved for those limiting values. For a radiation dominated Universe $\omega = 1/3$, the equations (4.3) give assuming $K = 0$:

$$\begin{aligned} \frac{\rho}{\rho_0} &= \left(\frac{a}{a_0}\right)^{-4}, \\ \frac{a}{a_0} &= \left(\frac{t}{t_0}\right)^{1/2} \end{aligned} \tag{4.6}$$

For a matter dominated Universe $\omega = 0$, leading to:

$$\begin{aligned} \frac{\rho}{\rho_0} &= \left(\frac{a}{a_0}\right)^{-3}, \\ \frac{a}{a_0} &= \left(\frac{t}{t_0}\right)^{2/3} \end{aligned} \tag{4.7}$$

For a vacuum dominated Universe $\omega = -1$ and:

$$\frac{\ddot{a}}{a} = \left(\frac{\dot{a}}{a}\right)^2 > 0, \tag{4.8}$$

hence the Universe experiences an accelerated expansion. If the vacuum energy is dominating, this equation takes a simple form:

$$\left(\frac{\dot{a}}{a}\right)^2 = \frac{8\pi}{3M_P^2} V_v, \tag{4.9}$$

which can be solved giving:

$$a(t) \sim a_0 \, e^{H(t-t_0)} \tag{4.10}$$

where $H \sim \sqrt{\frac{8\pi}{3M_P^2} V_v}$.

Inflation is usually described, by means of a scalar field the Inflaton χ. The Lagrangian for such a field can be generally described by:

$$\mathcal{L} = \frac{1}{2} g^{\mu\nu} \partial_\mu \chi \partial_\nu \chi - V(\chi). \tag{4.11}$$

The equations of motion for this field in a expanding background are obtained by substituting the $g_{\mu\nu}$ metric by (4.1), and are quite similar to (4.3). If we assume that the field is homogeneous and neglect spatial derivatives in the energy, we obtain for the equation of state:

$$p = \omega\rho, \tag{4.12}$$

$$\omega = \frac{\frac{1}{2}\dot{\chi}^2 - V(\chi)}{\frac{1}{2}\dot{\chi}^2 + V(\chi)} \sim -1. \quad (\text{if } V(x) >> \dot{\chi}^2)$$

The equations of motion of the Inflaton can be written as:

$$H^2 = \frac{8\pi}{3M_P^2}\Big(\frac{\dot{\chi}^2}{2} + V(\chi)\Big), \tag{4.13}$$

$$\ddot{\chi} + 3H\dot{\chi} + V'(\chi) = 0.$$

with $V'(\chi) = \frac{dV}{d\chi}$ and again neglecting (by homogeneity) $\partial_i^2\chi$. Both the initial condition for the Inflaton field, that is treated as a classical field, and the explicit form for the potential, are free to choose.

If the potential energy dominates over the kinetic term these equations can be easily solved in the so called "slow-roll" approximation. It involves neglecting the kinetic energy versus the potential one, as well as the $\ddot{\chi}$ term in the equations of motion (4.13). The accuracy of this approximation is controlled by three parameters, called the slow-roll parameters:

$$\begin{aligned} \epsilon &= -\frac{M_P^2}{16\pi}\Big(\frac{V'}{V}\Big)^2, \\ \eta &= \frac{M_P^2}{8\pi}\Big(\frac{V''}{V}\Big), \\ \xi^2 &= \frac{M_P^4}{(8\pi)^2}\Big(\frac{V'V''}{V^2}\Big) \end{aligned} \tag{4.14}$$

They enter the equations of motion (4.13) in the way:

$$\begin{aligned} \frac{\ddot{\chi}}{H\dot{\chi}} &\simeq \epsilon - \eta, \\ \frac{\dot{\chi}^2}{V} &\simeq \frac{\epsilon}{3} \end{aligned} \tag{4.15}$$

If $\epsilon \ll 1$ and $\epsilon - \eta << 1$ these equations can be simplified to:

$$\dot{\chi} \sim -\frac{1}{3H}V', \qquad (4.16)$$
$$H^2 \sim \frac{8\pi}{3M_P^2}V$$

This is the "slow-roll" limit. When the potential derivatives are such that the system enter this limit is said that the Inflaton field is "slow-rolling" and the Universe inflates, since:

$$\frac{\dot{H}}{H^2} = -\epsilon \rightarrow H \sim cte, \qquad (4.17)$$
$$\frac{\ddot{a}}{a} = H^2(1-\epsilon) > 0.$$

All the observable quantities can be expressed as powers of these "slow-roll" parameters. Usually it is enough to keep just the first order terms.

Last, but not least, I must say that, as previously pointed out, the inflationary description does not fix either the form of the potential $V(\chi)$ or the initial condition for χ. For that reason there are several models that are profusely studied in the literature. It is not the issue of this thesis to present an exhaustive review of all this models, since it is performed in the context of one of them, the Hybrid Inflation model. Nevertheless, it is worth to say something about model building and how to rule out models. The most important way to filter which models are suitable to be physically realized is the accuracy of their predictions for the CMB anisotropies. That is, the way they connect the initial Inflaton fluctuations with the temperature fluctuations of the CMB. The important observational quantities in terms of the potential and the slow roll parameters are given by:

$$|\delta_H|^2(k) = \frac{1}{150\pi^2 m_{pl}^4}\frac{V_{\mathcal{H}}}{\epsilon_{\mathcal{H}}}, \qquad (4.18)$$
$$n(k) - 1 = -6\epsilon_{\mathcal{H}} + 2\eta_{\mathcal{H}},$$
$$\frac{dn}{d\ln(k)}(k) = -16\epsilon_{\mathcal{H}}\eta_{\mathcal{H}} + 24\epsilon_{\mathcal{H}}^2 + 2\xi_H^2.$$

The $\mathcal{H}$ subscript means evaluation of V, ϵ, η and ξ at the appropriate number of e-folds. Without the aim of being exhaustive, this quantities are referred to the mode k of the perturbations in the energy density. The first is the

amplitude of the density fluctuation for the mode k, the second is called the spectral index, and the third is the running of the index. The standard inflationary perturbation theory establishes that the modes of any perturbation are amplified till they leave the horizon, at time $t_{\mathcal{H}}$. At this time they are "frozen" until they reenter the horizon later on. For that reason and to be compared with the observations coming from the CMB, for a particular inflationary model, these quantities must be evaluated at time $t_{\mathcal{H}}$. This time depends on the particular scale of each mode k. The experimental scale of reference is k_0 which is the WMAP pivot scale $k_0 = 0.05\text{Mpc}^{-1}$. At this scale the values of these parameters[1] have been measured [5, 6] to be:

$$\begin{aligned} &|\delta_H|^2(k_0) = (3.8 \pm 0.5) \times 10^{-10}, \\ &1 - n(k) = 0.037^{+0.015}_{-0.014}, \\ &\frac{dn(k)}{d\ln(k)} = -0.037 \pm 0.028 \end{aligned} \tag{4.19}$$

In order to compare the experimental values with the ones provided by the models, these last must be evaluated at the time the corresponding scale crossed the horizon. This time is expressed by means of a quantity called the number of e-folds N_k before inflation ends.

The experimental values together with the requisite that the energy stored in the Inflaton field at the end of inflation must be the electroweak energy scale, allows to discard several models. The energy scale condition is required to provide a reheating temperature of the Universe lower than the electroweak phase transition, otherwise the symmetry would be restored. This reheating temperature arises from the fact that, after the end of inflation, the Inflaton field still has a remnant potential energy. This energy can be transferred to the other degrees of freedom of the system. This process would end at equipartition at a determined temperature, the reheating temperature. The way this reheating process is actually performed follows three different mechanisms of interest: Usual perturbative reheating, trough perturbative particle decay [7] $\sim$ [11], resonant preheating [11], [12], [13], [14], and finally the one of interest for this work, the tachyonic preheating, in which the coupling of the Inflaton to an additional scalar field (Higgs) induces the end of inflation and triggers the symmetry breaking as a low temperature transition [15], [16], [109] and [111].

[1] Actually there are four more parameters used to perform the fit to the data: Hubble constant h, matter density $h^2\Omega_m$, barion density $h^2\Omega_b$ and optical depth τ. See [5] and [6].

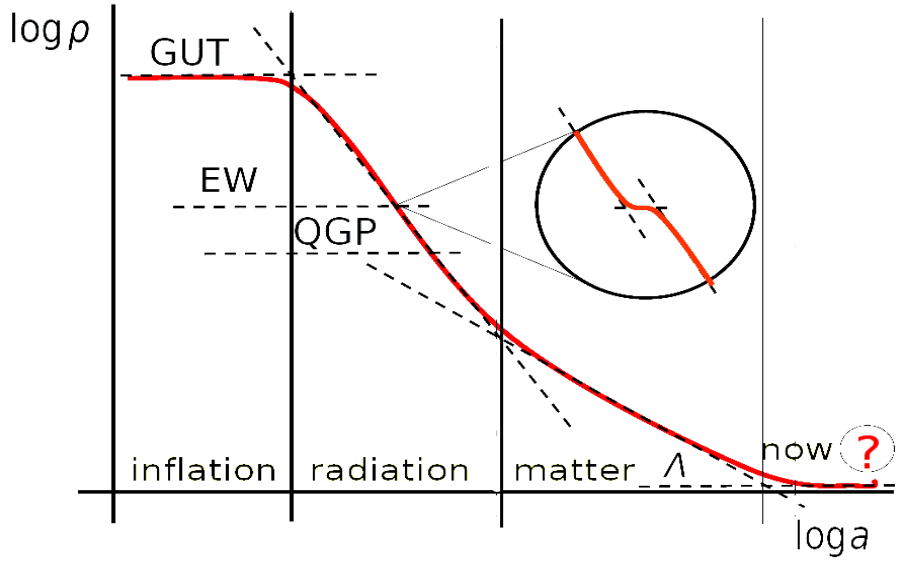

Figure 4.1: Log-log schematic plot of the behavior of the energy density with the scale factor. The inflationary processes are plateaux in the figure. In the detail within the circle, we also show the short inflationary period at the EW scale, which is expected to last only a few e-folds. Also showed is a possible main inflationary process at the GUT scale, responsible of the CMB anisotropies. From "Signatures from preheating", J. García-Bellido, KITP Seminars (UCSB).

One of the models that would produce inflation at the electroweak energy scale, is the Hybrid inflation model. However it is not obvious the existence of electroweak inflationary models which satisfy both the observables (4.18) according with the experimental ones and support the necessary 60 e-folds to explain the CMB anisotropies. Hence it is problematic if one tries to fix CMB with low scale inflation. Fortunately we do not have to require that. In our approach, we only need an electroweak inflationary process that last for a few e-folds, enough to cool down the Universe, providing the appropriate initial conditions for our purposes, as will see in chapter 6. We leave the production of the CMB anisotropies to another inflationary process, maybe at GUT scale, that happened before and is independent of this electroweak scale one. This is schematically illustrated in figure 4.1.

4.3 Hybrid inflation.

After the discussed generalities about inflation, in the following we shall concentrate in the particular model we are using to describe the short electroweak scale inflation presented in figure 4.1. We are considering that the electroweak symmetry breaking is a dynamical process that is produced as inflation ends. We choose to describe this inflationary process one of the minimal extensions to the Standard Model that allow inflation: The Hybrid inflation model.

The Hybrid inflation model is attained by extending the Standard Model with the addition of a single scalar field, the Inflaton, singlet under the gauge group. It is the dynamics of this Inflaton field which drives inflation and triggers the symmetry breaking. This is achieved by the coupling of the Inflaton to the Standard Model Higgs field, which determines the dynamics of the later. The scalar sector of the model thus includes the Higgs field, that in our case is taken in a quaternion representation: $\Phi = \frac{1}{2}(\phi^0 \, \mathbb{1} + i\phi^a \tau_a)$ (τ_a are the Pauli matrices) and the singlet Inflaton χ which couples only to the Higgs via the scalar potential:

$$\mathrm{V}(\Phi, \chi) = \mathrm{V}_0 + \frac{1}{2}(g^2\chi^2 - m^2)\,|\phi|^2 + \frac{\lambda}{4}|\phi|^4 + \frac{1}{2}\mu^2\chi^2\,, \tag{4.20}$$

where $|\phi|^2 \equiv 2\mathrm{Tr}\,\Phi^\dagger\Phi$, μ is the Inflaton mass in the false vacuum and $m_{\scriptscriptstyle \mathrm{H}} = \sqrt{2}\,m \equiv \sqrt{2\lambda}\,v$ is for convenience the Higgs mass, with $v = 246$ GeV the Higgs vacuum expectation value at the electroweak scale. The gauge sector contains both the SU(2) and the hypercharge U(1) fields with

$$\mathcal{G}^a_{\mu\nu} = \partial_\mu \mathcal{A}^a_\nu - \partial_\nu \mathcal{A}^a_\mu + g_{\scriptscriptstyle \mathrm{W}} \epsilon^{abc} \mathcal{A}^b_\mu \mathcal{A}^c_\nu \tag{4.21}$$

and

$$\mathcal{F}^{\scriptscriptstyle \mathrm{Y}}_{\mu\nu} = \partial_\mu \mathcal{B}_\nu - \partial_\nu \mathcal{B}_\mu, \tag{4.22}$$

their respective field strengths. The covariant derivative is:

$$\mathcal{D}_\mu = \partial_\mu - \frac{i}{2} g_{\scriptscriptstyle \mathrm{W}} \mathcal{A}^a_\mu \tau_a - \frac{i}{2} g_{\scriptscriptstyle \mathrm{Y}} \mathcal{B}_\mu, \tag{4.23}$$

with $g_{\scriptscriptstyle \mathrm{W}}$ the SU(2) gauge coupling and $g_{\scriptscriptstyle \mathrm{Y}}$ the hypercharge coupling. In this work we can safely ignore fermionic fields since the time scales involved in the perturbative decay of the Higgs and W boson fields into fermions are much larger than the ones considered here. Actually we expect that the main

process for fermion production is the Higgs boson perturbative decay, which is expected to be very weak. A simple calculation, using a decaying rate of about $\sim 0.1\text{GeV}(m_{\text{H}}/(100GeV))$, suitable for the range of Higgs masses we are dealing, we get a time for the first fermions about $mt \sim 1000$, which is far of our latest times $mt \sim 300$.[2] We can also ignore the expansion of the universe at these stages, since expansion rate ($H \sim 10^{-5}\text{eV}$) is very small for the studied times, and perform the analysis presented in this work in Minkowski space.

With all these definitions the Lagrangian density of the model becomes:

$$\mathcal{L} = -\frac{1}{4}\mathcal{G}^a_{\mu\nu}\mathcal{G}^{\mu\nu}_a - \frac{1}{4}\mathcal{F}^{\text{Y}}_{\mu\nu}\mathcal{F}^{\mu\nu}_{\text{Y}} + \text{Tr}\Big[(\mathcal{D}_\mu\Phi)^\dagger\mathcal{D}^\mu\Phi\Big] + \frac{1}{2}\partial_\mu\chi\partial^\mu\chi - V(\Phi,\chi)\,. \quad (4.24)$$

This Lagrangian depends of several parameters, some of them unknown. We discuss the details of the choice of parameters in chapter 6, now we only remark that for our analysis we have fixed the W mass and the Z to W mass ratio to the experimental values [122]. That means we choose the physical values for the gauge couplings g_Y and g_W. The parameter V_0 is the total initial energy, which is set to $1/4\,\lambda\,v^4$. We are free to choose the value of the Higgs to W mass ratio: $m_{\text{H}}/m_{\text{W}} = 2\sqrt{2\lambda}/g_{\text{W}}$. For different reasons coming from both technical and physical considerations, we analyze several values of this ratio, as will be explained in chapter 6. Of the other unknown parameter, the Higgs-Inflaton coupling has been fixed to $g^2 = 2\lambda$ as in supersymmetric models [15, 109]. The dependence of the behavior of the system with the ratio λ/g^2 is also studied in [15]. It was found that for values of this ratio ~ 1 both the Higgs and the Inflaton fields oscillate transferring energy between them. Otherwise if $\lambda >> g^2$ or $\lambda << g^2$, oscillations in one of the fields are strongly dumped. Recently [133] has also studied the effect of the value of this ratio in the production of gravitational waves. Finally, we have taken the Inflaton bare mass to be very low $\mu = 10^{-5}gv \approx 0$.

4.4 The breaking of the EW symmetry.

Once we have the model, let us briefly explain qualitatively how the inflationary process is realized by the Inflaton field and how it drives the Electro Weak symmetry breaking.

[2] Recentely reference [134] discussed in detail the decays of W and Higgs, reaching similar conclusions, although using a different inflationary model. Detailed studies in hybrid models can be found, for instance, in [113] and [114]

For simplicity we neglect the effect of the gauge fields in the whole inflationary episode, and in the first stages before the symmetry breaking. This will be further justified in chapter 6, where the quantitative details of the system are presented. The starting point is then the Lagrangian of the scalar sector. Along the inflationary process, where we start our study, the Inflaton field is described as a background field, being represented by its zero mode alone. This inflationary period is characterized by the fact that the Higgs and the Inflaton fields are displaced from the true minimum of the potential[3]. The Lagrangian is dominated by the false vacuum energy $V_0 = \lambda v^4/4$ which drives the Inflaton dynamics. It is "slowing-rolling" from high values of the zero mode χ towards $\chi \sim 0$ values. More exactly the Inflaton satisfies during the whole inflationary process that $\chi > \chi_c$, where $\chi_c = m/g$. The point where $\chi \sim \chi_c$ marks the end of Inflation, where the energy is no longer dominated by the vacuum one, and will trigger the symmetry breaking. The influence of the Higgs along inflation is expected to be negligible. It does not affect significantly the Inflaton dynamics[4]. However the Inflaton evolution influences drastically the dynamics of the Higgs field, modifying the Higgs potential. In the deeper stages of inflation, the Higgs potential is dominated by the term:

$$V(\phi) = \frac{1}{2} g^2 \chi^2 |\phi|^2 \tag{4.25}$$

which is a very narrow quadratic potential centered in $\phi = 0$. As inflation evolves, the potential of the Higgs is spreading, due to the competence of the terms in $(g^2\chi^2 - m^2)$. At the end of inflation, $\chi = \chi_c$, the quadratic term of the Higgs is null, and the potential of the Higgs field is given by just the quartic term. After that, the Higgs potential presents a negative quadratic term since $m^2 > g^2\chi^2$, which in addition to the quartic potential gives the usual "mexican hat" for the Higgs potential.

Summarizing, the coupling of the Higgs to the Inflation, represents an effective mass for the Higgs:

$$m_{eff}^2 = (g^2\chi^2 - m^2). \tag{4.26}$$

During inflation this effective mass squared is positive, providing a quadratic potential for the Higgs field. After inflation this parameter is negative, giving

[3]The expression: "displaced from the true minimum" could seem that the Inflaton field and the Higgs field are in an instability point of the potential. This is not true. The "false vacuum" is the minimum of the potential along inflation and is stable.

[4]Although there exist radiative corrections to the Inflaton mass. As explained when discussing inflation, they affect its duration.

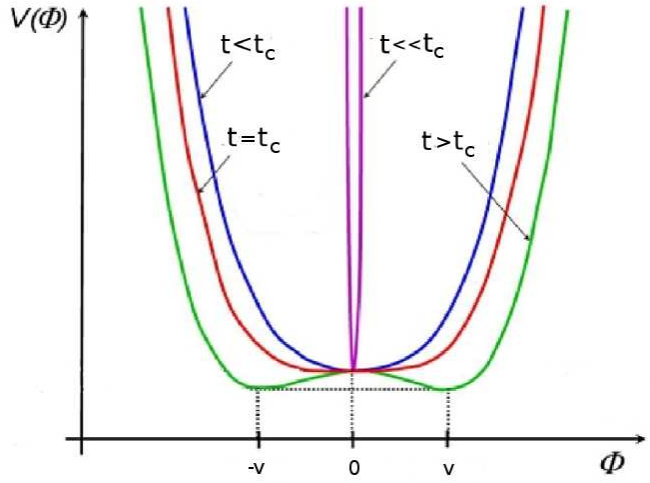

Figure 4.2: Higgs potential evolution during and after inflation. We show the initial narrow quadratic Higgs potential in the deeper stages of inflation, and the final "mexican hat" potential, where symmetry breaking has taken place. t_c stands for the time in which $\chi(t_c) = \chi_c$.

an imaginary or tachyonic mass for the Higgs, which together with the self-interacting quartic term, provides the usual symmetry breaking potential. The whole process can be seen in figure 4.2. The evolution after the end of inflation, can be summarized by the following items:

- End of inflation, which leaves the Universe cold and empty.
- Preheating epoch, which is triggered by tachyonic instability. This is a very non-perturbative out of equilibrium epoch.
- Reheating, a period of transit to equipartition.

4.5 Tachyonic preheating.

As indicated in the previous section, at the end of Inflation symmetry breaking is triggered, through a fast period of energy transfer from the Inflaton into the Higgs field, producing a process known as tachyonic preheating. One aspect that was omitted in the previous section, and which represents one of the main points in the way in which preheating is performed, is the particular dependence with time of the effective mass for the Higgs. The explicit

dependence of the effective mass coupling for the Higgs in our model is introduced in chapter 6. Here we present a much simpler model, in order to explain the essence of this process. This model is the so called "quenched" model, with only one scalar field, that takes the place of the SM Higgs, and in which the effective mass dependence with time, is replaced by a flip in the sign of the coupling m^2_{eff} at a given time, say $t = 0$. No Inflaton is present on this simplified model. The Lagrangian for this model reads:

$$\mathcal{L} = \frac{1}{2}\partial_\mu\hat{\phi}\partial^\mu\hat{\phi} - \frac{m^2_{eff}(t)}{2}\hat{\phi}^2 \tag{4.27}$$

This is the free scalar field Lagrangian, but the coupling $m^2_{eff}(t)$ is time dependent. The time dependence of this parameter is quite simple in this model. If $t < 0$ it is constant and positive, say $m^2_{eff}(t) = m^2$, if $t > 0$ then $m^2_{eff}(t) = -m^2$.

In both cases, the model accepts an analytical solution. We can express the quantum field in terms of its Fourier modes:

$$\hat{\phi}(\vec{x}, t) = \int d^3k\hat{\phi}_k(t)e^{i\vec{k}\vec{x}} \tag{4.28}$$

The equation of motion for each individual Fourier mode is:

$$\ddot{\hat{\phi}}_k = -(k^2 + m^2_{eff}(t))\hat{\phi}_k$$

For $t < 0$ the solution is the one of the harmonic oscillator:

$$\hat{\phi}_k(t < 0) = \frac{1}{\sqrt{2\omega_k}}\Big(\hat{a}_k \exp(-i\omega_k t) + \hat{a}^\dagger_k \exp(i\omega_k t)\Big)$$

where $\omega_k = k^2 + m^2$. This oscillatory feature ensures a similar behavior for any mode in the spectrum.

However if the time is positive, the solution is quite different. Now $\omega_k = k^2 - m^2$, so two differentiated regions split the Fourier modes depending on the value of k. If $|k| > m$ the ω_k value is real and the solution has the same oscillatory behavior as above. But if $|k| < m$, ω_k becomes a complex number and the solution turns into:

$$\hat{\phi}_{|k|<m}(t > 0) = \frac{1}{\sqrt{2\omega_k}}\Big(\hat{c}_k \exp(|\omega_k|t) + \hat{c}^\dagger_k \exp(-|\omega_k|t)\Big)$$

which means an exponential growth of the modes ϕ_k with $k^2 < m^2$, the greater the lower is the value of $|k|$. The operators $\hat{c}_k$, $\hat{c}^\dagger_k$ are related to the

$\hat{a}_k$, $\hat{a}_k^\dagger$ by a Bogoliubov transformation. The enhancement of the modes gives a high population of the correspondent occupation numbers. The definition of the occupation number of a mode is:

$$n_s(k) = \langle s|a_k a_k^\dagger|s\rangle \tag{4.29}$$

where the s states for an arbitrary state of the system. $n_s(k)$ is zero for every k if $|s\rangle$ is $|0\rangle$, a state that satisfies $a_k|0>=0\ \forall k$. From the expression for $\hat{\phi}_k(t<0)$ we can see that the occupation number is related to the correlation function as:

$$n_s(k,t) + 1/2 = \omega_k \langle s|\hat{\phi}_k^\dagger(t)\hat{\phi}_k(t)|s\rangle \tag{4.30}$$

It gives $n_s(k,t) = 0$ if evaluated is $s = 0$. We can evaluate the correlation function after the quench. Just after it the state of the system is the ground state of the harmonic oscillator: $|0\rangle$. For the growing modes $|k| < m$:

$$\langle 0|\hat{\phi}_k^\dagger(t)\hat{\phi}_k(t)|0\rangle\omega_k = \frac{1}{2}[e^{2|\omega_k|t}\langle \hat{c}_k^2\rangle + \langle \hat{c}_k\hat{c}_k^\dagger\rangle + \langle \hat{c}_k^\dagger\hat{c}_k\rangle + e^{-2|\omega_k|t}\langle c_k^{\dagger 2}\rangle] \tag{4.31}$$

The dominant term in the right hand side of this expression is the one with the exponential, so for the growing modes:

$$n(k,t) \sim e^{2|\omega_k|t} \tag{4.32}$$

giving a system with a high population of the low momentum modes.

Summarizing, two differentiated regions appear in the spectrum of ϕ once the flip of m_{eff}^2 is produced. An oscillatory region for modes with $|k| > m$, and a second region of exponentially growing modes for $|k| < m$. In our model, the process is much more complicated, but keeping the same essence at the end. Further information about this complex tachyonic preheating and its implications will be described in chapter 6. Nevertheless this quench model has been extensively used with interesting results. Some studies of this model are [15, 109], in the context of baryogenesis [115], or for particle production [113].

Chapter 5

Lattice gauge theories. A review.

Lattice tools are an essential ingredient to perform the analysis object of this thesis. In this chapter I will briefly review the lattice gauge theory essentials, technicalities specific to our work are postponed to chapter 6 and Appendices A and B. The aim here, is to give some sort of introduction for those not familiar with the lattice notation. We will make particular emphasis in those aspects directly relevant for this thesis. In this sense this is not a usual lattice review.

5.1 The Lattice set-up.

The lattice is a method commonly used in quantum field theory, since it provides both a natural cuttoff for the theory and a non-perturbative way to study strongly coupled systems. In this thesis the lattice is used to transform a classical gauge theory into a classical lattice gauge theory, in order to perform a numerical resolution of the equations of motion. Since the most important application of the lattice in this work has been this treatment of a classical gauge theory, we will develop all the concepts in this chapter in that classical context.

The starting point of this lattice review for non specialists, is to try to show the usefulness of the lattice formulation. First of all, I would like to note that the lattice, as a first approach, is just a discretization of the space and usually the time in terms of some arbitrary quantities, that are called the lattice spacings. I say first approach because this discretization has several

non-trivial implications, than go beyond what a simple discretization could seem, and that makes the lattice theory much more rich and complicated. Moreover the inclusion of gauge fields, in some sense, represents a complication on the lattice, that is solved in an elegant way by the use of the link variables, and goes a little further than a mere discretization. All this is explained below, but for the moment the discussion will focus just in a theory without gauge fields.

In this chapter I will also only concentrate in bosonic fields. The treatment of the fermions is out of the scope of this thesis and omitted in the discussion. Moreover the fermionic fields imply extra complications that are elegantly but not simply addressed on the lattice. For those interested in this kind of problems and their solutions we recommend the refs. [48], [49], [50], [51].

The way to introduce the lattice in a theory is to discretize the space-time. There is no unique way to do it. It would depend on several factors, like the geometry of the problem. But the most convenient is a hypercubic lattice where the minimal discrete units of space-time are hypercubes. For example, a three dimensional space cubic lattice would have the form showed in figure 5.1. Now for each dimension space-time points belonging to the lattice can be parametrized as:

$$x_\mu = a_\mu n_\mu$$

where n_μ is a vector of integers and a_μ are the lattice spacings in each direction. Without loss of generality and for simplicity let us take $a_\mu = a$, the same spacing for each space-time direction. Of course the aim of any lattice discretization is to remove this spacing everywhere, as limiting procedure $a \to 0$, in order to extract continuum information.

The use of such a kind of hypercubic lattice has several advantages, where the most important one is the existence of a remnant of a discrete translational invariance. This invariance allows to preserve a well defined Fourier transform, which is very useful in the present work. Of course, any lattice formulation breaks Lorentz invariance, including the rotational invariance the space. Instead, the hypercubic lattice retains a discrete rotational invariance under transformation by elements of the cubic group. All the continuum symmetries are restored in the limit in which the lattice is infinitely populated, that is, in the continuum limit $a \to 0$.

Once space-time is discretized, we have to translate the continuum the-

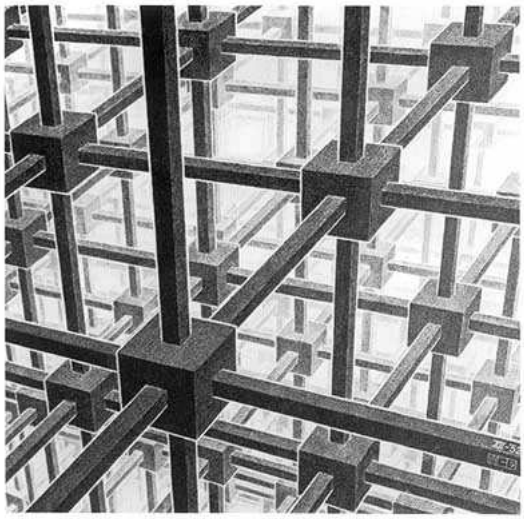

Figure 5.1: "Cubic space division" by M.C. Escher (1952).

ory into the lattice world. The only requirement has to be that continuum physics is recovered in the limit $a \to 0$. Under this condition the correspondence lattice-continuum is not unique. Different lattice discretizations can correspond to the same continuum limit. This duality, instead of being a complication, is something of great utility as can be seen below. For the moment, we shall choose of all these equivalent lattice theories, the simplest one.

Having all this into account, it is easy to find a dictionary to translate continuum Lagrangians into the lattice. To begin, let us introduce the simplest classical field theory, that of a single scalar field:

$$\mathcal{L}(x) = \frac{1}{2}\partial_\mu\phi(x)\partial^\mu\phi(x) - \frac{1}{2}m^2\phi^2(x) \tag{5.1}$$

where $\phi(x)$ is a real valued function of space-time. First the fields are defined only in the lattice sites $\phi(x_\mu) = \phi(an_\mu)$. Since any lattice formulation is susceptible to be used in a numerical computation, it is useful to define the discrete dimensionless variables $\phi(n) = a\phi(an)$, and the dimensionless mass ma, and express everything in terms of them. These definitions almost solve the translation into the lattice, but a definition for the lattice derivative is needed. Following the prescription of simplicity, the simplest lattice operator that gives a derivative in the continuum limit is:

$$\Delta_\mu f(n) = (f(n+\mu) - f(n))$$

where μ is an unit vector in the μ direction and $f(n)$ is an arbitrary dimensionless lattice function. It is trivial to see that in the limit $a \sim 0$ it gives the usual ∂_μ derivative, since

$$f(n+\mu) \sim f(n) + a\partial_\mu f(n)$$

in that limit. This derivative is usually called forward derivative. So the lattice Lagrangian reads[1]:

$$L(n) = \frac{1}{2}\Delta_\mu\phi(n)\Delta^\mu\phi(n) - \frac{1}{2}m^2\phi^2(n) \xrightarrow{a\to 0} a^4\mathcal{L}(x)$$

It is not necessary to take care of the extra a^4. If we define the lattice action as:

$$S = \sum_n L(n)$$

in the continuum limit:

$$S \sim \sum_n a^4\mathcal{L}(x) \sim \int dx^4\,\mathcal{L}(x)$$

giving the continuum action trough the limit $\sum_n a^4 \sim \int dx^4$ (remember $x = an$, $\forall a$).

The previous setting assumes in principle, an infinite number of lattice points. However in practical (computational) realizations the number of points in any direction is finite. This computational limitation has two important consequences:

First, $a = 0$ can not be reached. This gives rise to the concept of lattice artifact, a non-physical effect that would come from the fact that you are not in the continuum limit. These artifacts need to be controlled in order to extract any physical conclusion. Second, the physical volume of the system is finite. So for a practical lattice, and supposing the possible artifacts coming from the non-zero lattice spacing are under control, you never recover the theory (5.1), but a finite volume version of it. This gives rise to the so-called finite volume artifacts. Just like the other discretization artifacts they need to be controlled. Since the volume is finite, the system presents boundaries where the fields of the theory have to be defined. Several boundary conditions can be used at this point. One of the most usual settings (and the one used in

[1]Whenever there could be confusion between continuum and lattice quantities, calligraphic notation will be used for continuum quantities.

this work) is to choose periodic boundary conditions. This eliminates possible boundary effects, although it still requires monitorization of the finite volume effects.

It is important to say that both non-zero lattice spacing and the setting of periodic boundary conditions have two important implications in Fourier space. The fact that $a \neq 0$ implies that the norm of the momentum is bounded from above or, what is the same, the momentum is constrained to fit inside a box (analogous to the first Brillouin zone in solid state physics). This can be seen through the Fourier transform definition. As illustration I present the demonstration for a one dimensional lattice.

The starting point is to notice that if we have a function in the lattice $f(n)$ and we perform a Fourier transformation, we obtain:

$$f(n) = \int_{k_l}^{k_u} \frac{dk}{2\pi} f(k)\, e^{-ikan}$$

Notice the function $e^{-ika\,n}$ is for each n periodic in k with periodicity $2\pi/a$. That means that all the information in the system is replicated in intervals of this length. Then, without loss of generality, the momentum can be chosen to fit inside the region $k_l = -\pi/a$ and $k_u = \pi/a$ (u: upper integration bound, l: lower integration bound).

The consequence of the periodic boundary conditions is to discretize the Fourier space. This is directly read from the periodicity of the fields. Let us go back to the one dimensional case and let L be the length of the spatial dimension:

$$f(n + L/a) = \int \frac{dk}{2\pi} f(k) e^{-ika(n+L/a)} = \int \frac{dk}{2\pi} f(k) e^{-ikan} = f(n)$$

this implies that $kL = 2\pi j$ where j is an integer or, in other words, k has a minimal momentum increment, $p_{\min} = 2\pi/L$. In the case of a multidimensional lattice each component of the momenta has the corresponding minimal increment $p^i_{\min} = 2\pi/L^i$.

Putting these two modifications of the Fourier space together in the cubic spatial lattice, one finds that, just as in the spatial case, in momentum space there are only $(L/a)^3$ momenta. That is, there is a finite amount of degrees of freedom, which makes this lattice setting computationally suitable.

To end the present section let me conclude with a brief discussion about how to fix these parameters in an actual situation. As will be extensively explained in chapter 6, the choice of values for a and L, that fix the size of the lattice, is very far from being arbitrary. Moreover, since the computational power is sometimes very restricted, there is a narrow window of values you can use if you want to keep artifacts under control. The best situation, that allows to have a good idea of how to set these values, is whenever the physical system presents a unique typical scale or correlation length ξ. The set-up is then clear. The parameters must be fixed to accomplish:

$$a << \xi << L$$

The situation is far more complicated when several very different scales enter the problem, making the settings not so evident. An example is the present work, where some other considerations come into play and mix large and small scales. A more detailled discussion of this case will be presented in chapter 6.

5.2 The treatment of gauge fields. Links and plaquettes.

In the present section I review the usual lattice formulation for the inclusion of gauge fields in the theory. This formulation was firstly proposed by Wilson [52]. As in the previous section I will only discuss here the topics of interest for the present work.

As can be seen in section 4, the hybrid model used in this work is basically a model with scalar fields coupled to gauge fields. So I will use this model as a reference for the discussion of this section. The first step then is to write the simplest classical continuum gauge theory, coupled with a scalar field, in a four dimensional space-time:

$$\mathcal{L} = \frac{1}{2}\mathcal{D}_\mu\phi(x)\mathcal{D}^\mu\phi(x) - \frac{1}{2}m\phi^2(x) + \mathcal{L}_G$$

where

$$\mathcal{L}_G = -\mathrm{Tr}\{\frac{1}{2}\mathcal{F}_{\mu\nu}\mathcal{F}^{\mu\nu}\} \tag{5.2}$$

where the trace is taken in the internal space.

The covariant derivative and the strength tensor have the usual form:

$$\mathcal{D}_\mu = \partial_\mu + ig\mathcal{A}_\mu(x); \quad \mathcal{A}_\mu(x) = \sum_a \mathcal{A}^a_\mu(x) T_a$$

$$\mathcal{F}^a_{\mu\nu} = \partial_\mu \mathcal{A}^a_\nu(x) - \partial_\nu \mathcal{A}^a_\mu(x) + g f^{abc} \mathcal{A}^b_\mu \mathcal{A}^c_\nu$$

The f^{abc} are the structure constants and T_a the generators of the gauge group in question. For simplicity and for suitability to the present work, we will take this gauge group to be $SU(2)$. In this case $T^a = \tau^a/2$ satisfying :

$$[\tau^a/2, \tau^b/2] = i f^{abc} \tau^c/2$$

where τ^i are the Pauli matrices, and the structure constants:

$$f^{abc} = \epsilon^{abc}$$

form the complete antisymmetric tensor.

As pointed out in the previous section we need a dictionary to translate this continuum field theory into a lattice formalism. What we discussed in the previous section still holds for the scalar field. What is now required is a way to discretize the gauge field $\mathcal{A}_\mu$. In order to do this, let us first define a gauge transformation in the lattice:

$$\phi'(n) = \Omega(n)\phi(n)$$

where $\Omega(n)$ is a matrix of the gauge group. It would be tempting to try a naive definition of the lattice gauge fields just as discretization of the continuum ones, maybe something like:

$$A_\mu(n) = a\mathcal{A}_\mu(na)$$

but this is wrong if one wants to achieve the correct gauge transformations on the lattice. This easily seen looking at the covariant derivative definition. In the continuum, the necessity for having a gauge field comes directly from the requirement that the derivative must transform covariantly under a gauge transformation for the fields:

$$(\mathcal{D}_\mu \phi(x))' = \Omega(x)\mathcal{D}_\mu \phi(x).$$

Since the usual derivative does not satisfy this relation it is mandatory to add a new field, the gauge field, with its particular gauge transformation. This requirement provides a natural way to introduce the gauge fields in the continuum, and defines the gauge field transformations univocally. It seems

then natural, if we are looking for a lattice gauge field candidate, to require the same condition for the lattice covariant derivative D_μ. It must satisfy:

$$(D_\mu \phi(n))' = \Omega(n) D_\mu \phi(n) \tag{5.3}$$

This condition has, like in the continuum case, an immediate consequence for the form of the covariant lattice derivative. The way it is explicit comes from the direct application of the gauge transformation to the lattice derivative:

$$\Delta_\mu \phi'(n) = \Omega(n)\Big(\Omega^\dagger(n)\Omega(n+\mu)\phi(n+\mu) - \phi(n)\Big).$$

The expression between brackets is not the derivative so it is necessary to add something more to fix it. It is the so-called link variable $U_\mu(n)$, whose gauge transformation must be:

$$U'_\mu(n) = \Omega(n) U_\mu \Omega^\dagger(n+\mu).$$

The definition of the lattice covariant derivative, with the appropriate gauge transformation, is hence:

$$D_\mu \phi(n) = U_\mu(n)\phi(n+\mu) - \phi(n).$$

Is easy to see that these link matrices belong to the gauge group due their transformation properties. By analogy with the continuum, it is in the link variables where the gauge information is stored in a natural way. Notice that, the role of the continuous gauge field is taken on the lattice by these link variables. The interpretation of these link variables is showed in figure 5.2. They live in the lines linking adjacent points in the lattice and they have an orientation. The link $U_\mu(n)$ goes from the point n to the point $n+\mu$ along the μ direction, whereas the link $U^\dagger_\mu(n)$ goes from $n+\mu$ to n. The links have all the gauge information of the system and they have a clear relation with the gauge fields. This relation can be directly obtained from the continuum limit of the covariant derivative. Since the link is a group matrix it can be parametrized by:

$$U_\mu(n) = e^{i\lambda^a_\mu(n)\sigma_a} = 1 + i\lambda^a_\mu(n)\sigma_a + ...$$

where the $\vec{\sigma}$ are the generators of the group, and $\lambda^j(n)$ are parameters of the matrix. If this is introduced in the lattice covariant derivative and the continuum limit is taken we get:

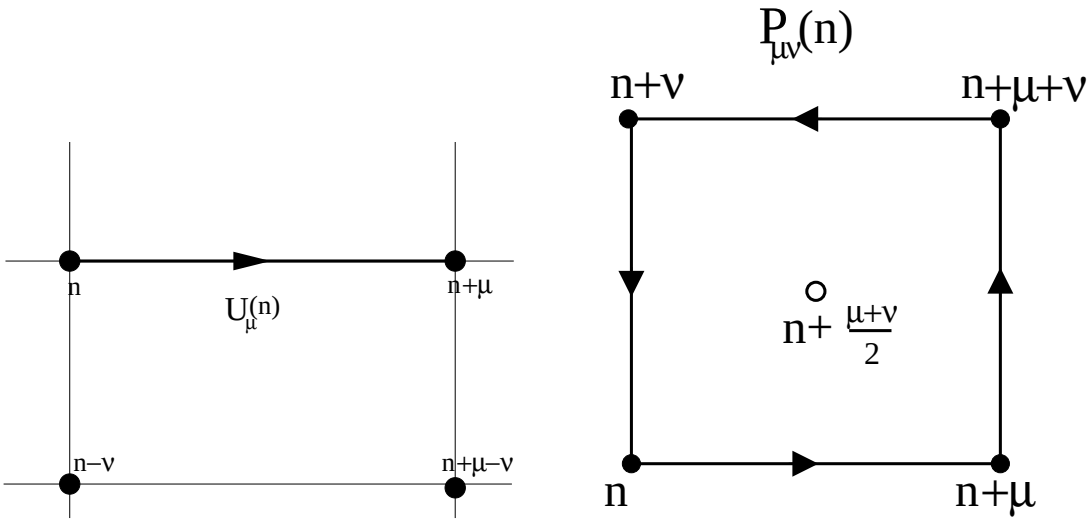

Figure 5.2: Left: Link variable. Right: Plaquette definition. The arrows represent the corresponding links. The empty point in the middle is not a lattice point but the point where the continuum limit $\mathcal{F}_{\mu\nu}$ tensor field is placed.

$$D_\mu\phi(n) = a\partial_\mu\phi(an) + i\lambda^j_\mu(an)\sigma_j\phi(an) + ... \sim a^2\mathcal{D}_\mu\phi(x)$$

so we can just set

$$\lambda^j_\mu = ag\mathcal{A}^j_\mu$$

neglecting all the terms bigger than $O(a^2)$ in the continuum limit ($a \sim 0$). This gives the correct form for the continuum lattice derivative. Consequently the link variables are by definition in the limit of small a:

$$U_\mu(n) = e^{iag\mathcal{A}^j_\mu(n)\sigma_j} \longrightarrow \mathbb{1} + iag\mathcal{A}^j_\mu(n)\sigma_j$$

Once the need of link variables is introduced, it is necessary to find out a lattice term that gives the $\mathcal{L}_G$ in the continuum limit. In principle we could tray again a naive substitution in equation (5.2) of the derivatives by the lattice ones and the gauge fields by the combination:

$$A_\mu(an) \sim \frac{-i}{ag}(U_\mu(n) - \mathbb{1}).$$

Obviously that is wrong again, since the resulting candidate for $\mathcal{F}_{\mu\nu}$ does not have the adequate gauge transformation properties. However it is possible to construct a term made only of links that has the same gauge transfor-

mation properties than $\mathcal{F}_{\mu\nu}$. This term can be read directly from the link's gauge transformation. One can realize that any ordered product of an arbitrary number of links along a closed path, transforms in the same way as $\mathcal{F}_{\mu\nu}$:

$$C(n,n) = U_\mu(n)U_\nu(n+\mu)U_\alpha(n+\mu+\nu).....U^\dagger_\beta(n).$$

Is easy to show that:

$$C'(n,n) = \Omega(n)C(n,n)\Omega^\dagger(n)$$

From it a gauge invariant term can be constructed, taking the trace of any closed path. The simplest closed path in a lattice is called the plaquette $P_{\mu\nu}$, shown in fig. 5.2. It is defined as:

$$P_{\mu\nu}(n) = U_\mu(n)U_\nu(n+\mu)U^\dagger_\mu(n+\nu)U^\dagger_\nu(n)$$

and its trace on the internal space indexes is the simplest gauge invariant made out of links. This invariant is called the Wilson loop:

$$W_{\mu\nu}(n) = \mathrm{Tr}\{P_{\mu\nu}\}.$$

Consider then the following simplest gauge invariant term that is made out of plaquettes:

$$L_G = \frac{1}{g^2} g_{\mu\nu}\mathrm{Tr}(\mathbb{1} - P_{\mu\nu})$$

as a candidate for the lattice version of the pure gauge Lagrangian. This term is called the Wilson Lagrangian and has two important properties:

First it vanishes in any vacuum configuration. This is trivial since the links in the vacuum are by definition just the identity matrix (up to a gauge transformation, irrelevant since the term is gauge invariant).
Second, it gives the correct continuum limit. If we expand the links in terms of a we get the expansion for the plaquette:

$$P_{\mu\nu}(an) = (1 + iag\mathcal{A}_\mu(an) + ...)(1 + iag\mathcal{A}_\nu(an + a\mu) + ...)$$

$$(1 - iag\mathcal{A}_\mu(an + a\nu) + ...)(1 - iag\mathcal{A}_\nu(an) + ...)$$

$$= 1 + iga^2\mathcal{F}_{\mu\nu}(an + \frac{(a\mu + a\nu)}{2}) - \frac{g^2a^4}{2}\mathcal{F}^2_{\mu\nu}(an + \frac{(a\mu + a\nu)}{2}) + ...$$

$$= e^{-iga^2\mathcal{F}_{\mu\nu}(an+(a\mu+a\nu)/2)}.$$

So in the limit $a \to 0$ we can neglect the terms of order bigger than $O(a^2)$. Now performing the trace and getting ride of the 1 we get:

$$\frac{1}{g^2}\mathrm{Tr}\{\mathbb{1} - P_{\mu\nu}(n)\} \sim \frac{a^4}{2}\mathrm{Tr}\{\mathcal{F}^2_{\mu\nu}(x)\} \tag{5.4}$$

where the trace is again taken on the indexes of the internal space. It gives precisely the wanted term. It is then not necessary to perform complicated combinations of plaquettes in order to obtain a lattice Lagrangian with the appropriated continuum limit. It is just the plaquette itself who has all the required information.

Once we have defined all gauge related terms, the complete lattice Lagrangian is:

$$L(n) = \frac{1}{2}D_\mu\phi(n)D^\mu\phi(n) - \frac{1}{2}(ma)^2\phi^2(n) - g_{\mu\nu}\frac{1}{g^2}\mathrm{Tr}\{\mathbb{1} - P_{\mu\nu}(n)\}$$

which posses the right continuum limit as well as the correct gauge transformation properties. The $g_{\mu\nu} = \mathrm{diag}(-1, 1, 1, 1)$.

This ends the discussion about the inclusion of the gauge fields in a lattice theory. This brief review contents all the essential ingredients needed for understanding of the developments of the present work, that are presented in the next chapter, and the major part of the appendices A and B.

5.3 The way to improvement.

This section is devoted to deeper considerations about the origin and treatment of lattice artifacts, without the intention of being exhaustive. I will focus on the issue of classical improvement which is the one relevant for this work.

As was pointed above, the artifacts are unphysical effects that come from the finiteness of the lattice spacing. Mathematically, one can think on them as the corrections to the quantities of interest, coming from the infinite number of terms in their a expansion. In principle if one gets a small a spacing (compared with the typical scale of the phenomena involved in the problem), one can get rid of these artifacts, but they very often are the main source of error to deal with.

5.3.1 Improving the lattice.

The simplest way to get rid of the lattice artifacts is just by a mere extrapolation of the data. If one is able to have results for a large set of different lattice spacings, it is possible to perform an extrapolation in the a dependence, and derive a continuum limit value. For instance, such an extrapolation for some quantities of interest for this thesis is presented in chapter 10.

In addition to this, the approach to the continuum limit can be improved by defining lattice operators which reproduce better, at finite a, the continuum result. This can be done by adding terms to these operators with only two restrictions: the resulting operator must have the appropriate behavior under gauge transformations, and the continuum limit must be the correct one. This allows to construct some operators in which some subleading lattice artifacts can be removed. In this section I will present some of the improved operators used in this thesis.

Of course, this kind of improved operators will be more involved and consequently more computational demanding. This usually does not represent a big problem since computational time complexity is very often less critical than the spatial complexity (memory requirements).

5.3.2 The improved derivatives.

Let me start with the presentation of an improved derivative. As can be seen from above the derivative Δ_μ is exact for any linear function. That is, if one takes the continuum derivative of a linear function $f(x) = c + bx$ one gets b. For the lattice the application of the forward derivative to a linear function $f(an) = c + b(an)$ is just:

$$\Delta f(n) = (f(n+1) - f(n))/a = b$$

Now we normalize by the lattice spacing in the derivative definition, for simplicity. So if the world was made of linear functions the use of the forward definition of the lattice derivative does not imply any artifact correction to the continuum one. For general functions the corrections to the continuum derivative are order a as can be seen from the expansion (5.1):

$$f((n+\mu)) = f(n) + a\partial_\mu f(n) + \frac{a^2}{2}\partial_\mu^2 f(n) + ...$$

However, it is possible to make a definition of an improved derivative, that is exact for functions up to quadratic terms $f(x) = c + dx + fx^2$.

To do this lets define first the so called backwards derivative. This derivative represents an example of a case in which a different lattice operator gives the same continuum limit:

$$\bar{\Delta}_\mu f(n) = (f(n) - f(n-\mu))/a \sim \partial_\mu f(x) + O(a) + ...$$

Now we can perform a combination of both forward and backward derivatives to get a new improved lattice derivative:

$$\Delta^I = \frac{\Delta + \bar{\Delta}}{2} = \frac{f(n+1) - f(n-1)}{2a} \sim \partial_\mu f(x) + O(a^2)$$

this is sometimes called the three point derivative. As can be seen from the power expansion of $(f(n+\mu) - f(n-\mu))$ any even power of a is removed. In the same way, one can trivially realize that this derivative is exact for any quadratic function.

This process of improvement never ends. One can improve the derivative to be exact for any polynomial function or, what is the same, to have a correction of order the power of a one desires. But this implies a high enhancement of the computational requirements. For example one can define a five point derivative with high order corrections as:

$$\Delta^{I5}_\mu f(n) = \frac{f(n-2\mu) - 8f(n-\mu) + 8f(n+\mu) - f(n+2\mu)}{12a} \sim \partial_\mu f(x) + O(a^4)$$

For the present work, it has been enough with the use of the simplest forward derivative and, in some cases like the one exposed in appendix B, the improved three points derivative. Both are on the other hand, the more often used in the literature.

The definition of the lattice derivative, as well as any possible improvement, affects the way the momentum appears while Fourier transforming differential equations, or what is the same, gives a sort of lattice momentum definition. The simplest one is given in terms of the continuum momentum, through the forward derivative. Making a Fourier transform of this derivative:

$$F(\Delta_i f(n)) \equiv v_i^f f(k) = \sum_n f(n) e^{-ikn}(e^{-ik_i a} - 1)$$

where the k in the exponential is the continuum one, and the f superscript stands for forward. So the definition of the lattice momentum is:

$$v_i^f \equiv (e^{-ik_i a} - 1)$$

a dimensionless quantity. Of course it has the appropriate continuum limit with $O(a)$ corrections:

$$v_i^f/a \sim -i\,k_i + \frac{k^2 a}{2} + ...$$

If the improved derivative is used instead of the forward one, an improved definition for the momentum follows. From the backwards derivative one has a backward lattice momentum:

$$v_i^b \equiv (1 - e^{ik_i a})$$

so the combination of both gives the improved momentum:

$$q_i = \frac{v^f + v^b}{2i} \sim ak_i + \frac{1}{6}a^3 k_i^3 + ...$$

which reproduces the continuum with artifacts order $O(a^2)$ giving a more accurate continuum limit if needed.

This ends the discussion on the improvement of the derivatives and momentum. Although it was not exhaustive it has attempted to be complete regarding the kind of tools used in this thesis.

5.3.3 Gauge Improvement: The Clover.

The previous section presents a discussion about the improvement used in lattice derivatives. The present section, is centered upon the improvement of terms and operators that involve gauge fields.

There are many ways to improve the gauge part of a lattice gauge theory. They rely on the same philosophy described above, that is, using the fact that the correspondence of the lattice operators and continuum ones, is not unique. In this section, I will focus in the improvement tool called clover, that is extensively used in the literature and in this thesis.

As can be seen from equation (5.4), since the tensor $\mathcal{F}_{\mu\nu}$ is traceless, the only terms that contribute to the a expansion of the Wilson action, are the terms that involve even powers of $\mathcal{F}_{\mu\nu}$. This implies that the leading order or first correction to the continuum action is order a^2. That is a good enough accuracy for this work so no improvement is needed in that case. But sometimes it is necessary to extract information directly from the

components of the $\mathcal{F}_{\mu\nu}$ tensor. Of course we can still use the plaquette to get the components of the tensor:

$$\mathrm{Im}(P_{\mu\nu}(n)) \sim a^2\mathcal{F}_{\mu\nu}(x + a\mu/2 + a\nu/2) + O(a^6)$$

That is, the tensor obtained by the plaquette in the lattice point n is placed in a continuum point, located in the center of the plaquette. Pictorially it can be seen in figure 5.2. This can be a critical source of error if we are interested in constructing observables that involve operations with lattice fields, whose continuum limits, due to this effect, are located in different points. As an example the Lorentz invariant made of the electric and magnetic lattice counterparts[2] $E^L(n)B^L(n)$:

$$E^L(n)B^L(n) = \frac{1}{2a^4}\mathrm{Im}(P_{0i}(n))\epsilon_{ijk}\mathrm{Im}(P_{jk}(n)) \sim E(x)B(x) + O(a).$$

The clover improvement is introduced precisely to take care of this displacement. Although the calculation is easy to perform, it can be clearly seen from figure 5.3 that this displacement is removed by taking the average of the adjacent plaquettes. This is just the clovering procedure. The name comes from the form that these plaquettes draw. The clover plaquette definition $P^C(n)$ (C stands for clovering) is then:

$$P^C_{\mu\nu}(n) = \frac{1}{4}(P_{\mu\nu}(n) + P_{\mu\nu}(n-\mu) + P_{\mu\nu}(n-\mu-\nu) + P_{\mu\nu}(n-\nu))$$

with a continuum limit:

$$\begin{aligned}\mathrm{Im}P^C_{\mu\nu}(n) \sim \frac{a^2}{4}(&\mathcal{F}_{\mu\nu}(x+\mu/2+\nu/2) + \mathcal{F}_{\mu\nu}(x-\mu/2+\nu/2)\\ &+\mathcal{F}_{\mu\nu}(x-\mu/2-\nu/2) + \mathcal{F}_{\mu\nu}(x+\mu/2-\nu/2)) + O(a^6)\\ &= a^2\mathcal{F}_{\mu\nu}(x) + O(a^6)\end{aligned}$$

In the present work the clovering procedure has been extensively used in the observables involving electric and magnetic fields like the helicity. Detailed information is presented in chapter 9 and appendix B.

[2]Here L stands for lattice. We use the script L in this case in order to avoid using calligraphic E and B for the continuum electric and magnetic fields, which could be quite unnatural.

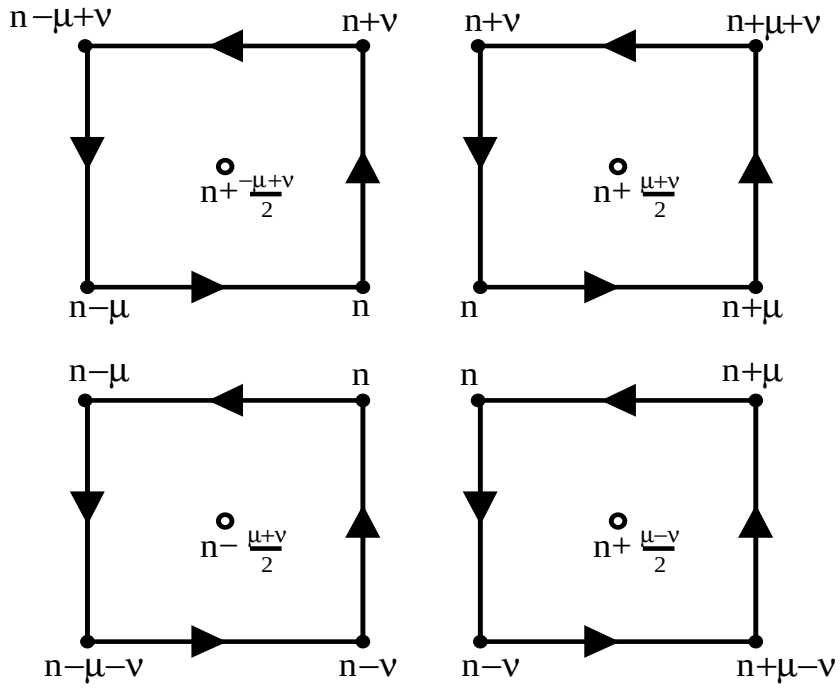

Figure 5.3: Plaquettes averaged in the clover definition. The continuum limit $\mathcal{F}_{\mu\nu}$ tensor is placed in the central point n.

To conclude let me review the most important points of this chapter, intended for non specialists. On it we presented some basic essentials of lattice gauge theories, focused in the classical gauge theories relevant for the present work. After that, some considerations on the kind of typical problems and peculiarities coming from the lattice discretization are reviewed, giving special emphasis to the discussion of lattice artifacts. Then some improvement tools used in this work are reviewed to end. Further details, as well as the discussion of the particular application of the concepts reviewed here, are presented in the following chapter.

Chapter 6

Methodology.

This chapter is a central one, where the techniques used to develop the work of this thesis are described. Basically it gives the line that links chapter 4 and chapter 5, connecting the Hybrid inflation model with a cold electroweak phase transition and the lattice numerical evolution. This connexion is given by the so-called classical approximation.

Due to the particularities of our model, and more specifically, due to tachyonic preheating, the use of this classical approximation represents a powerful tool that provides a way to reduce the huge complexity of the full quantum behavior of the system. This classical reduction is not the last step. The resulting system is too complicated for an analytic treatment and requires a numerical approach, implemented on the lattice.

In what follows we will describe in detail the methodology used in this thesis. We separate it in two groups. First, the justification for the use of a classical approximation in a full quantum system. Second, the methodology used to translate the classical system coming out of the approximation into a system suitable for a numerical evolution. This last group will also contain the methodology used to set the initial conditions for the numerical procedure.

Before starting, a remark concerning notation. From this chapter on, the notation convention is that calligraphic quantities are continuum quantities whereas non-calligraphic variables are lattice ones.

6.1 The classical approximation.

In this section I briefly review the classical approximation, which is an essential item in this work. Although no new insights will be provided in this

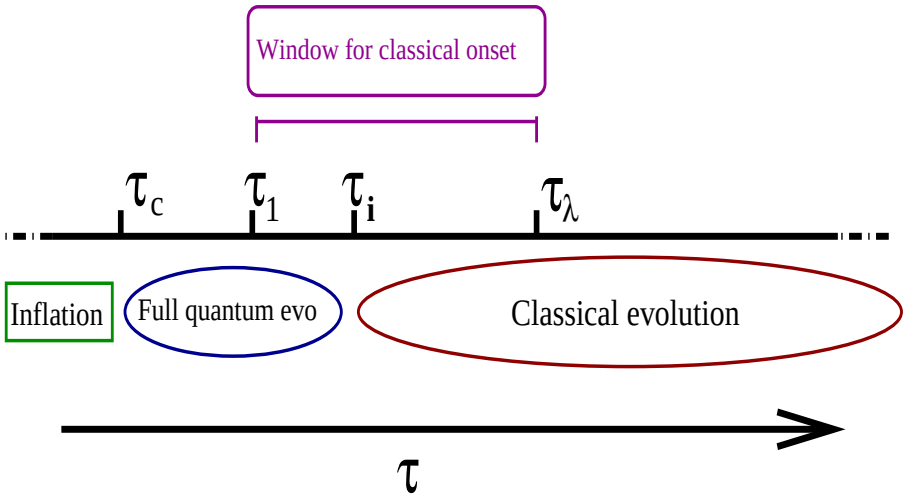

Figure 6.1: Schematic evolution line. On it the times relevant for the series of approximations are represented: τ_c: end of Inflation, τ_1: time where enough modes have been enhanced to be classical, in order to keep an accurate description of the system, τ_i: time where the quantum evolution is substituted by a classical one, τ_λ: time where the λ term of the Lagrangian can not be neglected anymore.

section, it is worth to discuss the applicability of this approximation within the context of this thesis. This discussion will follow the line of references [111, 112] and [116].

As discussed in chapter 4, due to the nature of the couplings between the fields and the dynamics of the phase transition, the preheating epoch is a highly out of equilibrium and non-perturbative scenario. The non-linear effects, arising from the selfcoupling of the Higgs field, make an analytical approximation to the study of the system inapplicable.

The starting point of the evolution is the end of inflation. Just after inflation the universe is cold, and all quantum fields can be considered to be in the quantum vacuum ground state. We can set all the gauge field components to be zero. This is a bit subtle an requires further explanation which can be found in the next section. For now, let us assume it as true, and let us concentrate in the discussion of the classical approximation. Hence, up to times of order t_λ where the non-linearities become important, we can ignore all degrees of freedom but the Higgs and the Inflaton, and neglect the Higgs selfcoupling λ. This approximation gives rise to what we call the linear quantum evolution.

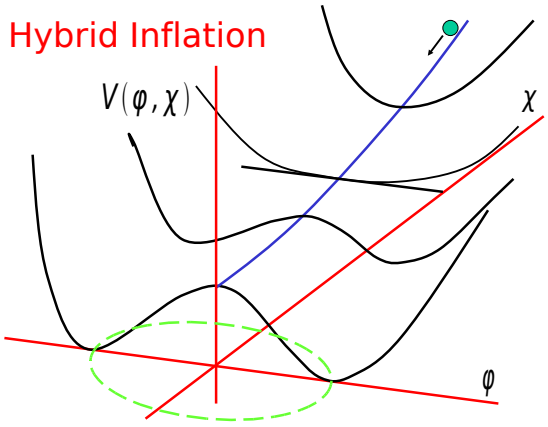

Figure 6.2: Representation of the Higgs-Inflaton system. Potential energy. From "Signatures from preheating", J. García-Bellido, KITP Seminars (UCSB).

6.1.1 Linear quantum evolution

As was qualitatively explained in chapter 4 and following Refs. [111, 112], we will address here the first stages of evolution starting at the end of inflation.

The period of inflation is characterized by the fact that the Higgs and Inflaton fields are displaced from the true minimum of the potential. In this case, inflation is driven by the false vacuum energy, $V_0 = \lambda v^4/4$. During this time the Inflaton homogeneous mode, $\chi_0 \equiv \langle\chi\rangle$, dominates the dynamics.

The interaction between the Higgs and Inflaton fields drives the end of inflation and triggers EW symmetry breaking. The way it proceeds is schematically seen at figure 6.2. On it the values of the Inflaton field correspond to a particular shape for the Higgs potential, which is driven from a quadratic sharp potential into a "mexican hat" potential.

Close to the time when inflation ends, denoted by t_c, the time evolution of the Inflaton zero mode can be approximated by:

$$\chi_0(t) = \chi_c(1 - Vm(t - t_c)) \tag{6.1}$$

where $\chi_c = \chi_0(t_c) \equiv m/g$. Here V denotes the Inflaton dimensionless velocity, defined through this equation and fixed to $V = 0.024$ in our analysis [111].

The variation of $\chi_0(t)$ induces, via the Higgs-Inflaton coupling, a time dependence of the effective Higgs mass parameter, which changes from positive to negative, triggering electroweak symmetry breaking. Accordingly, the time when inflation ends, t_c, is characterized as the critical point where the Higgs field becomes massless.

As described in detail in Refs. [111, 112], it is possible to solve exactly the quantum evolution of the system around t_c if non-linearities in the Higgs field and the interaction with the gauge fields are neglected.

With these approximations, the Lagrangian (4.24) gives a simplified action, which is a quadratic action for the Higgs field with a time-dependent mass:

$$\mathcal{S} = \int d^3x\, dt\, \frac{1}{2}[(\dot{\phi})^2 - (\nabla\phi)^2 - m_\phi^2(t)\phi^2], \tag{6.2}$$

where the mass $m_\phi(t)$ is defined in (4.26) and can be rewritten around critical time in terms of the Inflaton zero mode velocity as:

$$m_\phi^2 \simeq -2Vm^3(t - t_c) \tag{6.3}$$

For simplicity now, we adopt the nomenclature of [111] redefining all variables with a new scale $M = (2V)^{\frac{1}{3}}m$ in order to have non-dimensional variables:

$$\begin{aligned} \tau = M(t - t_c) \quad &\longrightarrow \quad \dot{\phi} = M\phi', \\ \mathbf{x} \equiv M\mathbf{x} \quad &\longrightarrow \quad \mathbf{k} \equiv \frac{\mathbf{k}}{M} \\ y = \frac{\phi(\mathbf{x},\tau)}{M}&, \end{aligned} \tag{6.4}$$

where prime stands for the τ derivative. The equation (6.2) can be rewritten in terms of the Fourier modes as:

$$\mathcal{S} = \int d^3k\, d\tau\, \frac{1}{2}[(y'(\mathbf{k},\tau))^2 - (k^2 - \tau)y^2(\mathbf{k},\tau)]. \tag{6.5}$$

The form of the Hamiltonian is the usual one for a harmonic oscillator with a time-dependent frequency:

$$\mathcal{H} = \int d^3k\, \frac{1}{2}[p(\mathbf{k},\tau)p^\dagger(\mathbf{k},\tau) + (k^2 - \tau)y(\mathbf{k},\tau)y^\dagger(\mathbf{k},\tau)] \tag{6.6}$$

where p stands as usual:

$$p = \frac{\partial \mathcal{L}}{\partial y'} = y', \tag{6.7}$$

The system is just an infinite ensemble of decoupled harmonic oscillators with a time-momentum dependent frequency:

$$w^2(k,\tau) = k^2 - \tau. \tag{6.8}$$

The quantum evolution of both $y(\mathbf{k})$ and $p(\mathbf{k})$ operators, can be written in terms of two complex valued functions, satisfying:

$$\begin{aligned} f_k'' + (\omega(\mathbf{k},\tau)^2) f_k &= 0 \\ g_k = g_{k1} + i g_{k2} &= i f_k' \\ f_k(\tau_0 = 0) &= \frac{1}{\sqrt{2k}}, \\ g_k(\tau_0 = 0) &= \sqrt{\frac{k}{2}}, \end{aligned} \tag{6.9}$$

in the way:

$$\begin{aligned} y(\mathbf{k},\tau) &= f_k(\tau) a(\mathbf{k},\tau_0) + f_k^*(\tau) a^\dagger(-\mathbf{k},\tau_0), \\ p(\mathbf{k},\tau) &= -i(g_k(\tau) a(\mathbf{k},\tau_0) - g_k^*(\tau) a^\dagger(-\mathbf{k},\tau_0)), \end{aligned} \tag{6.10}$$

where $a^\dagger(\mathbf{k},\tau_0))$ and $a(\mathbf{k},\tau_0))$ are respectively the creation and annihilation operators for the mode $\mathbf{k}$ at τ_0.

The exact form for these functions is given in terms of Airy functions and their derivatives:

$$\begin{aligned} f_k(\tau) &= C_1(k) Bi(\tau - k^2) + C_2(k) Ai(\tau - k^2), \\ g_k(\tau) &= i C_1(k) Bi'(\tau - k^2) + i C_2(k) Ai'(\tau - k^2), \\ C_1(k) &= -\frac{\pi}{\sqrt{2k}}[Ai'(-k^2) + ikAi(-k^2)], \\ C_2(k) &= \frac{\pi}{\sqrt{2k}}[Bi'(-k^2) + ikBi(-k^2)], \end{aligned} \tag{6.11}$$

All the physical information of the system is stored in the two point correlation functions, since the simplified system is a Gaussian one. These functions are expressed as:

$$\langle 0, \tau_0 | v_a(\mathbf{k},\tau) v_b(\mathbf{k}',\tau') | 0, \tau_0 \rangle = \Sigma_{ab}(k,\tau,\tau') \delta^3(\mathbf{k} + \mathbf{k}'), \tag{6.12}$$

where v_a stands for $\hat{p}$ and $\hat{y}$ for $a = 1,\ 2$ respectively, whereas the right hand side of the equation comes from $a(\mathbf{k}, \tau_0)|0, \tau_0\rangle = 0$, $\forall \mathbf{k}$. The matrix Σ for any pair of times τ, τ' can be obtained from its value at time τ_0:

$$\Sigma(k, \tau, \tau') = \mathbf{M}(k, \tau)\Sigma(k, \tau_0, \tau_0)\mathbf{M}^T(k, \tau'), \tag{6.13}$$
$$\Sigma(k, \tau_0, \tau_0) = \begin{pmatrix} \frac{k}{2} & -\frac{i}{2} \\ \frac{i}{2} & \frac{1}{2k} \end{pmatrix},$$

where $M(k, \tau)$ is the usual evolution matrix in Fourier space. From this expression is easy to extract the time expectation values $\Sigma(k, \tau, \tau)$, just by making use of equations (6.11) in terms of the so called W.K.B phase $F_k(\tau)$:

$$F_k(\tau) = Im(f_k^* g_k), \tag{6.14}$$

in the way:

$$\Sigma(k, \tau, \tau) = \begin{pmatrix} |g_k(\tau)|^2 & F_k(\tau) - \frac{i}{2} \\ F_k(\tau) + \frac{i}{2} & |f_k(\tau)|^2 \end{pmatrix}. \tag{6.15}$$

The form of the Σ matrix is quite interesting. The real part of this matrix is just the same as the one coming, instead of the expectation value of quantum operators, from the expectation value of two independent random variables $y(\mathbf{k}, \tau)$ and $\bar{p}(\mathbf{k}, \tau)$ generated according to a random Gaussian probability distribution, in a way such the averaged values satisfy:

$$\langle y^2(k, \tau)\rangle_{Gauss} = |f_k(\tau)|^2 \tag{6.16}$$

where *Gauss* just stands to remark the fact that this expectation value, is just a random Gaussian variable average, in the classical statistics context, and:

$$\langle p^2(k, \tau)\rangle_{Gauss} = |g_k(\tau)|^2 \tag{6.17}$$

where $p(k, \tau)$ is a new variable made of the previous two as:

$$p(\mathbf{k}, \tau) \equiv \bar{p}(\mathbf{k}, \tau) + [\frac{F_k(\tau)}{|f_k(\tau)|^2}]y_k \tag{6.18}$$

which also satisfies $\langle y(k, \tau)p(k, \tau)\rangle_{Gauss} = \langle p(k, \tau)y(k, \tau)\rangle_{Gauss} = F_k(\tau)$.

The Gaussian probability distribution function is given by the Wigner function:

$$W_{0k}(y, p) = \frac{1}{\pi^2} exp\left(-\frac{|y|^2}{|f_k|^2} - 4|f_k|^2\Big|p - \frac{F_k}{|f_k|^2}y\Big|^2\right). \tag{6.19}$$

It is remarkable that the real part of the matrix Σ can be obtained by just a statistical random Gaussian variables average. It is only in the imaginary part of the matrix where the quantum nature of the problem is manifest. This also stands for any quantum operator. Having any quantum operator $O(y,p)$ a total symmetrized operator in y and p, $O_W(y,p)$, can be constructed. This operator behaves like a classical commuting object. For that reason it can be expressed as just a function of random variables, that can be computed by means of classical probability densities:

$$\langle 0,\tau_0|O_W(y,p)|0,\tau_0\rangle = \langle O_W(y,p)\rangle_{Gauss}, \tag{6.20}$$

The expectation value of the original operator can then be written as an expansion in terms of the commutator:

$$\langle 0,\tau_0|O(y,p)|0,\tau_0\rangle = \langle O(y,p)\rangle_{Gauss} + \sum_{n\geq 1}\mathcal{O}([y,p]^n), \tag{6.21}$$

that can be computed in terms of Gaussian random variables. If the first term dominates over all orders in the expansion, the expectation value of the operator can be approximated to a classical Gaussian random average, which is the essence of the classical approximation.

In general this first term dominates the expansion if:

$$\langle 0,\tau_0|\{p,y\}|0,\tau_0\rangle \gg |\langle 0,\tau_0|[p,y]|0,\tau_0\rangle|, \tag{6.22}$$

which is achieved for a Fourier mode, if $F_k \gg 1$. This requirement is satisfied by the modes in the system with $k^2 << \tau$. Indeed, the equations (6.11) take a simpler form for the Fourier modes in that interval. Performing an expansion for values of time $k^2 << \tau$ the solution functions have the form:

$$\begin{aligned} f_k(\tau) &\sim (\tau-k^2)^{-1/4}e^{\frac{2}{3}(\tau-k^2)^{3/2}}, \\ g_k(\tau) &\sim i(\tau-k^2)^{-1/2}e^{\frac{2}{3}(\tau-k^2)^{3/2}}. \end{aligned} \tag{6.23}$$

Hence, long wavelength modes suffer a faster than exponential enhancement as they enter the region $k^2 << \tau$. Modes outside this region, keep oscillating around their zero value.

For the enhanced modes the expression for F_k reads:

$$F_k(\tau) = (\tau-k^2)^{-3/4}e^{\frac{4}{3}(\tau-k^2)^{3/2}}, \tag{6.24}$$

which is bigger than one for the infrared modes.

Using the $F_k >> 1$ classicality condition it is possible to determine the time at which a mode k can be considered as a classical mode. It has been proved in the cited reference [111], that at a time value τ, all modes satisfying $0 \leq k < \sqrt{\tau}$ can be classically treated in the way of (6.22), whereas the rest of the modes keep oscillating around their quantum vacuum value, with a low occupation number. So it is a good approximation to neglect them keeping them at zero, and considering only the system composed by the classical modes. That is not completely true, because the whole infinite tower of high frequency momenta, although with a negligible occupation number, has an non negligible quantum effect. This effect can be taken into account as a renormalization of the couplings of the Lagrangian [111], [112].

The strategy followed in previous works and used in the present one, is then clear: find a set of parameters for the Lagrangian that allows to have a time window between the initial time, where inflation ends and the low frequency modes start to grow, and the time (τ_λ) where the effect of the non-linearities couldn't be neglected any more. In advance, we must say that thinking of the following numerical treatment of the system, the number of modes in the interval $k^2 << \tau$ is finite (as any numerical quantity). Hence the window has to be suitable to allow enough modes to be enhanced, in order to have an accurate numerical description of the system, once the rest of the non perturbed modes are neglected. Let us call $\tau_1 < \tau_\lambda$, to the time where the number of modes which entered the $k^2 << \tau_1$ region is enough to satisfy the numerical requirements . Till this time, the simplified quantum evolution of the system is computed. At τ_i satisfying $\tau_1 < \tau_i < \tau_\lambda$ the quantum system is replaced by a classical one, composed of the enhanced low momenta modes of the system, and setting the remaining to zero. This classical system is no longer the simplified one, but it is the full one. With full we mean that it has included the gauge fields as a dynamical variables, the Higgs field self-interactions, and the Inflaton field is no longer described by just a zero mode. A classical non-linear numerical evolution follows. This is the advantage of the classical approximation the usual lattice discretization of the classical evolution, although quite demanding computationally, can be performed.

The appropriate range of values $\tau_1 < \tau_i < \tau_\lambda$ is then determined by the range of τ_i for which the evolution accomplishes two facts: the S.S.B is far from τ_i and the evolution itself is independent of the actual value of τ_i. Several attempts have been performed, keeping several different times in the proper range for further tests. Some of these tests are discussed in appendix D.

The treatment of the gauge fields, as pointed out before, is a little bit

subtle. A detailled discussion can be found in references [111], [112]. The introduction of the additional $U(1)$ gauge field does not affect the discussion. However, for completeness some important points are worth an explanation. At the end of Inflation, both abelian and non-abelian gauge fields are in their quantum vacuum. They get populated through their coupling to the Higgs field. In this case there is a natural choice for the value of the gauge fields. It is the gauge choice $\mathcal{A}_\mu = 0$. This gauge choice provides a simple form for the Higgs equations and makes the previous analysis, in which the action for the Higgs field is a quadratic one, applicable. There is no loss of generality since the quantities of interest computed in the evolution, are performed in a gauge invariant manner. Hence it seems a natural way to proceed to set all gauge fields equal to zero at the end of inflation (τ_c). However, we keep the gauge fields to zero, not only at initial time, but along a time interval $[\tau_0, \tau_i]$, where the simplified quantum evolution (6.11) is performed. It is at τ_i where the classical evolution is plugged in, when the gauge fields start to be dynamical quantities. Further justification is needed at this point. We follow the discussion of [112], where this approximation was explained in detail. Basically the argumentation follows the line that if the gauge fields could have any effect in the subsequent evolution until the spontaneous symmetry breaking, the dynamics of the system would be quite dependent of the time τ_i where the gauge fields are "waken up". Figure 6.3 shows the behavior of the evolution for the $SU(2)$ gauge field and the evolution of Higgs-Inflaton system, by modifying the onset time of classical evolution. It can be seen that no important differences arise between them. This fact is further supported by the observed in figure (6.5). In this figure, the behavior of the energies of the system with the change of the gauge coupling, is shown. It can be seen the slow reaction of the energy stored in the system after the plug in of the gauge fields. The behavior of all the energy evolution before the S.S.B. does not depend of the actual strength of the gauge coupling, confirming the fact that the all modes to zero assumption for the gauge fields is self consistent. In this work the addition of the $U(1)$ gauge fields, does not represent any difference. Figure 6.4 represents the behavior of the gradient and kinetic energy of the Higgs, under changes of the abelian gauge coupling. As in the non-abelian case, no important effect is presented before the S.S.B. Again this can be interpreted as a self consistent test, that setting "all gauge fields to zero" before τ_i is reasonable.

Hence we can make use of the condition "all gauge fields to zero", as initial condition for the classical numerical evolution, at τ_i. However, although

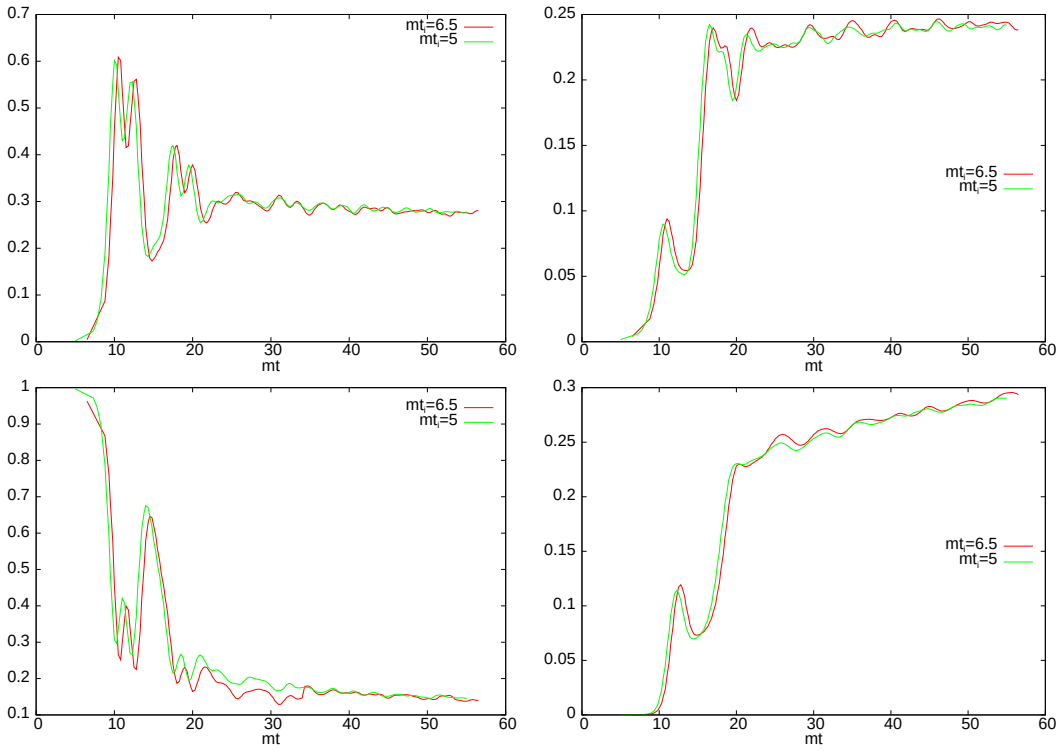

Figure 6.3: Evolution of the energies for two different onsets of the initial time. Top left: Kinetic energy; Top right: Gradient energy. Bottom left: Potential Energy; Bottom right: SU(2) energy.

this has been showed to be accurate, the same is not true for the derivatives of the gauge fields at the initial time of the classical evolution. They can not be set to zero due to the Gauss law, that acts as a constraint for the longitudinal derivative components of the fields. This will be explained with some more detail in the following sections.

6.2 The initial condition.

In the previous section we have described certain generalities about the quantum evolution for the simplified model, from the end of inflation at time t_c or (τ_c) to the time of the onset of the classical evolution t_i (τ_i). The transition from the simplified quantum system to the full classical system was justified by the use of the classical approximation, in which use this work relies. This transition however, may seem inconsistent. Starting from a quantum sys-

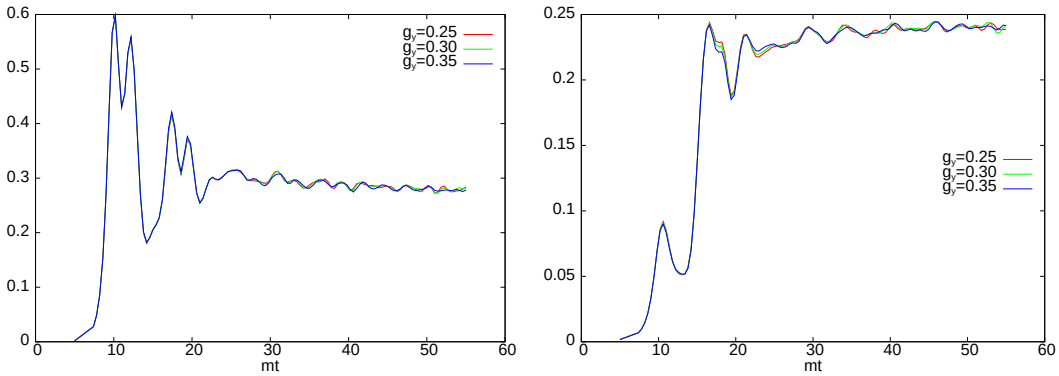

Figure 6.4: Behavior of the energies with the g_Y coupling. Left: Kinetic energy. Right: Gradient energy.

tem we end up in a deterministic classical one. This apparent inconsistency is removed if one thinks of equation (6.21). The quantum average can be emulated by the classical one evaluated on Gaussian random fields. These random fields enter through the initial condition for the classical evolution equations (see eqs. (6.16), (6.17) and (6.19)). This randomness is a remnant of the quantum nature of the system. The initial condition has to satisfy several requirements to make it compatible with the quantum evolution. In the present work the set up of the initial condition has been performed in the following way:

For the Inflaton field the initial condition is quite trivial. It is described just by its zero mode along the quantum evolution. This zero mode is described in the proximity of t_c as a linear function with t. The rest of the Inflaton quantum modes, are consistently set to zero. Hence, initially the Inflaton is described as:

$$\chi_0(t) = \chi_c(1 - Vm(t_i - t_c)), \tag{6.25}$$

where the only free parameter is the dimensionless Inflaton velocity V (remember that χ_c is determined by the end of inflation to be $\chi_c = m/g$ and m is fixed for convenience to be $m = \sqrt{\lambda}v$). Typically the speed of the Inflaton is such that the process takes place in less than one Hubble time, a condition known as the waterfall condition, which ensures the absence of a second period of inflation after the bifurcation point. The actual value of V depends very much on the model and the scale of inflation. For this work we have made use of the value studied in [112], $V = 0.024$. There are two main reasons to choose this value. The first is related to the numerical set up of

the modes. For the typical values of t_i, relevant momenta (the ones behaving classically) are $k < M\sqrt{\tau_i}$, where $M = (2V)^{1/3}m$ is a characteristic scale associated with the Inflaton initial velocity. The choice of that value for V is suitable to reduce the hierarchy of scales M/m, allowing a better numerical description, with less computational requirements. Another consideration concerns the time scales for backreaction (t_λ) and symmetry breaking (t_{sb}). There should be a hierarchy of scales such that $t_i \ll t_\lambda \ll t_{sb}$. The value of the Inflaton velocity is related with the time of symmetry breaking. This relationship was calculated in [111] to be:

$$mt_{sb} = (2V)^{-1/3}\Big[\Big(3.5 + \ln\frac{2\pi^2}{4\lambda(2V)^{2/3}}\Big)^2 - 8\Big]^{0.31} \tag{6.26}$$

The non-linear time t_λ it is also related with the Inflaton velocity. This time is the solution of the transcendental equation (see [111]):

$$mt_\lambda = (2V)^{-1/3}\Big[\Big(3.5 + \ln\frac{(2V)^{2/3}\pi^2\, mt_\lambda}{\sqrt{8\lambda}}\Big)^2 - 8\Big]^{0.31} \tag{6.27}$$

The value chosen for V ensures the correct hierarchy between time scales.

The initial condition for the Higgs is more complicated. From the change of variables (6.4), it is easily seen that the only parameter that determines the initial evolution, and therefore the initial condition for the classical evolution, is the parameter $M = (2V)^{1/3}m$. As pointed out before the Higgs field modes with $k/M > \sqrt{M(t_i - t_c)}$ are non tachyonic at t_i, and are consequently set to zero. The remaining tachyonic modes are determined by imposing that the quantum expectation values of Weyl ordered operators, are exactly reproduced by the initial condition (see equations (6.15)-(6.18)). In Ref. [111], it is described in detail, how this can be attained by drawing the initial Higgs field momentum modes, ϕ_k^α, from a Gaussian random field, of zero-mean and amplitude distributed according to the Rayleigh distribution:

$$P(|\phi_k^\alpha|)\, d|\phi_k^\alpha|\, d\theta_k^\alpha = \exp\Big(-\frac{|\phi_k^\alpha|^2}{(\sigma_k^\alpha)^2}\Big)\frac{d|\phi_k^\alpha|^2}{(\sigma_k^\alpha)^2}\,\frac{d\theta_k^\alpha}{2\pi}\,, \tag{6.28}$$

with a uniform random phase $\theta_k^\alpha \in [0, 2\pi]$ and dispersion given by

$$(\sigma_k^\alpha)^2 = k^{-3}P(k, t_i). \tag{6.29}$$

$P(k, t_i)$ is not an arbitrary function but is the power spectrum of the

initial Higgs quantum fluctuations given by [111]:

$$\langle|\phi(\vec{x},t_i)|^2\rangle \equiv \frac{4}{\mathcal{V}}\sum_{\vec{k}\neq\vec{0}}\frac{1}{k}\,P(\vec{k},t_i)\,. \tag{6.30}$$

where $\mathcal{V}$ stands for the volume of the system. This formula can be extracted from eq. (6.11). In the region of low momentum modes, $P(\vec{k},t_i)$ is very well described by:

$$P_{\rm app}(\vec{k},t_i) = \frac{1}{2m^2\pi^2}\,k^2\,(A(t_i)\,e^{-B(t_i)\,k^2/m^2}+1)\Theta(\sqrt{2Vmt}-k)\,, \tag{6.31}$$

where $A(t_i)$ and $B(t_i)$ are parameters extracted from a fit of this form to the exact power spectrum given in [111], and Θ is the Heaviside step function. Since for the tachyonic modes the Wigner function is "squeezed", it is possible to consider the distribution function for the $\dot{\phi}^\alpha_k$ as a delta function. So the initial condition for the time derivative of the Higgs components is totally determined by the value of the $\phi^\alpha(k)$ component, in the way:

$$\dot{\phi}^\alpha_k = \frac{F_k}{|f_k|^2}\phi^\alpha_k. \tag{6.32}$$

This ends the discussion about the initial condition for the Higgs modes.

In what respects to the gauge fields we follow the strategy to fix initially all modes to zero. In the previous section, we provided a brief argumentation and some test of consistency supporting this choice. We also explained that our formulation is gauge invariant and the measured quantities do not depend on the particular gauge choice. However, the fixing for the initial configuration requires further explanation.

Once the initial setting to zero of the spatial components of the gauge fields is justified, one could think that, at this initial time, the same is true for the time derivatives of the gauge fields. This is, however, not possible due to the necessity of implementing the Gauss constraints for both $SU(2)$ and $U(1)$ fields. The exact implementation of the constraints in this work can be found in appendix A.

For the considerations here it is enough to borrow from there the continuum form of the constraints. They are expressed, in the gauge $\mathcal{A}_0 = 0$, $\mathcal{B}_0 = 0$, as:

$$\begin{aligned} D_i\mathcal{G}^a_{0i}(\mathbf{x},t) &= j^a_0(\mathbf{x},t) = D_i[\partial_0\mathcal{A}^a_i](\mathbf{x},t), \\ D_i\mathcal{F}_{0i}(\mathbf{x},t) &= j^Y_0(\mathbf{x},t) = D_i[\partial_0\mathcal{B}_i](\mathbf{x},t), \end{aligned} \tag{6.33}$$

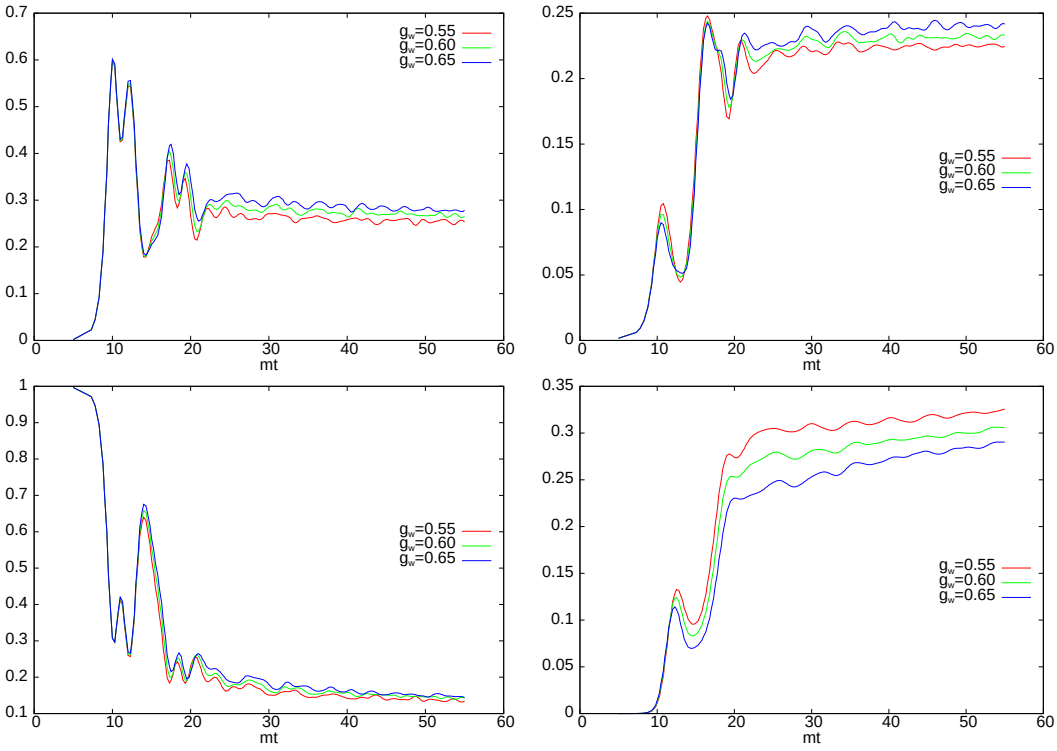

Figure 6.5: Dependence of the energies on the g_W coupling. Top left: Kinetic energy; Top right: Gradient energy. Bottom left: Potential Energy; Bottom right: SU(2) energy.

where the first equation holds for the $SU(2)$ part of the gauge group, and the one below for the $U(1)$ hypercharge group. Notice the symmetry of the expressions for both gauge subgroups, that allow us to follow the calculation for the $U(1)$ group from the calculation of the $SU(2)$ group, which is showed in the following.

At the initial time t_i where the gauge fields are set to zero, these equations are simplified since the covariant derivatives become trivial ones. Expressed in terms of Fourier modes the $SU(2)$ equation provides a way to initialise the temporal derivatives for the gauge fields:

$$\partial_0 \mathcal{A}^a_j(\mathbf{k}, t_i) = ik_j \frac{j^a_0(\mathbf{k}, t_i)}{k^2}, \tag{6.34}$$

where the explicit form of $j^a_0(\mathbf{k}, t_i))$ is given in terms of the Higgs Fourier modes at the initial time as:

$$j^a_0(\mathbf{k}, t_i)) = ig_W \mathrm{Tr}\{\tau_a[(\partial_0\Phi)\Phi^\dagger - \Phi(\partial_0\Phi)^\dagger]\}(\mathbf{k}, t_i). \tag{6.35}$$

An analogous expression is found for the $\mathcal{B}_i(\mathbf{k}, t_i)$ field, but with the correspondent hypercharge current:

$$j^Y_0(\mathbf{k}, t_i)) = ig_W \mathrm{Tr}\{\tau_3((\partial_0\Phi)\Phi^\dagger - \Phi(\partial_0\Phi)^\dagger)\}(\mathbf{k}, t_i), \tag{6.36}$$

where, as is further explained in appendix A.

6.3 The lattice approach.

This section is devoted to set the connexion between the classical system with the initial condition discussed above, and the numerical evolution, performed by the use of the lattice.

Once the initial condition is fixed the lattice approach is standard. The Lagrangian (4.24) which describes the complete system is:

$$\mathcal{L} = -\frac{1}{4}\mathcal{G}^a_{\mu\nu}\mathcal{G}^{\mu\nu}_a - \frac{1}{4}\mathcal{F}^{\mathrm{Y}}_{\mu\nu}\mathcal{F}^{\mu\nu}_{\mathrm{Y}} + \mathrm{Tr}\Big[(\mathcal{D}_\mu\Phi)^\dagger\mathcal{D}^\mu\Phi\Big] + \frac{1}{2}\partial_\mu\chi\partial^\mu\chi - V(\Phi,\chi)\,. \tag{6.37}$$

We would like to remind here the form of the most important terms. The potential that couples the Higgs and the Inflaton fields is:

$$\mathrm{V}(\Phi,\chi) = \mathrm{V}_0 + \frac{1}{2}(g^2\chi^2 - m^2)\,|\phi|^2 + \frac{\lambda}{4}|\phi|^4 + \frac{1}{2}\mu^2\chi^2\,, \tag{6.38}$$

and the Yang-Mills terms for the gauge fields are:

$$\mathcal{G}^a_{\mu\nu} = \partial_\mu \mathcal{A}^a_\nu - \partial_\nu \mathcal{A}^a_\mu + g_{\rm W} \epsilon^{abc} \mathcal{A}^b_\mu \mathcal{A}^c_\nu \tag{6.39}$$

for the $SU(2)$ gauge group, and

$$\mathcal{F}^{\rm Y}_{\mu\nu} = \partial_\mu \mathcal{B}_\nu - \partial_\nu \mathcal{B}_\mu, \tag{6.40}$$

for the Hypercharge fields.

The classical evolution of this system is driven by the classical equations of motion. These equations are extracted from the Lagrangian by the usual Euler-Lagrange method:

$$\frac{\partial \mathcal{L}}{\partial \xi} = \frac{d}{dt} \frac{\partial \mathcal{L}}{\partial \dot{\xi}} \tag{6.41}$$

where ξ stands for any dynamical variable. The set of classical equations coming out of this method is:

$$\begin{aligned} D_\mu D^\mu \Phi + \lambda(|\Phi|^2 - v^2)^2 \Phi + g^2 \chi^2 \Phi = 0 \\ (\partial_\mu \partial^\mu + \mu^2 + g|\Phi|^2)\chi = 0 \\ D^\mu \mathcal{G}^a_\mu \nu = j^a_\nu \\ D^\mu \mathcal{F}_\mu \nu = j^Y_\nu \end{aligned} \tag{6.42}$$

where j and j^Y are defined in equations (6.35) and (6.36) respectively.

In order to perform the numerical evolution of the system, the classical equations are discretized preserving full gauge invariance of the system, using the lattice formalism. This formalism is discussed in chapter 5. The procedure chosen is to translate the Lagrangian (4.24) into its lattice counterpart, which is:

$$\begin{aligned} \mathcal{L}_L &= \mathcal{L}_Y(n) + \mathcal{L}_{SU(2)}(n) \\ &+ {\rm Tr}\{({\rm D}_\mu \Phi({\rm n}))^\dagger {\rm D}^\mu \Phi({\rm n})\} + \frac{1}{2}\Delta_\mu \chi({\rm n}) \Delta^\mu \chi({\rm n}) - \kappa {\rm V}(\Phi({\rm n}), \chi({\rm n})), \end{aligned} \tag{6.43}$$

κ is a discretization parameter whose meaning is discussed in appendix A. Note also that the gauge content of the system is now stored in the link variables, and the Yang-Mills terms are now the lattice counterparts made of plaquettes (see chapter 5):

$$\mathcal{L}_Y(n) = \frac{2}{\kappa g_{\rm Y}^2} \sum_i {\rm Tr}[1 - P^{ab}_{0i}(n)] - \frac{\kappa}{g_{\rm Y}^2} \sum_{i \neq j} {\rm Tr}[1 - P^{ab}_{ij}(n)]\,, \tag{6.44}$$

$$\mathcal{L}_{SU(2)}(n) = \frac{2}{\kappa g_W^2} \sum_i {\rm Tr}[1 - P_{0i}(n)] - \frac{\kappa}{g_W^2} \sum_{i \neq j} {\rm Tr}[1 - P_{ij}(n)]\,. \tag{6.45}$$

and where all the derivatives are lattice derivatives and all matter fields are adimensional lattice fields. The *ab* superscript stands for plaquettes which only involve abelian fields. In the potential $V(\Phi(n),\chi(n))$ all masses are dimensionless masses $M_L = ma$, $\mu_L = \mu a$, so the potential has the explicit form:

$$\begin{aligned} V(\Phi(n),\chi(n)) = & - M_L^2 \mathrm{Tr}\{\Phi^\dagger(\mathrm{n})\Phi(\mathrm{n})\} \\ & + \lambda(\mathrm{Tr}\{\Phi^\dagger(\mathrm{n})\Phi(\mathrm{n})\})^2 + \frac{\mu_L^2}{2}\chi^2(\mathrm{n}) \\ & + g^2\chi^2(n)\mathrm{Tr}\{\Phi^\dagger(\mathrm{n})\Phi(\mathrm{n})\}. \end{aligned} \tag{6.46}$$

Performing the same Euler-Lagrange analysis than in the non discretized case, one can obtain the equations of motion for the lattice dynamical variables:

$$\begin{aligned} (\Delta_\mu \bar{\Delta}^\mu \chi)(n) &= \kappa\Big\{\mu_L^2 + 2g^2\mathrm{Tr}[\Phi^\dagger(\mathrm{n})\Phi(\mathrm{n})]\Big\}\chi(\mathrm{n})\,, \\ (D_\mu \bar{D}^\mu \Phi)(n) &= \kappa\Big\{ - M_L^2 + g^2\chi^2(n) + 2\lambda\mathrm{Tr}[\Phi^\dagger(\mathrm{n})\Phi(\mathrm{n})]\Big\}\Phi(\mathrm{n}), \\ \frac{1}{\kappa}\bar{D}^A_\nu G^{\mu\nu}(n) &= J^\mu(n)\,, \\ \frac{1}{\kappa}\bar{D}^Y_\nu F^{\mu\nu}(n) &= J^\mu_Y(n)\,, \end{aligned} \tag{6.47}$$

where the currents are given by:

$$\begin{aligned} J^\mu_a(n) &= \frac{ig_W}{2}[\Phi(n)(D^\mu\Phi)^\dagger(n) - (D^\mu\Phi)(n)\Phi^\dagger(n)]_a\,, \\ J^\mu_Y(n) &= \frac{ig_Y}{2}[(D^\mu\Phi)^\dagger(n)\Phi(n) - \Phi^\dagger(n)(D^\mu\Phi)(n)]_3\,, \end{aligned} \tag{6.48}$$

Details on the lattice Lagrangian and the lattice discretization of the equations of motion are presented in Appendix A.

Having the lattice version of the equation of motion, the numerical evolution is easy to perform, since the set of equations is expressed in terms suitable for computer programming. The connexion between the numerical discretized evolution and the continuum one is performed by the usual continuum limit of the quantities in the lattice formalism, which is discussed in chapter 5. From the lattice formalism, we will also use the artifact control techniques, as will be shown in chapter 10.

6.3.1 The Electromagnetic field.

In order to analyze the production of electromagnetic fields we have, first, to extract the $\mathrm{U}(1)_{\mathrm{em}}$ content of the SU(2)×U(1) fields in the Lagrangian (4.24). Let us remind that this can only be done unambiguously when the Higgs field is on the vacuum, i.e. in the broken symmetry phase. Fixing the unitary gauge, $\Phi(x) = \rho(x)\,\mathbb{1}$, the Z-boson field and the electromagnetic field are extracted from appropriate orthogonal combinations of the SU(2) and hypercharge vector potentials:

$$\mathcal{Z}_\mu(x) = \cos\theta_W\,\mathcal{A}^3_\mu(x) + \sin\theta_W\,\mathcal{B}_\mu(x)\,, \tag{6.49}$$

$$\mathcal{A}^\gamma_\mu(x) = \sin\theta_W\,\mathcal{A}^3_\mu(x) - \cos\theta_W\,\mathcal{B}_\mu(x)\,. \tag{6.50}$$

with $\varphi(x) = \Phi(x)(1,0)^{\mathrm{T}}$ the Higgs doublet. However even in that phase there can be points where the Higgs field vanishes and the symmetry is locally restored (a typical example of a configuration exhibiting such behavior is the sphaleron). At those points there is no unique way to define the electromagnetic fields. In chapter 8 we will analyze how this takes place in our set up.

As in the case of the continuum equations, it is necessary to extract the electromagnetic information out of our lattice variables. In the lattice formulation the gauge fields are no longer independent entities, and the gauge information is stored in the link variables, which are matrices of the gauge group. Thus, something similar to the linear combination used in the continuum case is here useless. Hence it is mandatory to have a definition for the lattice electromagnetic fields. This definition starts by realizing that one can compute, in a gauge invariant way, the field associated to the Z boson potential as:

$$Z_\mu(n) = \frac{-i\hat{n}\cdot\left((\hat{D}_\mu\hat{\Phi})(n)\hat{\Phi}^\dagger(n)\right)}{|\hat{\phi}(n)||\hat{\phi}(n+\mu)|} \xrightarrow{a\to 0} \quad a_\mu g_Z \mathcal{Z}_\mu\,, \tag{6.51}$$

where we have introduced the adjoint unit vector $\hat{n} = n_a\tau_a$, with components:

$$n_a(n) = \frac{\varphi^\dagger(n)\tau_a\varphi(n)}{|\varphi(n)|^2}\,, \tag{6.52}$$

with $\varphi(n) = \Phi(n)(1,0)^{\mathrm{T}}$ the Higgs doublet. The Z boson coupling is denoted by g_Z and $a_{\mu\neq 0} = a$, $a_0 = a_t$. D_μ is the lattice covariant derivative operator defined in equation (A.3) of appendix A. Our definition of the Z boson potential corresponds to the standard one in the unitary gauge.

We define the Z boson and hypercharge field strengths through the clover averages:

$$F^{\mathrm{Z}}_{\mu\nu}(n) = \langle \Delta_\mu Z_\nu(n) - \Delta_\nu Z_\mu(n) \rangle_{\mathrm{clov}} \stackrel{a\to 0}{\longrightarrow} a_\mu a_\nu g_Z \mathcal{F}^Z_{\mu\nu}(n) \tag{6.53}$$

and

$$F^{\mathrm{Y}}_{\mu\nu}(n) = \langle \Delta_\mu \theta_\nu(n) - \Delta_\nu \theta_\mu(n) \rangle_{\mathrm{clov}} \stackrel{a\to 0}{\longrightarrow} a_\mu a_\nu g_{\mathrm{Y}} \mathcal{F}^Y_{\mu\nu}(n)\,, \tag{6.54}$$

where $B_\mu(x) \equiv \exp(i\theta_\mu \tau_3)$ is the hypercharge link, Δ_μ is the lattice derivative operator introduced in Eq. (A.5) and $\langle O \rangle_{\mathrm{clov}}$ denotes the clover averages defined in Eq. (B.6). In terms of them we can compute the field strength of the $\mathrm{U}(1)_{\mathrm{em}}$ field as:

$$F^\gamma_{\mu\nu}(n) = \sin^2\theta_W F^{\mathrm{Z}}_{\mu\nu}(n) - F^{\mathrm{Y}}_{\mu\nu}(n) \stackrel{a\to 0}{\longrightarrow} a_\mu a_\nu e \mathcal{F}^\gamma_{\mu\nu}(n)\,, \tag{6.55}$$

This provides a gauge invariant definition of the electromagnetic field which verifies everywhere the lattice version of the Bianchi identities. A proof of this statement as well as the definition in the lattice of the Maxwell's equations can be found in appendix B.

6.4 Model and Lattice parameters.

In this section we consider the fixing of the parameters in the previous formulation, as a part of the methodology. In this fixing there are involved both Lagrangian parameters (with physical meaning) and lattice (discretization or artificial) parameters. Since they have different role, we will separate them in different sections. However, as we will see, they are tightly related.

6.4.1 Model parameters.

Let us first concentrate in the fixing of the parameters in the Lagrangian (4.24). This fixing is what we call a model. The Lagrangian has eight parameters: v, V_0, m, μ, g, g_Y, g_W and λ. Some of them were fixed when we presented the model of hybrid inflation in chapter 4. Let us remind that they were $V_0 = \lambda v^4/4$, $\mu \sim 0$, $g^2 = 2\lambda$, $m = \sqrt{\lambda} v$. In our formalism v is taken as a value of reference and all quantities are expressed in v units. It is then only necessary to fix it if we are interested in giving physical units.

Now we will fix the remaining parameters. At this point some considerations must be taken into account. The first parameters we are going to fix

are the gauge couplings g_W and g_Y. $g_W = 0.65$ is fixed to its physical value, and the value for g_Y is given by the value of g_W and the physical Weinberg angle, leading $g_Y = 0.35$[1]. This makes both masses of the W boson $m_{\rm W}$ and the Z boson $m_{\rm z}$ fixed to their physical value.

The next parameter to fix is λ. This is an important parameter since its value influences the time of the non linearities , (t_λ), and the symmetry breaking time (t_{sb}). As discussed in the section devoted to the initial condition, they must satisfy a hierarchy: $t_1 << t_i << t_\lambda$. The greater is λ the narrower is the window for t_i, that is the window for plugging the classical evolution. Hence low values of λ would be preferred. However λ is related with the mass ratio between the Higgs and the W bosons:

$$\frac{m_{\rm H}}{m_{\rm W}} = \frac{\sqrt{2}m}{m_{\rm W}} = 2\sqrt{2}\frac{\lambda}{g_W} \tag{6.56}$$

Some of the artifacts in the evolution have showed to be very sensitive to the value of $am_{\rm W}$. It was showed in [112] that optimal values to keep them under control were values $am_W \lesssim 0.3$. Here ma is fixed by lattice considerations as will see in the next section (fixing $p_{\rm min}$ and N_s), and so $m_{\rm H}$. The restrictions for the value of $am_{\rm W}$ determines the value of λ. For typical values of $am \sim 0.7$ the ratio should be $m_{\rm H}/m_{\rm W} \gtrsim 3$ to keep the artifacts controlled. Taking smaller values for ma, we can go to mass ratios $m_{\rm H}/m_{\rm W} \gtrsim 2$. However, as we will see below, these smaller values are computationally more expensive. Whereas the previous Lagrangian parameters have been fixed in all our simulations, what determines the model is the value of the $m_{\rm H}/m_{\rm W}$ ratio. We have used three different mass ratios. These models are shown in table 6.1. Values for $m_{\rm H}/m_{\rm W}$ below two are unreachable with our computational power, and would be future work. There is a ratio that is quite far from the most expected range for Higgs mass values. This is $m_H/m_W = 4.65$. There have been two main reasons to keep such a rare model. One has been historical motivations. This model was deeply studied (although the model there was quite more artificial, since the m_W mass was not the physical one, in difference with the one used here) in the reference works [111, 112]. In some sense, a part of this work has been a further test of the exposed there, going to greater times, adding extra $U(1)$ degrees of freedom, and testing to the limit the classical approximation. So it is interesting to use the same model in order to compare the influence of the differences in this new modification.

[1] $g_W = 2m_{\rm W}/v$, $m_{\rm W} = 80$GeV, $m_{\rm z} = \sqrt{g_W^2 + g_Y^2}v/2$, $v = 246$GeV and $tan\theta_W = g_Y/g_W = 0.54$

$\lambda = g^2/2$	V	$g_{\rm W}$	$g_{\rm Y}$	$m_{\rm H}/m_{\rm W}$
1.156	0.024	0.65	0.35	4.65
0.48	0.024	0.65	0.35	3.0
0.21	0.024	0.65	0.35	2.0

Table 6.1: List of model parameters used in our analysis. We have taken the Inflaton velocity $V = 0.024$ and the Inflaton bare mass $\mu = 10^{-5} gv \approx 0$. The Hypercharge and SU(2) couplings are such that the W mass and the Z to W mass ratio reproduce the experimental values.

The other reason is no one knows exactly the value of the parameter λ, and consequently the actual m_H/m_W ratio. Hopefully, the near onset of LHC will solve this problem. For the moment it would be desirable to have a study of how the system depends of the exact value of this mass. One striking result coming from this thesis is, even in the case of $m_H/m_W = 4.65$, the major part of the quantities studied (as we will see, the quantity that has showed to be more model dependent has been the mean helical susceptibility) have resulted to be quite model independent if they are given in m units.

6.4.2 Lattice parameters.

Lattice computations are constrained by the available computational power. This is unavoidable, as is unavoidable that some restrictions in the calculations arising in this kind of works, come just from this computational part. This thesis is not an exception. Hence it is necessary to have a discussion, about the kind of technical problems related with some parameter choices, and their associated computational difficulties. In tables 6.2 and 6.3 we enumerate the different lattices and physical volumes used in our simulations. Lattice spacings a and a_t correspond respectively to spatial and temporal directions. The physical volume, $\mathcal{V} = L^3$ is given in terms of the minimal momentum: $L = 2\pi/p_{\rm min} = N_s\, a$.

In the following, it is presented a discussion about what are the relevant scales of the problem, how they are determined by the Lagrangian parameters and the classical approximation, and how the lattice parameters are to be chosen in order to give (an always difficult) compromise between an accurate description of the system and a viable computational power request.

N_s	ma	ma_t	$p_{\min}/m$
32	1.31	0.025, 0.018	0.150
48	0.87	0.025, 0.018	0.150
64	0.65	0.025	0.018

Table 6.2: List of lattice parameters: a and a_t are respectively the spatial and temporal lattice spacings, N_s is the number of lattice points and $p_{\min} = 2\pi/(N_s a)$ is the minimal momentum.

First I would like to spend some lines on the description of the computational power that has been used to perform the present work. For the first part of this thesis, corresponding to the references [120] and [119](2005), a Beowulf cluster was used. It was composed by four nodes with two processors each, and the following specifications:

- two nodes with two processors Dual Athlon MP 1900+ (1.6GHz) each and 512MB of shared RAM.
- one node with two processors Dual Athlon MP 1900+ (1.6GHz) and 1024MB of shared RAM.
- one node with two processors Dual Athlon MP 2400+ (2.0GHz) and 1024MB of shared RAM.

with this computational power the results presented in [120] and [119](2005), took around a year. The lattice sizes and volumes studied with it are showed in table 6.2. These sizes have proved to be enough for some observables of interest, but not for all. It was hence necessary to go to bigger sizes. For the rest of the work exposed in this thesis, bigger computers were required. The clusters Marenostrum (Universidad Politécnica de Barcelona, Spain) and Lisa (Sara Cluster Netherlands) were used during the earlier testing period. The results presented here and in references [118] and [121] were obtained with the cluster Ciclope (I.F.T/Universidad Autónoma de Madrid, Spain) with the following specifications:

- 32 nodes with dual processor Intel Xeon 3.2 GHz EM64T 2MB cache
- 2 GB DDR-2 RAM

N_s	ma	ma_t	$p_{\min}/m$
64	0.65	0.025, 0.033, 0.050	0.150
80	0.52	0.025	0.150
100	0.42	0.025	0.150
100	0.52	0.025	0.125
100	0.65	0.025	0.100
120	0.65	0.025	0.080

Table 6.3: List of lattice parameters: a and a_t are respectively the spatial and temporal lattice spacings, N_s is the number of lattice points and $p_{\min} = 2\pi/(N_s a)$ is the minimal momentum.

On it was possible to achieve the lattice sizes presented in table 6.3. These lattice sizes, have been shown to be accurate enough to keep a good control for the lattice artifacts, as is shown in chapter 10. The typical running time has been around 3 days per configuration.

After this technical information, I would like to present some considerations about the choice of lattice parameters.

For the reader unfamiliar with lattice gauge theories a brief overview was given in chapter 5. In the case of this thesis we are interested in a lattice time evolution, so the time direction has to be treated in a special way, differently from the spacial ones. Due to this, we have to fix three lattice parameters: the spatial lattice spacing ma (an arbitrary unphysical parameter, which determines the spatial coarseness of our lattice), the time spacing ma_t (another arbitrary unphysical parameter providing the time resolution), and a physical non arbitrary parameter: the physical spatial length mL, which gives the spatial extent of our system. The parameter m comes from the Lagrangian of the model (4.24), and is used in order to take care of the dimensionality of both a and L.

The way to fix the size and coarseness of the lattice, depends on the physical scales of the problem we are dealing with. These parameters are freely chosen but under certain restrictions. The choice must ensure that the lattice parameters are such that they resolve the physical system properly. If the system is described by only one physical spatial scale ξ:

$$ma << m\xi << mL$$

As mentioned above, we are dealing with a lattice numerical evolution in time, so the first scale we would like to fix is the lattice time spacing.

As usual, it is desirable to have a compromise between the accuracy in the description of the time evolution and the temporal extent of the simulation. The requirement is that the typical time scale (let us call it mt_c) of a change in the solution is several times bigger than ma_t. So knowing t_c one could get to a compromise between $ma_t << mt_c$ and a reasonable computational time. To estimate the optimal choice for ma_t we have compared several different values for this parameter, checking the stability of the results. From these values, we have selected three different lattice spacings $ma_t = 0.05,\ 0.033,\ 0.025$. An essential requirement is that they provide enough accuracy to describe the total Energy and Gauss constraint conservation. That was more extensively studied in [120]. The behavior of both observables has showed to be quite sensible to the change of time spacing. Inside the interval $ma_t \lesssim 1/20$ the total energy is conserved with deviations below a 0.5%, whereas the Gauss constraint was satisfied to machine precision ($\sim 10^{-15}$) at initial times. Afterwards, due to rounding errors, this value is increasing along the evolution, but kept far below any measurable limit ($\sim 10^{-14}$ at $mt = 100$ in the evolution). At the end, the most often used value for ma_t is 0.025.

In the case of the spatial scales, the situation is slightly different. We have two different scales in order to set up our lattice parameters. The first one, the physical volume of the lattice, has to be big enough to avoid finite-volume artifacts. This is achieved, as usual, if the physical length of the relevant structures in the system is small compared with the physical length of the lattice. In our case the relevant scale is determined by the applicability of the classical approximation. As was pointed out in section 6.1, at time $\tau = \tau_i$ all momenta satisfying $k/m << \sqrt{\tau_i}M/m$ (we now refer the momentum to the quantity m, which is used as lattice momentum, see chapter 5) are tachyonic and become classical. Our lattice scale has to provide an accurate description for this range of momenta. For that, the momentum discretization induced by the finite volume has to be small enough when compared with $\sqrt{\tau_i}M/m$. The relation between the physical length of the lattice and the minimun momentum is as usual:

$$\frac{p_{\min}}{m} = \frac{2\pi}{mL}. \tag{6.57}$$

Hence the condition for a good description is $p_{\min}/m << \sqrt{\tau_i}M/m$. As was discussed in the section devoted to the initial condition, M is given by the Inflation velocity V ($M = (2V)^{1/3}m$). The chosen value $V = 0.024$ makes M big enough and helps to satisfy this condition.

In the present work this $p_{\min}$ is used as a free parameter, to regulate the

physical volume. By analyzing the $p_{\min}$ dependence we have found that the system is well described for $p_{\min} \lesssim 0.15m$. Most of our results correspond to $p_{\min} = 0.15m$ although we have also used $p_{\min}/m = 0.125$, 0.1, 0.08, in order to have a better description of the system, and as a way to contrast that the volume artifacts are under control. These four values of $p_{\min}$ have the following associated physical lengths:

$$\begin{aligned} p_{\min}/m = 0.150 &\rightarrow Lm = 41.88 \\ p_{\min}/m = 0.125 &\rightarrow Lm = 50.27 \\ p_{\min}/m = 0.100 &\rightarrow Lm = 62.82 \\ p_{\min}/m = 0.080 &\rightarrow Lm = 78.54. \end{aligned} \tag{6.58}$$

The scale ma that gives the coarseness of the lattice is given, once we have fixed $p_{\min}$ by the number of points of the lattice N_s:

$$mL = 2\pi m/p_{\min} = N_s\, ma. \tag{6.59}$$

Thus, optimizing both requirements of a small $p_{\min}$ and a small ma requires a greater N_s which is computationally expensive. In table (6.3) we list the values of N_s and $p_{\min}/m$ we have used and their associated ma value. Our best lattice has been the $N_s = 100$. Most of the results presented in this work correspond to it. We have found that for $p_{\min} \sim 0.15m$ lattices with $N_s < 64$ exhibit large lattice artifacts. Optimal values are then $ma \lesssim 0.7$.

Chapter 7

Some considerations on helicity and MHD.

The multi-disciplinary nature of this thesis could make it difficult, specially for the ones non familiar with the field, to appreciate the details of the last chapters of this work, where the results are presented. For that reason, the aim of the present chapter is to place the reader into a context essential to understand the main results of this thesis. We are referring to the Magneto Hydro-Dynamical plasma description, which is the context where the major part of the studies in the field of cosmic or large scale magnetic fields are placed. This MHD description provides a theoretical framework to relate the plasma dynamics and the evolution of the magnetic fields embedded on it, representing a powerful tool for a big brand of research areas involving magnetic phenomena, as Tokamak physics, astrophysics and solar corone physics and cosmic magnetic fields. Hence, a considerable part of the extent of this chapter is dedicated to present some considerations about the elements of MHD and plasma physics, making special emphasis in its by far more used limits: The ideal and the resistive MHD. At some point of this presentation of MHD, we will advance a particular and interesting property of our system, which will be manifest in chapters 8 and 9, and which is that our particular system, although retaining certain properties of the limits of MHD, has showed not to fit completely into this description. Interesting phenomena will arise from this misfitting, but their study is postponed to the cited chapters.

In addition to the brief review of MHD, this chapter presents also an introduction to a concept that plays a crucial role, not only in our particular case, but in general in the field of magnetogenesis. This concept is the magnetic helicity. We dedicate the second part of this chapter to study first

its definition and physical interpretation, and later its role in the MHD. It is in this MHD context where the relevance of the helicity in the study of the large scale magnetic fields will be manifest. At that point, we will particularize from the meaning of the helicity in a general MHD context, to the particular issue of interest for this thesis, which is the role of the magnetic helicity in the evolution of the large scale magnetic fields. We dedicate a section to review the main results achieved by other authors, which can be summarized in one: It is not only believed, but quite established, that the presence of helical fields in the system, reduces the dissipation rate of magnetic energy and produces an extra enhancement of the correlation length of the fields. It will be manifest, after that section, that the helicity is the main character in the large scale magnetic field theater. This thesis is not an exception as we will see.

Along the discussion of this chapter the helicity is presented as an "ad hoc" quantity, that exists in the system without apparent origin. In this thesis, however, we will address the creation of magnetic helicity, as a natural mechanism in our scenario, which goes together with the creation of magnetic field. This is explained in chapter 8. The mechanism found in our case, reminds very much the one proposed by Vachaspati-Cornwall (see refs. [68]-[70] and [72]), providing a particular realization of the later. We dedicate the last section in this chapter to close the discussion about helicity and its role, by addressing the pending issue of its generation. We will develop that section along the lines of the Vachaspati-Cornwall mechanism.

Summarizing: This chapter is devoted to review some important concepts involving MHD and magnetic helicity. In the first place the Magnetohydrodynamical limit, is reviewed. Secondly, a brief dissertation about the definition and role of the magnetic helicitiy in a plasma system is presented. We will end the chapter devoting a couple of sections to the role of the helicity in the LSMF evolution. The importance of this quantity in our work will then become manifest.

To end this introduction I must say that this chapter is far away from being exhaustive, nevertheless I will try to give an useful overview of the main issues related with the work object of this thesis.

7.1 The Magnetohydrodynamics Equations.

In this section we present the basic equations and ideas that are present in any magneto hydrodynamical study. Our discussion will be developed in a non-relativistic framework for simplicity. It does not imply a qualitative loss of generality, since the main concepts of interest for the present work are nicely reproduced in the non-relativistic limit, as is shown in references [58],[61], [60] and [62]. In addition, our system is mainly composed by heavy W boson particles, instead of lighter particles. At the temperatures observed in this study, this fluid is not clearly relativistic. As we will see, the fluid does not completely fit into the non-relativistic, neutral and high conducting approximation we are going to discuss, but presents certain aspects in common.

This section is mainly based in reference [63]. A classical plasma is a system with N individual particles. In order to know the exact description of the system at a time t it is necessary to know $6N$ variables at each time, that means to solve $6N$ equations of motion. This is too much for being solved analytically. This problem is in the basis of any statistical treatment of a complex system. The way to deal with it, is the standard statistical mechanics approach, in which the system is described just by macroscopically averaged variables, that are functions that enclose the relevant information of the system, without attending to its actual state. Fluids are then described by variables as their energy density, charge, velocity density etc... We will not go into details of the development of the non-relativistic equations of the fluid because it is too long to be reviewed, and not very relevant for the purpose of this thesis. Let us just present them as they are:

$$\begin{aligned} \frac{\partial \rho}{\partial t} + \vec{\nabla}\rho\vec{V} &= 0 \qquad (7.1) \\ \rho\Big(\frac{\partial \vec{V}}{\partial t} + \vec{V}\vec{\nabla}\vec{V}\Big) &= \rho_q\vec{E} - \nabla p + \vec{j}\times\vec{B} + \vec{\nabla}\Pi \\ \frac{\partial p}{\partial t} + \vec{V}.\vec{\nabla}p &= -\Gamma p\vec{\nabla}.\vec{V} + (\Gamma-1)[-\vec{\nabla}.\vec{q} + \Pi : \vec{\nabla}\vec{V} + \eta j^2] \end{aligned}$$

where ρ is the mass density, $\vec{E}$, $\vec{B}$, $\vec{j}$ are the electromagnetic fields and the currents, ρ_q is the charge density, $\vec{V}$ is the fluid local velocity, $\vec{q}$ is the heat flux trough the boundary of the system, η is the resistivity and Π is the viscous stress tensor, which is obtained from the strength tensor P:

$$P_{ij} = p\delta_{ij} - \Pi_{ij} \qquad (7.2)$$

These equations come from the development of the energy flow equation for a fluid with an electromagnetic field present on it, together with the energy conservation and the continuity equation. The only approximation made so far is the ideal gas approximation for the fluid, in which the energy is given by the pressure through the adiabatic coefficient Γ:

$$\rho_e = \frac{p}{\Gamma - 1} \tag{7.3}$$

where ρ_e is the energy density. The symbol : stands for the total contraction of the indexes for two tensors:

$$\Pi : \vec{\nabla}\vec{V} = \sum_i \sum_j \Pi_{ij} \partial_i V_j. \tag{7.4}$$

Something noticeable of the equations (7.1) is that they are two scalar and one vectorial equation. So in total five independent equations. Hence there are many more unknowns than equations, so for the system to be solved further information is required. The information regarding to relations between $\vec{B}$, $\vec{E}$, ρ_q, and $\vec{j}$ comes from the Maxwell equations. The rest will require further discussion and is enclosed in the so called closures. The parameter Γ, however, is known.

There are some important considerations coming from the combination of the Maxwell equations and the equations of the fluid (7.1). Indeed these implications, as we will see below, are related closely with the applicability (or more exactly the lack of it) of standard non-relativistic MHD to our system.

The Maxwell equations are:

$$\vec{\nabla}\vec{E} = \rho \tag{7.5}$$
$$\vec{\nabla}\vec{B} = 0 \tag{7.6}$$
$$\vec{\nabla} \times \vec{E} + \partial_0 \vec{B} = 0 \tag{7.7}$$
$$\vec{\nabla} \times \vec{B} - \partial_0 \vec{E} = \vec{j} \tag{7.8}$$

where we are using natural units $c = \mu_0 = \epsilon_0 = 1$. The way to couple these Maxwell equations to the fluid ones is just by a new equation: Ohm's Law. It establishes that, in a system of reference co-moving with the fluid, the electric field and the current are related by :

$$\vec{E}' = \eta \vec{j}. \tag{7.9}$$

The E' is related with the E field in the stationary frame with a Lorentz transformation:

$$\vec{E}' = \frac{\vec{E} + \vec{V} \times \vec{B}}{\sqrt{1 - V^2}}, \tag{7.10}$$

The Maxwell equations are Lorentz invariant, but the fluid ones we presented are only Galilean invariant equations. They are thus two different formulations and need to agree. As discussed above we choose a non-relativistic formulation. It is easy to make the Maxwell equations Galilean invariant, by keeping just the first order in the V expansion. We will get the non-relativistic MHD limit.

In this way the Galilean Ohm's law can be obtained from:

$$\begin{aligned} \vec{E}' &\sim \vec{E} + \vec{V} \times \vec{B}, \\ \vec{E} + \vec{V} \times \vec{B} &= \eta \vec{j}. \end{aligned} \tag{7.11}$$

This is the first consequence of the loss of Lorentz invariance. The second one is a widely used approximation. In the Ampere's Law there are two terms than contribute to the current: $\partial_0 \vec{E}$ and $\vec{\nabla} \times \vec{B}$. We can define ω as the typical frequency of temporal variation of a field in the system, whereas the spatial typical variation length is defined by l^{-1}. So the ratio between the norm of both terms in Ampere's law can be written as:

$$\frac{|\partial_0 \vec{E}|}{|\vec{\nabla} \times \vec{B}|} \sim \frac{E_0 \omega}{B_0 / l} = \frac{E_0}{B_0} V_0 \sim V_0^2 \ll 1 \tag{7.12}$$

where E_0 and B_0 are the averaged amplitudes of the fields over the extent of the typical variation. We also define the velocity V_0 as an averaged velocity in the plasma, given by $V_0 = l\omega$. It is easy to estimate the ratio E_0/B_0. From the equation (7.11) we get:

$$\begin{aligned} \vec{E}_0 + \vec{V}_0 \times \vec{B}_0 = \eta \vec{j_0}, \\ \left| \frac{E_0}{B_0} \right| \sim V_0 \end{aligned} \tag{7.13}$$

where the term $\eta \vec{j_0}$ has been neglected due to the fact that as a good approximation η is a small parameter for the majority of the plasmas. Thus the

term with the time derivative (the displacement current) can be neglected[1] in Ampere's Law giving the definition for the current in non-relativistic MHD:

$$\vec{j} = \vec{\nabla} \times \vec{B} \tag{7.14}$$

Similarly the term with the charge density ρ_q in the second equation of (7.1) can be neglected since, by the same arguments as before, it can be shown that the Lorentz force dominates:

$$\frac{|\rho_q \vec{E}|}{|\vec{j} \times \vec{B}|} \sim V_0^2 \ll 1 \tag{7.15}$$

Summarizing, the complete set of non-relativistic MHD equations is:

$$\begin{aligned}
\frac{\partial \rho}{\partial t} + \vec{\nabla} \rho \vec{V} &= 0 \qquad (7.16)\\
\rho\Big(\frac{\partial \vec{V}}{\partial t} + \vec{V}\vec{\nabla}\vec{V}\Big) &= -\nabla p + \vec{j} \times \vec{B} + \vec{\nabla}\Pi \\
\frac{\partial p}{\partial t} + \vec{V}.\vec{\nabla} p &= -\Gamma p \vec{\nabla}.\vec{V} + (\Gamma - 1)[-\vec{\nabla}.\vec{q} + \Pi : \vec{\nabla}\vec{V} + \eta j^2] \\
\partial_0 \vec{B} &= -\vec{\nabla} \times \vec{E} \\
\vec{\nabla} \times \vec{B} &= \vec{j} \\
\vec{E} + \vec{V} \times \vec{B} &= \eta \vec{j}
\end{aligned}$$

7.1.1 The Ideal MHD.

The equations (7.16) represent a reduction of the unknowns of the system (7.1) and an increment on the number of equations. There are actually 14 equations for 27 unknowns: ρ (1 unknown), $\vec{E}$ (3), $\vec{B}$ (3), $\vec{V}$ (3), η (1), $\vec{j}$ (3), p (1), $\vec{q}$ (3), Π (9). We need still 13 additional relations to solve the system. These equations are extracted from the closures. They usually come from the extra knowledge about the nature of the fluid. The simplest closures are just plasma models, that basically consist in the argument of values to several of the unknown parameters. In the following we only concentrate in the particular models of interest for this study.

[1] Reference [45] discuss the situation when the displacement current can not be neglected. It also presents an interesting comment about the relationship between relativistic MHD and strong collective effects.

Let us first discuss a medium that is isotropic and presents no net heat flux. Hence $\Pi = 0$ (hence $\Pi : \vec{\nabla}\vec{V} = 0$ and $\vec{\nabla}\Pi = 0$), and $\vec{q} = 0$. This fluid is also a perfect electrical conductor and has no viscosity or thermal conductivity. Such a medium is not present in Nature and could seem a quite artificial idealization of a real medium. However it turns out that this idealization describes very well some properties of real strongly magnetized plasmas, which usually present a high (not perfect) conductivity. The most important property of such a medium is that $\eta = 0$. In that case Ohm's Law gives a relation between $\vec{E}$ and $\vec{B}$:

$$\vec{E} = -\vec{V} \times \vec{B}, \tag{7.17}$$

For such a medium the equations (7.16) simplify to a set called the ideal non-relativistic MHD equations:

$$\begin{aligned}
&\frac{\partial \rho}{\partial t} + \vec{\nabla}\rho\vec{V} = 0 \\
&\rho\Big(\frac{\partial \vec{V}}{\partial t} + \vec{V}\vec{\nabla}\vec{V}\Big) = -\nabla p + (\vec{\nabla} \times \vec{B}) \times \vec{B} \\
&\frac{\partial p}{\partial t} = -\vec{V}.\vec{\nabla}p - \Gamma p\vec{\nabla}.\vec{V} \\
&\partial_0 \vec{B} = \vec{\nabla} \times (\vec{V} \times \vec{B})
\end{aligned} \tag{7.18}$$

Notice here the simple form for the magnetic field evolution.

Ideal MHD is often used in the context of the primordial magnetic fields, as an approach to their evolution. Two important characteristics arise in the ideal MHD. The first is related with the integrated helicity, and will be discussed in the next section. The second is known as the Frozen Flux Theorem (FFT). This theorem has important physical consequences that are profusely used in the literature concerning the cosmic magnetic fields, including the stellar ones.

The FFT theorem states that the magnetic lines of force are "frozen" into the fluid flow lines. This means that the fluid cannot move crossing the magnetic field, but is however free to move along the magnetic lines. The demonstration of this statement starts with the definition of the magnetic flux. If C is a closed line co-moving with the fluid, the magnetic flux across the surface S enclosed by this line is:

$$\Phi = \int_S \vec{B} d\vec{S} \tag{7.19}$$

The changes with time in this flux come in two different ways. First the change due to changes in $\vec{B}$ keeping S and C fixed. And the second the change in S produced as C moves with the fluid. As C moves each line element produces a change of S given by $\vec{dS} = \vec{V} dt \times \vec{dl}$, where $\vec{V}$ is the fluid velocity, and dt is the time interval. The two variations together gives the total time derivative of the flux:

$$\frac{d\Phi}{dt} = \int_S \frac{\partial \vec{B}}{\partial t} d\vec{S} + \oint_C \vec{B}.(\vec{V} \times \vec{dl}) \tag{7.20}$$

Making use of the Maxwell equation that relates $\partial_0 \vec{B} = -\vec{\nabla} \times \vec{E}$ it gives:

$$\frac{d\Phi}{dt} = -\oint_C (\vec{E} + \vec{V} \times \vec{B}).\vec{dl} \tag{7.21}$$

which is identically zero by Ohm's law in ideal MHD. Thus the flux is conserved for any surface enclosed by a curve co-moving to the fluid, what implies that the field lines are glued to the fluid movement, and the fluid moves along the magnetic lines.

The FFT has important consequences for the evolution of the plasmas which fit inside the Ideal MHD description. As will see below, relaxations of this theorem will produce interesting phenomena related with helicity non-conservation. It is particularly interesting its local relaxation, which allows changes in the magnetic local structure, and has consequences for the correlation length of the fields. Further details can be found at the end of the chapter.

At this point, all the IMHD concepts important for the object of this thesis, have been briefly reviewed. This ends the discussion about ideal MHD for the moment. We will come back to the issue when studying the relationship between IMHD and helicity.

7.1.2 Resistive MHD.

As mentioned in the previous section, ideal MHD is a strong idealization of a magnetic fluid, that is far from real plasmas. Although it succeeds in describing many of their properties it also misses some important ones. We will see an example below but, for the moment, let us only say that sometimes it is necessary to go to less restrictive conditions than the ones

of ideal MHD. There are several different models that are extensions of this ideal MHD, which are given by the particular choice of the closure relations. The simplest and minimal extension to ideal MHD is called resistive MHD. Although it is still a quite simple model, it possesses interesting properties relevant for plasma and magnetic physics.

The resistive MHD encompasses the same assumptions as the ideal MHD, except for Ohm's Law. That is, both $\vec{q}$ and Π are chosen to be zero, but the η parameter is not set to zero. With this, the complete set of equations for the resistive MHD is :

$$\begin{aligned}
&\frac{\partial \rho}{\partial t} + \vec{\nabla}\rho\vec{V} = 0 \\
&\rho\Big(\frac{\partial \vec{V}}{\partial t} + \vec{V}\vec{\nabla}\vec{V}\Big) = -\nabla p + (\vec{\nabla}\times\vec{B})\times\vec{B} \\
&\frac{\partial p}{\partial t} = -\vec{V}.\vec{\nabla}p - \Gamma p\vec{\nabla}.\vec{V} \\
&\partial_0\vec{B} = \vec{\nabla}\times(\vec{V}\times\vec{B}) - \vec{\nabla}\times(\eta\vec{\nabla}\times\vec{B})
\end{aligned} \tag{7.22}$$

The first implication of having a non zero resistivity η is the break down of the validity of the frozen flux theorem. Now the time derivative of the magnetic flux is given by:

$$\frac{d\Phi}{dt} = \oint_C \eta\vec{j}d\vec{l} \neq 0 \tag{7.23}$$

This implies that the magnetic lines are no longer frozen to the fluid motion. This fact will have important consequences that will be exposed bellow.

The second important characteristic comes from the last equation of (7.22). If η is a constant parameter the equation takes the form:

$$\partial_0\vec{B} = \vec{\nabla}\times(\vec{V}\times\vec{B}) + \frac{1}{\sigma}\nabla^2\vec{B} \tag{7.24}$$

where $\sigma = \eta^{-1}$ is the electrical conductivity of the fluid, a more familiar quantity. Notice that, the second term on the right hand side, is a diffusion term. The effect a non-zero η is hence the presence in the system of a diffusion capacity. In a highly conducting fluid the diffusion term is negligible and the first term, called dynamo term, dominates. On the contrary, if the conductivity of the plasma is small, the system would be dominated by

diffusion effects. In this limit the solution can be approximated to the pure diffusive solution:

$$\vec{B}(\vec{x},t) \sim \int d^3y \frac{e^{-\frac{|\vec{x}-\vec{y}|^2}{4t}}}{\sqrt{t}} \vec{B}(\vec{y},0) \tag{7.25}$$

This brief introduction to Resistive MHD (RMHD) pretended to show that a minimal extension of IMHD allows to describe a rich phenomenology, in which the magnetic field is no longer frozen into the plasma, and diffusive effects are allowed. The inclusion of a resistive term represents a better description for realistic plasmas. However the utility of the RMHD description resides, as we will see in the last section of the chapter, in that it opens the window for other kind of processes, like reconnection or one of most interesting for this thesis: the inverse cascade mechanism. We end here the discussion about RMHD, but we will retake it when we talk about the role of helicity in this approximation, and the inverse cascade mechanism.

To end the discussion about general MHD and as an advance of the results, I must say that, for this thesis, the set of approximations performed to obtain the equations for both MHD models, must be carefully treated. It is then worth to remember that they were:

- The modification of Ohm's Law to make it Galilean
- The modification also of Ampere's Law
- The neglect of the electrostatic force versus the Lorentz's one.

Is important to point out that they all come from the so called "long wave" MHD approach, that makes the Maxwell equations to fit the non-relativistic scenario.

As pointed out at the beginning of the section, the results presented in chapters 8 and 9, will strongly indicate that all these approximations fail when applied to our system, and for that reason they must be carefully revised. However, our system presents certain properties, which remind phenomena belonging to both approximations. This could indicate the existence of a part of the W bosons fluid that behaves similarly to the non-relativistic MHD. As we will show, at the very early stages of the evolution, our plasma seems to be very tied to the magnetic lines of force, something that reminds, in some sense, the ideal MHD. These structures remain stable and with an almost preserved flux, during some (brief) time extent in the evolution, which

is also in common with ideal MHD. We have strong indications that soon after, some diffusive effects enter the picture, the magnetic lines merge and change their spatial structure and helicity, let us say their "topology", phenomena that are characteristic of a resistive MHD (see the next section). However we certainly know that the plasma is not in this limit, or at least, in its simpler realization with a constant σ.

As is explained in the conclusions, we demonstrate that the relativistic effects cannot be entirely neglected. The (longitudinal) electric field presents a component that plays and important role in the plasma, what prevents the neglection of the $\partial_0 \vec{E}$ term. We also know, after performing several attempts to extract information of the plasma parameters, that η is a tensorial quantity which depends on both the point and the direction, and that the plasma presents regions of high charge separation, giving rise to a important electrostatic force compared with Lorentz's force. In chapters 8 and 9, further details are presented supporting these statements.

7.2 The role of the helicity in the MHD scenario.

As we will see, an interesting feature coming out of the present work is the generation of a non trivial helical susceptibility during preheating. For that reason, in the following I will review some basics aspects of the concept of magnetic helicity as well as the physical interpretation for this quantity. After that, we will present some considerations about the role of the helicity in the MHD limit, concretely in the two approximations mentioned above: the ideal and the resistive MHD. These review sections are mainly based on the works [53], [54], [55], [67] and [70].

As a starting point let me say that, the complexity of fluid systems like the one subject of this thesis, which presents the characteristics of a strongly magnetized plasma, makes it difficult to keep a detailed track of the evolution of the structures and phenomena arising there. It is then useful to find invariants that allow to quantify the characteristics of the plasma. The most familiar magnetic related invariants are the flux and the energy, preserved under certain conditions. There is however, when dealing with magnetic systems, a third invariant which is preserved in the ideal MHD limit: the integrated helicity.

The integrated helicity is a measure of the topological properties of the magnetic field lines. The physical interpretation of this quantity is the quan-

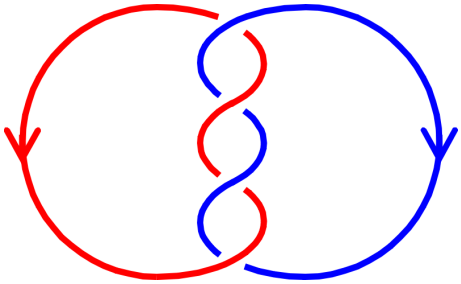

Figure 7.1: Two linked lines with linking number 2. *Source: Wikipedia.*

titative measurement of the degree of linkage, twisting and kinking of the magnetic lines. They all contribute to the integrated helicity.

By definition the integrated helicity in a closed volume (i.e. $\vec{B}.\hat{n}_S = 0$ at the boundary S of the volume) is given by the formula:

$$H = \int d^3x \vec{A}(x).\vec{B}(x) \tag{7.26}$$

where $\vec{A}(x)$ is the usual vector potential. The connexion between this expression and the linking of lines follows from the Gauss linking number. This number counts the linking of two closed curves and is expressed by:

$$L_{12} = -\frac{1}{4\pi} \oint_1 \oint_2 \frac{d\vec{x}}{d\sigma} \frac{\vec{r}}{r^3} \times \frac{d\vec{y}}{d\tau} d\tau d\sigma \tag{7.27}$$

where τ and σ are two parameters that parametrize both curves. Figure 7.1 shows two linked lines which the respective linking number.

Instead of field lines we can think of the magnetic field as a collection of flux tubes. The helicity integral gives a measure of the linking of these flux tubes. For further details see reference [53]. There are also contributions to this quantity often called self-helicity when the flux is twisted with respect to a central axis. In the more general case, and as we will see later, in the case of the system studied in this thesis, the magnetic field axis can be changing itself in a way that contributes to the helicity. Figure 7.2 shows a typical example. In such cases the self-helicity has two contributions, the one given by the internal twist along the axis and the quantity known as the writhe, that measures the kinking and the winding of the axis.

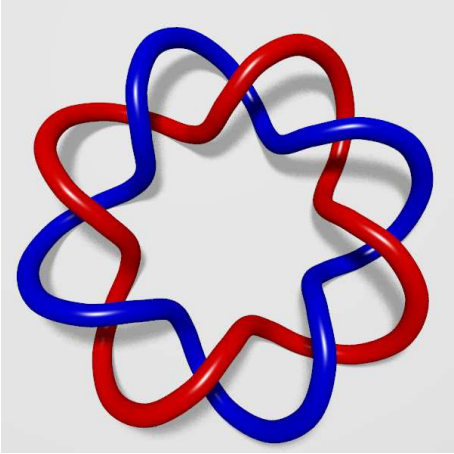

Figure 7.2: Two flux tubes with $L_{12} = 4$ and with both internal twist and writhe. *Source: Wikipedia.*

7.2.1 Helicity in the ideal MHD limit.

After reviewing the meaning and role of the integrated helicity, we can now explore its relationship with ideal MHD.

As said previously it is advantageous when studying a system to find constants that are preserved in the evolution. This is the case of the integrated helicity in the ideal MHD limit.

To explain it, let me first give a qualitative argument based in the application of the Flux Frozen Theorem. The integrated helicity would be conserved in the evolution if there is no way to change the topology of the field lines. So if we think on two linked lines as the ones in figure 7.1, the way to change their integrated helicity is to change either the flux or the linking number. The magnetic flux is a preserved quantity in the model, so it could only be the linking number. But any change in the linking number implies a crossing of the lines, which would imply a fluid movement across the magnetic lines, not allowed in ideal MHD. The same is true for the internal twist.

Quantitatively, the time derivative of the integrated helicity (7.26) is in general given by:

$$\frac{dH}{dt} = -2\int_V d^3x\, \vec{E}.\vec{B} - 2\oint_S \phi\vec{B}.\vec{n}\, d^2x \tag{7.28}$$

where ϕ is the electrostatic potential, $\vec{E} = -\vec{\nabla}\phi$, V is the volume and S is the surface enclosing the volume, and $\vec{n}$ is as usually, the unitary vector normal to the surface. The second term can be removed by a choice of

boundary conditions $\phi\vec{B}.\vec{n} = 0|_S$, giving the more familiar expression:

$$\frac{dH}{dt} = -2\int d^3x\, \vec{E}.\vec{B} \tag{7.29}$$

But from the ideal Ohm's law $\vec{E} = -\vec{V} \times \vec{B}$, so $\vec{E}.\vec{B}$ is identically zero. This demonstrates that no-helicity changes are allowed in the ideal MHD limit.

7.2.2 Helicity in the resistive MHD.

As discussed above, the applicability of ideal MHD, although quite extended under certain circumstances, is not of general use, especially if the fluids under consideration are far from being good conductors. There are even situations in which, although being excellent conductors, the systems might be studied out of the ideal MHD. The reason is that ideal MHD looses certain phenomena that are crucial for understanding the evolution of realistic systems. The extension of such an ideal situation into a resistive MHD introducing a small, but non zero, value for η implies an improvement of this situation.

One of the most important characteristics, which is highly desirable in almost any situation (coronal magnetic fields in the sun, laboratory plasmas, magnetic fields in stars and planets, etc...), and more specially, in the evolution of cosmic magnetic field, is the reconnection process. In this process two close magnetic lines reconnect to make two new ones (sometimes one new) in order to achieve a lower energy state. This reconnection process plays a fundamental role in cosmic magnetic field evolution, being responsible of phenomena as the dynamo mechanism. It also could represent a method to enlarge the magnetic coherence length by means of several different magnetic lines that reconnect to make new larger ones. Of course this reconnection process implies the topology of the magnetic field lines is changing. This represents a significant difference with the situation in ideal MHD, where due to the invariance of the topology of the lines, the reconnection process is nonexistent.

There is a lot of literature about resistive MHD processes in several scenarios, attending to several of its characteristics. In the present work, apart from the dissipative effects of the non-zero η necessary in any realistic plasma description, we are particularly interested in the fact that in this limit the Frozen Flux Theorem is not satisfied. There is no doubt that the most important consequence of the breaking of the FFT is that the integrated helicity

is consequently not preserved. Moreover, in the resistive limit the variation of the integrated helicity with time takes a simple expression:

$$\frac{dH}{dt} = \eta \int d^3x \, \vec{j}\vec{B} \tag{7.30}$$

This expression implies that in the resistive limit, the variation of the integrated helicity is associated to places where the current and magnetic vectors are not orthogonal. In general the processes that modify the helicity are present at any scale in the system. However, under certain assumptions it is argued (not totally established), that the changes on helicity could be only of local nature. We dedicate the next section to further explanations along this line.

As pointed out in the previous section, we have found that, although our system has shown to be too complicated to fit into the resistive MHD, it presents certain characteristics of this limit. One of these characteristics is the non preservation of the integrated helicity. Another similarity with resistive MHD is the non orthogonality of the current and the magnetic field. In chapter 8 we study in some extent the relationship between both quantities. More exactly, a brief discussion is presented about their spatial structure and the angle that these two vectors form. As we will see, although the spatial distribution is slightly dominated by regions with nearly orthogonal vectors, there is an important deviation from orthogonality. These similarities support the idea that some sort of, maybe very complicated, resistive process is acting in the system, being a starting point for the understanding of some of the results presented in chapter 9.

All this ends this section devoted to the role of the helicity in the magnetic fluids. To conclude I would like to point out that several works [41], [57]-[62], [70, 72, 74, 80, 124], propose that the presence of helicity in the primordially generated magnetic fields, may speed up the growth of the magnetic field coherence length, providing larger mangetic strength at larger scales than the non helical magnetic fields. This important result is relevant for the present work, since as will be seen, the system contains a mechanism for generation of non-trivial magnetic helicity. Hence, the next section is devoted to review several consequences of the presence of a non-trivial helicity in the evolution of the large scale magnetic fields, as well as, some of the most important results coming of the cited references.

7.3 The role of the helicity in the LSMF evolution.

It is a general belief, supported by both theoretical and numerical argumentation, that the presence of a non trivial helicity in a magnetic system, influences its later evolution in a determinant manner. In particular in the context of cosmological or large scale magnetic fields it would help to solve the main problem of the causal generation mechanisms. Leaving to the next section, the issue of whether the magnetic field generation mechanisms can produce non vanishing helicity, this section is devoted to the study of helical magnetic field evolution.

Let us remember for a moment, what was presented in chapter 3 as the main problem of the magnetic field generation mechanisms based in causal effects. The most important difficulty they have to deal with, is the smallness of their correlation length, since it is restricted to fit inside the size of the Hubble horizon at the time in which the mechanism is active. In the case of this thesis, the mechanism proposed is acting at the electroweak epoch, in which the Hubble size of the Universe is about $\sim$ 3cm. Supposing the magnetic field was produced with a correlation length of the size of the Hubble radius, and taking into account the expansion of the Universe from that epoch, they would have a correlation length today of about 10^{15}cm. This quantity is reduced in two orders of magnitude by protogalactic contraction, giving a final value of 10^{13}, or $1AU$, for the dynamo seeds. This has been probed to be too small for seeding the best developed dynamo theories , which need fields with a coherence scale of order 100pc at least.

The references [41, 45], [57]-[62], [70, 72, 74] and [80] investigate the possibility that magnetohydrodynamical effects can lead to a substantial increase of the scale of the produced magnetic fields. The total amount of the increment is not completely clear. It differs from numerical to analytical studies under various approximations, and it depends very much of the model under consideration. All of them, however, agree on the conclusion that the produced amplification could be several orders of magnitude greater, in the case in which the initial magnetic fields are strongly helical. This effect is further realized in case the fields are "maximally" helical, as studied for example in [57] or [62]. In what follows we briefly review the main lines that lead to this important conclusion, as well as, some of the results in both helical and non-helical cases.

The context where these studies have been developted is the resistive MHD limit with the addition of a viscosity term. In equations (7.22) this term is neglected, but its inclusion only changes the equation where the temporal derivative of the velocity is involved:

$$\rho\Big(\frac{\partial\vec{V}}{\partial t}+\vec{V}\vec{\nabla}\vec{V}\Big)=-\nabla p+(\vec{\nabla}\times\vec{B})\times\vec{B}+\nu\nabla^2\vec{V} \tag{7.31}$$

The effect of this ν term is to set the scale where the kinetic energy is dissipated.

It was shown in [59] that the decaying Hydro-Dynamical turbulence present in this limit, could lead to a faster growth of the magnetic correlation than what one would expect from the expansion of the Universe alone. The argumentation is based in the fact that the resistive MHD provides a mechanism for the growth of the scale: the selective decay. This mechanism is inherited from the fluid part of the resistive MHD equations, that is, from fluid Hydro Dynamics, and is a characteristic feature of hydrodynamical systems described by it.

It is well known that the fluids in dissipative Hydro Dynamics develop a turbulent decaying process, or direct cascade, where the energy is transferred from long wavelength modes to short ones due to the non-linearities in the fluid equations. This turbulent process is so complicated than till the date it has no satisfactory solution. Paradoxically, the most important insight into the properties of the turbulent spectrum was obtained by means of a simple dimensional analysis. This theory is due to Kolmogorov [64] (see also [65]). The selective decay is based on the fact that the smallest spatial structures decay faster than the biggest ones. In this sense the value ν provides a cut off in momentum space, giving a upper bound to the maximum momentum in which the energy can be transferred. The process can be schematically seen in picture 7.3. On it, we represent a fluid composed of several eddies of different scales. The mean scale of the system is represented in red. As time goes by, the smallest eddies are dissipated, and only the biggest ones remain. Hence, the typical scale is larger than before. Assuming that these eddies carry with them magnetic field, the magnetic scale could be enhanced as well. The same is true with any other quantity associated to the eddies.

Taking into account a simple dimensional analysis (based in the one of Kolmogorov, but assuming certain conditions as equipartition of the kinetic and magnetic energy) D. T. Son in reference [59] finds that the smallest wavelength that survives to this dissipation process at time t can be expressed

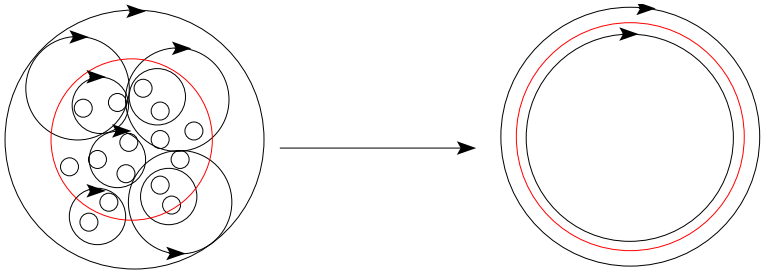

Figure 7.3: Schematic example of a turbulent dissipation process. The mean scale is represented as a red curve. The arrow represents the time evolution.

as:

$$l(t) \sim \left(\frac{t}{t_0}\right)^{2/5} l_0$$

both t_0 and l_0 are reference scales with a physical meaning. The same dimensional analysis gives a time dependence for the energy:

$$E(t) \sim B_0^2 \left(\frac{t}{t_0}\right)^{-6/5}.$$

The temporal behavior implies a big enhancement of the coherence length that could be about two orders of magnitude greater. The correlation length could reach 100AU insted the 1AU coming from the EW horizon expansion alone.

These results are implicitly assuming that the spectrum at low k remains unmodified during the time scale of decay of the high k modes, which is usually a fast process. This is certainly true for the major part of hydrodynamical fluids but it seems to be uncertain in MHD. The reason is the inverse cascade turbulence, which is a very particular phenomenon of MHD. Actually, the knowledge of how the turbulence is realized in MHD, is even smaller that in the fluid Hydro Dynamics described above. It is believed that it has certainly many differences, for instance, it will be no longer an isotropic process since the magnetic field provides a preferred direction in space. In [66] it was suggested that this inverse cascade is a generic feature of MHD turbulence. They came to this conclusion by assuming a particular form of the magnetic spectrum at low momentum. However it has been shown in [59], [57]-[62] that there is an extra condition for the inverse cascade to be met: The integrated magnetic helicity of the system must be non-zero. In [59] was also checked that in the case of zero integrated helicity no inverse

cascade was present in the MHD turbulent decay. We leave to the next section the discussion of how such a non-trivial helicity fields can be generated. Now let us develop, a bit further, the main lines of the argument in favour of a relationship between helicity and inverse cascade.

As pointed out in a previous section, the integrated helicity (7.26) is a preserved quantity in ideal MHD evolution. In this ideal limit the fluid is tied to the magnetic lines, so not only the integrated helicity is a preserved quantity, the "local" helicity is also preserved as a consequence of the Frozen Flux Theorem. This local helicity is defined by restricting the volume integral in (7.26), to smaller volumes bounded by field lines.

In the case of non-zero η term the conservation of the helicity is less obvious. Indeed, if the η term dominates, the magnetic field dies exponentially fast and helicity is not conserved. But if the fluid velocity is not negligible the evolution depends on both terms of equation (7.24). In this case there is no resolution for the evolution. However, Taylor in [56] presented a conjecture that, in the case both terms of the equation are competitive, the "local" helicity of the fields changes due to reconnections of the field lines, and hence is not conserved; however the global (or integrated over the whole volume) helicity remains approximately conserved, since it is the sum over a lot of local random changes. This conjecture is, of course, taken under certain restrictions of the values of the η and $\vec{V}$ parameters. This unproved conjecture gave a successful explanation of the "reversed field pinch" problem, a traditional problem in plasma physics, and where the conjecture was originally proposed. The Taylor conjecture seems also to be numerically confirmed.

Assuming the Taylor's conjecture is true, the conservation of the "global" helicity has an important consequence for the evolution of the magnetic field. When dealing with a system in which the "global" helicity is non-vanishing, the short scale modes are not simply washed out during the decay. Their magnetic helicity must be transferred to the remaining ones, with larger scale, when they dissipate. Along with the magnetic helicity, some magnetic energy is also saved with it from the turbulent decay. This process produces the inverse cascade mechanism.

Hence, there are some calculations following this line. Assuming also that the quantity $\vec{A}.\vec{B}$ has the same sign all over the space, some estimations can be extracted along the same basis of dimensional analysis used in the non-helical case. These analytical calculations give [59]:

$$l(t) \sim \left(\frac{t}{t_0}\right)^{2/3} l_0$$

which means a significant increment with respect of the non-helical case where no inverse cascade is present. The dissipation of the magnetic energy is slower than the non-helical one:

$$E(t) \sim B_0^2 \Big(\frac{t}{t_0}\Big)^{-1/2}$$

However other numerical calculations [60],[57],[61], giving the same value for the exponent of the energy decay, obtain a value of 1/2, instead of 2/3, for the exponent for the length.

To end this section let me point out two things. The first is that in order to calculate the actual scale of the magnetic fields nowadays the previous formulas for the length and the energy behavior, have to be taken into a cosmological framework. These equation are flat non-expanding equations, but they can be used, provided the time used is the conformal time. The complete calculation is presented in several of the references listed in this section, and also can be followed in chapter 3 for our particular case. Secondly, in our particular system, we have found a stronger inverse cascade than 1/2, even greater than the 2/3 obtained in [59]. In our case the inverse cascade leads to a ~ 1 exponent and, even more strikingly, our simulations present an injection of energy in the low modes instead of the dissipation effect. These results, again, enforce the idea that our system does not fit into a usual MHD description, or at least into its simpler forms, as are the ones used in the references provided in this section.

7.4 Generation of helical magnetic fields

In the previously discussed, the helicity has been presented as an "ad hoc" quantity, which is, or is not, present at the system. We did not pay attention to its origin, or if it is, or is not, possible to generate it in a natural manner. In this section we address the issue of the magnetic field generation with non-trivial helicity. We will now concentrate in a particular generation mechanism which is relevant in our case: The Vachaspati-Cornwall mechanism. More exactly, we will adopt the Vachaspati's point of view (see [72] for Cornwall's proposal), more appropriate for our particular system. In the following this mechanism will be qualitatively reviewed.

Vachaspati's mechanism is based on the idea that there is a connection between the helicity of the primordial magnetic fields and the process of Electro Weak Baryogenesis. In this process, the changes of the Chern-Simons

number are produced by the creation and dissipation of non-perturbative configurations such as the sphalerons or the linked loops of EW strings. It is believed that such kind of configurations would be produced by the complicated dynamics of the EW phase transition and afterwards they would decay. However the change in the Chern-Simons that they produce can not be washed out after the decay by new configurations. This basic idea is in the basis of the mechanism for the magnetic helicity generation. The same that happens with the Chern-Simons number could be true if we think of the magnetic helicity. Both quantities present a very similar form, so the parallelisms are very tempting. Moreover, such non-perturbative configurations are expected to carry some fluxes of abelian and non-abelian fields. The conservation of this fluxes along the decay process of these configuration, could represent a way to preserve both the magnetic field and the helicity, once the configurations decayed.

A particularly simple and illustrating example of the process is given by Vachaspati in [70], and we reproduce it here. We can think of a simple case of such a non-perturbative configuration, carrying non-trivial helicity or linking. It could be the case of the two linked Z-string loops. The evaluation of the integrated helicity of this configuration gives clearly a non-zero value. The decay of the strings occurs by means of their breaking into a segment, with a monopole and an anti-monopole as endings. Notice than assuming the initial plasma is a good conductor, the magnetic flux must be conserved, so at the endings of the segment the flux contained in the Z-string is continued as magnetic flux. The process is schematically represented in figure 7.4. When the Z-strings completely decay, the magnetic flux still retains the previous helical structure, that would enter the turbulent process described above, and influence the inverse cascade.

To relate this discussion with what we observe, let me say that we have found these Z-strings to be abundantly present at the initial stages of the evolution of our system, and to be strongly correlated with the magnetic fields lines. We also found that both the magnetic field and the Z boson present identical integrated helicity (see chapter 9) but in the case of the Z boson it tends to decay, whereas the tendency is inverse in the magnetic helicity case. Nevertheless, the mechanism that seems to be at work in our case is not exactly this, although directly related. Our observations support what will be one of our main results: the preheating scenario presents a concrete realization of the Vachaspati's magnetic field generation mechanism presented in [68]. This mechanism proposes that the generation of the Z-strings and the magnetic fields are produced by gradients in the Higgs field,

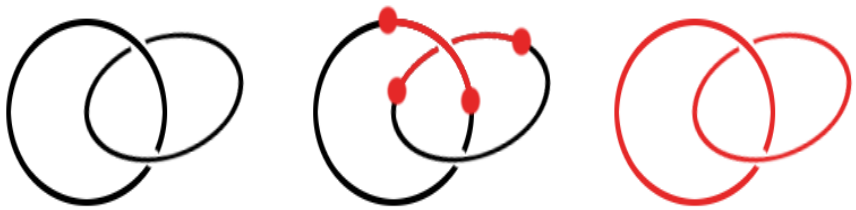

Figure 7.4: Representation of the decay of a two linked loops of Z-string (in black). The creation of a monopole anti-monopole pair, leads a magnetic flux remnant, represented in red. Adapted from [70].

and is further discussed in chapter 8. Moreover, our results seem to point to certain relations between the gradients of the Higgs field, the magnetic field, the helicity and the Z-strings with sphaleron like configurations, providing them as initial non-perturbative configurations from where the helicity is created. At this time this is only a speculation, which needs further study, and is planned as future work. However, the connection between the sphaleron and the magnetic fields has been studied recently by Copi et al. [124], hinting in the same direction as our conjecture.

Chapter 8

The mechanism underlying magnetic field generation.

In this chapter a study of the production of magnetic fields during the first stages of our cold EW preheating scenario is presented.

Our study has showed that it is useful and clearer, to separate the whole evolution into two different parts, attending to the kind of processes relevant during each one. As will become clear after reading the two following chapters, the separation is marked by the behavior of the Higgs field norm. This is illustrated in figure 8.1. It shows the behavior of the vacuum expectation value for both Higgs and Inflaton fields, two important observables in the evolution. It can be appreciated how the Higgs vev starts the evolution at very low values, and gets a value $\sim v$ around time $mt = 10$ (actually this time is $m_{\rm H}/m_{\rm W}$ dependent and ranges from $\sim 10 - 13$). At the same time, the Inflation vev goes from a high value $\sim \chi_c$, to a value ~ 0. Figure 8.2 is an schematic view of fig. 8.1. On it these two regions are marked with the two red ellipses. We must say that the boundaries of this separation are not sharp boundaries. There is a smooth transition between regions, whose location depends on the ratio of masses ($m_{\rm H}/m_{\rm W}$) considered. In that figure some important phenomena occurring during the periods are also indicated into boxes. Actually the study has differentiated a third important stage in the evolution: The initial time. However, for simplicity, we will present it as a part of the SSB region.

All the considerations in this chapter will concern the SSB region in fig. 8.2. The second region or "late time" region will be discussed in the next chapter. These earlier stages are characterized by the realization of the Spontaneous Symmetry Breaking, and the strong oscillatory behavior of the Higgs

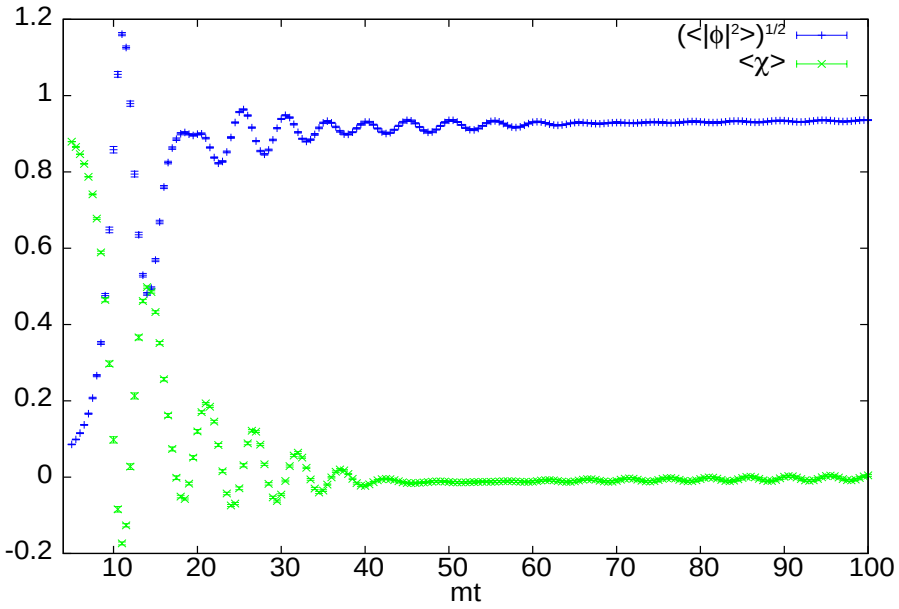

Figure 8.1: Evolution of the Higgs and Inflaton vevs, referred to v and χ_c respectively. From $mt = 5$ to $mt = 100$. For $ma = 0.42$ and $m_{\rm H}/m_{\rm W} = 2$.

v.e.v. The analysis of this period of SSB is performed in several steps. The first, is the study of the initial configuration, with the development of a proposal for an initial magnetic field generation mechanism. Some tests showing that it is at work during the initial time region follow. We investigate the presence, size and structure, of the magnetic fields generated by our Gaussian random field initial distribution. This distribution has shown to be quite related with the initial electromagnetic field generation. This study of the initial configuration is complemented by the results presented in Appendix 4.

After this initial stage of magnetic field generation, we will track the evolution of these magnetic fields through the highly non-linear stages associated to EW symmetry breaking. This is a crucial period where there are no viable alternatives to our methodological approach.

8.1 Initial Magnetic fields

One of the more surprising results coming for the analysis performed in this work, is the fact that at the initial time t_i (or τ_i), where the classical evolution is plugged in, there is already a rather strong magnetic field present in the

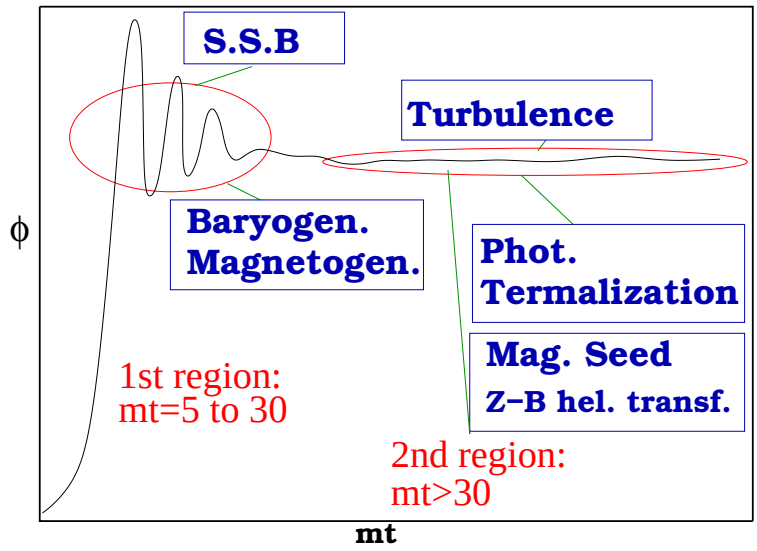

Figure 8.2: Schematic picture of the evolution of the Higgs vev. The two differentiated behaviors of the vev translate into two regions where different processes of interest arise. Some of them are indicated within the boxes. Z-B hel. transf. stands for the process of helicity transfer between the Z and the magnetic fields.

system. We choose for the all the results presented in this thesis (except the ones presented in appendix D) a initial time of $mt_i = 5$. The fact that there is a magnetic field present at this time is reflected in a non vanishing magnetic energy showed in figure 8.11. This could be a quite striking fact, when one thinks of the universe just after inflation at a very low temperature, with the gauge fields resting in their vacuum state and even, set to be equal to zero (as discussed in the previous chapter). But this is easily understood taking a closer look at our expression of the photon field (6.55). It not only involves gauge fields (or link variables in this case) but includes information coming from the Higgs field. This is the basis of this initial magnetogenesis. I would like to note that with this statement I mean that this initial magnetic field, is not an artifact of the definition chosen for the magnetic field. On the contrary, it provides a natural way for the generation of magnetic fields in this and similar scenarios. The discussion on how this comes about follows a line of argument very similar to that developed by Vachaspati in [68]. The line proposed in Vachaspati's work can be summarized in the fact that, in cosmological phase transitions, the Higgs field develops gradients around its vacuum expectation value. These gradients can result in the creation

of a non-negligible electromagnetic field. The magnetic field generated in this way, could even persist after the phase transition, leaving some sort of magnetic remnant. This is argued from the existence, in the electromagnetic tensor, of a term involving such gradients, as can be read from [68]. In that paper, a generalization of the electromagnetic field strength is given. This generalization can be used even in those places where the system is in the false vacuum. It is based on the same idea than the generalization of the electromagnetic vector potential :

$$\mathcal{A}^{\gamma}{}_{\mu} = sin\theta_W \, n^a \mathcal{A}^a_{\mu} + cos\theta_W \, \mathcal{B}_{\mu} \tag{8.1}$$

This expression comes from the definition of the electromagnetic vector potential given by t'Hooft in Ref. [123], where he pointed out the consequences of the ambiguity of the usual definition in the Georgi-Glashow model, tying it to the appearance of non-trivial configurations like monopoles or strings, acting as sources of magnetic fields. The vector n is a unit vector, which gives the unbroken direction in the algebra of the $SU(2)$ gauge group. This unit vector is defined as:

$$n^a = -\frac{4}{v^2}\phi^{\dagger}\sigma^a\phi \tag{8.2}$$

where ϕ is the Standard Model Higgs. Using the same criteria, the electromagnetic field strength is defined as:

$$\mathcal{F}_{\mu\nu} \equiv \partial_{\mu}\mathcal{A}^{\gamma}{}_{\nu} - \partial_{\mu}\mathcal{A}^{\gamma}{}_{\nu} - i4g_W^{-1}v^{-1}\sin\theta_W[(\partial_{\mu}\phi)^{\dagger}\partial_{\nu}\phi - (\partial_{\nu}\phi)^{\dagger}\partial_{\mu}\phi] \tag{8.3}$$

where $\mathcal{A}^{\gamma}{}_{\mu}$ is the photon gauge field, v is the true vacuum expectation value of the Higgs and g_W is the $SU(2)$ gauge coupling constant. Notice that even in the case where all the $\mathcal{A}^{\gamma}{}_{\nu}$ vanish, if the $\sin\theta_W$ is non zero, there can be still non-vanishing electromagnetic fields.

We have been found, that this general proposal for the generation, is realized in a particular way in the scenario object of this thesis: the tachyonic preheating. On it, of course, $\sin\theta_W \neq 0$. The high Higgs field gradients are present, even at initial times, due to the inhomogeneities of the multicomponent Gaussian Higgs field.

As was pointed out before, in chapter 6, the full quantum evolution of the preheating system gives an initial distribution for the classical Higgs field. This distribution is given in Fourier space (for more details see 6 and appendix D), and presents the form of a Gaussian random field. Despite the

randomness in Fourier space, since the momenta taken into account for this initialization are the low momentum ones, the initial Higgs field configuration presents a very smooth behavior, as can be seen from figure 8.3.

The initial configuration is conformed by bubbles, made of higher values of the Higgs field norm. The Higgs field within the bubbles is oscillating with time, specially in the SSB region. These bubbles are surrounded by locus of points where the Higgs field norm presents low values. We have observed that the locus of minima present certain tendency to remain for a long time in the system. This is illustrated in picture 8.3. On it the centers of the bubbles present a Higgs norm about ~ 0.5. The values under ~ 0.35 fill almost the whole volume and are filtered as white color values. As pointed out before and can be seen from this figure, these bubbles are very spherically symmetric, and only present some deviations of their sphericity in the regions where two or more bubbles are very close.

Figure 8.3 also shows the norm of the gradients of the Higgs field. According to the proposal by Vachaspati, the important quantity for the production of electromagnetic fields is the product of different components of the gradients. Nevertheless, the norm of the Higgs gradient gives an idea of the locations where gradients could be important, and their relation with the Higgs structures. The important information in this figure is that there are zones with a considerable extension where the gradients have an important strength, and the points where the norm of these gradients is greater do not correspond to the points where the maxima of the Higgs bubbles are placed. A closer look shows that this high gradient norm zones are located surrounding Higgs bubbles. This fact has important consequences for the location of the points where the magnetic field will be generated, as we will see below.

Summarizing, we find that the initial configuration at the start of our simulations (remember we choose time $mt = 5$ for this starting point), presents a non uniform and rich spatial distribution, in which bubbles of high Higgs norms and strong norm gradients are present, providing all the ingredients for an scenario similar to the one suggested by Vachaspati.

Having this qualitative picture of how the initial Higgs field looks like, and how it produces high gradient structures, let me now expose how the gradients of the Higgs field enter the magnetic field production in our particular scenario. I would like to note, that in this initial configuration the SU(2) and hypercharge gauge fields remain small. This was argued in chapter 6. This statement is incorporated into our initial conditions by setting the hypercharge and SU(2) magnetic-like fields to zero, and fixing the corresponding

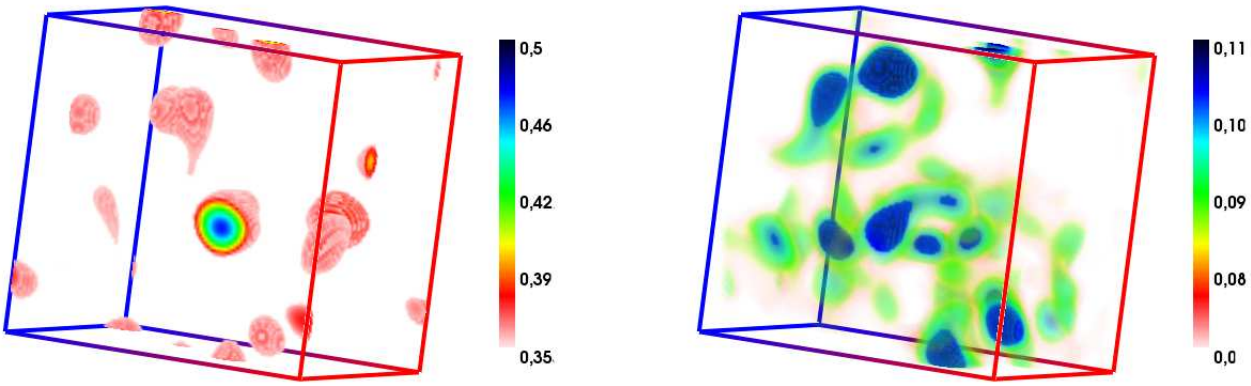

Figure 8.3: Left, locus of Higgs norm maximum points. Right, locus of points with maximum Higgs-gradient norm. Both at initial time.

electric fields in order to satisfy the Gauss constraint. We work in the $A_i = 0$ gauge, which on the lattice corresponds to $U_j(t = t_i) = B_j(t = t_i) = \mathbb{1}$. Using this fact, the translation of equation (8.3) into our formalism, proceeds through the definition of the Z field (the magnetic field is introduced through the definition of the Z boson field strength, see equation (6.55)). For vanishing gauge fields the definition of the Z field presents a simple form, and so does the photon field, obtaining:

$$\begin{aligned} Z_\mu(x) &= \frac{1}{2g_z}\,\mathrm{Tr}\left[\, i\hat{n}\,\Omega(x)\partial_\mu\Omega^\dagger(x)\,\right] \qquad (8.4)\\ F^{\mathrm{Z}}_{\mu\nu}(n) &= \frac{1}{2g_z}\,\mathrm{Tr}\left[\, i\hat{n}\left(\partial_\nu\Omega(x)\partial_\mu\Omega^\dagger(x) - \partial_\mu\Omega(x)\partial_\nu\Omega^\dagger(x)\right)\right] \\ F^{\gamma}_{\mu\nu}(x) &= \tan\theta_W F^{\mathrm{Z}}_{\mu\nu}(x) \equiv \frac{\sin\theta_W}{2g_W}\,\mathrm{Tr}\left[\, i\hat{n}\left(\partial_\nu\Omega(x)\partial_\mu\Omega^\dagger(x) - \partial_\mu\Omega(x)\partial_\nu\Omega^\dagger(x)\right)\right], \end{aligned}$$

where $\hat{n}$ is defined in equation (6.52). These equations are expressed in terms of the SU(2) matrix:

$$\Omega(x) = \frac{\Phi(x)}{|\phi(x)|}\,. \qquad (8.5)$$

It becomes clear that electromagnetic fields are non-zero and sourced by the presence of inhomogeneities in the Higgs field orientation. This is, as pointed out above, one of the essential ingredients in Vachaspati's proposal for magnetogenesis. In our case, a particular realization of this mechanism

is achieved. We showed that even at our initial time gradients are present in the spatial configuration of the Higgs field, but as is evident from the formulas, the gradients must be combined in a particular way to produce a non vanishing electromagnetic strength tensor. We will show in the following, how this is our case and magnetic field is indeed profusely generated in our system.

Thus, having a mechanism for the magnetic field generation, it is reasonable to question ourselves about the nature of the produced magnetic fields. Since all the phenomena arising at this initial stage are determined by the nature of the Higgs field initial condition, the size and spatial distribution of the initial electromagnetic and Z fields can be obtained from the multicomponent Gaussian random field. In appendix D, details on the influence of the choice of parameters for the Gaussian random field are presented. Here we will focus on another aspect of the magnetic fields, which is particularly interesting for the later evolution. That is the spatial distribution of points where the magnetic field intensity is larger. It is reasonable to say that these high norm points are the places where the magnetic field is generated.

To investigate this issue, we show in Fig. 8.4 a 3-dimensional plot displaying the locus of points where the magnetic energy density is above $0.03m^4$ for our initial configuration at $mt = mt_i = 5$. Notice that the regions of higher magnetic energy density exhibit a string-like geometry. Indeed, this spatial distribution tracks exactly the location of regions of low Higgs field value, which are also presented in the figure.

The interpretation of this phenomenon is that the magnetic field is created at the boundaries of the Higgs bubbles, where the Higgs field is minimum. Looking at the figure the strings seem to end at certain spatial points, but this is simply a reflection of the spreading of magnetic flux lines. Changing the plot range one can follow the closed string paths. It is important to note that our electromagnetic field satisfies the Maxwell equations without magnetic sources or sinks (see appendix B). These string-like configurations contain a consistent magnetic flux. The magnetic vectors along such a string are all ordered pointing along the direction given by the string. Another important characteristic of the strings, is that the strength of the field is approximately constant along them, and quite similar between different strings. I would like to remark that, according to our formulas, the strength tensor of the Z-boson is directly proportional to the one corresponding to the photon field, and consequently has identical structure. As will be pointed below this relation has a physical interpretation and is maintained some time after this initial condition, until the S.S.B.

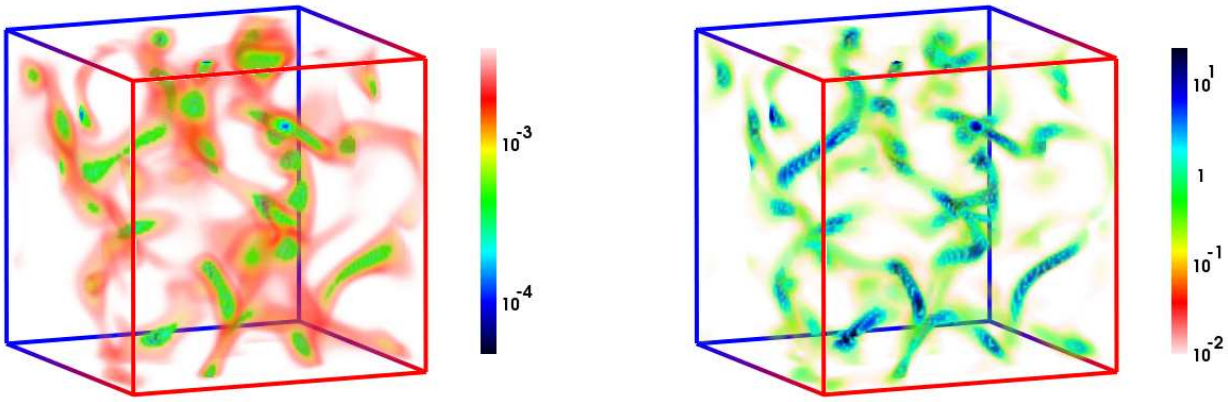

Figure 8.4: (Left) Locus of points where the value of the Higgs field norm is below $0.03m$. (Right) Locus of points where the magnetic energy density is above $0.03m^4$ (Right). Data correspond to $mt = 5$ and $m_{\rm H} = 2m_{\rm W}$.

There is another important feature of the magnetic field at this initial stage which is worth mentioning, since it represents a quite new and striking result. It corresponds to the fact that the initial configuration gives rise to a sizable magnetic helicity. As was pointed in chapter 7, several previous studies have shown that the presence of a non-vanishing helicity in the magnetic structures is not only desirable but necessary. This makes these structures more stable under thermal fluctuations and conserved under certain restrictions in magnetohydrodynamic processes. It also opens the window for an inverse cascade mechanism, nonexistent in the case of vanishing integrated helicity. To study the presence in the system of helicity, a finite volume definition has been used, given by:

$$H \equiv \int d^3x\ h(x) = \int d^3x \vec{A}\cdot\vec{B} \equiv \frac{-i}{\mathcal{V}}\sum_k \frac{\vec{k}}{|\vec{k}|^2}\cdot(\vec{B}(\vec{k})\times\vec{B}^*(\vec{k})) \qquad (8.6)$$

The gauge invariance of this quantity is ensured by our periodic boundary conditions. Notice that this equality makes use of Maxwell's condition $\vec{\nabla}\vec{B} = 0$, which is ensured everywhere by our magnetic field definition (see eq. (8.4), see also appendix B). The last expression of equation (8.6) depends only on the magnetic field, which is convenient for our formalism. Similarly a definition for the magnetic helicity of the Z field can be performed by chang-

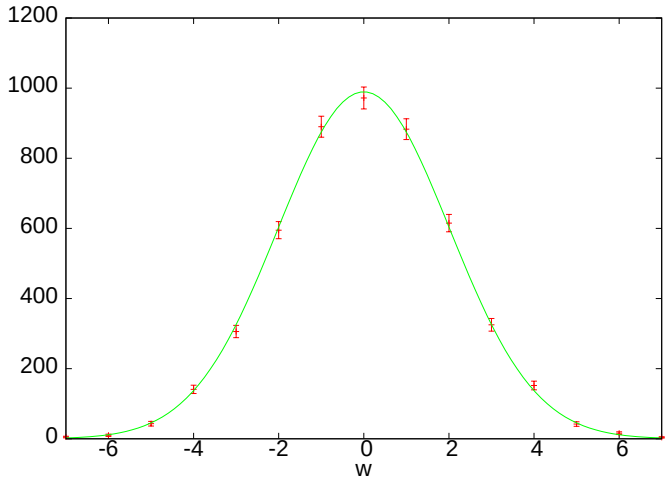

Figure 8.5: Histogram of Higgs winding for the initial configuration $mt = 5$ for $p_{\min} = 0.15$.

ing in equation (8.6) $\vec{B}$ by $\vec{\nabla} \times \vec{Z}$ and $\vec{A}$ by $\vec{Z}$.

An important property derived from the expression for the helicity is that, at our initial time, by virtue of equations (8.4), the helicity integral is proportional to the initial winding of the Higgs field. It can be clearly read, for instance, from the Z-field helicity:

$$H_Z = \int d^3x \vec{Z}(\nabla \times \vec{Z}) \propto \tag{8.7}$$
$$\int dx^3 \epsilon_{ijk} \mathrm{Tr}\{(\Omega(x)\partial_i\Omega^\dagger(x))(\Omega(x)\partial_j\Omega^\dagger(x))(\Omega(x)\partial_k\Omega^\dagger(x))\}$$

The winding is defined as the index of the map from the spatial volume to the group SU(2)=S_3, provided by the matrix $\Omega(x)$.

The influence of the Higgs winding on the system goes a bit further. At this initial stage, the helicity of the Z field is proportional to the helicity of the photon field. This proportionality is read from equation (8.4):

$$A_\mu(x) = \tan\theta_W \frac{1}{2g_z} \mathrm{Tr}\left[i\hat{n}\,\Omega(x)\partial_\mu\Omega^\dagger(x) \right] = \tan\theta_W Z_\mu(x) \tag{8.8}$$

So both helicities are related by:

$$H = \tan^2\theta_W H_Z \tag{8.9}$$

Again at this initial stage, the random Gaussian condition for the Higgs field may provide a non-vanishing total helicity. Since there are no CP violating

terms in the Lagrangian, the mean value of the winding number averaged over configurations is zero, as expected. To show this, a histogram of the winding obtained for our initial Gaussian random field configurations is displayed in figure 8.5. The data are well described by a Gaussian distribution with zero mean. However, we observe a non-zero dispersion from which one can obtain a non-zero volume-independent topological susceptibility $\chi = 0.52 \times 10^{-4} m^3$. This translates into a corresponding non-vanishing helical magnetic susceptibility $\chi_H \equiv \langle H^2 \rangle / \mathcal{V} = 0.38(3) m^3$. Thus, initially $\chi_Z \equiv \tan^{-4} \theta_W \, \chi_H$. Later on, we will come back to the issue of the proportionality between susceptibilities.

As indicated by the non-zero dispersion in the helicity, it is possible to find in one isolated realization of the scenario, a non vanishing total helicity. An interesting question arises: how is this helicity distributed or created in space?. To answer it, it is necessary to point out two things. The first one is that, although the integrated helicity is a gauge invariant quantity, this is not true, in general, for the helicity density:

$$h(x) = \vec{A}(x)\vec{B}(x) \rightarrow h(x) + \vec{B}(x)\vec{\nabla}\varphi(x)$$

where the arrow stands for the action of a $U(1)_{em}$ gauge transformation $\vec{A}' = \vec{A} + \vec{\nabla}\varphi$, and φ is a scalar function. However the helicity density associated to the Z field is a $U(1)_{em}$ gauge invariant quantity, since the Z field has no electric charge. So this quantity is representative of the spatial structure of this first stage generated helicity. Figure 8.6 represents a 3-dimensional plot of this quantity for a single configuration. As can be seen again, and not surprisingly, the points where the helicity is distributed are grouped into strings that follow exactly the strings of the magnetic fields, or what is the same, the minima of the Higgs. Another important feature is that, from the figure, one can see that the sign of the helicity is changing along the strings, but the turnover length is not negligible compared with the length of the string. We will come back to this issue in the following sections.

The rich phenomenology present in this initial stage does not end with what we have described. As one can easily realize from equation (8.4) the gradients of the Higgs are also involved in the definition of the electric field:

$$E_i(x) \equiv \frac{\sin\theta_W}{2g_W} \mathrm{Tr}\left[i\hat{n}\left(\partial_0\Omega(x)\partial_i\Omega^\dagger(x) - \partial_i\Omega(x)\partial_0\Omega^\dagger(x)\right)\right],$$

Hence, like in the magnetic field case, this generation mechanism could

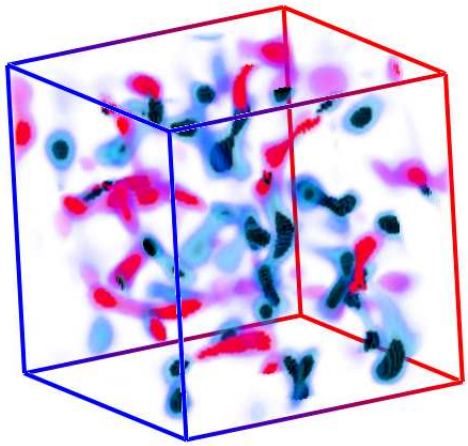

Figure 8.6: Initial Z helicity density. Red: Locus of points with high positive helicity density. Blue: Locus of points with highly negative helicity density.

also provide a non vanishing electric field. The points with the higher electric energy are again located along strings, that are located at the same points as the magnetic ones, and subsequently at the same places of the Higgs minima. The electric energy is also produced at the frontiers of the bubbles of the true vacuum. This initial electric field can be decomposed into two different components, a transverse component and a longitudinal one (see appendix B). These two components behave differently, and their separation provides an important analysis tool. The longitudinal electric component is provided by the charge present at this initial stage in the system. At the initial time, the electric field components have showed to be non vanishing, pointing to the presence of a charge distribution in the system. It is then desirable to extract how this charges are distributed in the space and the kind of structures they form. Of course they are determined by the structure of the electric field and viceversa. In order to calculate the charge density we used the Maxwell equations (actually we use the lattice version, see appendix B):

$$\vec{\nabla}\vec{E}(x) = \rho(x)$$

This charge density comes from the W^+ and W^- fields, that are the only charged species present in our system. As usual, their charge comes from the charged components of the Higgs field that are eaten by the gauge fields. Not surprisingly, we have found that this charge is concentrated along the strings. More suprising is the fact that this initial charge density is not

homogeneously distributed along the strings, but there is a strong charge separation or clustering. The positive and negative charge distribution are placed at the opposite sides of the magnetic-electric field strings. This image is physically compatible with the one observed in other contexts when working with high magnetized plasmas, like stellar plasmas and Tokamaks, where strong non uniform magnetic fields are present.The picture will be more clear as the system will evolve through the SSB or non-linear region, where the charge separation will be enhanced by the dynamics.

Another aspect of these initial stages of the evolution, is the role of the Inflaton field. We have pointed out before, that the role of the Inflaton along the inflationary process, is to drive the change in the potential of the Higgs, setting its tachyonic preheating. The Inflaton field is initialized just to its zero mode at the starting of the simulations, however it acquires very soon, a structure correlated with the Higgs field one. The figure 8.7 shows the strong correlation between the maxima of the Higgs norms and the minima of the Inflaton field norm, not at the initial configuration but at just a couple of evolution steps after. This strong correlation was extensively discussed in [111] in the context of a system without gauge fields, and is still preserved here. We have also studied the influence of the structure of the Inflaton field in the system at later times. The effect of the Inflaton inhomogeneities in the afterwards evolution, will be presented in chapter 9.

With all this, we hope to have shown that, this initial stage of the evolution gives rise to an interesting scenario that provides both a magnetic field with a non-trivial spatial structure and a non vanishing helical susceptibility, something that is not generically achieved by other magnetic field generation mechanisms.

Open questions still remain at this point, as the evolution of the phenomena observed in this first stage and their influence in the subsequent behavior of the system, the possible late time remnants, the magnetic seed etc... Some of these questions, need to be addressed while discussing the second region in figure 8.2. But before that, in the next section we will study the evolution of this helical magnetic field during the highly non-linear epoch of symmetry breaking, as well as, the behavior and persistence of the rest of the phenomena found in the very initial stage. This will hint a connection between magnetic field helicity, Z-strings and the occurrence of configurations carrying non-trivial Chern-Simons number.

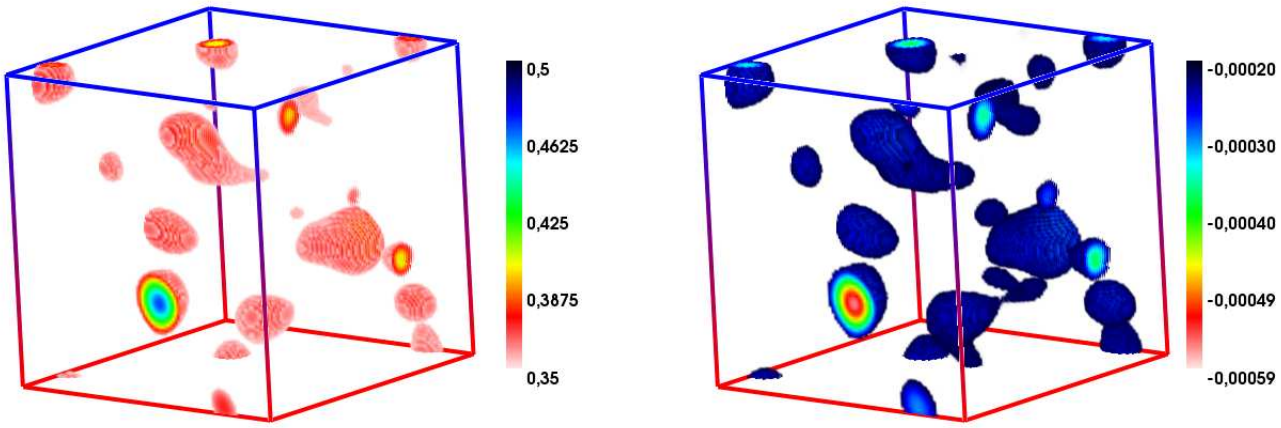

Figure 8.7: Left, locus of Higgs norm maxima. Right, locus of Inflaton norm minima. At two steps of evolution after initial time ($mt = 5.05$).

8.2 The symmetry breaking period: Non-linear effects.

As can be seen from figure (8.1) around $mt \sim 10$ the evolution for the mean value of the Higgs and the Inflaton fields, suffers a quite drastic change. The relatively slow increasing, or decreasing in the case of the Inflaton, trends are substituted by a violent oscillating behavior, until after some time they stabilize again around their respective true vacuum values. However this stability is relative, because both fields keep oscillating for a long time. These oscillations are more important in the Inflaton field that seems to resonate at certain late times in the evolution. We will come back to this issue and analyze the possible effect of such oscillations in the next chapter. For now, we will concentrate in this first strongly oscillating period, where the symmetry breaking is in fact realized. To remark the fact that, this strongly non-perturbative process affects the system at all levels, Fig. 8.8 shows the evolution of the spatial histogram of Higgs norm values. As can be seen from it, not only the Higgs expectation value is changing as a whole, but the spatial structure of the Higgs field itself, is highly modified by the SSB process, as expected, and as will be shown more pictorially bellow.

The symmetry breaking period was studied in detail [109], [111] and [112].

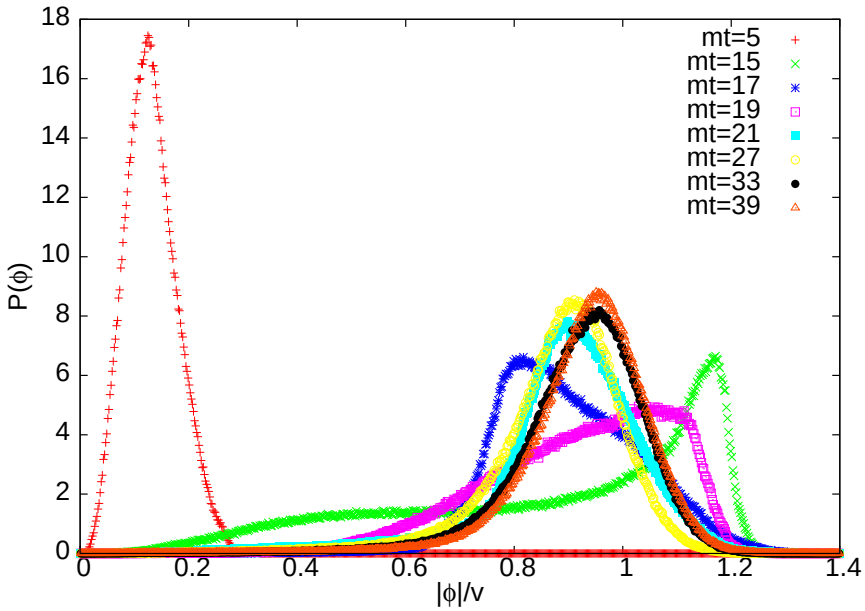

Figure 8.8: Evolution through the spontaneous symmetry breaking region of the histogram for the Higgs expectation value

It was pointed out that the symmetry breaking is achieved by the nucleation and merging of the bubbles present at the initial condition, which at this epoch, have grown in size and start to oscillate and collide which each other. As a consequence of the merging of bubbles, the spherical symmetry of the initial bubbles that was nicely shown in figure 8.4 is now broken. The new picture of the spatial distribution for the Higgs norm maxima is shown in figure 8.12 top left. The pink coloured zones represent the places where the Higgs norm is greater. This picture is taken at $mt = 15$ just inside the symmetry breaking region, and a time where the Higgs vacuum expectation value is closer to a minimum and the electromagnetic energy is closer to a maximum value. On it, one can easily appreciate the nucleation and merging of the bubbles, that at the time of the figure, seem to fill the box almost completely. There is another property that is worth to mention. As was said before (see chapter 4 and chapter 6), in the development of this thesis several models have been used. These models are described by the relationship between the Higgs and W mass, or what is the same, the value of the parameter λ. But in the full quantum evolution there is no λ dependence since the self-interaction of the Higgs field is neglected (see chapter 6). As a consequence, at initial time $mt = 5$ all the models are the same, and all the measured quantities, when expressed in m units (this is important since the quantum evolution

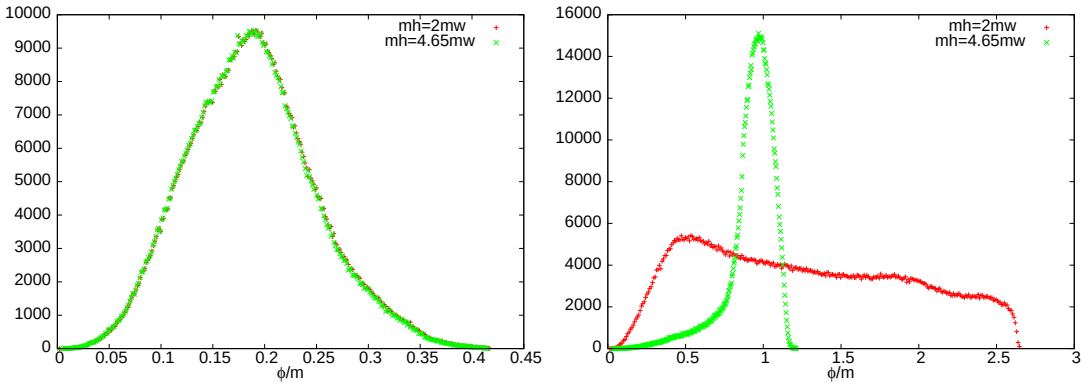

Figure 8.9: Higgs norm histogram for models $m_{\rm H} = 2m_{\rm W}$ and $m_{\rm H} = 4.65m_{\rm W}$, for $mt = 5$ (left) and $mt = 15$ (right).

depends on λ through m), have the same initial value. This is exact at initial time, and approximately preserved during the first times of the evolution while non-linearities are still negligible. It is in the symmetry breaking period where this approximate λ independence is removed and each model has a different evolution. As an example, figure 8.9 shows the Higgs norm (ϕ/v) histogram. From it can be seen that at SSB times the histogram of norms is completely different for the two most extreme models, $m_{\rm H} = 4.65m_{\rm W}$ and $m_{\rm H} = 2m_{\rm W}$. However they are the same at the initial time when expressed in m units. This can be seen from equation (6.30), where it is evident that the initial value of the Higgs field is given in terms of:

$$\langle|\phi(\vec{x}, t_i)|^2\rangle = m^2 f(t_i) \tag{8.10}$$

where $f(t_i)$ is an adimensional function that only depends on the value of t_i. Further information about the differences between models can be found later on, in chapter 10. For the moment I just say that these differences are basically a shift on the onset time for the SSB. As was pointed out in chapter 6, the value of λ drives the SSB onset (see equation (6.26)). This is shown in figure 8.10. The SSB is shifting to the right as the value of λ is smaller. These differences give rise at the end, to a similar qualitative behavior for all models in the majority of the quantities of interest.

Now lets focus in how the complicated non-linear dynamics of the scalar fields during this epoch, affects the evolution of the rest of the system. For the magnetic fields, we will now study the time evolution from the initial Gaussian random field situation until the onset of symmetry breaking, through the non-linear period of time. To have a global picture of the process we

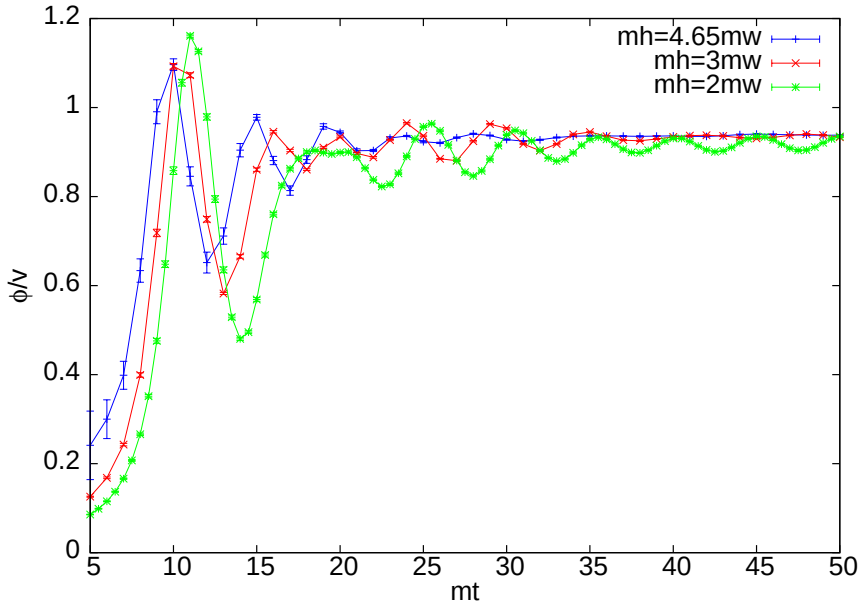

Figure 8.10: Evolution of the Higgs norm for all models. The symmetry breaking time ranges from $mt \sim 10$ to $mt \sim 12$. For $ma = 0.42$.

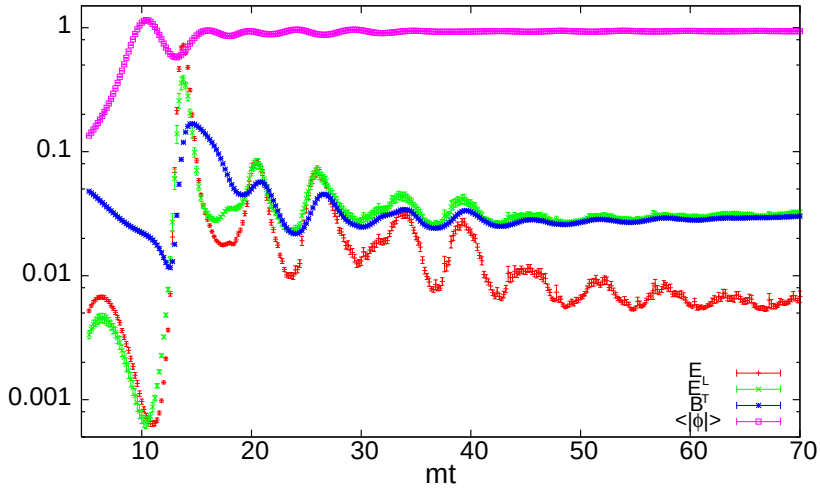

Figure 8.11: We show the time evolution of transverse and longitudinal electric and magnetic energy densities averaged over 150 configurations for $m_{\rm H} = 3m_{\rm W}$ and $ma = 0.42$. The vertical axis is in logarithmic scale.

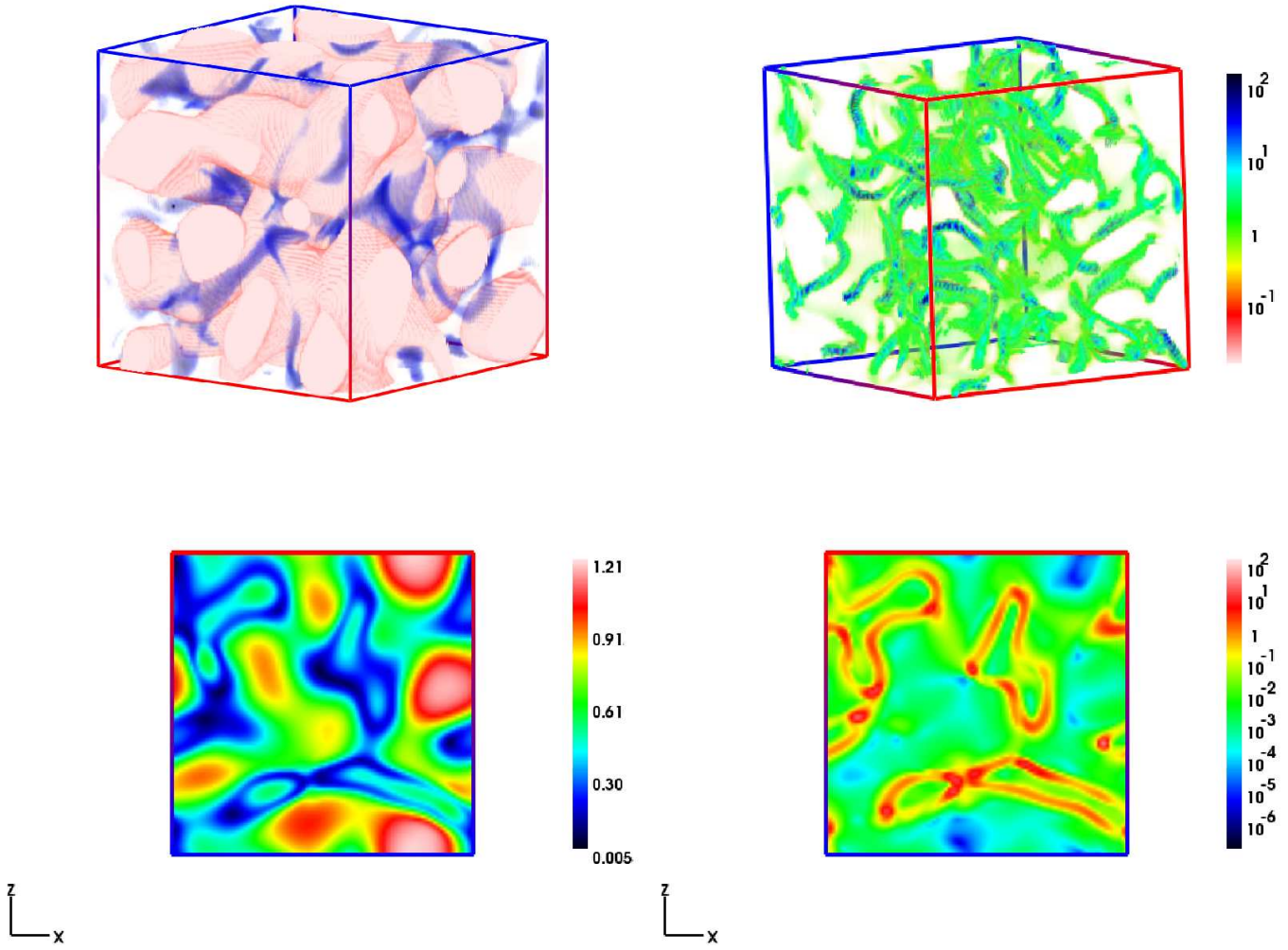

Figure 8.12: Top: (Left) The location of the bubbles in the Higgs field norm (in red) with a lower cutoff set at $0.7\,v$ and the locus of points with twice the magnetic energy density ($|\vec{B}(\vec{x})|^2$) (in blue) higher than $0.01\,m^4$. (Right) Locus of points where the magnetic energy density is above $0.03\,m^4$. Bottom: (Left) Two-dimensional contour plots of the Higgs field norm. (Right) Two-dimensional contour plots of the magnetic energy density. Data correspond to $mt = 15$ and $m_{\rm H} = 2m_{\rm W}$.

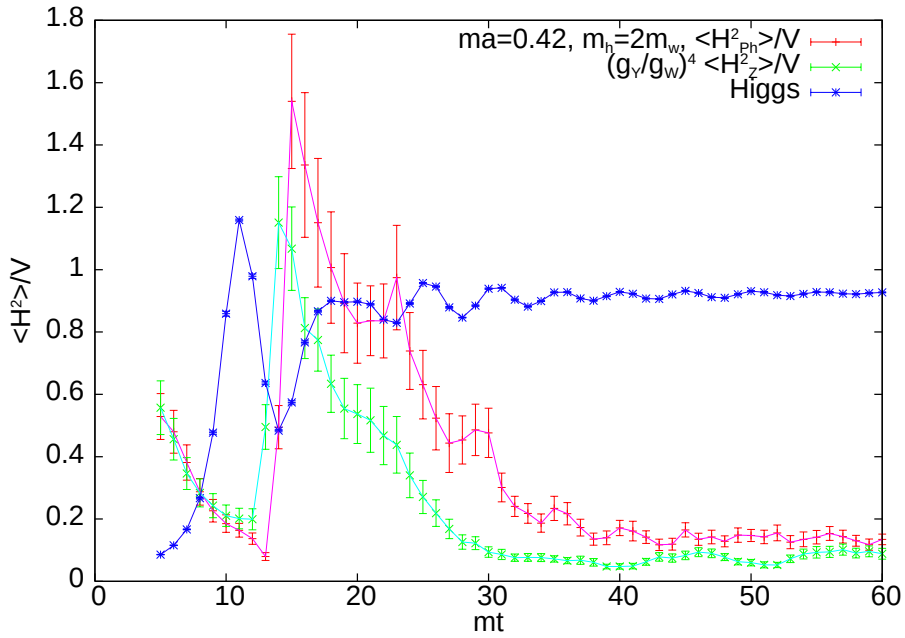

Figure 8.13: Magnetic and Z-boson susceptibility evolution during the SSB epoch. The latter is rescaled by $\tan^4\theta_W$ to match the magnetic one at mt_i.

show in Fig. 8.11 the time evolution of the expectation value of the Higgs field from the initial time $mt_i = 5$ of our classical evolution. Notice, again, the strong initial oscillations for times smaller than $mt = 20$, which are then progressively damped at larger times. The figure also displays the fraction of the total energy density carried by electromagnetic fields. We split it into its magnetic and electric components, and for the latter we analyze separately longitudinal and transverse parts. The technicalities involved in the lattice definition of transverse and longitudinal fields as in the definition of the W bosons charge densities and currents are discussed in Appendix B.
We observe that between $mt = 10$ and $mt = 15$, there is an explosive growth of the electromagnetic fields correlated with the first minimum in the oscillation of the Higgs field expectation value. This first minimum on the Higgs norms was previously studied in [111],[112]. It was found that a second burst of deep Higgs minima, appears in the system at that stage, still located at the boundaries of the Higgs field bubbles. These minima present stronger gradients, due to the growth in size of the bubbles, which squeezes the regions between them. According with the generation mechanism previously discussed, stronger gradients provide stronger magnetic fields. Thus this explains the electromagnetic energy injection in the system. The data in the

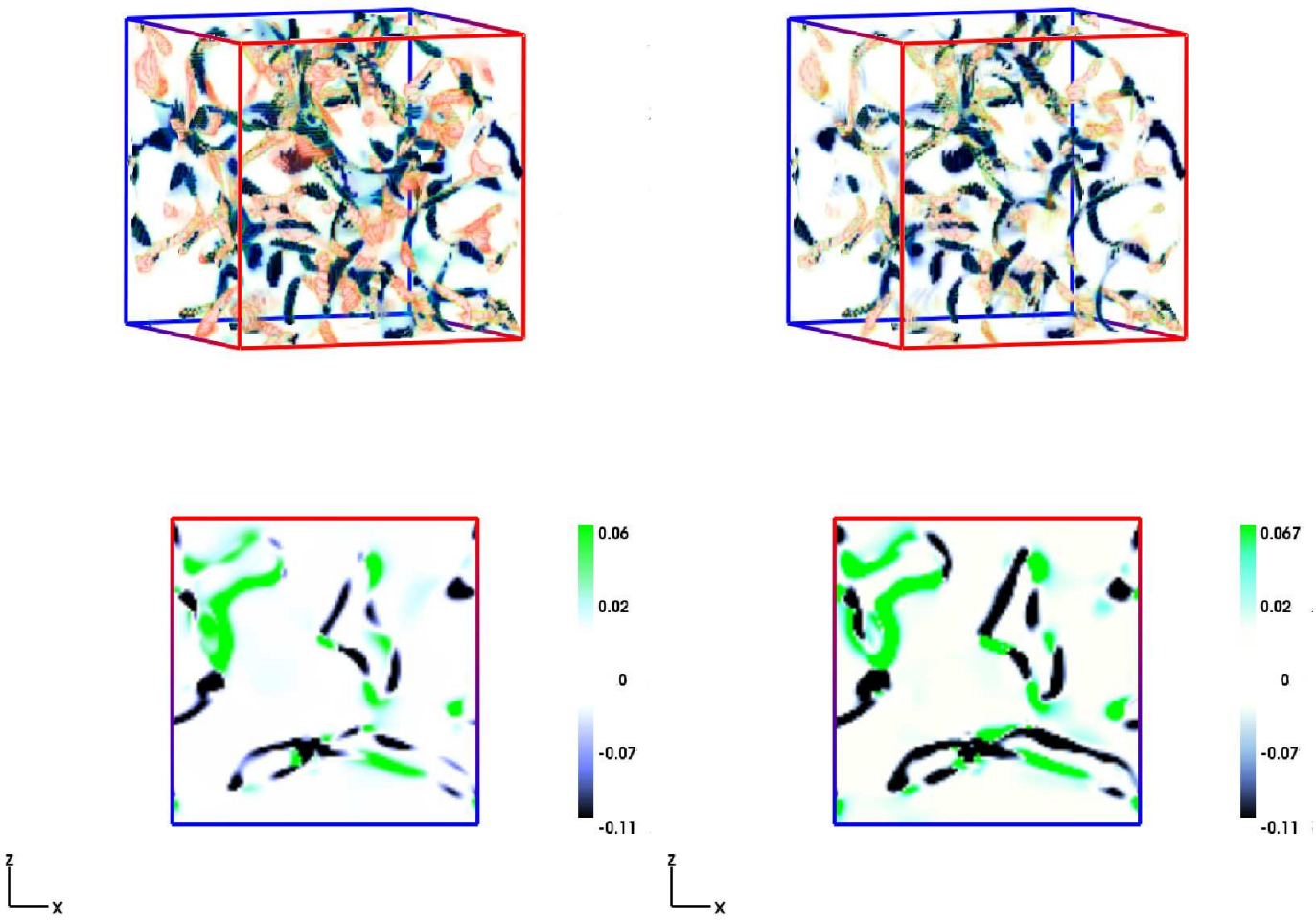

Figure 8.14: Top: (Left) Helicity of the magnetic field. (Right) Helicity of the Z-boson field. Bottom: (Left) Two dimensional contour plots of the helicity of the magnetic field. (Right) Two dimensional contour plots of the helicity of the Z-boson field. Data correspond to $mt = 15$, for $m_{\rm H} = 2m_{\rm W}$.

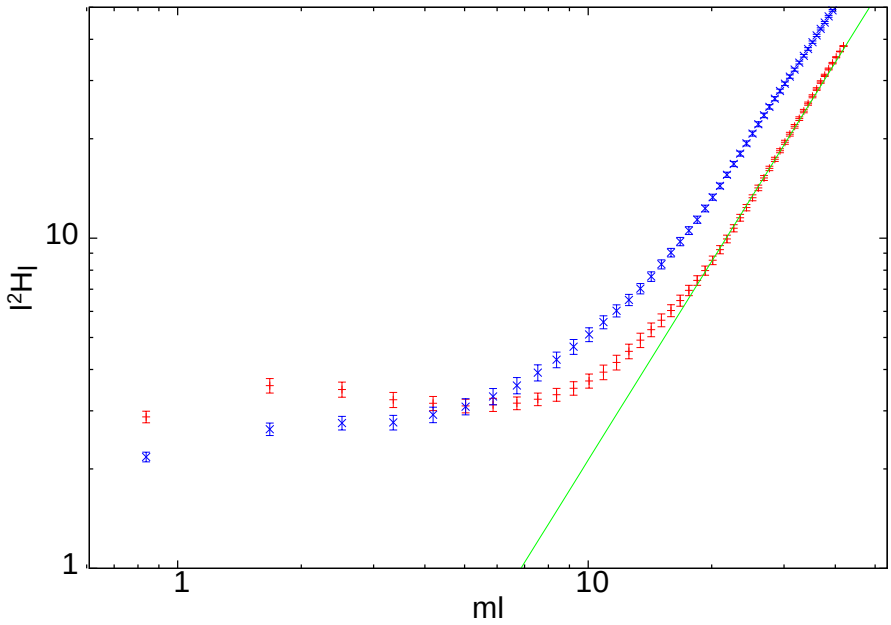

Figure 8.15: Averaged $l^2 H_l(r_0)$, Eq. (8.11), at $mt = 15$. We also show the l^2 asymptotic behaviour for the $m_{\rm H}/m_{\rm W} = 4.65$ model. The other data corresponds to $m_{\rm H}/m_{\rm W} = 2$.

figure corresponds to $m_{\rm H} = 3m_{\rm W}$, but similar behaviour is observed for the other ratios studied.

We will now present the spatial structure observed for the magnetic fields at $mt = 15$ inside the strong oscillation region. This is illustrated in the top left of Fig. 8.12, where we display a snapshot of the Higgs field norm at $mt = 15$. On it, the string-like structure is even more evident than in Fig. 8.4. At this time the bubble shells (in red), squeeze the magnetic fields (shown in blue in the figure). These regions are made by the intersection of two dimensional structures, the boundaries of the bubbles, which make one dimensional strings of Higgs minima. This linkage between magnetic strings and Higgs field minima is even more evident in the two dimensional contour plots presented in the bottom half of Fig. 8.12.

Figure 8.13, shows the evolution of the magnetic susceptibility defined by equation (8.6) from the initial time through the SSB region. On it we also display the Higgs expectation value, in order to track better the non-linear region, and the Z-boson susceptibility. As was pointed out before, the latter quantity is initially proportional to the magnetic susceptibility by a factor

$\tan^4\theta_W$, and it is rescaled by it in the figure. From this figure one can see that both Z and magnetic helicities remain similar during the times before the SSB, reinforcing the idea that the evolution is quite slow at the beginning and the non-linearities have no role at this stage. But around $mt \sim 15$ the two quantities separate presenting different values.We will see in chapter 9 the behavior of these two quantities for greater times. Now, let us try to answer the question of why they do separate. The non-linearities in the evolution of the Higgs produces an injection in the $SU(2)$ and Hypercharge energy. When these energies are no longer negligible, it is the mixture between the $SU(2)$ and Hypercharge fields in the photon and Z field definition, what produces the different behavior for the two quantities.

As at the initial configuration, the structures observed in the regions of maximal magnetic density are reproduced when looking at the helical part alone. This is exemplified by the comparison of Fig. 8.14 with Fig. 8.12. The figure also shows how the correlation between magnetic and Z boson fields, implicit in our initial conditions, is still preserved once gauge fields and non-linearities have started to play a role. An interesting observation can be made here concerning the connection with baryon number generation. Analysis of the cold EW transition show that sphaleron-like configurations, with non-trivial Chern-Simons number, are also located between bubble shells [112]-[115]. For non-zero Weinberg angle, sphalerons look like magnetic dipoles [125] and it is tempting to correlate the observed helical magnetic flux tubes with the alignment of sphaleron dipoles. Although we have not performed a detailed investigation of this correlation, and it is regarded as a future work, our results for the distribution of magnetic helicity do hint in that direction. An evaluation of the net helicity at late times and a discussion on its persistence will be postponed to the next chapter 9.

In the previous figures, the closed string-like structure of the helicity and magnetic field appears much more clearly that in the Gaussian random field initial condition at $mt_i = 5$. To quantify the string-like character, we have analyzed the following quantity:

$$H_l(r_0) = \frac{1}{l^3}\int_{L(r_0)} dx^3 |\vec{h}(x)|\,, \tag{8.11}$$

where $\vec{h}(x)$ denotes the helicity density and the integration is on a box of length l, centered at a point r_0 at the center of one of the strings. Figure 8.15 shows the l-dependence of $l^2 H_l(r_0)$, averaged over several configurations. The figure is intended to show the one-dimensional character of the distribution in accordance to our string picture. In that case, $l^2\, H_l(r_0)$ should be l-

independent in contrast with the l^2-behaviour characteristic of an isotropic distribution. Both regimes are clearly observed in the figure. The stringy behaviour is displayed up to $ml \sim 10$, beyond which the plot shows how the data tends nicely to a straight line of slope equal to 2. This is to be expected once the box is big enough to contain several strings. This leads to an estimate of the string separation of $m_{\rm H} l \sim 14$, which is a significant fraction of the total length of the box. The same behavior is found for the analogous quantity in the magnetic field case:

$$B_l(r_0) = \frac{1}{l^3} \int_{L(r_0)} dx^3 |\vec{B}(x)|^2 \,, \tag{8.12}$$

giving approximately the same length.

8.3 Charge and current.

Up to now, and regarding the SSB period, we have focused on the distribution of magnetic and Z-boson fields. But there is important additional information on the nature of the primordial plasma during these stages of preheating. Maybe the most striking feature of our system and the one that makes it quite peculiar, is the distribution of charge present on this primordial plasma. Remember that our initial conditions provide a source for charged W-currents and a non-trivial charge density. This initial charge is not neutralized by the evolution through the SSB, giving at the end of this period a locally non-neutral plasma. Fig. 8.18 shows the evolution of the charge histogram through the SSB, from time $mt = 5$ to $mt = 45$. It can be seen that the charge distribution at initial time, although very peaked at zero charge, presents a small dispersion. The evolution effect is to spread this distribution leading to a Gaussian shape. Notice that this spreading is symmetric so the total charge in the system is zero as it should. A closer look into the system shows that it is locally non neutral. Moreover there is a charge separation even at the initial time. This charge separation is realized by means of charge clusters. Positive and negative charges are clustered into separate lumps which track the magnetic field lines. During the SSB region, the size of these clusters is enlarging with time. Figures 8.16 and 8.17 show this effect at $mt = 15$ and $mt = 10$, respectively. Note that there is a strong correlation between the magnetic field lines and the distribution of charges of opposite sign around them. The effect is particularly clear at early times, $mt = 10$, where the magnetic flux tubes are also well defined, and there are

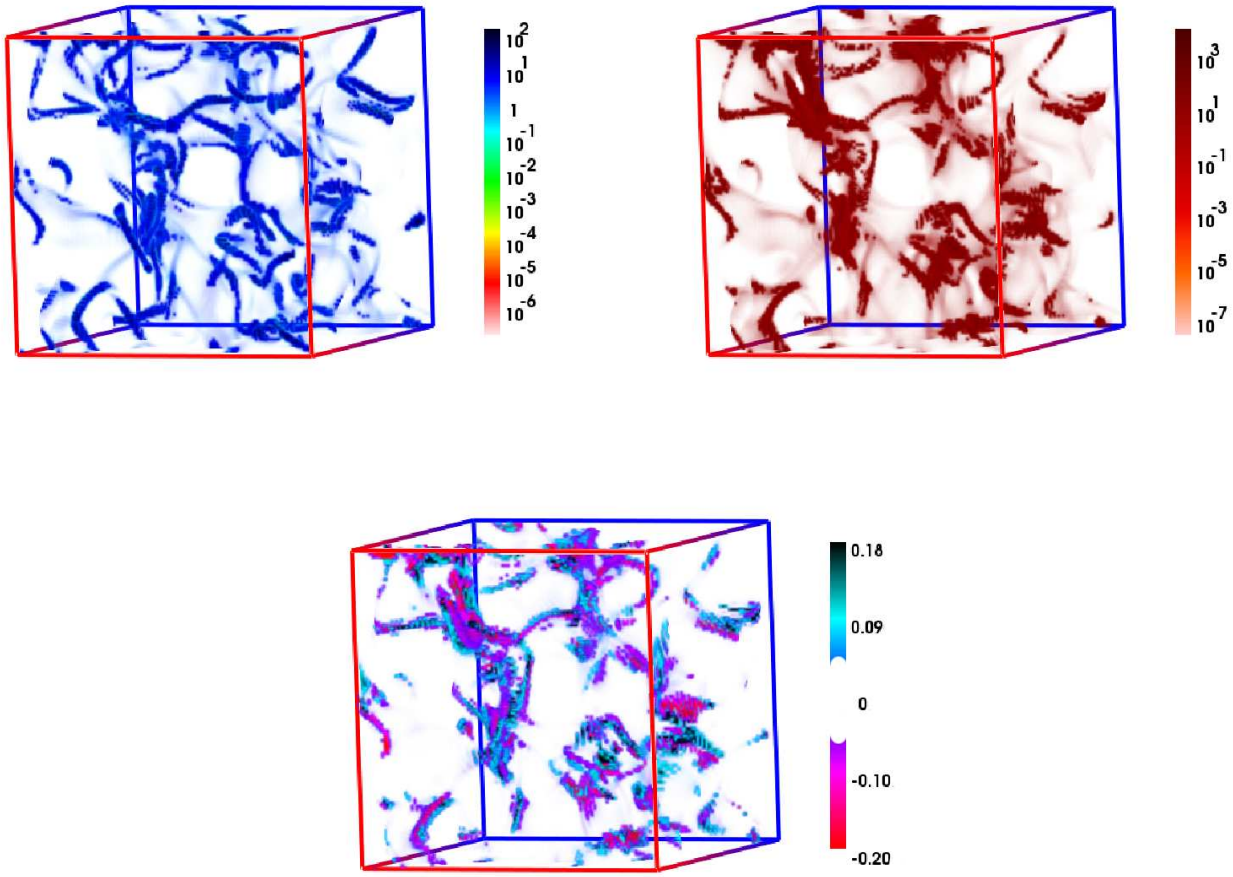

Figure 8.16: Top Left: Locus of points with magnetic energy density $|\vec{B}(x)|^2$, above $0.01\,m^4$. Top Right: Locus of points with electric energy density $|\vec{E}(x)|^2$ above $0.01\,m^4$. Bottom: The distribution of $W^{\pm}$ charge density, tracking the magnetic field lines. Pink and blue areas represent negative and positive charge densities respectively. Data correspond to $mt = 15$, for $m_{\rm H} = 2m_{\rm W}$.

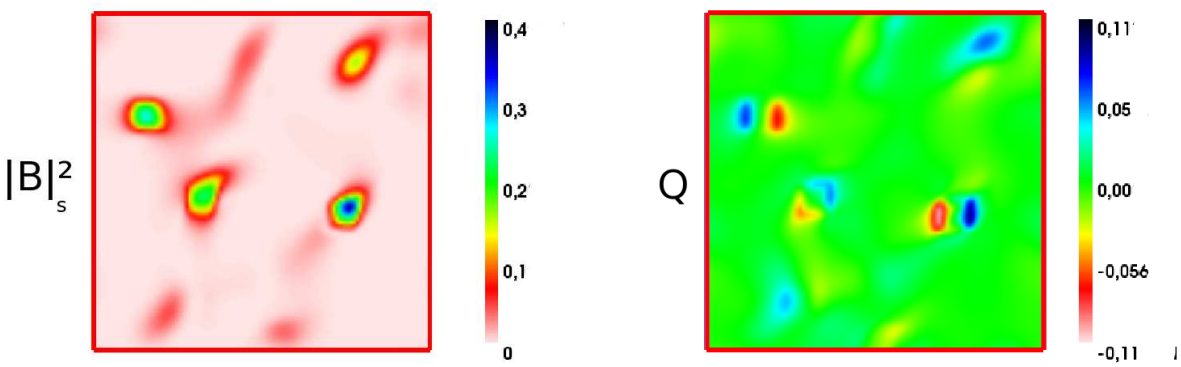

Figure 8.17: Left: Locus of points with magnetic field density $|\vec{B}(\vec{x})|^2$ above $0.01\, m^4$. Right: The 2-dimensional W-charge distribution localized in lumps of opposite sign facing each other. Note that the location of the charge lumps is strongly correlated with the magnetic field flux tubes. These figures correspond to early times, $mt = 10$, for $m_{\rm H} = 3m_{\rm W}$.

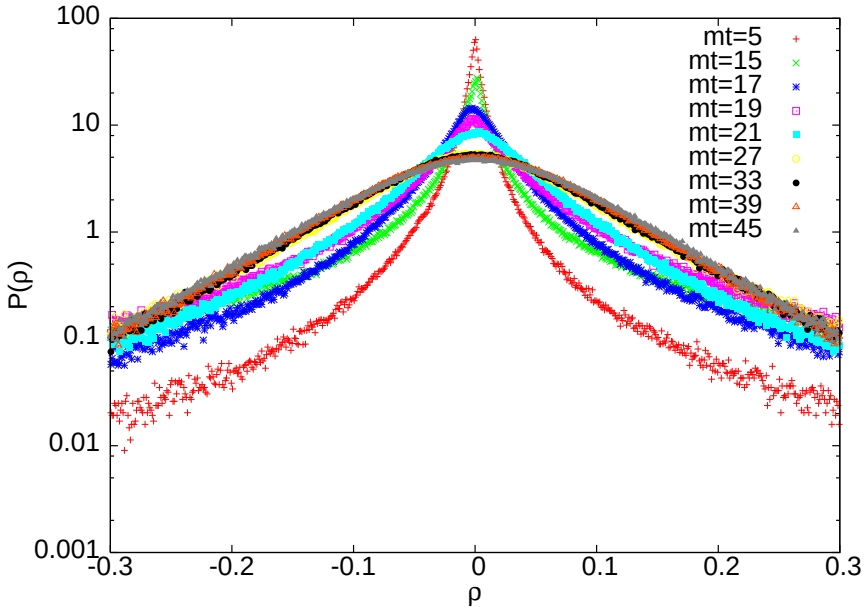

Figure 8.18: Evolution of the charge histogram across the SSB. The time period goes from $mt = 5$ to $mt = 45$. For $ma = 0.42$, $m_{\rm H} = 2m_{\rm W}$.

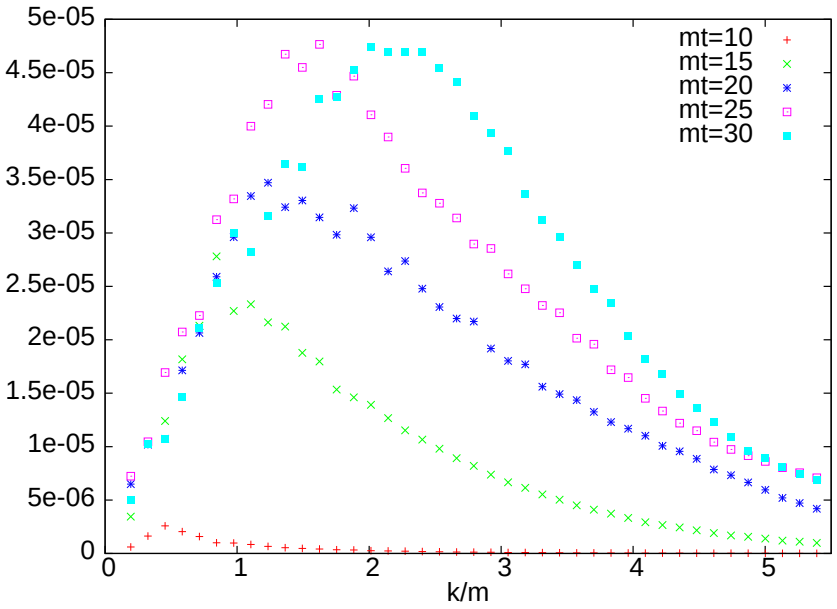

Figure 8.19: Charge spectrum evolution through the SSB. From the initial time to $mt = 30$. For $ma = 0.42$ and $m_{\rm H} = 2m_{\rm W}$.

fewer of them. Figure 8.17 is chosen to present the transverse sections of several flux tubes. Notice the charge clusters are separated in the transverse direction to the flux, so the charge clusters are located at the opposite sides of the flux tube. This charge separation is consistent with the effect that would be produced by a combination of the drift currents, induced by gradients in the magnetic field, and curvature effects from the magnetic flux tubes.
A significant quantity that is worth to mention is $|\rho(k)|^2$. This quantity is related with the dispersion in the charge distribution:

$$\sigma_\rho^2 = \langle\rho^2\rangle - \langle\rho\rangle^2 = \int d^3x\rho^2(x) = \frac{1}{L^3}\sum_k |\rho(k)|^2 \tag{8.13}$$

since $\langle\rho\rangle = 0$ and we are dealing with a finite volume and, consequently, discrete momentum. This spectrum $|\rho(k)|^2$ is represented in fig. 8.19. As can be seen it suffers a very fast growth during the SSB period. Moreover there is a displacement with time of the maximum of the spectrum to high momentum. We will see below that this displacements stops after the SSB, and a change of regime into a slow evolution appears.

Figure 8.23 shows the same plane than figure 8.17, but for two different latter times, $mt = 20$ and $mt = 25$. One can appreciate how the charge, instead of annihilating, tends to clusterize into bigger structures, taking ap-

part the positive from the negative charges. As will see, this clusterization of the charge remains for a very long time in the system.

The electric field is also strongly correlated with the location of the charge lumps, as expected. This charge separation might be responsible for the very slow screening observed for the longitudinal electric field, which will be discussed in the next chapter.

Another important aspect of the primordial plasma is the kind and structure of currents that are present on it. In order to study these currents we have used the definition coming from the Maxwell equations (see appendix B), using as fundamental input both the curl of the magnetic field and the time derivative of the electric one.

The physical picture that makes sense for the system we are dealing with, is the one presented in figure 8.20. In this naive idealization the currents make spires around the magnetic field tube. The magnetic field inside the tube is constant in norm along the path and changes only slightly in direction. In that case the currents are also constant and transverse to the direction of the tube. Of course, our magnetic field strings are much more complicated than the ones of the picture. First, the magnetic fields present strong curls and inhomogeneities, even in the places where the strings are separated enough to avoid the merging. Secondly, the presence of a non-negligible and even dominating drift current ($\dot{\vec{E}}$). The presence of this term is, and will be, a constant along the evolution, and is associated with the fluctuations of the clustered charges. As an indication, see the energy stored in this E_L component in fig. 8.11. However this schematic point of view holds approximately. As expected, we have found that the points with higher current norm are correlated with the magnetic strings. But it has been technically too difficult to resolve their deeper structure around the flux tubes.

In order to keep track at least of the orthogonality of these currents with respect to the flux tube, we have studied the histogram of the angles of the three quantities of interest with respect to the magnetic field in the tubes. To make these histograms, the points chosen to appear, have been limited to be those placed in the magnetic strings. The three quantities are $\vec{\nabla} \times \vec{B}$, $\dot{\vec{E}}$ and the current $\vec{j}$. In the case of the idealized picture 8.20, one would expect that both the $\vec{\nabla} \times \vec{B}$ and so $\vec{j}$ to be orthogonal to the magnetic field in the string. In that case the electric field time derivative is zero, since no electric field is present. However, in our case the picture is quite different. The results for $\dot{\vec{E}}$ and the current $\vec{j}$, are presented in fig. 8.21. We omitted the histogram

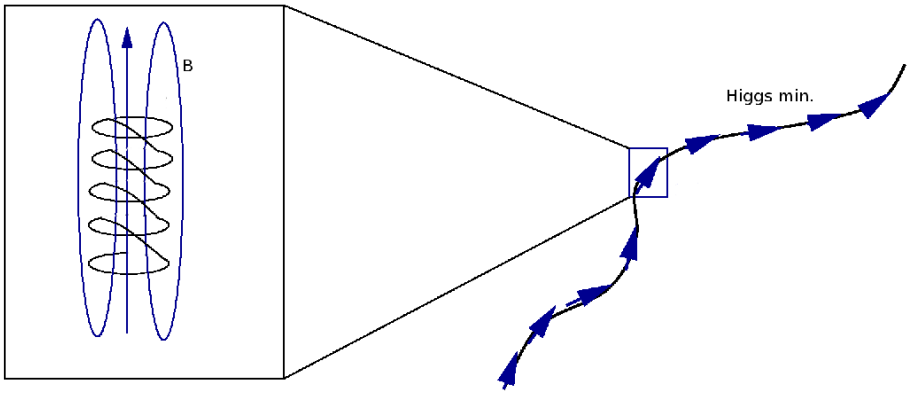

Figure 8.20: Schematic idealization of the currents associated with the magnetic flux tubes.

for $cos(\widehat{\vec{\nabla} \times \vec{B}},\ \vec{B})$, because it is very peaked at 0, and at the scales of the graph, looks like a delta function. From that, one can realize that although both $\vec{E}$ and $\vec{\nabla} \times \vec{B}$ are quite orthogonal to $\vec{B}$, the current presents a wider distribution. At the moment we have not studied deeply the implications of this result neither the behavior or evolution of the currents themselves. This is regarded as future work. However, there are other scenarios where this non orthogonality has interesting implications. As an example, the one discussed in chapter 7 about resistive MHD. In that context, the non orthogonality of the magnetic field and the currents allows the possibility for changes in the integrated helicity with time.

To end this chapter, I must say that the plasma of W bosons generated during the first stages of evolution is, as we have shown, somewhat different from standard non-relativistic MHD plasmas (composed usually by lighter particles, together with photons). Here, long range string-like structures are observed in the electromagnetic fields, and opposite W-charges cluster in large regions of space inducing non-trivial electric fields. As was exposed in chapter 7, this is in strong contradiction with some assumptions that are in the core of the non-relativistic highly conducting MHD approximation. These are:

First the neglect of the drift currents $\dot{E}$ compared with the $\vec{\nabla} \times B$ term, that here does not hold, at least for the initial times. As illustration, figure 8.22 presents the evolution of the quantities:

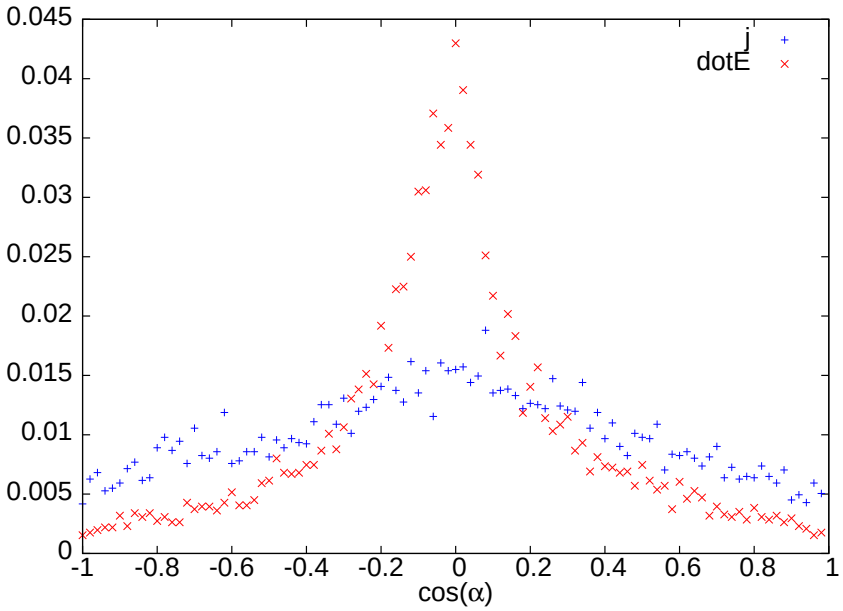

Figure 8.21: Histogram for $\cos\alpha$ in the magnetic strings for one configuration. For $\alpha = \widehat{\vec{j}\vec{B}}$ and $\alpha = \widehat{\dot{\vec{E}}\vec{B}}$. $mt = 15$ and $m_{\rm H}/m_{\rm W} = 2$.

$$\sigma_{L/T} = \sqrt{< |\dot{E}_{L/T}|^2 >} \qquad (8.14)$$
$$\sigma_B = \sqrt{< |\vec{\nabla} \times B|^2 >},$$

where L/T stands for longitudinal and transverse. On it, it can be seen that before times ~ 80, $\sigma_{L/T} > \sigma_B$. The situation changes for later times as we will see in the next chapter.

Secondly the neglection also of the electrostatic force in comparison with the Lorentz force, which implied neglecting the charge distribution in the equations. As is exposed above, the charge distribution is strongly clustered, and this phenomenon must be taken into account. However, as the subsequent evolution will show, the trend seems to be slowly removing the charge on the system, as the energy stored in the longitudinal part of the electric field (see next chapter). It is also expected that, any remnant of these charge lumps, will eventually disintegrate when the W-fields decay into light fermions (quarks and leptons), which travel at the speed of light and diffuse the charge more easily than the heavier W-bosons. This could lead at late times to a standard MHD plasma. A brief discussion about this point is presented in the next chapter.

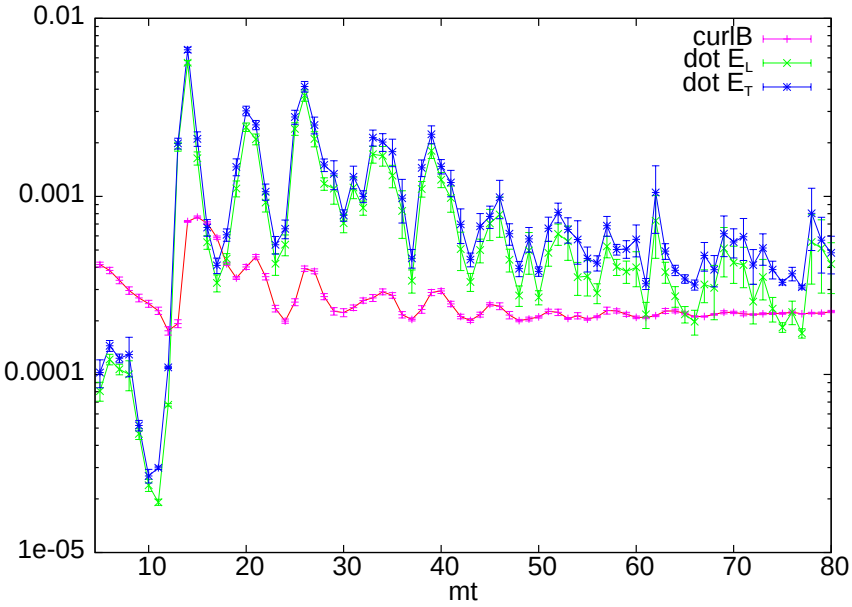

Figure 8.22: Evolution for σ, as defined in equation (8.14) averaged over 80 configurations. From the initial time ($mt = 5$) to $mt = 80$. Model $m_{\rm H}/m_{\rm W} = 3$.

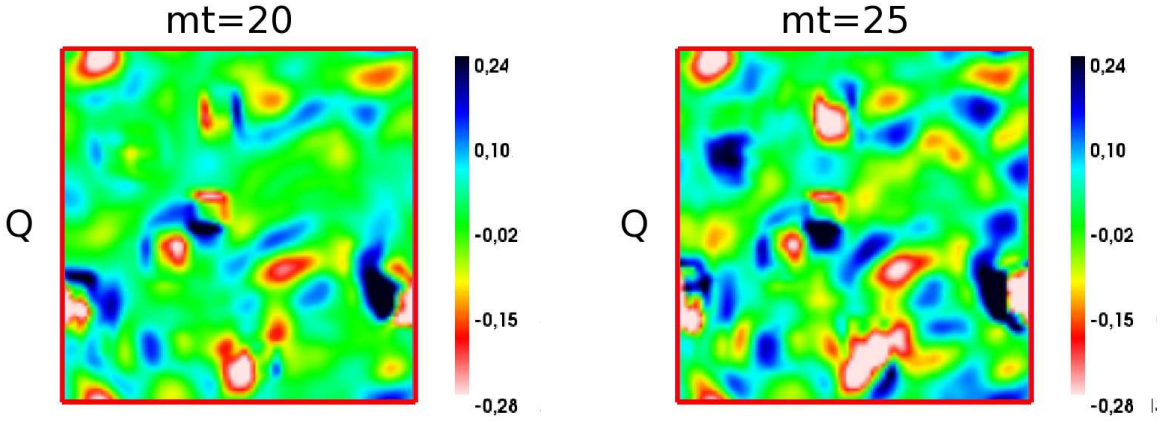

Figure 8.23: Clusterization of W charges, at the same plane of fig. 8.17. Left $mt = 20$, right $mt = 25$.

Chapter 9

Late time evolution.

9.1 Late time evolution.

In the previous chapter we have presented a discussion, that attempted to be complete, about the very interesting phenomena arising in the SSB region. This region has been showed to be a high instability period, where the electromagnetic fields are generated and receive an energy injection, where non-trivial structure is generated (for both electromagnetic and susceptibility quantities), and where the charge is generated and clustered in a very particular way. In summary, where all the quantities in the system leave their steady state and, in a really fast manner, are pushed by the dynamics of the Higgs and Inflaton, into a non-trivial excited state.

As was pointed out before, although some important questions are solved by studying the dynamics of this epoch, many questions are still open. All of them can be summarized at the end, in one: What does happen with all the created quantities in the subsequent evolution?.

In this chapter we discuss the late time evolution of the system, in what we call the "late time region" (see figure 8.2). This region lasts from times $mt \sim 70$ to the end of our simulations $mt \sim 300$. This second region, as opposed to the first one, is not a fast period of instability. On the contrary, it corresponds to a quite slow process (compared with the characteristic time in the SSB region) in which the system evolves towards the equilibrium. Although it is tempting to think that there is no interesting phenomenology coming out of this trend to the equilibrium, this is wrong. It is in this region where some important phenomena arise, that are crucial to achieve the objective of this thesis. In particular, in order to claim a mechanism

for cosmological magnetogenesis, we have to address the essential question of whether the amplitude and correlation length of the generated fields are enough to seed the large scale magnetic fields observed today. In this chapter we will present evidence that a significant fraction of long range helical magnetic fields remains after EW symmetry breaking and is even amplified at later times. As we will see below, our estimate for the amplitude of the magnetic field seed gives a fraction $\sim 10^{-2}$ of the total energy density at the EW scale. This could be enough to seed the cluster and supercluster values without the need for a dynamo mechanism. We will also show that during this process the system will develop a period in which kinetic turbulence has been observed [119, 126], and some other interesting phenomena are present.

More difficult is to address the issue of whether the magnetic field spectrum experiences inverse cascade, i.e. transference of energy from high to low momentum modes [45]-[62]. Inverse cascade is required to make the coherence length of the magnetic field grow (almost) as fast as the horizon until the time of photon decoupling. Our approach does not allow to extrapolate the time evolution for sufficiently long times. Nevertheless, we will provide some evidence that inverse cascade might be at work. However, additional work is required to analyze if it can be sustained for a sufficiently long time. This might require a full magnetohydrodynamics treatment of the time evolution for which our set up will provide an initial condition.

9.2 Magnetic helicity, charge and electromagnetic energy densities.

We will first analyze in detail how electromagnetic fields evolve in time, paying particular attention to the evolution of the magnetic field helicity long after SSB.

As mentioned in the previous chapter, the relevant quantity for helicity in the absence of CP violation is the helical susceptibility χ_H. Its time evolution, for different values of the $m_{\rm H}/m_{\rm W}$ ratio, is displayed in Fig. 9.1. At the same time we display the helical susceptibility of the Z boson magnetic field, rescaled by $\tan^4\theta_W$ to make it agree with the initial electromagnetic helicity (see discussion after equation (8.6)). The late time behaviour, after $mt \sim 60$, gives further support to the Vachaspati-Cornwall's conjecture. It corroborates that, while the Z-boson helicity is damped in time, the magnetic helicity is preserved and even increases with a power law dependence in time given by t^α with $\alpha = 0.7(1), 0.8(1), 0.3(1)$ for $m_{\rm H}/m_{\rm W} = 2, 3$ and

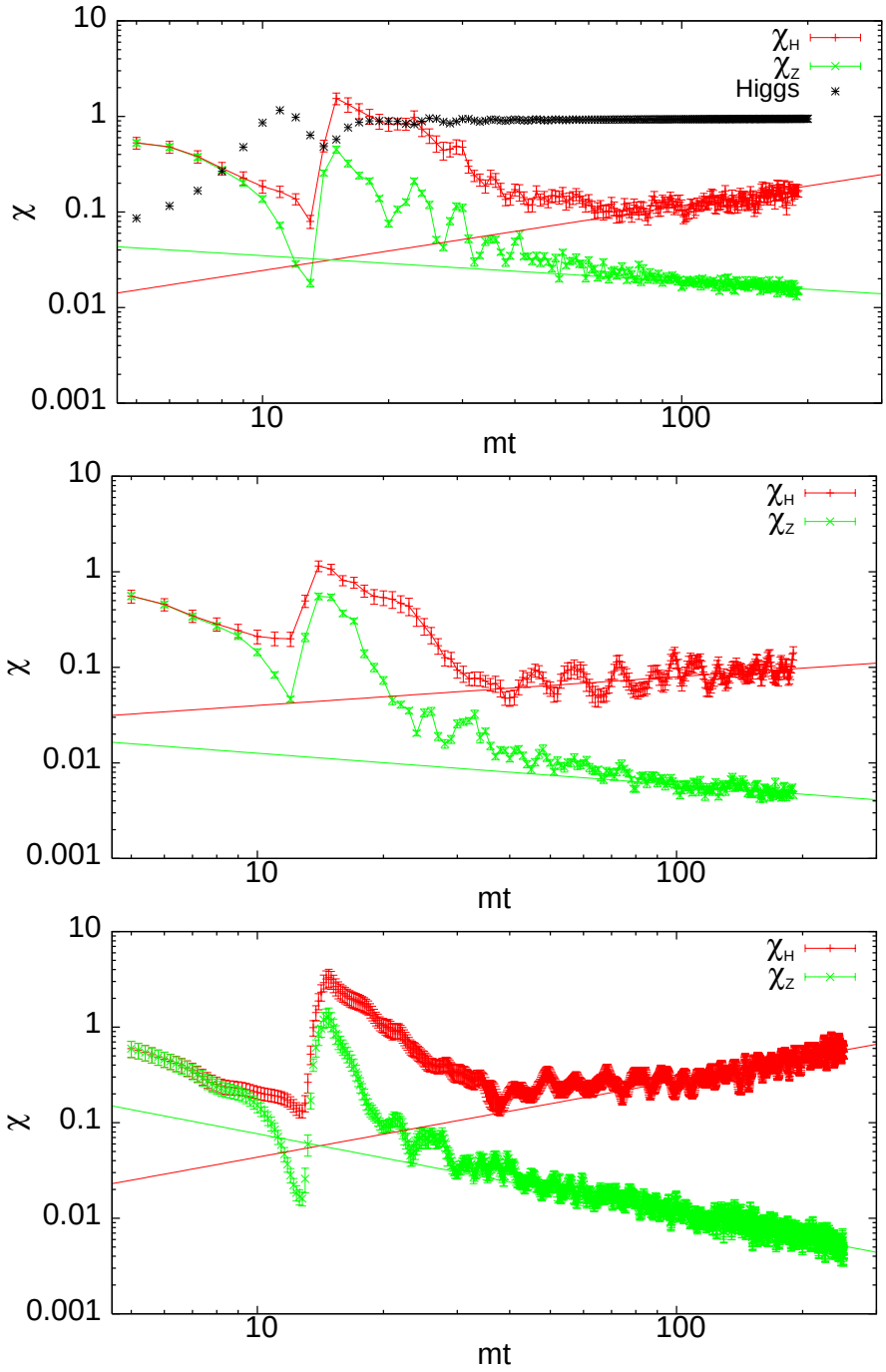

Figure 9.1: We display the time evolution of the helical susceptibilities for the magnetic field (with fit t^{α}) and the Z-boson field (with fit t^{β}). The latter is rescaled by $\tan^4\theta_W$ to match the initial electromagnetic helicity. Top left is for $m_{\rm H}/m_{\rm W} = 2$, averaged over 80 configurations, with $\alpha = 0.7(1)$ and $\beta = -0.27(4)$. Top right is for $m_{\rm H}/m_{\rm W} = 4.65$, averaged over 80 configurations, with $\alpha = 0.3(1)$ and $\beta = -0.33(5)$. Bottom is for $m_{\rm H}/m_{\rm W} = 3$, averaged over 200 configurations, with $\alpha = 0.8(1)$ and $\beta = -0.82(4)$. All data correspond to $ma = 0.42$ and $p_{\rm min} = 0.15\,m$. The top left figure also shows the time evolution of the Higgs mean to illustrate the time when SSB takes place.

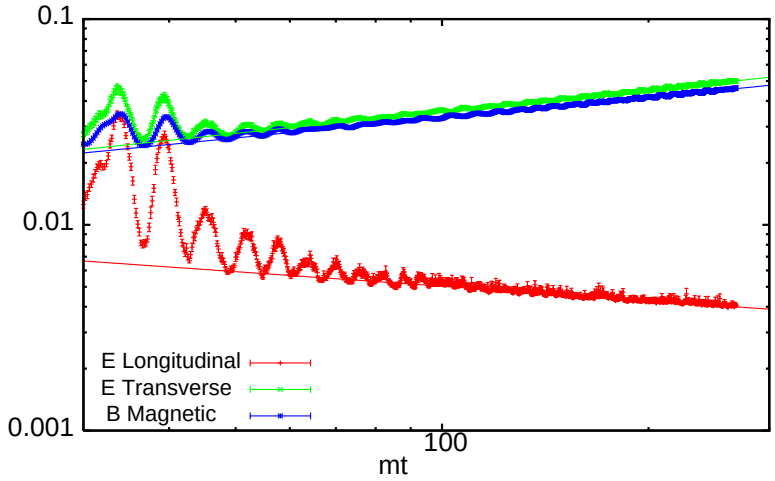

Figure 9.2: We display the log-log plot of the time evolution of the electric (transverse and longitudinal) and magnetic energy densities. The exponents of the power law fits are: Transverse electric field: 0.350(1); Magnetic field: 0.330(1) and Longitudinal electric field: $-0.234(2)$. For $m_{\rm H} = 3\,m_{\rm W}$, $ma = 0.42$ and $p_{\rm min} = 0.15\,m$, averaged over 200 configurations.

4.65 respectively. The corresponding helical susceptibilities at $mt = 100$ are $0.11(2), 0.26(1), 0.12(2)\ m^3$. Note that the model with $m_{\rm H} = 3m_{\rm W}$ is more efficient than the others in generating helicity at late times. This suggests a non monotonic dependence of the helicity on the Higgs to W mass ratio, a feature also observed in the generation of Chern-Simons number [112, 115]. In the remaining of this chapter we will focus on results for this particular value of the mass ratio. Comments upon the dependence on $m_{\rm H}/m_{\rm W}$ are deferred to chapter 10.2.

The late time evolution of the integrated magnetic, longitudinal and transverse electric energies, normalized to the initial energy and for $m_{\rm H} = 3m_{\rm W}$, is presented in Fig. 9.2. A large fraction of the electromagnetic fields generated after SSB is preserved by the time evolution. From $mt \sim 60$ onwards, the transverse energy densities increase with time, again with a power law dependence: t^α, with $\alpha = 0.350(1)$ and $0.330(1)$ for electric and magnetic energy densities respectively. At these late times, transverse electromagnetic fields are composed of an admixture of radiation and long range seed fields. In section 9.5 we will see how to separate these two components

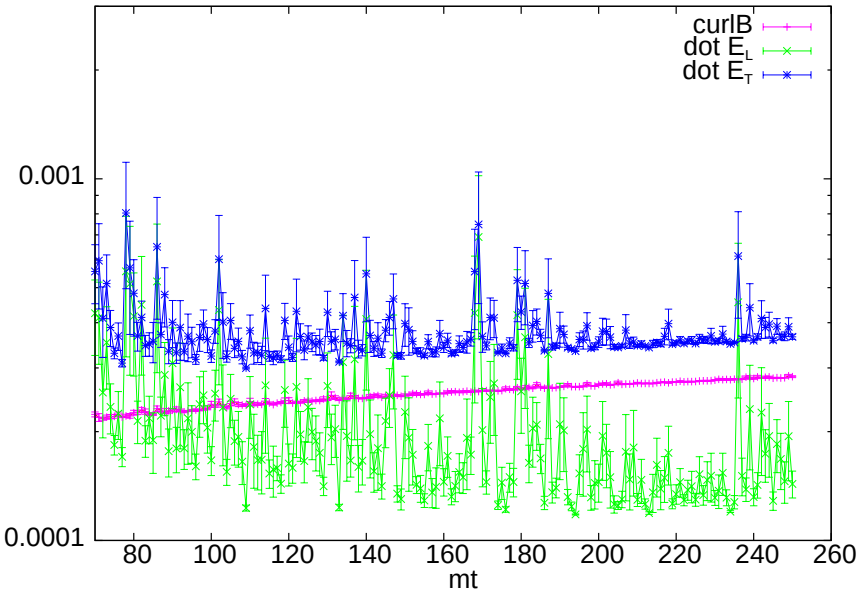

Figure 9.3: Late time evolution of the $\sigma_{T/L,B}$ averaged over 80 configurations. Model $m_{\rm H} = 3m_{\rm W}$.

by analyzing the electromagnetic field power spectra. Note also that there is a significant fraction of longitudinal electric fields, even at the later stages of the evolution. As already mentioned, the slow screening of the longitudinal component of the electric field is tied to the presence of large charged lumps around magnetic field lines, (see Figs. 8.16 and 8.17), which persist even at late times. However, as can be seen at the figure 9.2, the trend of the longitudinal energy is to decrease, a fact with is related with the slow annihilation of the clustered charges. This effect is particularly clear from figure 9.4. Compared with figure 8.19, in which a fast enhancement of the spectrum of charge, was produced through the SSB, now the spectrum is slowly decreasing. If we also compare the magnitude of both figures, we see that the magnitude of the peak in fig. 9.4 is several times lower than the one in fig. 8.19. As was pointed out in the previous chapter, it is expected that following this trend, the system would remove the charge and could enter the MHD limit in the future. Figure 9.3 shows how the behavior observed in figure 8.22 changes around times ~ 100. Although it can not be said that σ_B clearly dominates over σ_L, it is however true, that this is the general trend, giving further support to the future non-relativistic MHD limit. Note also that in the case of free radiation $\sigma_T = \sigma_B$, suggesting that the excess is produced by a non-radiation transverse component.

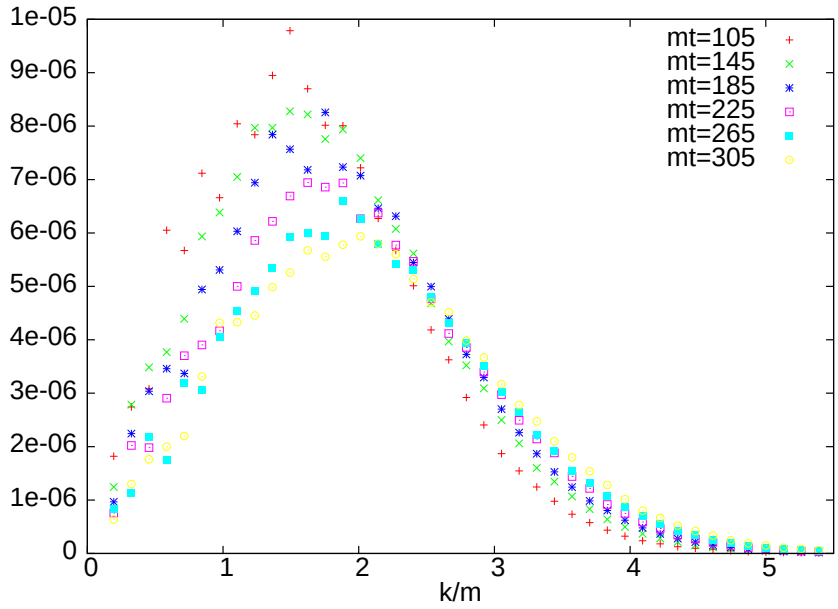

Figure 9.4: Charge spectrum evolution from $mt = 105$ to $mt = 305$. For $ma = 0.42$ and $m_{\rm H} = 2m_{\rm W}$.

Actually our system is conformed by W-bosons, that are the only charged particles. Their high mass produces the lack of mobility, and so make the charge clusters not being easily removed. The inclusion of light fermions, with a higher mobility, would help the washing out the charge inhomogeneities, and would also help to a better fit for our picture into a MHD scenario. This is of course an speculation. The influence in the system of the fermions will take place at much later times than those available in our simulations, as was discussed in chapter 4.

9.3 Kinetic turbulence.

As [126] pointed out before, systems like the one we are studying suffer a process of turbulent behavior towards the thermalization stage. In our system, at the end of inflation, all the energy is stored in the potential energy of the Inflaton which produces a tachyonic resonance of the Higgs field, and a fast transfer of energy to the rest of degrees of freedom of the system, once SSB has taken place. This energy is basically stored in the lower momentum modes of the fields of the system at the very beginning, and then starts a process of energy transport to high energy modes. This transference of

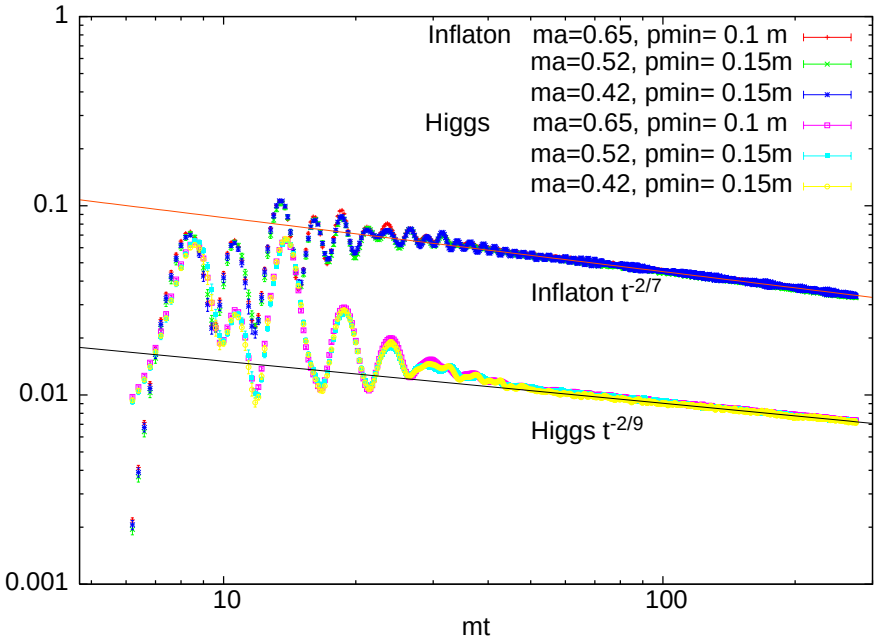

Figure 9.5: Turbulent behavior in the scalar sector of the model, for several lattice spacings. Model $m_{\rm H} = 3m_{\rm W}$.

energy between modes takes place as a turbulent process. This turbulence is characterized by a particular behavior of the scalar fields of the system and a self-similar behavior of the distribution functions towards the equilibrium. In this work a scalar field behavior according with the predicted in [126] has been found, as can be seen in figure (9.5). This turbulent behavior is characterized by the time law followed by the variances:

$$\sigma_f^2 = \langle f^2 \rangle - \langle f \rangle^2 \sim t^{-\nu}\,; \quad \nu = \frac{2}{(2m-1)}, \tag{9.1}$$

where f stands for any one of the scalars. The parameter ν is expressed in terms of the parameter m, which stands for the number of particles related in the effective interaction that dominates the energy-momentum transfer. A property found in our work is that the m-particle interaction that drives the turbulence is model dependent. Whereas this m has been found to be 4 for the Higgs and 3 for the Inflaton in the model with $m_{\rm H} = 4.65m_{\rm W}$, it happens to be 5 for the Higgs and 4 for the Inflaton in model $m_{\rm H} = 3m_{\rm W}$, and 3 for the Higgs and 5 for the Inflaton in the $m_{\rm H} = 2m_{\rm W}$ model.

Altough Ref. [126] analyzes models containing only scalar fields it predicts another signal of the turbulent behavior given by the self-similarity

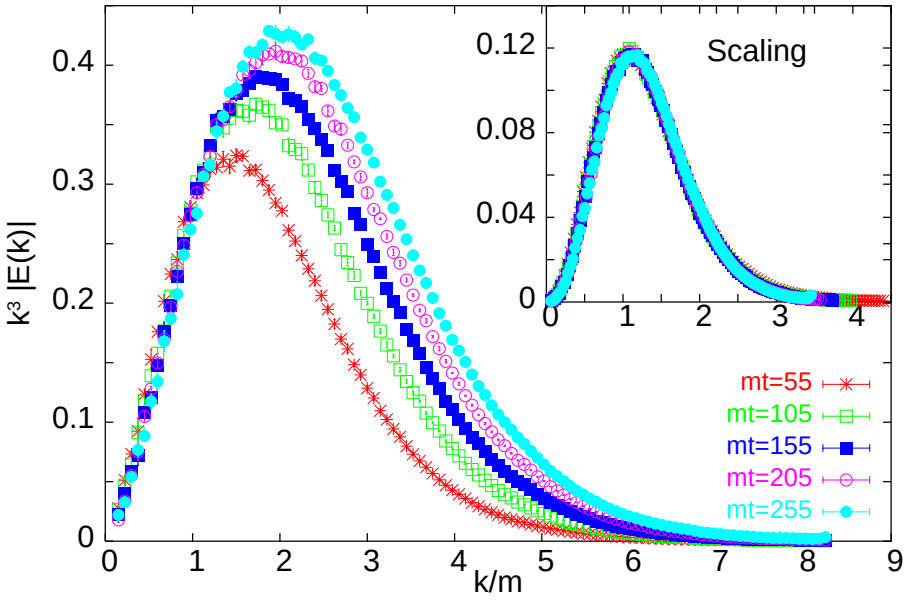

Figure 9.6: Signal of turbulence in the $SU(2)$ magnetic spectra. From time $mt = 55$ to $mt = 235$. $ma = 0.65$ and $m_{\rm H} = 4.65 m_{\rm W}$.

of the energy spectrum. This has been confirmed in this work, and quite remarkably, it has been also observed out of the scalar sector, in the self-similar behavior of the momentum spectra of the SU(2) degrees of freedom, long after the SSB. We only studied this phenomenon in detail for the model $m_{\rm H} = 4.65 m_{\rm W}$, although we expect, and we have found signals in this direction, that it is a general feature for all the models. The behavior of this SU(2) magnetic spectrum is shown in figure 9.6. The expected behavior for the self-similarity in the energy spectra is:

$$n(k,t) = t^{-q} n_0(kt^{-p}), \tag{9.2}$$

where $n(k,t) = E(k,t)/k$. The parameters p, q are related again with the effective vertex of the dominant interaction that drives the energy momentum transmission. They follow the numerical relation found out in [126] $q = 3.5p$. This relationship is also satisfied in this case. The relation $p = 1/(2m-1)$ also holds, where p has been found in our case $p = 1.1/7$, which gives a value of $m = 4$, for the model $m_{\rm H} = 4.65 m_{\rm W}$.

One striking property of this system is the early onset of the turbulent behavior. Whereas the characteristic starting time of the turbulent regime,

proposed for instance in [126], is order $mt > 3000$, long after the SSB, in the present case it happens at much earlier times, $mt \gtrsim 50$. This presumably is due to the larger number of coupled degrees of freedom, that makes easier the energy transfer. This early onset of the turbulent behavior is remarkable, because it could allow to perform an extrapolation of the time evolution beyond the limitations of the numerical approach.

The turbulent process deserves further discussion. Looking at the figure 9.6, one can see that the turbulence process observed in the SU(2) magnetic part of the spectrum, drives the energy stored in long wave modes of the system into short length scales. It is a direct cascade. As will be presented later, in the next part of the chapter, such a turbulent behavior has not be found in the $U(1)_{em}$ magnetic spectrum, or more exactly, not the whole spectrum of the photon field follows such a behavior. Although not studied in detail, the high momentum part of the photon energy spectrum presents signs of direct turbulence. However, and we have focused in this phenomenon, the low momentum part of this energy spectrum seems to present some sort of inverse cascade turbulence [57]-[59] that drives high momentum structures into low momentum ones.

9.4 The Influence of the Inflaton.

Looking at the figures of this chapter one can realize that, at late times, all of them present an oscillatory behavior besides the global trend. These oscillations, smooth and with certain temporal extension, seem to be related with some physical process, and not with artifacts coming from the discretization of the evolution. Fig. 9.7 shows a detail of the Higgs and Inflaton mean behavior at latter stages of the evolution. On it, one can see that again both quantities present an oscillatory behavior, specially in the Inflaton field case. At some times of the evolution, it seems to present, even, a resonant phenomenon. It is then interesting to show if there is a relationship between the resonances of the Inflaton and the oscillatory behavior of the rest of the components in the system or, on the contrary, if it is the proper system of charges and electromagnetic fields which is responsible of it.
In order to study this influence, we unplugged the Inflaton dynamics from the system at a certain time after the SSB, once the global trend of the system is established. The result for the magnetic energy is shown in figure 9.8. No important difference is appreciated in this quantity. Only the magnetic energy is plotted, but the same behavior has been found for the other im-

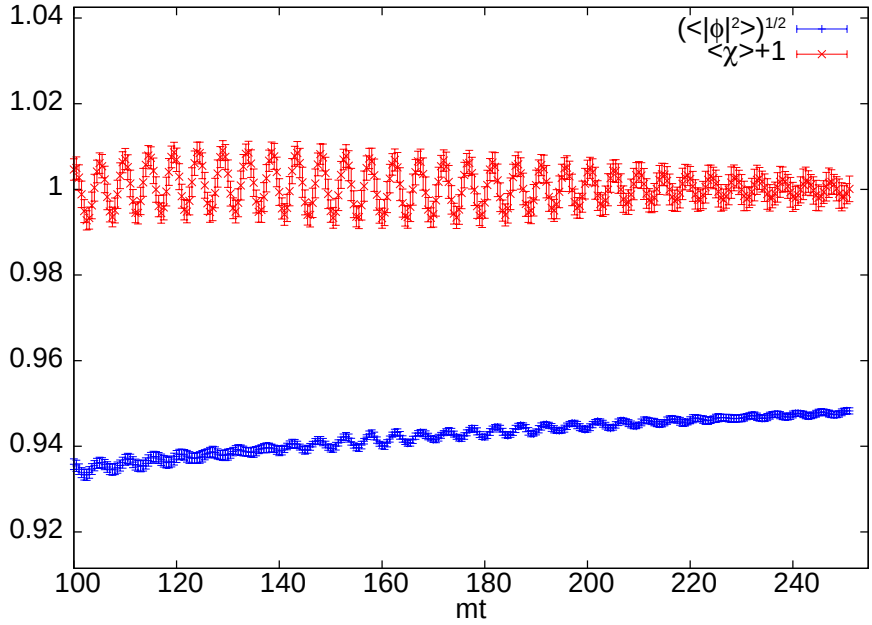

Figure 9.7: Evolution of the Higgs and Inflaton vevs from $mt = 100$ to $mt = 260$. The Inflaton vev is shifted by 1 for a better plot. For $ma = 0.42$ and $m_{\rm H} = 2m_{\rm W}$.

portant quantities. This late time Inflaton independence has also been found for the other values of mass ratios.

9.5 Magnetic seeds.

As said before, Fig. 9.2 presents the late evolution of the integrated magnetic, longitudinal electric and transverse electric energies. However, it would be desirable in order to achieve the objective of this thesis, to determine which part of this magnetic energy, is suitable to be proposed as a seed for long range magnetic fields. Such a seed is expected to accomplish two factors. First it has to present a suitable strength in order to match the values of magnetic fields observed today, at least for the lowest efficiency dynamo mechanism. And second, it has to acquire a long correlation length. Of course, as pointed out before, since our mechanism is a casual mechanism it has, in principle, a maximum correlation length, that is the size of the horizon at the time when the fields were generated. As explained in chapter 3, this caveat is solved if there is a mechanism that enhances the scale of the structures of the system, and makes it grow as the horizon itself. The most often used mechanism is

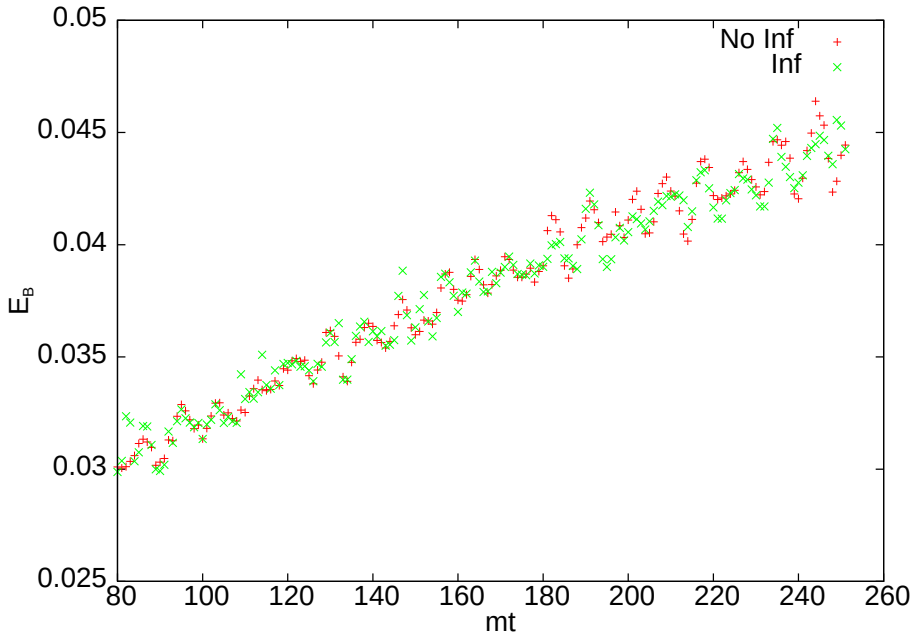

Figure 9.8: Evolution of the magnetic energy density normalized to the total energy density. With and without the Inflaton field. For $ma = 0.42$ and $m_{\rm H} = 3m_{\rm W}$.

the inverse cascade.

In order to analyze all these points I must say before, that two complications arose on the way that are worth to mention. One is related to the fact that the system is embedded in a self-produced thermal bath of photons. This thermal photon bath (I refer to it as thermal but, as we will see below, quasi-thermal would be a more accurate description) dominates the energy density and masks any subyacent signal of non thermal long structures. Of course these are the ones of interest, because the magnetic field of the radiation photons is not expected to be a long correlation one, at least at temperatures of order the electroweak temperature (actually our temperature is smaller but comparable). The reason is the typical scale of the thermal radiation is directly related with the inverse of the temperature. The calculation for the actual temperature of the system gives a small correlation length, compared with the corresponding to the non thermal structures, which is explained below. It is necessary then, to separate the radiation component of the system from the one originating the seed fields. Several methods have been tested during the development of this thesis.

The other technical problem is related with the finite volume artifacts.

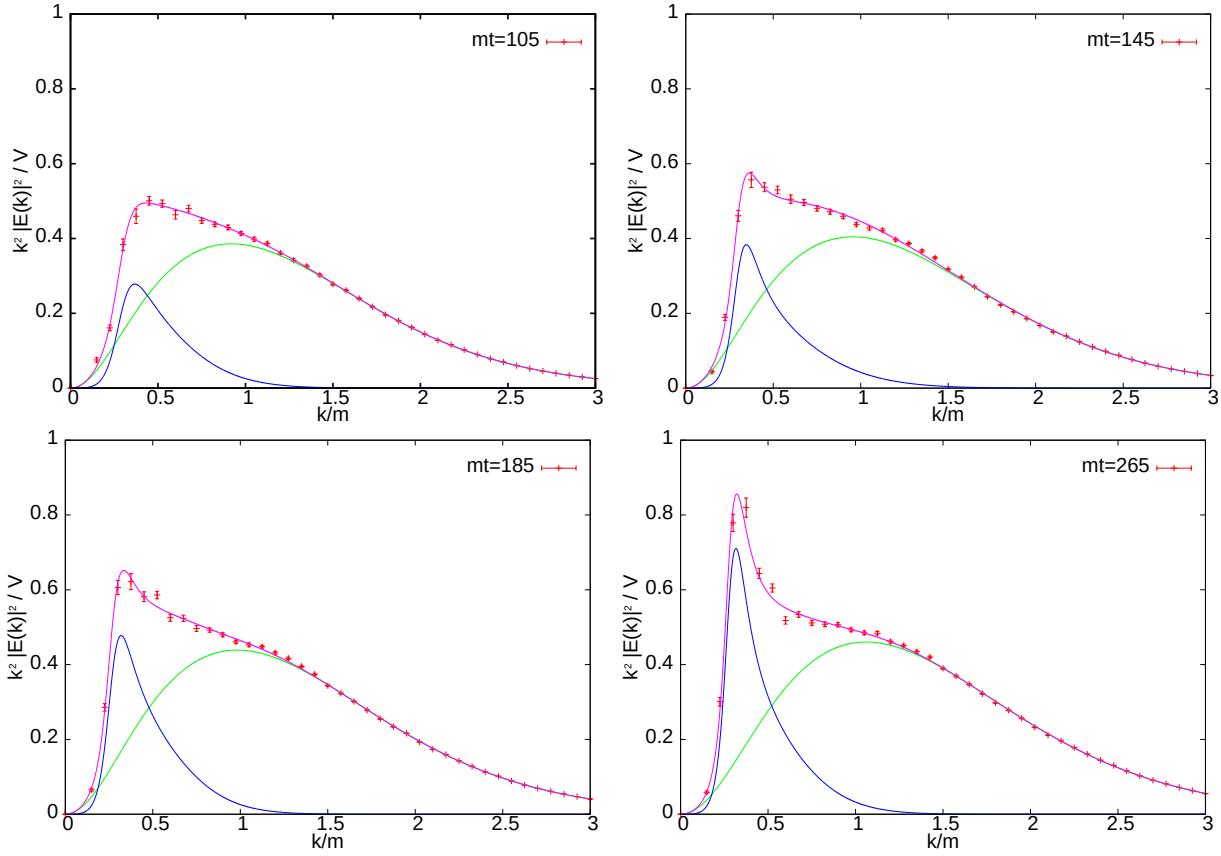

Figure 9.9: We plot $\langle k^2|\vec{E}(k)|^2\rangle/\mathcal{V}$ vs k, averaged over 150 configurations. The lines represent fits to the radiation and seed field electromagnetic components according to Eqs. (9.5), (9.7) respectively. Results are presented at $mt = 105$, 145, 185 and 265. In all cases $m_{\rm H} = 3m_{\rm W}$, $ma = 0.42$ and $p_{\rm min} = 0.15\,m$.

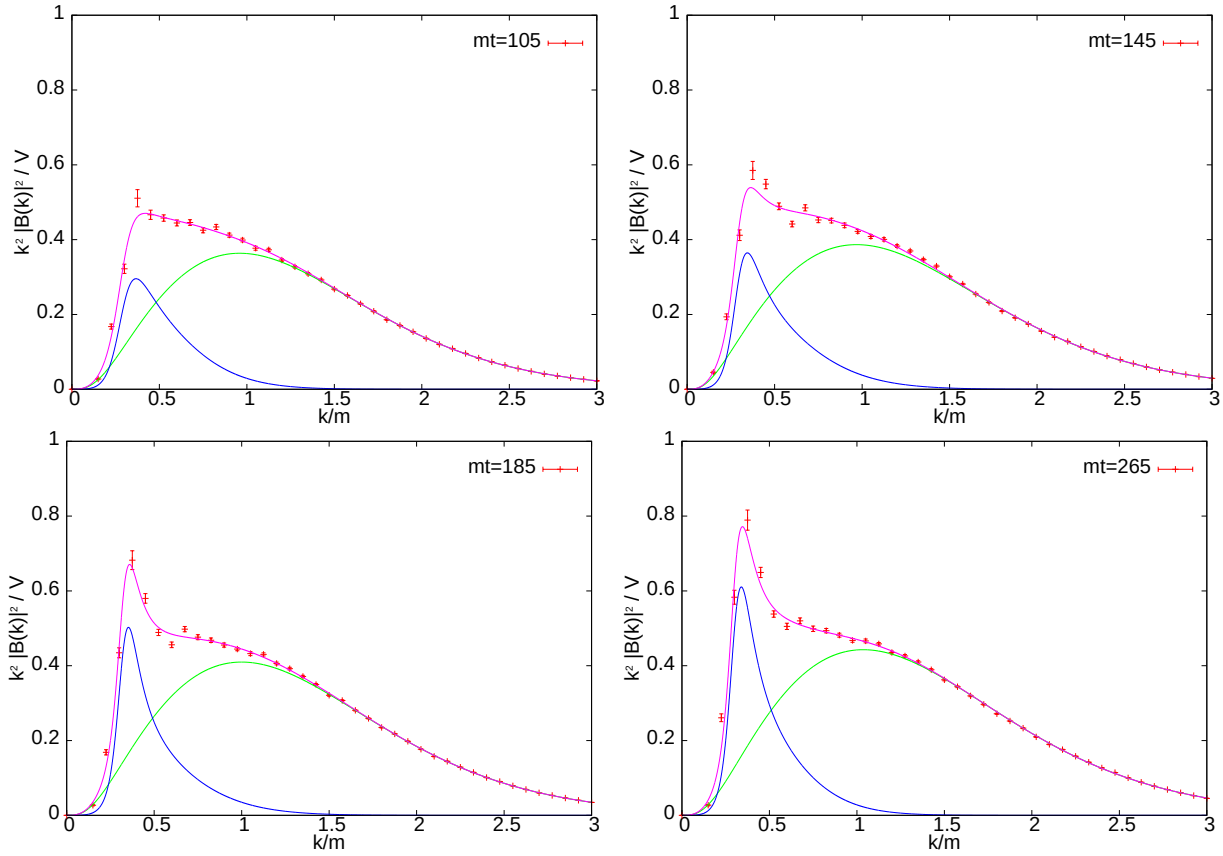

Figure 9.10: The same as in Fig. 9.9 but for the magnetic component: $\langle k^2|\vec{B}(k)|^2\rangle/\mathcal{V}$.

As was explained in chapter 5, the finite volume of the system forces the choice of a particular set of boundary conditions. A natural setting is to take just periodic boundary conditions, which has several advantages. But this limits the large scale description of the system, which is precisely the one we are interested in. This is due to the existence of a minimal momentum unit in the system. We will solve this, by averaging the quantities of interest over several p_{min} values, in order to have an estimation of the systematical errors.

Along the study of the several mass ratios, we have found that the model $m_{\rm H} = 3m_{\rm W}$ presents a cleaner separation between the radiation and the seed field. For that reason, in the following, we concentrate in model $m_{\rm H} = 3m_{\rm W}$. Nevertheless, a similar study for model $m_{\rm H}/m_{\rm W} = 2$ will be presented in chapter 10.

9.6 Electromagnetic field spectrum.

To investigate whether inverse cascade is active during the late time evolution, we have analyzed the electromagnetic Fourier spectrum. This spectrum has showed to be a very useful tool in order to achieve the separation between thermal photons and long scale magnetic fields. Figs. 9.9 and 9.10 display the time evolution of $\langle k^2|\vec{E}(k)|^2\rangle/\mathcal{V}$ and $\langle k^2|\vec{B}(k)|^2\rangle/\mathcal{V}$, where $\vec{E}(k)$ and $\vec{B}(k)$ are the Fourier components of the electromagnetic fields and $\mathcal{V}$ is the physical volume.

The most remarkable feature in the spectrum is the peak at small momenta that develops with time, which is distinctly separated from the high momentum component. This behaviour suggests that the spectrum contains two uncorrelated distributions which describe respectively electromagnetic radiation and the long range electric and magnetic seed fields. Following this indication, we have performed fits to the spectrum where this separation is made explicit:

$$\vec{F}(k) = \vec{F}^{\rm seed}(k) + \vec{F}^{\rm rad}(k) \tag{9.3}$$

with $\vec{F} = \vec{E}$ or $\vec{B}$. For the expectation values of the electric and magnetic correlators we obtain accordingly:

$$\begin{aligned} \langle|\vec{E}(k)|^2\rangle &= \langle|\vec{E}^{\rm seed}(k)|^2\rangle + \langle|\vec{E}^{\rm rad}(k)|^2\rangle \\ \langle|\vec{B}(k)|^2\rangle &= \langle|\vec{B}^{\rm seed}(k)|^2\rangle + \langle|\vec{B}^{\rm rad}(k)|^2\rangle \end{aligned} \tag{9.4}$$

where, of course, both radiation and seed components are taken as independent variables, so the cross averages can be neglected.

mt	T_E/m	m_E/m	μ_E/m	T_B/m	m_B/m	μ_B/m
105	0.32(1)	0.77(1)	0.61(1)	0.32(1)	0.66(1)	0.60(1)
125	0.33(1)	0.74(1)	0.58(1)	0.33(1)	0.61(2)	0.57(2)
145	0.34(1)	0.75(1)	0.58(1)	0.33(1)	0.60(2)	0.56(2)
165	0.34(1)	0.76(2)	0.59(1)	0.34(1)	0.61(2)	0.57(2)
185	0.34(1)	0.82(1)	0.63(1)	0.34(1)	0.65(2)	0.60(2)
205	0.35(1)	0.84(1)	0.64(1)	0.34(1)	0.64(2)	0.59(2)
245	0.35(1)	0.93(1)	0.68(1)	0.35(1)	0.64(1)	0.59(2)
265	0.36(1)	0.93(1)	0.67(1)	0.35(1)	0.65(2)	0.59(2)

Table 9.1: Parameters of the fit to the high momentum part of the transverse electric and magnetic spectra in Eq. (9.5), for $m_{\rm H} = 3m_{\rm W}$, $ma = 0.42$ and $p_{\rm min} = 0.15\, m$. Errors in parenthesis combine both systematic and statistical effects.

In the remaining of this section we will describe these two components, starting with the electromagnetic radiation and ending with the infrared component which describes the magnetic field seed.

9.6.1 Electromagnetic radiation.

The radiation component dominates the electromagnetic energy density, its contribution being a factor of 5-10 larger than the one coming from seed fields. Its profile is very well described by:

$$\begin{aligned} \frac{1}{\mathcal{V}}\langle|\vec{E}^{\rm rad}(k)|^2\rangle &= \frac{2w_E}{e^{\beta(w_E-\mu_E)}-1} \\ \frac{1}{\mathcal{V}}\langle|\vec{B}^{\rm rad}(k)|^2\rangle &= \frac{2k}{e^{\beta(w_B-\mu_B)}-1}\,, \end{aligned} \tag{9.5}$$

with $w_{E(B)} = \sqrt{k^2 + m^2_{E(B)}}$ and parameters given in Table 9.1. As illustrated in figures 9.9 and 9.10, this distribution fits very well the high momentum part of the spectrum but fails in reproducing the low momentum peak. Eq. (9.5) represents free massive thermal radiation with non zero chemical potential at temperatures slightly rising with time, which we interpret as an effect induced by the plasma of the W-fields.

Similar information can be extracted from the distribution of local values of the norm of the transverse electric and magnetic fields. For free photons

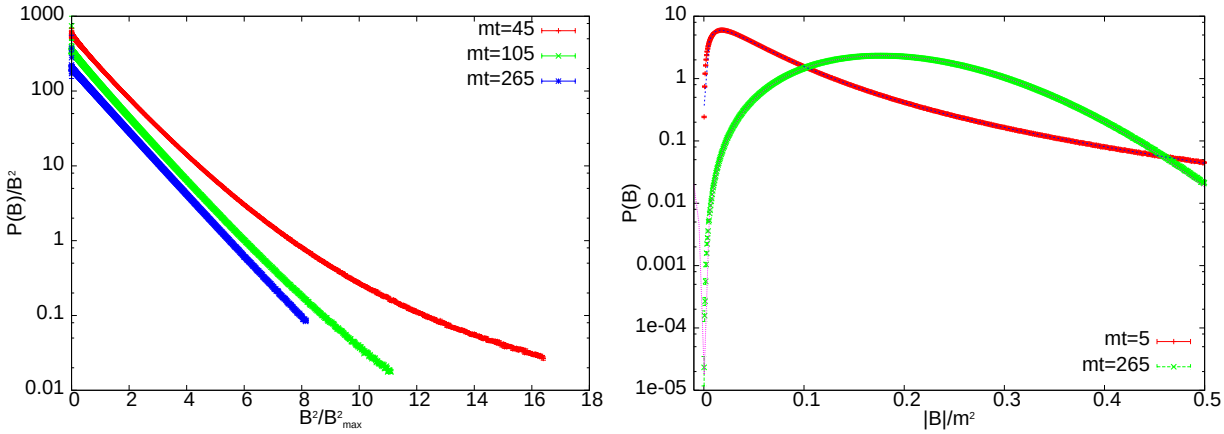

Figure 9.11: We show the time evolution of the distribution of magnetic field norms. Left: For $m_{\rm H} = 3m_{\rm W}$ we display the log of $P(B)/B^2$ vs $B^2/B^2_{\rm max}$ (i.e. normalized to the value at the peak of the distribution) . Right: For $m_{\rm H} = 3m_{\rm W}$ we compare the initial distribution of the local magnitude of the magnetic field at $mt = 5$ with the one obtained at $mt = 265$, the latter fitted to a Maxwellian distribution. The fit to the $mt = 5$ data is described in Appendix D.

this should follow a Maxwellian distribution (see Appendix C):

$$P(B) = \sqrt{\frac{2}{\pi}}\Big(\frac{3}{\langle B^2\rangle}\Big)^{3/2} B^2\ e^{-\frac{3B^2}{2\langle B^2\rangle}}, \tag{9.6}$$

where $B = |\vec{B}(\vec{x})|$. Our data does indeed reproduce this behaviour at late times. In Fig. 9.11 we display the time evolution of the distribution of magnetic field norms, starting from $mt = 5$. Although initially the distribution differs significantly from the Maxwellian one, it is approached as time evolves and photons thermalize. There is, however, a systematic mismatch when we fit the tail of the Maxwellian distribution, even at large values of mt. This signals again a deviation from free radiation, like the one observed in the low momentum part of the magnetic and electric spectra. It is in this deviation where the contribution of the seed magnetic fields resides.

Electric and magnetic seeds.

We turn now to the analysis of the infrared part of the spectrum, which is the relevant one for the generation of the LSMF seed field. This low momentum

mt	$\hat{T}_E/m$	$\hat{m}_E/m$	$\hat{\mu}_E/m$	$\hat{k}^0_E/m$
105	0.11(1)	0.33(5)	0.30 (4)	0.29(1)
125	0.13(1)	0.24(4)	0.22(3)	0.29(1)
145	0.14(1)	0.21(5)	0.18(3)	0.30(1)
165	0.13(1)	0.25(5)	0.23(3)	0.29(1)
185	0.09(2)	0.49(8)	0.48(6)	0.27(1)
205	0.11(1)	0.36(6)	0.35(3)	0.29(1)
225	0.10(2)	0.39(10)	0.38(3)	0.28(1)
245	0.11(1)	0.37(7)	0.35(3)	0.30(1)
265	0.10(1)	0.45(7)	0.44(4)	0.28(1)

Table 9.2: Parameters of the fit to the low momentum part of the transverse electric spectrum in Eq. (9.7), for $m_{\rm H} = 3m_{\rm W}$, $ma = 0.42$ and $p_{\rm min} = 0.15\, m$.

part has been fitted to:

$$\frac{1}{\mathcal{V}}\langle|\vec{E}^{\rm seed}(k)|^2\rangle = \frac{2k}{e^{\hat{\beta}_E(\hat{w}_E-\hat{\mu}_E)}-1}\,, \qquad \frac{1}{\mathcal{V}}\langle|\vec{B}^{\rm seed}(k)|^2\rangle = \frac{2k}{e^{\hat{\beta}_B(\hat{w}_B-\hat{\mu}_B)}-1}\,, \tag{9.7}$$

with $\hat{w}_{E(B)} = \sqrt{(k-k^0_{E(B)})^2+\hat{m}^2_{E(B)}}$ and parameters given in Tables 9.2, 9.3. This could represent again massive radiation at non-zero chemical potential if it were not for the peculiar shift k_0 in the frequency $\hat{w}$. We interpret the value of $k_0 \sim 0.3m$ as a characteristic momentum scale of the long range electromagnetic fields.

A quantitative estimate of the energy density and correlation length of the seed electromagnetic fields can be obtained from our fits to the low momentum part of the spectrum. The mean energy density is computed from the integral of the seed field spectrum as

$$\langle\rho^F_{\rm seed}\rangle = \frac{1}{2\mathcal{V}}\sum_{\vec{k}}\frac{|\vec{F}^{\rm seed}(k)|^2}{\mathcal{V}}\,, \tag{9.8}$$

with $F = E(B)$. The correlation length, $\xi_{E(B)}$, is extracted from

$$\xi = \frac{2\pi}{\bar{k}}\ ,\ \text{with}\ \bar{k}^2 = \frac{\sum_{\vec{k}} k^2\ |\vec{F}^{\rm seed}(k)|^2}{\sum_{\vec{k}}|\vec{F}^{\rm seed}(k)|^2}\,. \tag{9.9}$$

Table 9.4 and Fig. 9.12 summarise our results. We have tested finite volume independence by comparing two different physical volumes: $p_{\rm min} = 0.125\, m$

mt	$\hat{T}_B/m$	$\hat{m}_B/m$	$\hat{\mu}_B/m$	$\hat{k}_B^0/m$
105	0.11(1)	0.32(7)	0.30(3)	0.29(1)
125	0.13(1)	0.24(7)	0.21(4)	0.31(1)
145	0.13(1)	0.24(6)	0.22(3)	0.29(1)
165	0.13(1)	0.27(6)	0.23(4)	0.29(1)
185	0.13(2)	0.18(10)	0.16(8)	0.32(3)
205	0.11(1)	0.31(7)	0.29(4)	0.30(1)
225	0.11(1)	0.26(5)	0.25(4)	0.31(1)
245	0.10(1)	0.37(9)	0.36(2)	0.29(1)
265	0.11(2)	0.33(9)	0.32(3)	0.30(1)

Table 9.3: Parameters of the fit to the low momentum part of the magnetic spectrum in Eq. (9.7). For $m_{\rm H} = 3m_{\rm W}$, $ma = 0.42$ and $p_{\rm min} = 0.15\, m$.

and $p_{\rm min} = 0.15\, m$. The numbers in Table 9.4 come from an average of the results obtained at these two physical volumes, with errors given by the dispersion between them.

We obtain a magnetic seed whose mean energy density increases linearly with time. Within the time ranges we have analysed, its fraction to the total comes out to be of order $\sim 10^{-2}$. Assuming the magnetic field expands as radiation, this would give magnetic fields today of order $0.5\,\mu G$, which are in the range of the observed ones in galaxies, and even in clusters of galaxies, where no-extra amplification through a dynamo mechanisms is expected.

Concerning the correlation length, it is difficult to make a definitive statement about the presence of inverse cascade, given the small time scales we can explore with our numerical simulation. Nevertheless, within the time span we have analyzed, our results clearly show a linear increase of the magnetic correlation length with time (see Fig. 9.12). This result is robust under changes of $p_{\rm min}$ and lattice spacing. The observed growth is described by $m\xi_B(t) = 20.1(4) + 0.033(2)mt$, giving at $mt = 265$ a characteristic length scale for seed magnetic fields of order $m\xi_B(mt = 265) \sim 30(1)$. This is much larger than the thermal correlation length, $m\xi_{\rm thermal} \sim 10$, and represents a significant fraction of the physical volume. It also implies a considerable increase from the initial value at $mt = 5$, obtained from the initial spectrum to be $m\xi_B(mt = 5) \sim 17$. From these results we can safely conclude that the time evolution has succeeded in amplifying the correlation length of the magnetic seed generated at SSB. Nevertheless, a more detailed study, including plasma effects, would be required to determine whether ξ will be further

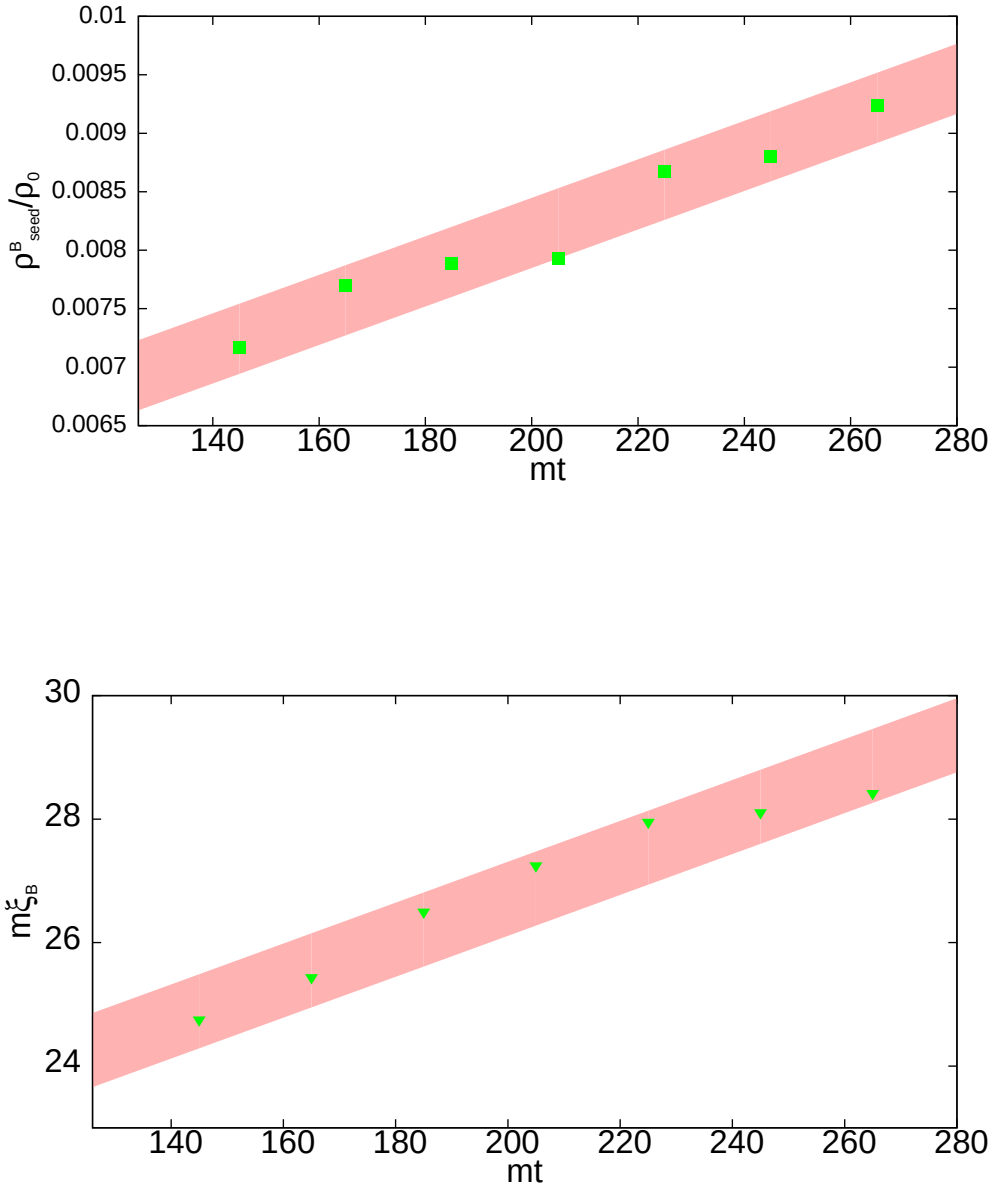

Figure 9.12: We show the time evolution of $\rho^B_{\rm seed}$ (left) and $m\xi_B$ (right), for $m_{\rm H} = 3m_{\rm W}$, $ma = 0.42$. The results are obtained by averaging the values obtained for $p_{\rm min} = 0.15\,m$ and $p_{\rm min} = 0.125\,m$, with bands representing the dispersion in the errors. The fits are $\rho^B_{\rm seed}/\rho_0 = 0.0035(5) + 2.3(3) \times 10^{-5} mt$ and $m\xi_B = 20.1(4) + 0.033(2)mt$ respectively.

mt	$\langle\rho^E_{\rm seed}\rangle(\times 10^2)$	$m\xi_E$	$\langle\rho^B_{\rm seed}\rangle(\times 10^2)$	$m\xi_B$
105	0.62(5)	25.3(1)	0.58(3)	25.7(6)
125	0.73(2)	25.2(1)	0.61(1)	24.5(9)
145	0.76(4)	24.8(9)	0.72(2)	24.8(3)
165	0.76(4)	26.0(10)	0.77(1)	25.4(6)
185	0.83(1)	27.6(1)	0.79(2)	26.0(10)
205	0.89(2)	27.7(2)	0.79(6)	27.2(5)
225	0.91(5)	27.9(5)	0.87(1)	28.0(5)
245	1.06(9)	27.6(4)	0.88(1)	28.1(2)
265	1.12(7)	27.9(2)	0.92(2)	28.4(7)

Table 9.4: Fraction of total energy and correlation length of the seed electromagnetic fields. They are both derived from the infrared spectrum as described in Eqs. (9.8) and (9.9). The results are obtained by averaging (over 150 configurations) the values obtained for $p_{\rm min} = 0.15\, m$ and $p_{\rm min} = 0.125\, m$, with errors reflecting the dispersion between them. Data correspond to $m_{\rm H} = 3m_{\rm W},\ ma = 0.42$.

amplified at late times.

In addition to the direct analysis of the spectrum we have also followed an alternative strategy to separate both the magnitude and the scale of the magnetic remnant from the radiation bath. A common way to do this, which has been extensively used in the literature, is through the computation of several spatial averages of the electromagnetic fields. Following Ref. [44], we introduce the following averages:

- A line average:
$$B_{(1)}(l) = \frac{1}{l}\int_C \vec{B}\cdot d\vec{x}\,, \tag{9.10}$$
with C a straight line of length l.

- The average magnetic flux over a surface of area l^2:
$$B_{(2)}(l) = \frac{1}{l^2}\int_S \vec{B}\cdot d\vec{S}\,, \tag{9.11}$$

- A volume average:
$$\vec{B}_{(3)}(l) = \frac{1}{l^3}\int_S \vec{B} d^3x\,. \tag{9.12}$$

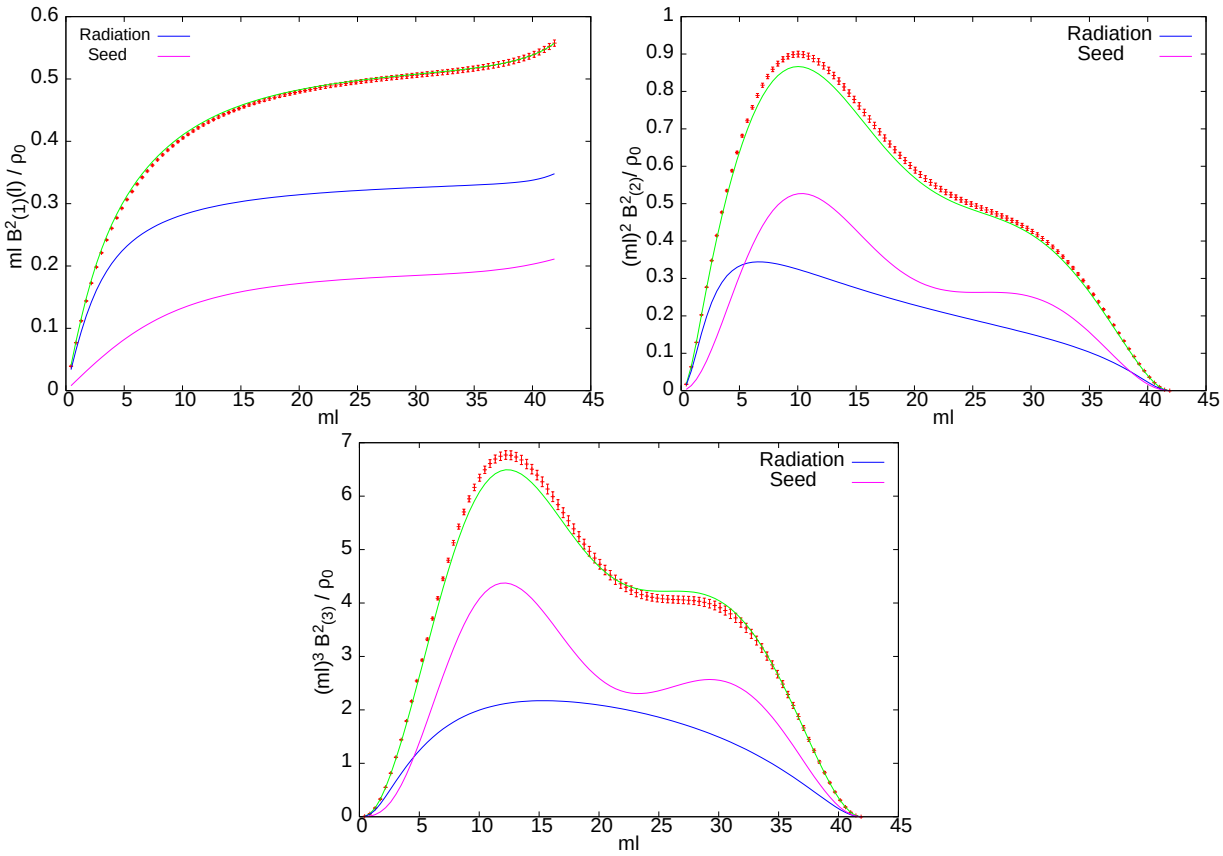

Figure 9.13: We show the dependence with ml of the three spatial averages (9.10)−(9.12), for $mt = 245$. The lines are extracted from our fits to the infrared and radiation parts of the spectrum. Note that the fall-off at large distances is just a volume effect.

As discussed in Ref. [44], the spatial and statistical averages $\langle B^2_{(i)}(l)\rangle$ can be easily computed in terms of the spectra of the fields. For instance, the line average for a volume $\mathcal{V}$ is given by:

$$\langle B^2_{(1)}(l)\rangle = \frac{1}{\mathcal{V}}\sum_{\vec{k}} \frac{|B_k|^2}{\mathcal{V}} W^2(k_1, l) \tag{9.13}$$

with

$$W(k_i, l) = \frac{2\sin(k_i l/2)}{k_i l}. \tag{9.14}$$

Analogous expressions can be found for the other two quantities. The advantage of these averages is that they filter out the high momentum part of the spectrum and allow to recover, at large l, information about the low momentum modes. We have checked that our fits to the spectrum correctly reproduce the spatial averages. This is illustrated in Fig. 9.13, where we present results for the three averages at $mt = 245$ compared with the predictions obtained from our fits to the spectrum. The quality of the agreement can be considered very good given that the continuum lines are directly obtained from the fits to the spectrum (Eqs. (9.5), (9.7) and Tables 9.1 - 9.3), and not as a result of a fit to the spatial averages.

9.7 The Helical length.

An interesting related quantity we also have studied in this work, is the correlation length associated with the helical susceptibility. This quantity could be related somehow with the observed magnetic length. Having in mind ideal MHD, the helical structures and the magnetic structures are strongly tied. In further extensions of ideal MHD, the reconnection processes makes both quantities related again, although not so directly. More exactly, as was explained in chapter 7, the qualitative interpretation of the inverse cascade given there, implies that the magnetic field scale increment is a consequence of the transference of the "local" helicity stored in the smaller structures, into larger ones. To investigate the helical correlation length, and if it is comparable with the one obtained from the magnetic field itself, we made use of an estimator of the former quantity, given by:

$$\frac{2\pi}{\xi_\chi} = \sqrt{\frac{\int dk^3 k^2 h^2(\vec{k})}{\int dk^3 h^2(\vec{k})}} \tag{9.15}$$

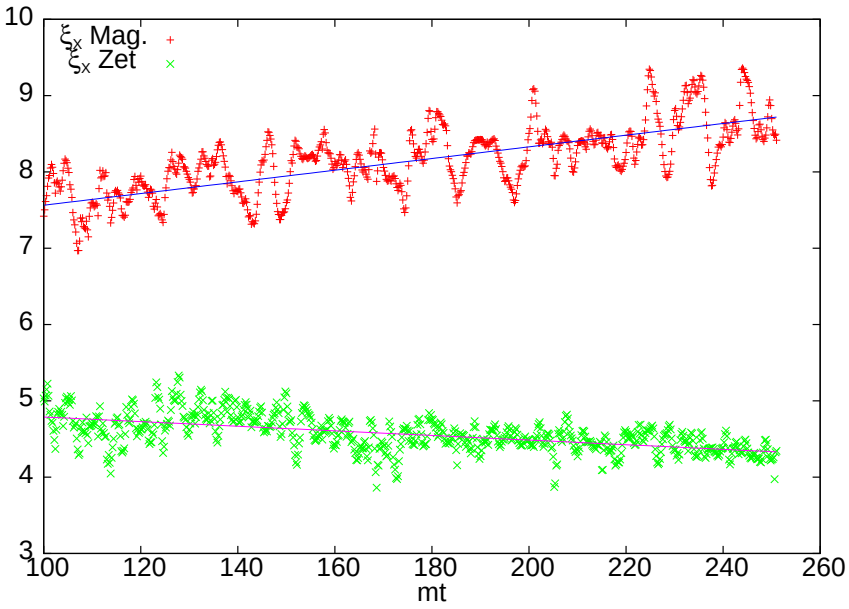

Figure 9.14: This figure shows the helical correlation length ξ_χ averaged over several configurations, for the magnetic field and the Z-boson. For $m_{\rm H} = 3m_{\rm W}$ and $ma = 0.42$.

where $h(\vec{k})$ is given by eq. (8.6):

$$h(\vec{k}) = \frac{-i\vec{k}}{|\vec{k}|^2} \cdot (\vec{B}(\vec{k}) \times \vec{B}^*(\vec{k})) \tag{9.16}$$

This quantity ξ_χ is plotted in figure 9.14, for both the magnetic susceptibility and the Z-boson one. Further corroboration of the Vachaspati-Cornwall's conjecture can be appreciated. The characteristic scale of the Z-boson susceptibility is decreasing with time, whereas the magnetic one is increasing with time. The characteristic scale of the magnetic susceptibility is smaller by a factor ~ 3 of its magnetic counterpart. We can argue from these results, that the enhancement of the length of the magnetic seeds and the increasing length estimated for the helicity, seem to be correlated phenomena. The explicit way they communicate remains however unknown, and may require a full description of MHD turbulence and inverse cascade.

The corresponding slopes of the fit have resulted to be $7.6(4)\,10^{-3}$ and $-3.0(2)\,10^{-3}$ for the helical magnetic field and the Z-boson respectively. The fit for the magnetic field shows a slower trend that the enhancement of the magnetic seed length ($\sim 3.3\,10^{-2}$). Extracting the exact relationship between them requires future work.

With all this we have reached the end of the present chapter. Several results have been presented. To summarize, we have found evidence of both a turbulent behavior for the scalars in the system and $SU(2)$ energy. We also discovered the presence of a long range helical magnetic field, whose amplitude and correlation length are linearly increasing with time. This is accompanied by the growth of a similar long range electric field. The fate of these electromagnetic field depends on the subsequent evolution of the plasma which is not addressable within our classical approximation and would require a magnetohydrodynamical treatment including the effects of fermion fields. Our results for the power spectrum of the seed fields could be used, under certain assumptions, and if the observed trends are extrapolated, as initial conditions for some sort of MHD treatment as the one developed in Ref. [58]. Several questions related with this are open, and will be further detailed in the section about prospects for the future (see section 12).

Chapter 10

Dependence on methodological and model parameters.

In this chapter we study the (in-)sensitivity of our results to the lattice and finite volume artifacts. We conclude that all our qualitative results are unaffected by both types of approximations. Furthermore, we estimate the size of the systematic errors induced by these cut-offs. The lattice artifacts, though sizable, follow the expected $\mathcal{O}(a^2)$ dependence allowing an extrapolation of the most relevant quantities to the continuum limit.

We also analyze the dependence of our magnetic field production mechanism on the Higgs to W-boson mass ratio $m_{\rm H}/m_{\rm W}$. It follows from our scenario that, initially, the helical susceptibility χ_H is independent of the Higgs self-coupling. At later times however, we observe a non-monotonic dependence upon the mass ratio, which is maximal at our intermediate value $m_{\rm H}/m_{\rm W} = 3$.

10.1 Lattice and finite volume artifacts

In order to determine the size of the errors introduced by our numerical approach, we have performed simulations at different values of the physical volume and of the spatial and temporal lattice spacings. The list of simulation parameters is given in Table 6.1. The selection of values implies a delicate compromise among different factors. As shown in Ref. [111], to avoid important finite volume effects, we need lattices with momentum discretization $p_{\rm min} = 2\pi/L \leq 0.15\, m$. On the other hand, concerning lattice artifacts, we have seen in Ref. [112] that cut-off independence of certain particular quantities (as the Chern-Simons number) requires $m_{\rm W} a \leq 0.3$. Most of our

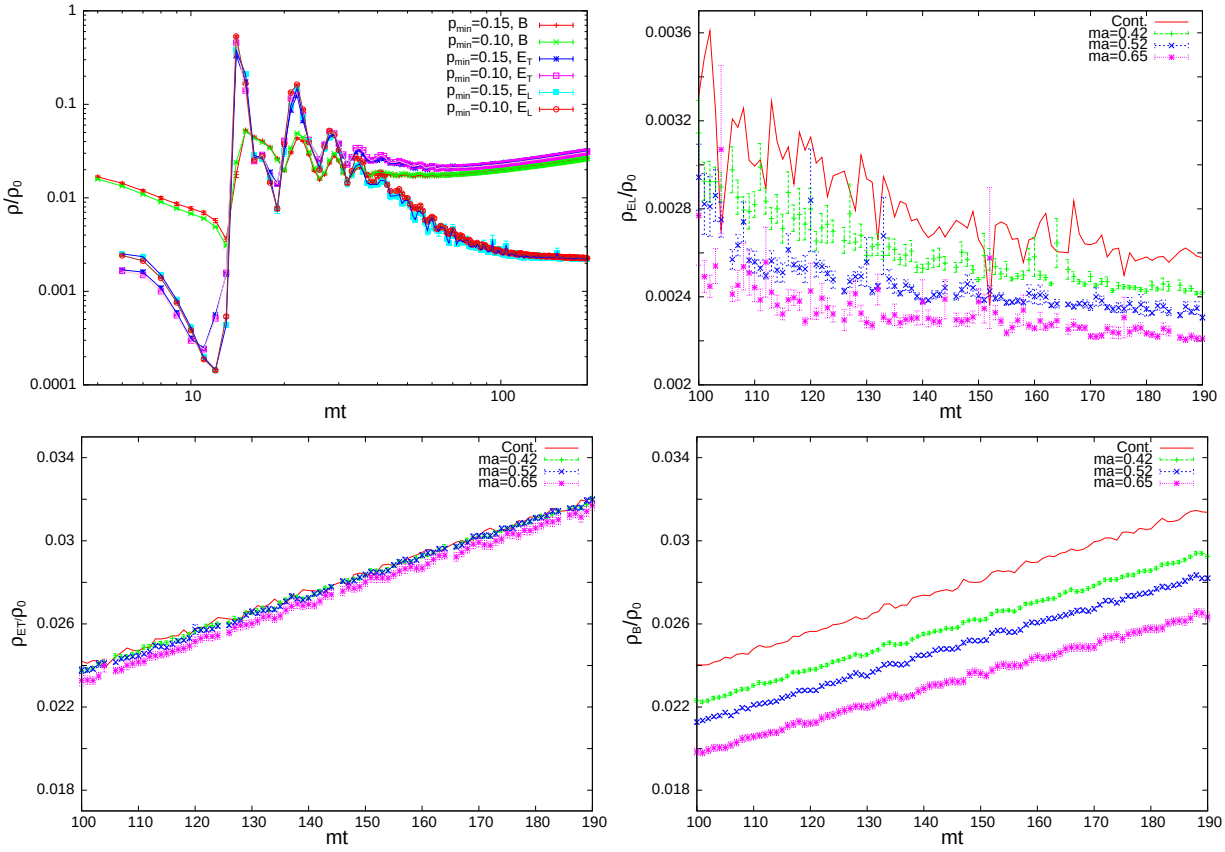

Figure 10.1: Comparison of the fraction of total energy carried by electric (transverse and longitudinal) and magnetic fields. Top left: for two different values of the minimum momentum: $p_{\rm min} = 0.1$ and 0.15 for fixed $ma = 0.65$. Top Right and down: 3 different lattice spacings ma= 0.65, 0.52,0.42, for the longitudinal, transverse and magnetic components of the energy. The lines are the extrapolation of the results to the continuum $a \to 0$ limit. For $m_{\rm H} = 2m_{\rm W}$ which, from the point of view of lattice artifacts, is the worst case situation.

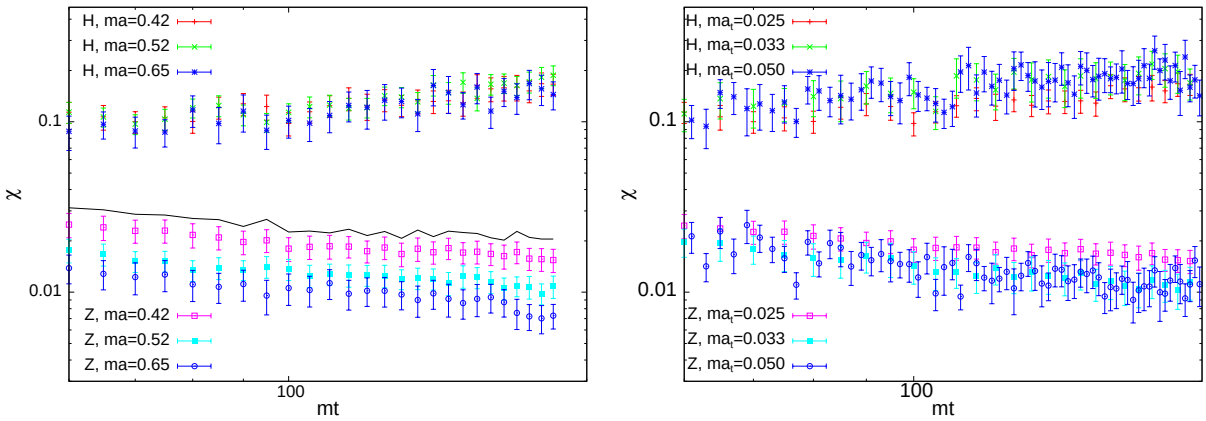

Figure 10.2: Left: Lattice spacing dependence of the magnetic susceptibility for $m_H = 2m_W, ma = 0.65,\ 0,52,\ 0.42$ and $N = 64,\ 80,\ 100$. Right: Temporal lattice spacing dependence of the magnetic susceptibility for $ma_t = 0.05, 0.025$.

lattices satisfy both requirements.

In Figs. 10.1 and 10.2 we present results exhibiting the lattice and finite volume dependence of the electromagnetic energy densities and of the magnetic helicity. They correspond to the most disfavourable case of $m_{\rm H} = 2m_{\rm W}$. No noticeable dependence on the volume is appreciated. Lattice spacing artifacts are somewhat stronger but do not change the general pattern of behaviour. To analyse this effect in more detail, we display in Fig. 10.3 the a^2 dependence of the electromagnetic field energy densities and Z-boson susceptibility at various times. In all cases the results are consistent with the expected quadratic dependence. This allows the extrapolation of the results to the continuum limit, displayed as a continuous line in Figs. 10.1 and 10.2. The right-hand side of the last figure shows that for the case of the magnetic susceptibility the values obtained for the different lattice spacings are compatible within statistical errors. Nonetheless, assuming that the lattice spacing dependence depends smoothly on time, we can obtain an extrapolation to the continuum limit lying approximately 5% above the values obtained for the smaller spacing.

With respect to finite size effects, long range quantities are expected to be the most affected. Thus, it is essential to test that the low momentum part of the magnetic power spectrum is not biased by finite volume artifacts. In Fig. 10.4 we present results for $p_{\rm min} = 0.125\, m$ and $0.15\, m$. The agreement is very good for the ratio $m_{\rm H}/m_{\rm W} = 3$ and preserves the same quality for the

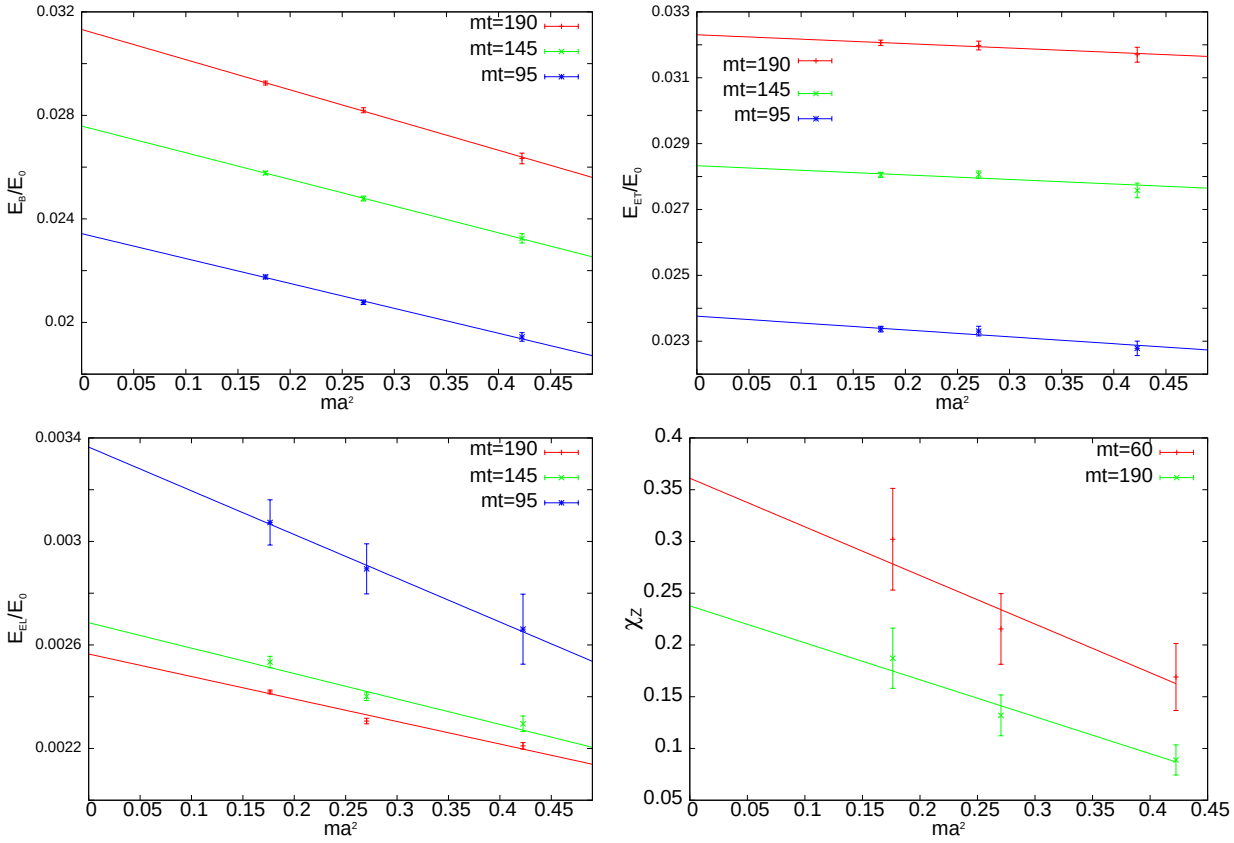

Figure 10.3: Continuum extrapolation of the magnetic, transverse electric, longitudinal electric and Z-boson susceptibility. For $m_{\rm H} = 2m_{\rm W}$ and $mt = 95$, 145, 190, and $mt = 60$, 190 for the susceptibility.

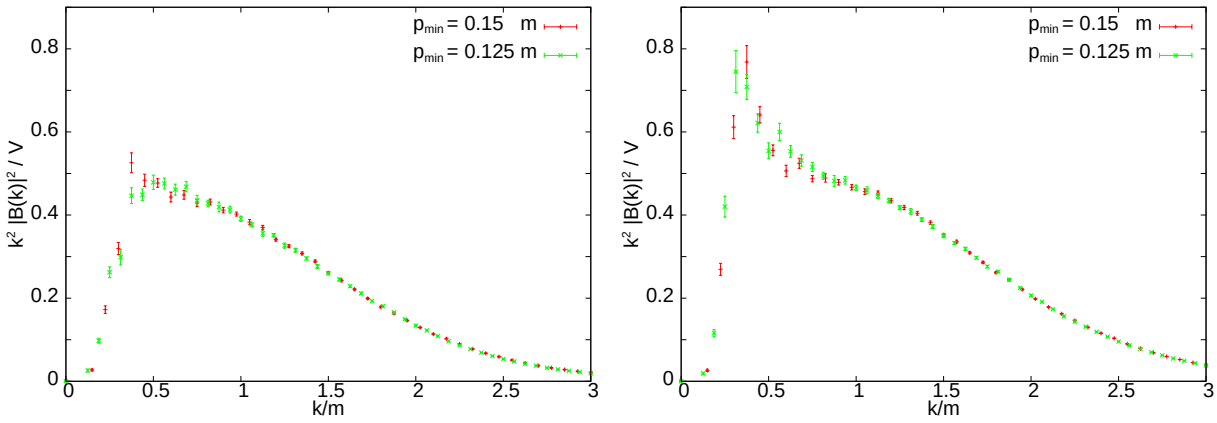

Figure 10.4: We plot $\langle k^2|B(k)|^2\rangle/\mathcal{V}$ vs k for the magnetic component of the electromagnetic energy. A comparison is made between results at $p_{\rm min} = 0.125\,m$ and $p_{\rm min} = 0.15\,m$. Results are presented at $mt = 105$ (Left) and 265 (Right). For $m_{\rm H} = 3m_{\rm W}$ and $ma = 0.52$.

other 2 values of the $m_{\rm H}$ to $m_{\rm W}$ mass ratios that we have studied.

10.2 The Higgs to W boson mass ratio

Most of the results presented in the previous chapters correspond to a Higgs to W-mass ratio of 3. Qualitatively the picture remains the same for the other two ratios analyzed: $m_{\rm H} = 2\,m_{\rm W}$ and $m_{\rm H} = 4.65\,m_{\rm W}$. In Fig. 10.5 we compare the electromagnetic energy densities and helical susceptibility as a function of time for different values of the ratio $m_{\rm H}/m_{\rm W}$. We have chosen here not to normalize the energy densities to the total one, in order to exhibit the independence of the initial magnitude of the electromagnetic fields and helical susceptibility on the value of Higgs self-coupling λ, which also determines the mass ratio. Other features of the initial configuration such as string lengths and widths are also λ-independent, and depend only on the mass parameter M that fixes the Higgs Gaussian random field (see Appendix D). This λ-independence is preserved in the first Higgs oscillation but lost afterwards, once non-linearities and the presence of the gauge fields modifies the dynamics. At late times equipartition would indicate that the total fraction of energy density carried by the electromagnetic field would again become λ-independent. Since $\rho_0 = m^4/4\lambda$, the fraction of energy densities in units of m^4 should tend to behave as $1/\lambda$ at late times. This is indeed the tendency observed in the data. The late time behavior of the

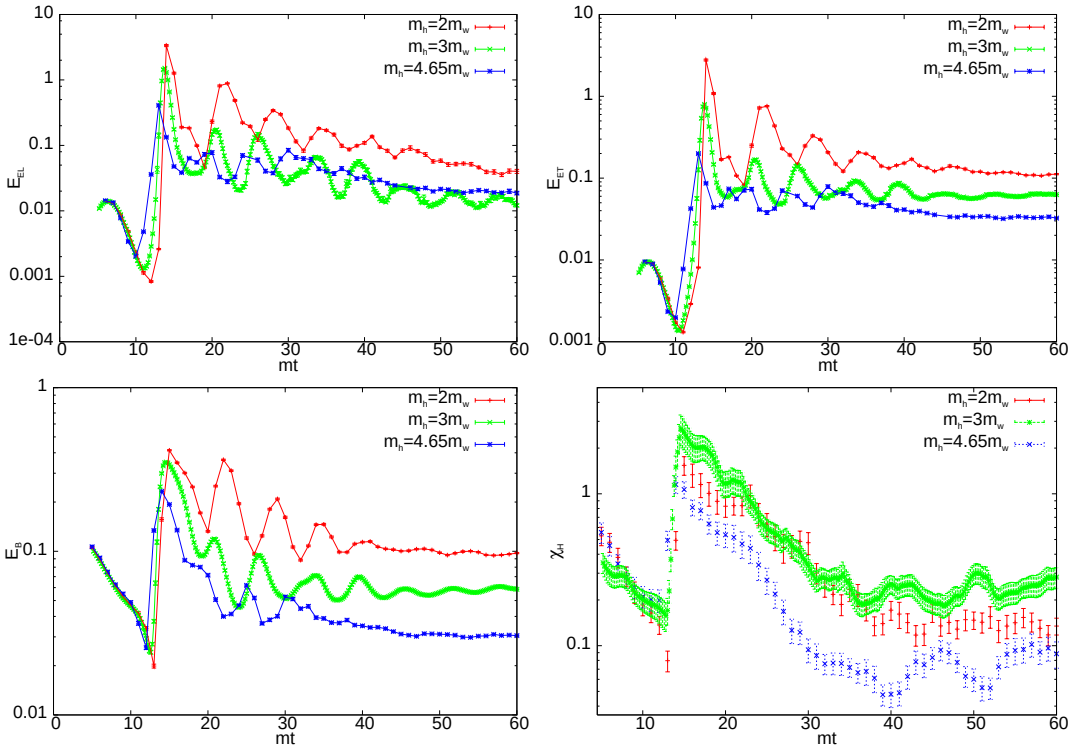

Figure 10.5: Time evolution of the energy densities, in m^4 units, in the: Top Left: longitudinal electric field; Top Right: transverse electric field; Bottom Left: magnetic field. Bottom Right: χ_H in m^3 units. Energy densities are not normalized to the total energy density in order to emphasize λ independence in the initial stages of the evolution.

density energies for all models, is showed in figure 10.6.

Let me discuss at this point two observations. First, some quantities, as the helical susceptibility, do not monotonically depend on the $m_{\rm H}/m_{\rm W}$ ratio. Similar non-monotonic behavior has been found in [115] for the Chern-Simons susceptibility and the CP violation amount. Second, as was pointed out when discussed the choice of Lagrangian parameters (see 6), the ratio $m_{\rm H}/m_{\rm W}$ gives the value of λ, which governs the onset of the SSB. The effect of the change on the mass ratio is basically a shift in the SSB time, as can be observed in figure 8.10 and also in figures 10.5. Nevertheless, the shift does not produce a significant qualitative effect.

Finally, we would like to discuss the quantitative effect of the model choice in the magnetic field seeds. We present here a similar analysis than the one

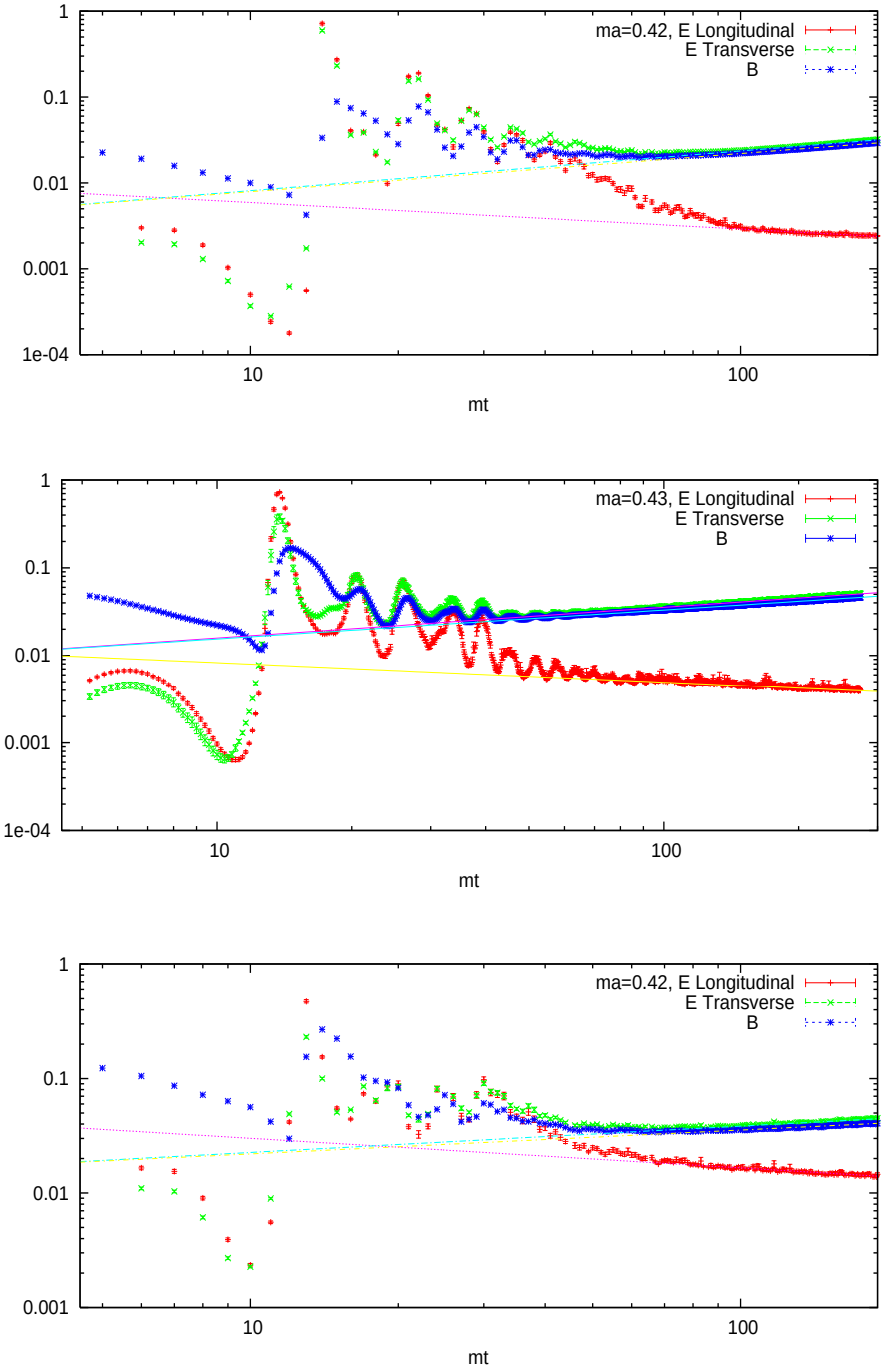

Figure 10.6: We show the time evolution of transverse and longitudinal electric and mag- netic elds averaged over 70 congurations for ma = 0.43. From top to bottom for $m_{\rm H} = 2$, 3 and 4.65 $m_{\rm W}$ The plot is Log-Log and the corresponding slopes are from left to right: Transverse electric field: 0.462(3), 0.350(1) and 0.230(7) ; Magnetic field: 0.444(3), 0.330(1) and 0.208(5); Longitudinal electric field: -0.31(2), -0.224(3) and -0.258(2).

we presented in chapter 9 for model $m_{\rm H} = 3m_{\rm W}$, but in this case for the ratio $m_{\rm H} = 2m_{\rm W}$. We have observed that this choice of mass ratio produces, besides a slightly later onset in the SSB, a delay in the whole evolution. Hence, the evolution seems to follow the one of $m_{\rm H} = 3m_{\rm W}$ but showing a slower trend.

Figure 10.7 presents the spectrum of the magnetic field for the $m_{\rm H} = 2m_{\rm W}$ model. It is also represented the fits analogous to the ones of figure 9.10. It is appreciated how the two-distribution fits nicely reproduce the form of the spectrum. However, the infrared peak present by the data in figure 9.10 is here not clearly established. Nevertheless, the infrared distribution (see (9.7)) presents signals of what could be an incipient peak, specially at times $mt = 225$ and 245, which is developting with time. We conjecture that due to the slower evolution of this model, there were not enough time for these to distributions to separate. We expect that for later times than $mt = 245$, this incipient peak could evolve into a shape similar to the $m_{\rm H} = 3m_{\rm W}$ model one. Actually, a closer look to both figures shows than, the shape of the spectrum at time $mt = 105$ in figure 9.10 is very similar to the shape at $mt = 245$ of figure 10.7.

It is important to note that this weaker separation of the distributions, makes more difficult to perform the fits. This difficulty is reflected in the extraction of the estimators (9.8) and (9.9). Figure 10.8 shows the evolution with time of the energy and the correlation length of the magnetic seeds, calculated from these estimators. The values of the energy fraction stored in the infrared part are slightly higher than the observed in model $m_{\rm H}/m_{\rm H} = 3$, and so is the slope of the fit. The fraction of energy is again order $\sim 10^{-2}$. As in the case of the other model, this correlation length is being enhanced linearly with time. The linear fit is $m\xi_B = 10.8(3) + 0.007(2)mt$. The slope is several times smaller. The systematic errors are slightly bigger since the two-distributions fits have shown to be more sensitive to the change of $p_{\rm min}$ than the ones for the $m_{\rm H}/m_{\rm W} = 3$ ratio. The estimated correlation length is also smaller, being $m\xi_B \sim 12$, that is about a half of the estimated for the other model. Nevertheless this correlation length represents a important fraction of the volume, and is several times greater than the correlation length estimated from the thermal distribution, which is $m\xi_{rad} \sim 5$ for this $m_{\rm H}/m_{\rm W} = 2$ ratio.

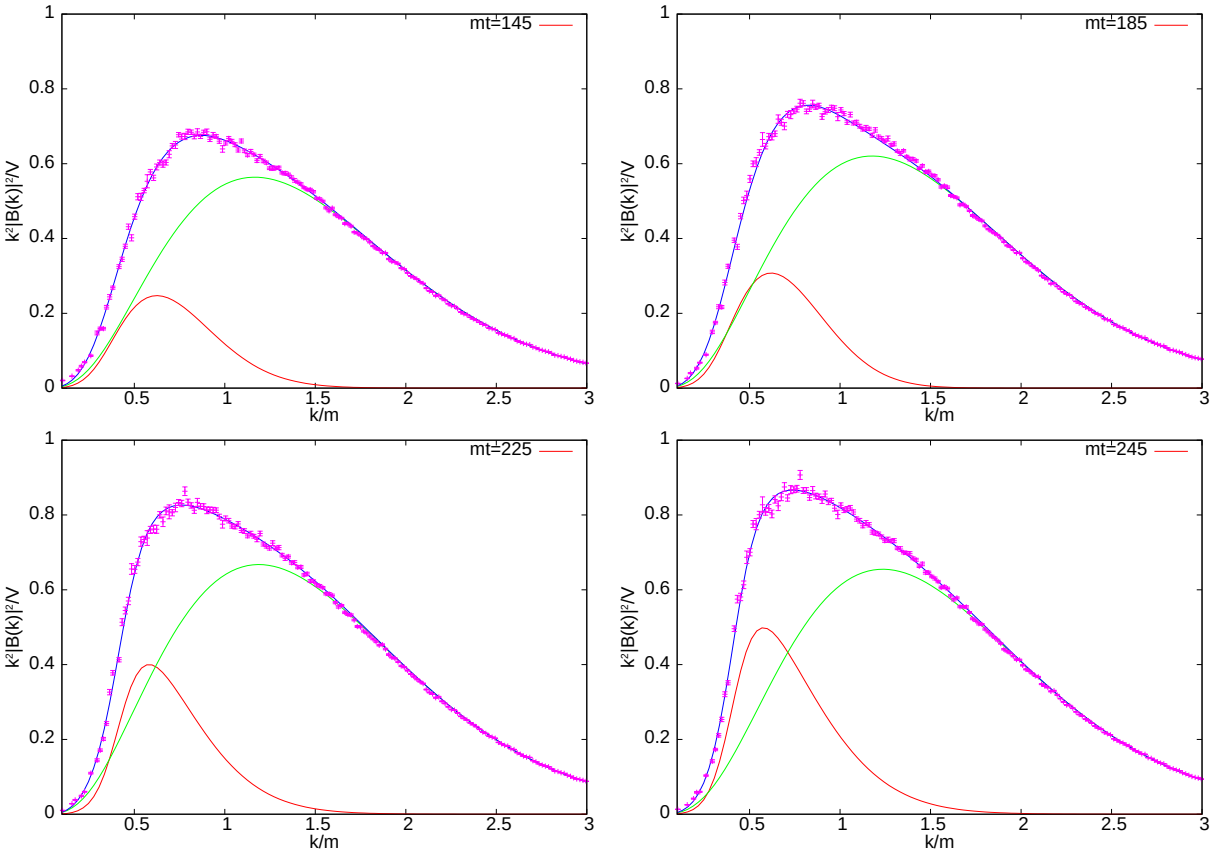

Figure 10.7: We plot $\langle k^2|\vec{B}(k)|^2\rangle/\mathcal{V}$ vs k, averaged over 70 configurations. The lines represent fits to the radiation and seed field electromagnetic components according to Eqs. (9.5), (9.7) respectively. Results are presented at $mt = 145$, 185, 225 and 245. In all cases $m_{\rm H} = 2m_{\rm W}$, $ma = 0.65$ and $p_{\rm min} = 0.1\,m$.

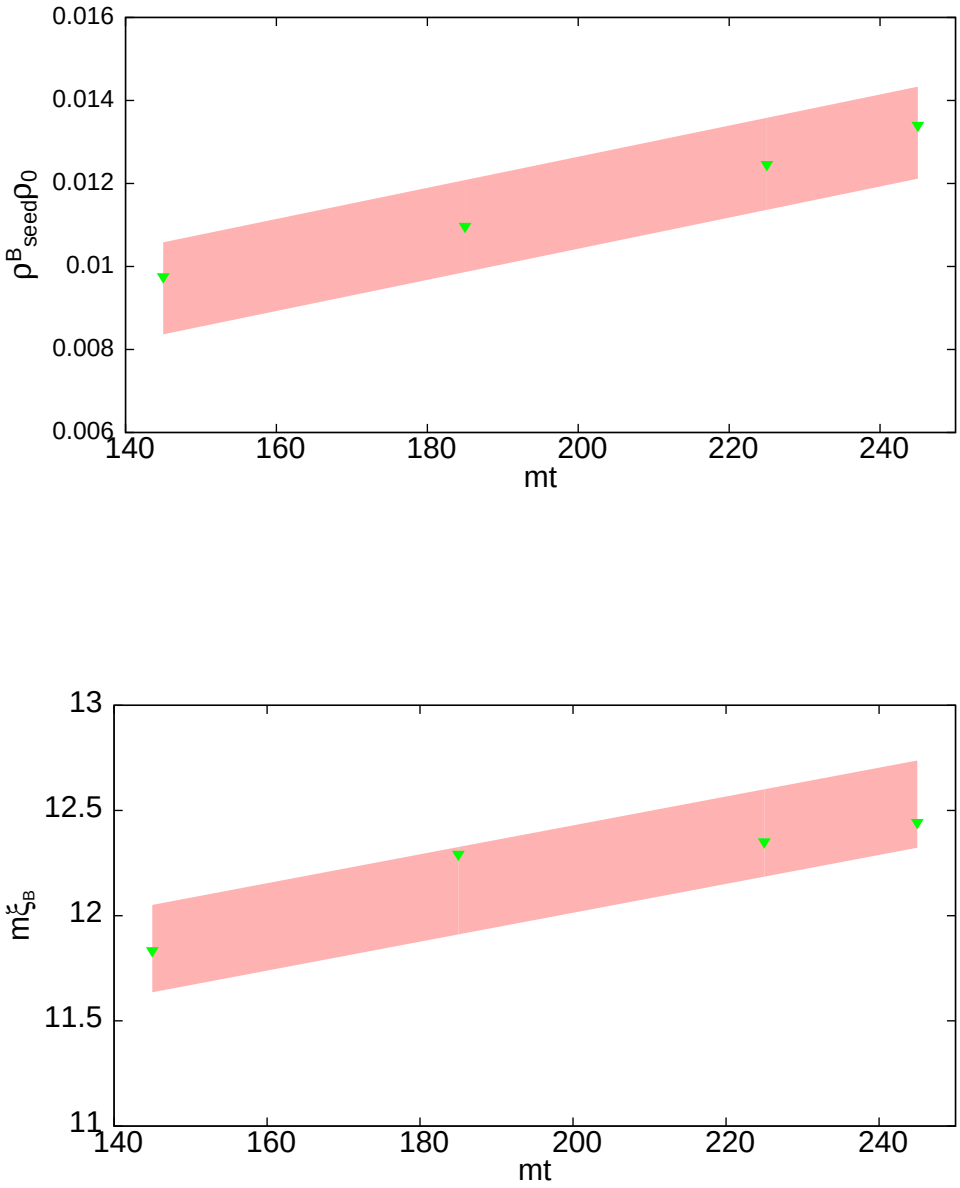

Figure 10.8: We show the time evolution of $\rho^B_{\rm seed}$ (left) and $m\xi_B$ (right), for $m_{\rm H} = 2m_{\rm W}$, $ma = 0.65$. The results are obtained by averaging the values obtained for $p_{\rm min} = 0.15\,m$ and $p_{\rm min} = 0.1\,m$, with bands representing the dispersion in the errors. The fits are $\rho^B_{\rm seed}/\rho_0 = 0.0040(3) + 3.7(2) \times 10^{-5} mt$ and $m\xi_B = 10.8(3) + 0.007(2)mt$ respectively.

Chapter 11

Conclusiones y trabajo futuro.

11.1 Conclusiones.

En la presente tesis hemos analizado la producción de campos magnéticos primordiales en el contexto de la transición Electro-Débil (ED) al final de inflación. Para ello hemos utilizado un modelo de inflación Híbrida de baja energía. Este estudio complementa y extiende los trabajos publicados en [118],[119] y [121]. Para este propósito hemos estudiado, con ayuda de métodos numéricos no perturbativos, una época en el universo temprano caracterizada por ser un periodo de alta inestabilidad y donde llegado el momento, cualquier tratamiento pertubativo es inaplicable. Este periodo es el de "preheating" o precalentamiento después de inflación, y las subsiguientes primeras etapas de recalentamiento que le siguen. Nuestro trabajo también incluye, por primera vez en la literatura, el Modelo Estándar completo, es decir el grupo gauge SU(2)×U(1) entero. Este modelo puede producir una inflación de baja energía de forma muy breve. No necesita los 60 e-folds completos que son necesarios para dar cuenta de las anisotropías de la radiación de fondo (ARF). Todo lo que necesita es un periodo de inflación térmica a la escala ED que enfríe el Universo durante al menos 10 e-folds, y que proporcione las condiciones adecuadas para una transición ED fría. Las fluctuaciones de la métrica responsables de la estructura a gran escala podrían ser producidas en la inflación primordial (a alta energía). Esta etapa secundaria solo produciría un "red-shift" de las escalas por un factor e^{10}, pero es irrelevante para las fluctuaciones que tienen el tamaño del horizonte hoy. Sin embargo es suficiente para diluir todas las especies relativistas y no relativistas que pudieran estar presentes en aquel tiempo. Este escenario, el de inflación híbrida de baja energía con final en la transición ED, fue prop-

uesto en la Ref. [108] en el contexto de bariogénesis y ha sido considerado recientemente en la Ref. [107].

El resultado principal de nuestro trabajo puede ser resumido en las siguientes tres observaciones. Primero, nuestro estudio proporciona una realización concreta del mecanismo propuesto por Vachaspati [68] y Cornwall [72], por el cual inhomogeneidades en las fases del campo de Higgs actúan como fuentes para la generación de campos magneticos y, esto es esencial, con una helicidad no trivial. Hasta donde alcanza nuestro conocimiento, esta es la primera vez que este mecanismo es observado en un contexto no perturbativo. Segundo, estos campos magneticos así generados podrían tener, debido a su "red-shift" hasta hoy, una amplitud del orden de $\sim 0.5\,\mu G$. Esta amplitud es suficiente para explicar los valores de los campos magnéticos observados en clústeres, mientras que para reproducir aquellos producidos en galaxias, necesitaría una pequeña amplificación por medio del mecanismo de dinamo usual. Tercero, hemos encontrado que la longitud de correlación de los campos magnéticos así generados, crece linealmente con el tiempo, al menos en el intervalo de tiempos que se ha analizado. Para $m_{\rm H} = 3m_{\rm W}$ hemos encontrado $m\xi_B \sim 0.03\,mt$, como se muestra en la figura 9.12 (ver también el capítulo 10 para la dependencia con el modelo). Este crecimiento lineal parece estar soportado por la dinámica no trivial del plasma primordial, hecho de bosones W y podría esperarse que continuara hasta el tiempo de decaimiento del Higgs, de los W y del Z en fermiones ligeros. Nuestra aproximación no permite extrapolar estos resultados a tiempos posteriores en la evolución. Sin embargo, la naturaleza helical de los campos magnéticos generados, garantiza que el efecto del plasma primordial sea el de preservar o incluso amplificar la magnitud de la helicidad y la longitud de correlación de los campos magnéticos [58]- [62].

Hemos distinguido tres etapas differentes en la evolución después del fin the inflación: La etapa de crecimiento taquiónico de los modos de Fourier del campo de Higgs, el periodo de ruptura de simetría (SSB) y la evolución tardía después de SSB. En lo siguiente presentamos un sumario de las principales características de cada una de estas etapas.

Durante la primera etapa taquiónica, las no linealidades en el potencial del Higgs así como los campos gauge pueden ser despreciados haciendo que la evolución cuántica completa del sistema pueda ser resuelta. Las fluctuaciones cuánticas de los modos infrarojos del campo de Higgs son descritos por medio de un campo aleatorio Gaussiano de componentes múltiples. Como es descrito en detalle en el capítulo 8, los campos magnéticos están ya presentes en esta época, presentando una susceptibilidad helical no trivial, y

directamente relacionada con la susceptibilidad de número de "winding" del campo de Higgs como una variable aleatoria Gaussiana. A pesar de que los campos gauge de SU(2) y de U(1) son muy pequeños al final de inflación, los campos magnéticos surgen a través de las inhomogeneidades de las fases del Higgs, corroborando por tanto la conjetura de Vachaspati. A lo largo de este periodo, la distribución espacial de los campos magnéticos está determinada por la del campo de Higgs, una característica ésta que es mantenida e incluso amplificada en la segunda etapa de la evolución correspondiente a la ruptura de simetría.

El periodo de SSB se realiza a través de la formación de burbujas en la estructura espacial de la norma del campo de Higgs, que se expanden y colisionan entre ellas. El campo magnético en este periodo es confinado por la expansión de estas burbujas en estrechas estructuras filamentosas localizadas en las regiones entre burbujas (ver la figura 8.12). Esta estructura filamentosa es reproducida tanto en la densidad de helicidad como en la componente magnética de la densidad de campo del bosón Z. Hemos estimado la longitud característica de separación entre filamentos en este periodo, que ha resultado ser del orden de $m_{\rm H} l \sim 14$. Unida a la aparición de filamentos magnéticos hemos encontrado una distribución no trivial de campo eléctrico, acompañada de una distribución de carga asociada a los bosones W y de densidad de corriente. Es importante resaltar, que hemos comprobado la existencia de grandes clústeres cargados que siguen exactamente la posición de los filamentos magnéticos. Esta separación de cargas diferentes induce campos eléctricos en el plasma. Hemos observado también que tanto las componentes transversas como las longitudinales de los campos eléctricos están fuertemente correlacionadas con las posiciones de los filamentos magnéticos. Los clústeres de carga persisten en el sistema durante un largo periodo de tiempo, y como consecuencia, observamos un apantallamiento muy lento de la componente longitudinal de la energía eléctrica en el sistema (ver figura 9.2). Conjeturamos que estos campos eléctricos serán eliminados del sistema tan pronto como el plasma de bosones W decaiga en fermiones ligeros que viajen a velocidades próximas a la de la luz, los cúales podrían neutralizar el plasma más rápidamente que los pesados bosones W. Estimamos que los primeros fermiones aparecerían en nuestro sistema a tiempos $mt \sim 1000$, mientras que el tiempo máximo que hemos alcanzado en nuestras simulaciones ha sido $mt \sim 300$.

La tercera etapa de la evolución, despues de la SSB, está caracterizada por una lenta búsqueda de la termalización. Para poder hablar de un mecanismo apropiado para una magnetogénesis, tiene que garantizarse

que la semilla magnética helical generada inicialmente no es eliminada con el tiempo. Hemos mostrado en el capítulo 9, que la magnitud de la susceptibilidad helical crece con el tiempo con una ley de potencia, $\chi_H \propto t^{\alpha}$, con $\alpha = 0.7(1)$, $0.8(1)$ y $0.3(1)$ para $m_{\rm H}/m_{\rm W} = 2, 3, 4.65$ respectivamente. Al mismo tiempo la susceptibilidad helical del boson Z decae, también con una ley de potencia con el tiempo. Hemos observado también que la magnitud de la susceptibilidad helical de los campos magnéticos generados no depende monótonamente de la relación entre la masa del Higgs y la del bosón W. De los valores de esta razón analizados, $m_{\rm H} = 3m_{\rm W}$ ha resultado ser el que genera una susceptibilidad mayor.

A lo largo del periodo de evolución completo que hemos estudidado, hemos encontrado que estamos muy lejos de las aproximaciones magnetohidrodinámicas (MHD) no relativistas más sencillas. Esta aseveración es soportada por las siguientes observaciones: Primero, el término $\partial_0 \vec{E}$, ha mostrado ser comparable al término $\vec{\nabla} \times \vec{B}$, de manera que no puede ser despreciado frente a éste. La omisión de este término está en el núcleo de la aproximación MHD no relativista, como puede verse en el cápitulo 7. Segundo, la densidad de carga ha resultado ser muy alta en las regiones donde surgen los clústeres separados de carga. Esta densidad de carga elevada no puede ser despreciada frente a la fuerza de Lorentz en esos lugares. La densidad de carga entonces, tiene que entrar en las ecuaciones de alguna manera, a diferencia de en la aproximación MHD estándar, donde los efectos de la densidad de carga son despreciados. Claramente una extensión de la MHD es necesaria si se pretende dar una descripción no sólamente númerica del comportamiento del sistema. Sin embargo, el propio sistema tiende lentamente a eliminar tanto los términos altos de $\partial_0 \vec{E}$ como las zonas de clústeres de carga. Esto junto con la conjetura de que serán eliminados totalmente con la entrada de los fermiones ligeros en escena, hacen viable la posibilidad de usar nuestros resultados como inicio de una simulación en el marco de la MHD resistiva.

Con la intención de extraer el comportamiento para tiempos grandes de la amplitud y la longitud de correlación de la semilla magnética, hemos desarrollado un análisis detallado del espectro de momentos para el modelo $m_{\rm H} = 3m_{\rm W}$. Este espectro magnético ha mostrado poseer dos componentes no correlacionadas y muy diferentes entre sí: un sector de radiación ultravioleta y un pico infrarrojo cuya amplitud crece con el tiempo (ver figura 9.10). La cola de radiación es perfectamente reproducida por una distribución de Bose-Einstein de fotones masivos, con un potencial químico no trivial, y a una temperatura que es del orden de $T \sim 0.23 m_{\rm H}$. Esta temperatura está

creciendo con el tiempo. La parte de momentos bajos del espectro almacena una fracción $f \sim 10^{-2}$ de la densidad total de energía. Como ha sido mencionado, tanto su magnitud como su longitud de correlación están creciendo linealmente con el tiempo en el intervalo de tiempos analizados, mostrando indicaciones de la presencia de un mecanismo de cascada inversa hacia el infrarojo. Sin embargo, nuestras escalas de tiempo no son lo suficientemente grandes para demostrar que esta cascada inversa es sostenida a tiempos incluso mayores cuando el plasma cambia significativamente. Por el momento, podemos sin embargo basarnos en los resultados obtenidos en las referencias [58]- [62] que muestran que los campos helicales son óptimamente amplificados por la evolución MHD. Este mismo estudio ha sido realizado también para el modelo $m_{\rm W} = 2m_{\rm W}$. Aunque la separación entre componentes del espectro es menos evidente en ese caso, se han podido extraer estimaciones para las cantidades de interés, mostrando una fracción de energía en los momentos bajos similar al otro modelo. Tanto la longitud de correlación como la pendiente de su crecimiento con el tiempo han resultado menores, siendo la primera del orden de $m_{\rm H}\xi \sim 17$.

También hemos observado en este último periodo de la evolución, algunas evidencias de turbulencia y cascada ultravioleta en el sector escalar. También en el espectro de energía SU(2) se han encontrado señales de estos procesos, representadas por el comportamiento auto similar de este espectro. Esto aunque no se ha estudiado en profundidad, puede dar lugar a futuros estudios. Recientemente, durante el proceso de escritura de esta tesis, Berges et al. [131] han presentado un interesante estudio relacionado con este tema.

Resumiendo, el proceso de precalentamiento híbrido a la escala ED puede ser responsable de los campos magnéticos observados asociados con grandes estructuras como las galaxias o cúlsteres de galaxias. Tanto la magnitud como la longitud de correlación de estos campos podían ser derivados de la evolución altamente no lineal y no perturbativa que viene después de la ruptura de simetría electrodébil. Nuestro análisis proporciona una realización concreta del mecanismo propuesto por Vachaspati y Cornwall varios años atrás. Este plasma primordial entra en un régimen en el que las líneas de campo magnético experimentan un proceso de cascada inversa hacia escalas espaciales mayores. Hemos observado como tanto la densidad de energía como la longitud de correlación magnéticas crecen linealmente con el tiempo. El mostrar que estos campos magnéticos evolucionan como se describe en la introducción, hasta la época del desacoplo de los fotones, requeriría un seguimiento detallado con simulaciones MHD cuyas condiciones iniciales podrían venir dadas por los resultados encontrados en este trabajo.

Este resultado de una longitud de correlacion creciente con el tiempo, soportaría nuestra proposición de que los campos magnéticos helicales producidos en una transición ED fría son responsables de los campos observados en galaxias y clústeres de galaxias.

11.2 Trabajo futuro.

La rica fenomenología encontrada en el presente estudio, junto con las dificultades técnicas, nos ha forzado a seleccionar y descartar para el estudio inmediato ciertos aspectos del sistema que, a priori, se han mostrado como interesantes. Esto proporciona una fuente de trabajo futuro que puede ser realizado a corto o medio plazo. A modo de resumen me gustaría resaltar algunos de estos aspectos que o están en proceso de estudio o proyectados para un futuro cercano:

- Una obtención más clara de la semilla magnética para el modelo $2m_{\mathrm{W}}$. Esperamos un análisis con menores errores si se consigue llevar la simulación a tiempos más grandes, donde se permita una separación más clara entre las componentes del espectro.

- Un estudio más profundo de la turbulencia, y la dependencia de los parámetros que gobiernan esta turbulencia con el modelo.

- Un tratamiento detallado del plasma primordial. Varios intentos sobre esta línea se han llevado a cabo a lo largo del desarrollo de esta tesis. El más exitoso ha sido el estudio de los procesos disipativos tomando como punto de partida configuraciones de nuestro sistema. No obstante este tipo de estudios no han sido del todo completos, porque fueron realizados en el contexto de la MHD resistiva no relativista, que ha demostrado ser una descripción poco aplicable a nuestro sistema, al menos a tiempos cortos. Aparte de esto, se han realizado varios intentos para la extración de información sobre la naturaleza del plasma primordial, como la conductividad o la permeabilidad magnética. Todos ellos han apuntado en la misma dirección: es necesario el uso de modelos extendidos para la descripción del fluído, así como relaciones de clausura mucho más sofisticadas, en vez de las ecuaciones del plasma en MHD no relativista. El estudio de descripciones más ricas con la inclusión de los efectos relativistas y de las densidades de carga puede merecer la pena en este sentido.

- Como hemos dicho más arriba, conjeturamos que en algún tiempo entre el final de nuestras simulaciones y el decaimiento de los bosones W, el límite MHD puede ser recuperado. Podría ser interesante entonces realizar simulaciones MHD con nuestro sistema como punto de partida. En esta línea, se está trabajando actualmente. Una vez el sub-sistema Higgs-Inflatón ha mostrado ejercer una muy pequeña influencia en el resto del sistema para las últimas etapas de la evolución, la evolución clásica completa con todos los grados de libertad gauge, puede ser reducida a una simulación con partículas cargadas interaccionando a través de la fuerza de Lorentz. Este tipo de simulaciones han presentado resultados muy interesantes en el estudio de los campos magnéticos cosmológicos [132].

- Varios estudios importantes sobre la creación de bosones W y su número de ocupación fueron realizados en la aproximacion "quenched" de la transición ED fría [115]. Esta aproximación "quenched" pierde la rica fenomenología que aparece en el proceso de la transición de fase, encontrada en el presente estudio. Además la posible influencia de los campos de Hipercarga no es tenida en cuenta. Es por esto que podría resultar interesante un nuevo estudio de estas propiedades de los bosones W en el contexto presentado en esta tesis. De hecho se está trabajando ya en esta línea.

- Una característica importante del estudio presentado aquí, es que algunas de las propiedades del sistema están presentes y son producidas por la configuración inicial del Higgs, dada por la condición de campo aleatorio Gaussiano. En las referencias [127]-[130], se presentan estudios detallados sobre los fenómenos que se aparecen en los campos aleatorios Gaussianos de una sola componente, así como sus aplicaciones fenomenológicas, como es la formación de estructura en el Universo temprano. En nuestro sistema, podría suceder que cantidades como la longitudes de correlación magnéticas, estuvieran relacionadas con propiedades del campo aleatorio Gaussiano, que en nuestro caso tiene varias componentes. Un análisis más detallado sobre los campos aleatorios Gaussianos multi-componente, en el contexto de la evolución clásica con campos gauge, podría resultar esclarecedor a este respecto.

- Como se explica en el capítulo 8, la relación entre los campos magnéticos y las corrientes presentes en el sistema parece ser bastante complicada. Nuestro presente estudio sólo explora ligeramente este fenómeno. Un

análisis más detallado con una mayor resolución espacial, o un modelo teórico para la distribución de corrientas, podría realizarse en el futuro, una vez que los primeros pasos en este sentido se han dado en este trabajo.

- La relación encontrada en este trabajo, entre la generación de tubos de flujo magnético y las zonas donde el campo de Higgs es mínimo, junto con la presencia a lo largo de estos tubos de una densidad de helicidad no trivial, sugiere una interesante interpretación física para este proceso. Trabajos anteriores han mostrado que configuraciones tipo esfalerón están presentes en las zonas donde el campo de Higgs presenta valores mínimos. Este hecho y el hecho de que los esfalerones se comportan como dipolos magnéticos para ángulos de Weinberg distintos de cero, hacen que sea tentador proponer estas configuraciones tipo esfalerón como los causantes de la generación de los campos magnéticos. El alineamiento de estos dipolos podría incluso explicar la gran correlación del campo en los tubos. Por supuesto, esto es sólo una tentadora suposición. Su prueba requiere de una futura investigación. No obstante, durante el proceso de escritura de esta tésis, ha sido publicado un interesante trabajo de C. J. Copi et al. [124], en el cuál se muestra como el proceso de decaimiento de los esfalerones produce la generación de campos magnéticos helicales. Este resultado parece dar fuerza a nuestras suposiciones.

Chapter 12

Conclusions and future work.

12.1 Conclusions

In this thesis we have analyzed the production of primordial magnetic fields in a model of low-scale EW hybrid inflation. It complements and extends the work published in [118],[119] and [121]. For that purpose we have studied, with the help of lattice non-perturbative techniques, the preheating and early reheating stages after the end of a inflationary period. Our work includes, for the first time, the full Standard Model, SU(2) $\times$ U(1), gauge degrees of freedom. The period of low-scale inflation which sets the initial conditions of our work could be brief. We do not need the full 60 e-folds that are necessary to account for the CMB anisotropies. All that is needed is a period of thermal inflation at the EW scale which would cool down the universe during at least 10 e-folds, and set the stage for a cold (quantum) EW transition. The metric fluctuations responsible for large scale structure could be produced at the primordial (high energy scale) inflation. This secondary stage only redshifts scales by another e^{10} factor, but is irrelevant for horizon size fluctuations today, while is enough to erase all relativistic and non-relativistic species. This scenario was first proposed in Ref. [108] and has recently been considered in Ref. [107].

The main results of our work can be summarized in the following three observations. First, this set up provides a concrete realization of the mechanism proposed by Vachaspati [68] and Cornwall [72], by which inhomogeneities of the Higgs field phases act as sources for the generation of magnetic fields and − this is essential − with non-trivial helicity. To the best of our knowledge this is the first time that this mechanism has been observed in a fully non-perturbative set-up. Second, the generated magnetic field would have, when

red-shifted until today, an amplitude of $\sim 0.5\,\mu$G. This is enough to explain the values of magnetic fields observed in clusters, while those in galaxies would require a small amount of enhancement via the usual dynamo mechanism. Third, the correlation length of the generated magnetic field grows linearly with time within the time span we have analyzed. For $m_{\rm H} = 3m_{\rm W}$ we find $m\xi_B \sim 0.03\,mt$, as shown in Fig. 9.12 (see also chapter 10 for the model dependence). This linear growth seems to be sustained by the non-trivial dynamics of the plasma made of W-bosons and could be expected to hold until the decay of the Higgs, the W and the Z bosons into light fermions. Our approach does not allow us to extrapolate these results from then onwards. Nevertheless, the helical nature of the generated magnetic field warrants that the effect of the primordial plasma would be that of preserving and even amplifying the magnitude of the helicity and the magnetic field correlation length [58]- [62].

We have distinguished three different stages in the evolution after inflation ends: tachyonic growth of the Higgs-field low momentum modes, symmetry breaking and late time evolution after SSB. In what follows we will summarize the main features characterizing each of these stages.

During the first tachyonic stage, non-linearities in the Higgs potential and gauge fields can be neglected and the quantum evolution of the system can be exactly solved. Quantum fluctuations of the Higgs-field infrared modes are described by a multi-component Gaussian random field. As described in detail in chapter 8, magnetic fields are already present at this stage with a non-trivial helical susceptibility directly related to the winding number susceptibility of the Higgs as a Gaussian random field. Although SU(2)$\otimes$ U(1) gauge fields are very small at the end of inflation, the magnetic fields arise through the presence of inhomogeneities in the Higgs field phase, thus corroborating Vachaspati's conjecture. Along this period, the spatial distribution of the magnetic field is determined by that of the Higgs field, a feature that is maintained and even enhanced during the second stage of evolution corresponding to symmetry breaking.

The period of SSB arises via the formation of bubbles in the Higgs field norm that expand with time and collide with each other. Magnetic fields are squeezed by the expansion in string-like structures localized in the regions between bubbles (see Fig. 8.12). This stringy structure is reproduced both in the helicity density and in the Z boson magnetic field density. We have estimated a characteristic string separation during this period of $m_{\rm H} l \sim 14$. Linked to the appearance of the magnetic strings we find a non trivial distribution of electric fields and W-boson charge and current densities. Most

remarkably, we see a very non-trivial distribution of the charge density with the formation of extended charged clusters which track the position of the magnetic string. This separation of unequal charges induces electric fields in the plasma. We observe both transverse and longitudinal electric fields also correlated with the string locations. The clusters persist for a very long time and, as a consequence, we observe a very slow screening of the longitudinal electric field with time, see Fig. 9.2. We conjecture that these electric fields will be erased as soon as the plasma of W-bosons decays into light fermions moving close to the speed of light, which will neutralize much faster than the heavy W-charges. We estimate the production of fermions to be at $mt \sim 1000$, whereas the maximum times of our simulations are $mt \sim 300$.

The third stage of evolution after SSB is characterized by a very slow approach to thermalization. To claim a feasible mechanism for magnetogenesis we have to guarantee that the initial helical magnetic seed is not removed with time. We have shown in chapter 9 that the magnitude of the helical susceptibility grows with time with a power-law behaviour, $\chi_H \propto t^\alpha$, with $\alpha = 0.7(1)$, $0.8(1)$ and $0.3(1)$ for $m_{\rm H}/m_{\rm W} = 2$, 3, 4.65 respectively. At the same time the Z-boson helical susceptibility decays also with a power law dependence with time. We have observed that the magnitude of the generated magnetic susceptibility does not depend monotonically on the Higgs- to W-mass ratio. Of the values we have analyzed, $m_{\rm H}/m_{\rm W} = 3$ is the one that generates larger helical fields.

Along the period of evolution we have analyzed, the system is quite far away from usual MHD approaches. This statement is supported by the following observations: First, the term $\partial_0 \vec{E}$ is comparable to the term $\vec{\nabla} \times \vec{B}$, so it can not be neglected. The omission of this term is in the core of the MHD approach, as can be seen in chapter 7. Second, there is a non-negligible charge density in the regions where the separated charge clusters arise. This high charge density can not be neglected compared with the Lorentz's force in those places. As a consequence, the charge density must enter the equations somehow, in contrast with the standard MHD where the charge density effects are neglected. An extension of the MHD is thus needed in order to give an non-numerical description of the behavior of the system. Nevertheless, the system slowly tends to remove both the high $\partial_0 \vec{E}$ and the charge clusters. This together with the conjecture than they will be further erased in the presence of light fermions, points to the possibility to use our results as a initial setting for a resistive MHD code.

In order to extract the late time behaviour of the amplitude and correlation length of the magnetic field seed, we have performed a detailed analysis of

the Fourier spectrum of the magnetic field energy for the $m_{\rm H}/m_{\rm W} = 3$ model. It shows two well differentiated and uncorrelated components: an ultraviolet radiation sector and an infrared peak whose amplitude increases with time (see Fig. 9.10). The radiation tail, is well described by a Bose-Einstein distribution of massive photons, with a non-trivial chemical potential, and at temperature $T \sim 0.23\, m_{\rm H}$. This temperature is slowly rising with time. The low momentum part of the spectrum carries a fraction $f \sim 10^{-2}$ of the total energy density. As mentioned before, both its amplitude as its correlation length are linearly growing with time within the analyzed time span, showing indications of an inverse cascade towards the infrared. However, our time scales are not long enough to demonstrate that inverse cascade will be sustained at even later times when the composition of the plasma changes significantly. For the moment we can, nevertheless, rely on the results in Refs. [58]- [62] which show that helical fields are optimally amplified by MHD evolution. A similar study has been performed for model $m_{\rm H}/m_{\rm W} = 2$. Although the separation between different components in the spectrum is less obvious, it has been possible to estimate the quantities of interest, showing a similar faction of energy stored in the infrared momentum than the one of the other model. Both the correlation length and the slope of its fit with time are smaller, being the former about ~ 12.

We have also observed in this last period some evidence of turbulence and ultraviolet cascade in the scalar sector. We also found signs of turbulence in the $SU(2)$ energy spectrum, which exhibits a self-similar behavior firstly observed in this work. This issue clearly deserves further investigation. Recentely, during the writing process of this thesis, an interesting and related work has been presented by J. Berges et al. [131].

In summary, hybrid preheating at the EW scale could be responsible for the observed magnetic fields associated with large scale structures like galaxies and clusters of galaxies. Both the magnitude and correlation length could be derived from the highly non-linear and non-perturbative evolution after EW symmetry breaking. Our analysis provides a concrete realization of the mechanism proposed by Vachaspati and Cornwall many years ago. This primordial plasma enters a regime in which helical magnetic field lines experience an inverse cascade towards larger scales. We observe how both their energy density and correlation length grow linearly with time. Showing that these magnetic fields evolve, as described in the introduction, until photon decoupling, would require a detailed follow up with MHD simulations whose initial conditions are provided by our work. The observed enhancement of the magnetic correlation length with time, would support our proposal that

the helical magnetic fields produced at the cold EW transition are responsible for the observed magnetic fields in galaxies and clusters of galaxies.

12.2 Future Work.

The rich phenomenology encountered in this work, together with the technical difficulties, has forced us not to address certain aspects of the system that, a priory, have shown to be of interest. This provides a source of interesting work to be developed in the near future. As an outline, I would like to point out some of the aspects that are now work in process or projected for future studies:

- A better isolation of the magnetic seed signal for the model $m_{\rm H} = 2m_{\rm W}$. We expect an analysis with smaller errors could be performed in this model, if the simulation is extended to times late enough to allow a clearer separation of the spectrum.

- A deeper study of turbulence, and the dependence of the parameters that drive this turbulence on the model.

- A detailed treatment of the primordial plasma. Several attempts have been performed along the development of this thesis in that line. The most successful one was the study of the dissipative processes with our configurations as starting points. They were however incomplete, since they were performed within the resistive MHD scenario, that has resulted of no applicability in our context, at least at early times. We also performed several attempts to extract information about the plasma nature, like the conductivity or the magnetic permeability. All of them point to the fact that extended fluid models as well as more sophisticated closure relations are needed instead of the MHD plasma equations. Richer descriptions as Hall MHD, drift ordering and transport models could deserve further study.

- As mentioned before, we conjecture that at some point between the last time reached by our simulations and the time of W decay, the MHD limit could be recovered. It would hence be interesting to perform MHD simulations with our system as initial condition. We are at the moment performing some work along this line. Once the Higgs-Inflaton system has showed to have null influence in the system at late times, the full classical evolution of gauge fields, can be reduced to a simulation

of charged particles interacting with the Lorentz force. This kind of simulations have given rise to interesting results in the study of cosmic magnetic fields [132].

- Several relevant studies of the creation and occupation numbers of W bosons have been performed in the "quenched" cold electroweak transition [115]. The "quenched" approach looses the rich phenomenology appearing at the phase transition, which has been found in this work. Also the possible effects of the Hypercharge fields are not taken into account in those studies. It would be interesting to perform a new study of the properties of W bosons in the context presented in this thesis. Some work is being done along this line.

- An important feature of the study presented here, is that some of the properties of the system are driven by the Gaussian random field distribution describing the Higgs field at the end of inflation. References [127]-[130], present a detailed study of one dimensional Gaussian random fields, and their phenomenological applications for processes as structure formation in the early Universe. In our system, it could happen that quantities as the magnetic correlation length, were related with the features of the multi-component Gaussian random field. Further analysis along this line could be interesting.

- As explained in chapter 8, the magnetic-current relationship appears to be quite complicated. Our present work has only studied very slightly this phenomenon. A better analysis with higher spatial resolution, or a theoretical model to explain the distribution of currents, would be desirable.

- The relationship found in this work, between the generation of magnetic flux tubes and the locus of Higgs minima, together with the presence of non trivial helicity along these tubes, suggests an interesting physical interpretation for this process. Previous works showed that sphaleron-like configurations were present in places where the Higgs field was closer to a minimum. Given the fact that sphalerons behave as magnetic dipoles for a non-zero Weinberg angle, it is tempting to conjecture that the sphaleron-like magnetic dipoles are responsible for the magnetic field creation. Their alignment could also explain the magnetic field long flux tubes. Of course, this is only a plausible conjecture, its verification requires further investigation. During the writting pro-

cess of this thesis, an interesting work of C. J. Copi et al. [124] has been published. It discusses how the sphaleron decay generates helical magnetic fields. This result seems to hint in the same direction as our conjectures.

Chapter 13

Agradecimientos.

Primero y sobre todo, quería dar las gracias a mi directora de tesis, Margarita García Pérez, por su ayuda, sus consejos y discusiones, y su paciencia sin límite. De esto último hablo con conocimiento, pues estoy seguro de que la he puesto a prueba en no pocas ocasiones. También por sus ánimos en los momentos más difíciles. En definitiva, gracias por todo.

Quiero tambíen agradecer muy especialmente a mi codirector, el profesor Antonio González-Arroyo, por su cercanía y por toda la ayuda científica y personal que me han dado durante estos años. Una especial mención merece también, el profesor Juan García-Bellido, por todos sus consejos y ayuda.

Me gustaría darle las gracias al profesor Jan Smit por darme la oportunidad de visitar por unos meses la Universidad de Amsterdam, donde pase un tiempo muy productivo y agradable. Quiero agradecerle también sus consejos e interesantes discusiones. Además quiero agradecerle a él y al centro de computación Sara la opurtunidad de usar sus recursos computacionales.

Quiero también dar las gracias al profesor Herbert Neuberger por permitirme visitar Rutgers University durante un par de meses, de los que tengo muy buenos recuerdos. Me gustaría también agradecerle sus comentarios y consejos.

Gracias a mis compañeros y amigos durante todos estos años, especialmente a Carlos, Fermín, Alberto, Alfonso, Eduardo y Ambite, por su ayuda, apoyo y esas acaloradas discusiones, durante horas, sobre física.

Por último quiero agradecer a mis padres y hermanas todo su apoyo, y especialmente a Gloria, por sus ánimos, por su paciencia, y por todos los fines de semana de tesis.

Chapter 14

Acknowledgments.

First and foremost, I would like to thank my supervisor Margarita García Pérez, for her help, her advise and discussions, and for her unlimited patience. Also for her support in the difficult times. Thanks for all!.

I want to thank my co-supervisor professor Antonio González-Arroyo for his useful discussions, experience and the help provided me along these years. A special mention is for professor Juan García-Bellido for his useful advise and help.

I would also like to thank Professor Jan Smit for his useful discussions and advises, and for the opportunity he brought me to spend some months at the University van Amsterdam, where I had a very productive and also good time. I also want to thank him and the Dutch super computing center Sara for letting me use their computational resources. I want to thank Professor Herbert Neuberger for bringing me the opportunity to stay for some months at Rutgers University. I had a great time there. I want to thank also his useful advice and discussions.

Thanks to all my friends, specially to Carlos, Fermin, Alberto, Alfonso, Eduardo and Ambite, for their help, support and those very long discussions about physics.

Finally, I want to thank my parents and sisters all their support, and specially Gloria, for her support, patience and for all the thesis-weekends.

Appendix A

The Lattice Equations of Motion

To solve the classical equations of motion we discretize them on a lattice preserving full gauge invariance. In this appendix we introduce the lattice formalism for our particular problem and write the lattice classical equations of motion.

As usual the lattice points are labeled as a vector of integers $n = (n_0, \mathbf{n})$, that in the continuum limit leads to $x = (a_t n_0, a\mathbf{n})$, where a_t and a are the temporal and spatial lattice spacings related by $\kappa = a_t/a$. We construct the adimensional lattice scalar fields from the continuum ones in the form: $\Phi(\mathbf{n})_L = a\Phi(\mathbf{x}/a)$ and $\chi(\mathbf{n})_L = a\chi(\mathbf{x}/a)$. In what follows we will omit the subscript L, since all fields will be lattice fields unless explicitly indicated.

We use a matrix notation for the Higgs field $\Phi = \phi^0 \mathbb{I} + i\phi^i \tau_i$, where the τ_i are Pauli matrices. The Standard Model Higgs doublet is obtained trough the projection: $\varphi = \Phi(1,0)^T$. In this notation the usual U(1) hypercharge transformation is implemented by acting on the Φ field with a right multiplication by a diagonal SU(2) matrix:

$$\varphi'(x) = e^{i\alpha(x)}\varphi(x) \longrightarrow \Phi'(x) = \Phi(x)e^{i\alpha(x)\tau_3}\,. \tag{A.1}$$

The complete $SU(2) \otimes U(1)$ gauge transformation then reads:

$$\Phi(n) \to \Omega(n)\Phi(n)\Lambda(n)\,, \tag{A.2}$$

where $\Lambda(n) = \exp(i\alpha(n)\tau_3)$ represents the $U(1)$ transformation and $\Omega(n) = \Omega^0\mathbb{I} + i\Omega^i\tau^i$ the $SU(2)$ one. This leads to the following form for the covariant derivative operator in order to preserve gauge invariance:

$$(D_\mu\Phi)(n) = U_\mu(n)\Phi(n+\hat{\mu})B_\mu(n) - \Phi(n)\,. \tag{A.3}$$

We will also need the adjoint covariant derivative operator:

$$(\bar{D}_\mu \Phi)(n) = U_\mu^\dagger(n-\hat{\mu})\Phi(n-\hat{\mu})B_\mu^\dagger(n-\hat{\mu}) - \Phi(n)\,. \tag{A.4}$$

The SU(2) matrix $U_\mu(n)$ and the diagonal SU(2) matrix $B_\mu(n)$ are the links corresponding to the non-abelian and abelian groups respectively and $\hat{\mu}$ is the unit vector in the μ direction. In addition we introduce forward and backward ordinary lattice derivatives given by:

$$\begin{aligned} (\Delta_\mu f)(n) &= f(n+\hat{\mu}) - f(n)\,, & \text{(A.5)}\\ (\bar{\Delta}_\mu f)(n) &= f(n-\hat{\mu}) - f(n)\,. & \text{(A.6)} \end{aligned}$$

The continuum limits of the links are as usual:

$$\begin{aligned} U_\mu(n) &\sim e^{\frac{i}{2}a_\mu g_W A_\mu^a \tau_a}\,, \\ B_\mu(n) &\sim e^{\frac{i}{2}a_\mu g_Y b_\mu \tau_3}\,, \end{aligned} \tag{A.7}$$

where is no implicit sum in the μ index, and where the vector $a_\nu = \{a_t, a, a, a\}$.

Under the transformation (A.2) links transform by:

$$\begin{aligned} U_\mu(n) &\to \Omega(n)U_\mu(n)\Omega^\dagger(n+\mu) \\ B_\mu(n) &\to \Lambda(n)B_\mu\Lambda^\dagger(n+\mu), \end{aligned} \tag{A.8}$$

giving the correct transformation for the covariant derivative.

The discretization of the pure gauge part of the Lagrangian is as usual, using the plaquette:

$$\begin{aligned} P_{\mu\nu}(n) &= U_\mu(n)U_\nu(n+\mu)U^\dagger(n+\nu)U^\dagger(n) \\ P_{\mu\nu}^{ab}(n) &= B_\mu(n)B_\nu(n+\mu)B^\dagger(n+\nu)B^\dagger(n)\,, \end{aligned} \tag{A.9}$$

with the transformation properties:

$$\begin{aligned} P_{\mu\nu}(n) &\to \Omega(n)P_{\mu\nu}\Omega^\dagger(n) \\ P_{\mu\nu}^{ab}(n) &\to \Lambda(n)P_{\mu\nu}^{ab}\Lambda^\dagger(n) = P_{\mu\nu}^{ab}. \end{aligned} \tag{A.10}$$

The continuum limit of the plaquettes is:

$$\begin{aligned} \mathrm{Tr}\{P_{\mu\nu}\} &\sim \mathrm{Tr}\{e^{\frac{i}{2}a_\mu a_\nu G_{\mu\nu}^a \tau_a}\} \sim 2 - a_\mu^2 a_\nu^2 \frac{G_{\mu\nu}^a G_{\mu\nu}^a}{4}, \\ \mathrm{Tr}\{P_{\mu\nu}^{ab}\} &\sim \mathrm{Tr}\{e^{\frac{i}{2}a_\mu a_\nu F_{\mu\nu}\tau_3}\} \sim 2 - a_\mu^2 a_\nu^2 \frac{F_{\mu\nu}F_{\mu\nu}}{4}\,. \end{aligned} \tag{A.11}$$

With this the pure gauge discretized Lagrangian reads:

$$\mathcal{L}_Y(n) = \frac{2}{\kappa g_Y^2}\sum_i \mathrm{Tr}[1-\mathrm{P}^{\mathrm{ab}}_{0\mathrm{i}}(\mathrm{n})] - \frac{\kappa}{\mathrm{g}^2_{\mathrm{Y}}}\sum_{\mathrm{i}\neq\mathrm{j}}\mathrm{Tr}[1-\mathrm{P}^{\mathrm{ab}}_{\mathrm{ij}}(\mathrm{n})]\,, \quad \text{(A.12)}$$

$$\mathcal{L}_{SU(2)}(n) = \frac{2}{\kappa g_W^2}\sum_i \mathrm{Tr}[1-\mathrm{P}_{0\mathrm{i}}(\mathrm{n})] - \frac{\kappa}{\mathrm{g}^2_{\mathrm{W}}}\sum_{\mathrm{i}\neq\mathrm{j}}\mathrm{Tr}[1-\mathrm{P}_{\mathrm{ij}}(\mathrm{n})]\,. \quad \text{(A.13)}$$

And the complete lattice Lagrangian is:

$$\begin{aligned}\mathcal{L}_L &= \mathcal{L}_Y(n) + \mathcal{L}_{SU(2)}(n) \quad \text{(A.14)}\\ &+ \mathrm{Tr}\{(\mathrm{D}_\mu\Phi(\mathrm{n}))^\dagger \mathrm{D}^\mu\Phi(\mathrm{n})\} + \frac{1}{2}\Delta_\mu\chi(\mathrm{n})\Delta^\mu\chi(\mathrm{n}) - \kappa\mathrm{V}(\Phi(\mathrm{n}),\chi(\mathrm{n})),\end{aligned}$$

where all the derivatives are lattice derivatives and all matter fields are adimensional lattice fields. In the potential $V(\Phi(n),\chi(n))$ all masses are expressed in terms of $M_L = am$, $\mu_L = a\mu$, so the potential has the explicit form:

$$\begin{aligned}V(n) = &- M_L^2\mathrm{Tr}\{\Phi^\dagger(\mathrm{n})\Phi(\mathrm{n})\} \quad \text{(A.15)}\\ &+ \lambda(\mathrm{Tr}\{\Phi^\dagger(\mathrm{n})\Phi(\mathrm{n})\})^2 + \frac{\mu_\mathrm{L}^2}{2}\chi^2(\mathrm{n})\\ &+ g^2\chi^2(n)\mathrm{Tr}\{\Phi^\dagger(\mathrm{n})\Phi(\mathrm{n})\}.\end{aligned}$$

We now have all the ingredients to obtain the lattice equations of motion:

$$\begin{aligned}(\Delta_\mu\bar{\Delta}^\mu\chi)(n) &= \kappa\Big\{\mu_L^2 + 2g^2\mathrm{Tr}[\Phi^\dagger(\mathrm{n})\Phi(\mathrm{n})]\Big\}\chi(\mathrm{n})\,, \quad \text{(A.16)}\\ (D_\mu\bar{D}^\mu\Phi)(n) &= \kappa\Big\{-M_L^2 + g^2\chi^2(n) + 2\lambda\mathrm{Tr}[\Phi^\dagger(\mathrm{n})\Phi(\mathrm{n})]\Big\}\Phi(\mathrm{n}),\\ \frac{1}{\kappa}\bar{D}^A_\nu\mathcal{G}^{\mu\nu}(n) &= J^\mu(n)\,,\\ \frac{1}{\kappa}\bar{D}^Y_\nu\mathcal{F}^{\mu\nu}(n) &= J^\mu_Y(n)\,,\end{aligned}$$

where the currents are given by:

$$\begin{aligned}J^\mu_a(n) &= \frac{ig_W}{2}[\Phi(n)(D^\mu\Phi)^\dagger(n) - (D^\mu\Phi)(n)\Phi^\dagger(n)]\,, \quad \text{(A.17)}\\ J^\mu_Y(n) &= \frac{ig_Y}{2}[(D^\mu\Phi)^\dagger(n)\Phi(n) - \Phi^\dagger(n)(D^\mu\Phi)(n)]_3\,,\end{aligned}$$

where the 3 stands for the τ^3 component in quaternions space. We have used the lattice metric, whose non-zero elements are: $\eta^{00} = \frac{1}{\kappa}$, $\eta^{ii} = -\kappa$. D_μ is

defined like in (A.3), whereas the other two different derivatives are defined as:

$$\begin{aligned} D^A_\mu \Phi(n) &= U_\mu(n)\Phi(n+\mu) - \Phi(n), \\ D^Y_\mu \Phi(n) &= \Phi(n+\mu)B_\mu(n) - \Phi(n), \\ D^A_\mu P_{\rho\nu}(n) &= U_\mu(n)P_{\rho\nu}(n+\mu)U^\dagger_\mu(n) - P_{\rho\nu}(n), \\ D^Y_\mu P^{ab}_{\rho\nu}(n) &= P^{ab}_{\rho\nu}(n+\mu) - P^{ab}_{\rho\nu}(n). \end{aligned} \tag{A.18}$$

In these equations of motion the tensors $\mathcal{G}_{\mu\nu}$ and $\mathcal{F}_{\mu\nu}$ are not the continuum ones but new lattice tensors defined by:

$$\begin{aligned} \mathcal{F}_{\mu\nu} &= \frac{i}{2g_Y}[P^{ab}_{\mu\nu}(n) - P^{ab}_{\nu\mu}(n)]\,, \\ \mathcal{G}^a_{\mu\nu} &= \frac{i}{2g_W}[P^a_{\mu\nu}(n) - P^a_{\nu\mu}(n)]\,. \end{aligned} \tag{A.19}$$

In order to simplify the problem of solving the lattice equations of motion it is convenient to fix the temporal gauge, realized on the lattice by fixing the temporal component of the hypercharge and SU(2) links to unity, $B_0(n) = \mathbb{I}$, $U_0 = \mathbb{I}$. In this way it is possible to solve for the fields at time $n_0 + 2$ in terms of the fields at times n_0 and $n_0 + 1$.

The lattice equations associated to the gauge fixed degrees of freedom become constraint equations analogous to the continuum Gauss law:

$$\begin{aligned} \frac{1}{\kappa}\bar{D}^A_j \mathcal{G}^{0j}_a(n) &= J^0_a(n), \\ \frac{1}{\kappa}\bar{D}^Y_j \mathcal{F}^{0j}(n) &= J^0_Y(n). \end{aligned} \tag{A.20}$$

Like in the continuum these equations are independent of time and must be satisfied for any time in the evolution.That implies that any choice of initial conditions must be compatible with this constraint. The way we fix the SU(2) Gauss constraint follows exactly the procedure described in [112]. Here we will detail the initial implementation for the U(1) constraint. At initial time all gauge fields are taken to zero, thus the links variables are equal to the identity matrix. The abelian Gauss constraint takes the simple form:

$$\bar{\Delta}_j \mathcal{F}_{0j}(n) = -\frac{ig_Y}{2}[(\Delta_0\Phi)^\dagger(n)\Phi(n) - \Phi^\dagger(n)(\Delta_0\Phi)(n)]_3\,, \tag{A.21}$$

where we used the metrics η to take down the indexes. The plaquette P_{0j} is expressed in terms of the gauge fields:

$$P_{0j}(n) = U_0(n)U_j(n+\hat{0})U_0^\dagger(n+\hat{j})U_j^\dagger(n) \tag{A.22}$$

As mentioned, our criteria are set all temporal links to identity as well as all spatial links at initial time. Hence, the plaquette reduces to $U_j(n+\hat{0})$. It is more convenient to express the Gauss constraint in Fourier space:

$$v_j(k)[U_j(k+\hat{0}) - U_j^\dagger(k+\hat{0})] = g_Y^2[(\Delta_0\Phi)^\dagger(k)\Phi(k) - \Phi^\dagger(k)(\Delta_0\Phi)(k)]_3\,, \tag{A.23}$$

where $v_j = (e^{-ik_j} - 1)$. This provides a condition for the imaginary part of the temporal displaced links at initial time.

Appendix B

Lattice version of the Maxwell equations

In this appendix we present the derivation of the lattice version of the Maxwell equations used in order to define the W charge and current densities. Starting from the continuum expressions:

$$\vec{\nabla}\vec{E} = \rho \quad , \quad \vec{\nabla}\vec{j} + \partial_0 \rho = 0 \tag{B.1}$$

$$\vec{\nabla}\vec{B} = 0 \tag{B.2}$$

$$\vec{\nabla} \times \vec{E} + \partial_0 \vec{B} = 0 \tag{B.3}$$

$$\vec{\nabla} \times \vec{B} - \partial_0 \vec{E} = \vec{j} \tag{B.4}$$

$$\tag{B.5}$$

we look for a discretization that preserves the Bianchi identities.

In section 6.3.1 we have introduced the photon field strength, $F^{\gamma}_{\mu\nu}(n)$, in terms of clover averaged Z and B field strengths. We define the clover average of a space-time tensor like $F_{0i}(n)$ by:

$$\langle F_{0i} \rangle_{\text{clov}} \equiv \frac{1}{2}\Big(F_{0i}(n) + F_{0i}(n - \hat{0}) \Big) , \tag{B.6}$$

while for a spatial tensor we have:

$$\langle F_{ij} \rangle_{\text{clov}} \equiv \frac{1}{4}\Big(F_{ij}(n) + F_{ij}(n - \hat{i}) + F_{ij}(n - \hat{j}) + F_{ij}(n - \hat{i} - \hat{j}) \Big) . \tag{B.7}$$

Each $F_{\mu\nu}$ is obtained in the lattice by the abelian plaquette of the $U(1)$ electromagnetic group of the system. As pointed in previous appendix, due to the representation of the Higgs field the $U(1)$ electromagnetic appropriate definition is the diagonal $SU(2)$ subgroup, with elements:

$$\Lambda = e^{i\alpha\tau_3} = \cos(\alpha) + \sin(\alpha)\sigma_3$$

where the $\sigma_3 = \tau_3$.

This provides the abelian plaquette to be (again calligraphic variables refer to continuum quantities):

$$P_{\mu\nu}(n) = \cos(a^2 \mathcal{F}_{\mu\nu}(n)) + \sin(a^2 \mathcal{F}_{\mu\nu}(n))\sigma_3$$

which gives the lattice $F_{\mu\nu}$ tensor as $\mathrm{Tr}\{P_{\mu\nu}\sigma_3^\dagger\}$, so:

$$B_i(n) = \frac{1}{2}\epsilon_{ijk} \langle \mathrm{Tr}\{P_{jk}\sigma_3^\dagger\}\rangle_{\mathrm{clov}} \tag{B.8}$$

$$E_i(n) = \langle \mathrm{Tr}\{P_{0i}\sigma_3^\dagger\}\rangle_{\mathrm{clov}}$$

In addition to the usual forward and backward derivatives, Eq. (A.6), we introduce an improved lattice derivative:

$$(\Delta_\mu^I) f(n) = \frac{1}{2a_\mu}\Big(f(n+\hat{\mu}) - f(n-\hat{\mu})\Big). \tag{B.9}$$

With this the electric and magnetic fields defined in terms of the clover photon field $F^\gamma_{\mu\nu}(n)$ verify the Bianchi identities:

$$\vec{\Delta}^I \cdot \vec{B} = 0, \qquad \vec{\Delta}^I \times \vec{E} + \Delta_0 \vec{B} = 0 \tag{B.10}$$

It is easy to realize this fact if one thinks in the pictorial interpretation of these equations. Using the clover improvement for the magnetic field (see also chapter 5) this field is interpreted as a double plaquette anti-clockwise oriented as represented in figure B.1. Actually it is not a double plaquette, because of the internal links. They are showed in the figure as dotted ones. But, as we will see below, for our purposes they don't affect the argument, since each one is present twice with both orientations. So although they are needed for the clover improved magnetic definition, let's forget about them for the following.

The magnetic field component i is orthogonal to the plane of the plaquette and is placed in the center of the double plaquette. The electric field, however, does not have a clover improvement in the temporal direction. The reason is that, due to the temporal spacing being much smaller than the spatial one, it is not needed. That is the reason why the graphical interpretation of the electric field is half a double plaquette. Notice also, that the electric field is not placed in the point x but in $x + \hat{0}/2$. That is, again, not important since the temporal resolution is much higher than the spatial one. So for practical purposes we can forget the displacement in the time direction and

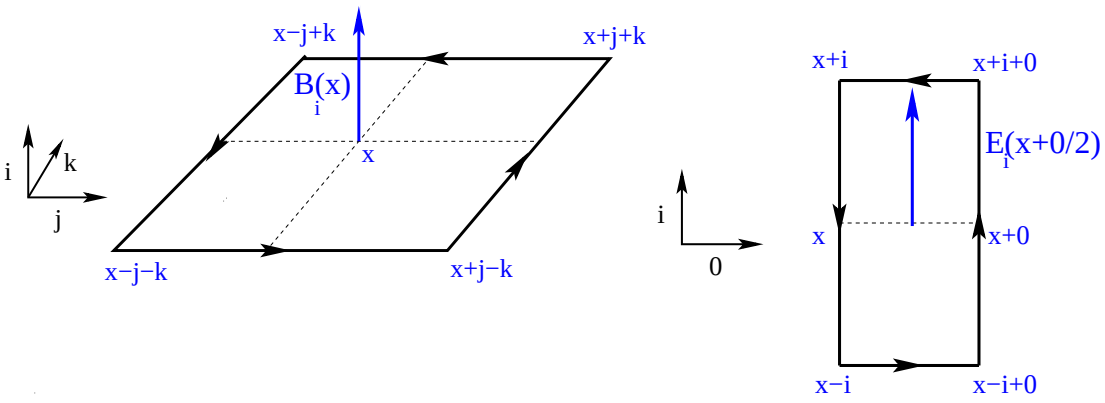

Figure B.1: Graphical interpretation for: Left, the magnetic field component in the i direction, $B_i(x)$. Right, the electric field component along the same direction $E_i(x + \hat{0}/2)$.

think on it as placed in x. Now the Bianchi identities have a nice graphical representation in the lattice. The action of the derivative B.9 on the magnetic or electric field, is to subtract two plaquettes as the ones in fig. B.1. For the identity:

$$\vec{\Delta}^I.\vec{B}(\vec{x}) = 0$$

the sum of all components has as a graphical representation a cube centered in the point $\vec{x}$. This is plotted in figure B.2 right. Notice that each link (including the internal ones in each face) appears twice in the cube and with opposite orientation each time. So the total sum of the plaquettes ordered in such way is real by construction. Since the electro-magnetic field, in our definition, is obtained from the imaginary part of the plaquette (see B.8), this Bianchi identity is just the imaginary part of the cube, that is identically zero. The same is true for the Bianchi identity that involves the electric field and is pictorially showed in figure B.2 left. Notice that, although the electric field is only space-improved, the argument is still valid, since again every link is present with both orientations.

Is important to notice that, to ensure the exact holding of the Bianchi equations, it has been necessary to use the improved derivative, since the magnetic field is itself clover improved. It is easy to guess from the pictures than if we had used the naive derivative instead, there would be links with only one orientation which caused the identities not to be satisfied exactly. Of course in that case the violation of this quantities would be order lattice spacing a. The same would be true with the combination of the improved

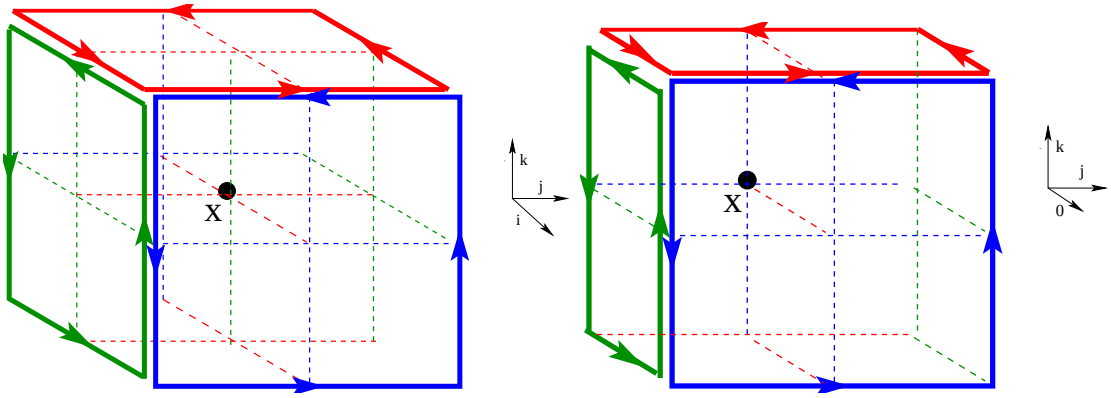

Figure B.2: Graphical representation of the lattice Bianchi Identities in the formalism of the present thesis: B field improved by the clover, E field only spatial improved, and improved lattice derivative Δ^I. Some internal plaquettes are plotted in dot lines for a better view.

derivative and the single plaquette electromagnetic definition. Of course the combination single plaquette and naive derivative would make the identities hold again, but with a less accurate definition for the fields.

B.1 The transverse and longitudinal components

In this section we will discuss the projections into longitudinal and transverse part of the electromagnetic fields.

The equations B.1 can be translated into momentum space. The projection of the electric and magnetic fields is done in momentum space with Fourier transformed fields:

$$\vec{E}(\vec{k}) = \int d^3x \; \vec{E}(\vec{x}) \; e^{-i\vec{k}\cdot\vec{x}}, \qquad \vec{B}(\vec{k}) = \int d^3x \; \vec{B}(\vec{x}) \; e^{-i\vec{k}\cdot\vec{x}}, \tag{B.11}$$

where the lattice momenta are given by $k_i = 2\pi n_i/(N_s a_s)$ with $n_i \in \mathbb{Z}$. The $\vec{k}$ vector privileges a determined direction in the space for each mode. Then both $\vec{E}(k)$, $\vec{B}(k)$ can be expressed in terms of a longitudinal and transverse parts:

$$\begin{aligned} \vec{E}_i(\vec{k}) &= (\delta_{ij} - \frac{k_i k_j}{k^2}) E_t^j(\vec{k}) + \frac{k_i}{k} E_L(\vec{k}) \\ \vec{B}_i(\vec{k}) &= (\delta_{ij} - \frac{k_i k_j}{k^2}) B_t^j(\vec{k}) + \frac{k_i}{k} B_L(\vec{k}) \end{aligned} \tag{B.12}$$

From the expression in Fourier space of the first Maxwell equations, two direct but important conclusions are automatically found. First the magnetic field is always transverse to the momentum, so B_L in equation B.12 is identically equal to zero. And secondly, taking into Fourier space the first Maxwell equation:

$$-i\vec{k}\cdot\vec{E}(\vec{k}) = \rho(\vec{k}) \tag{B.13}$$

only the longitudinal to $\vec{k}$ part of the electric field ($\vec{E}_L$), is related with the charge distribution, whereas the transverse part does not influence the charge in any way.
For the last equation in eq. B.1 one can obtain some similar considerations for $\vec{j}$. This equation in momentum space reads:

$$-i\vec{k}\times\vec{B}(k) - \partial_0 E(\vec{k}) = \vec{j}(\vec{k}) \tag{B.14}$$

Again we can differentiate two components for the current. The longitudinal one is again associated with the charges in the system. It could be directly read from the continuity in eq. B.1:

$$\vec{j}_L(\vec{k}) = -i\frac{\partial_0\rho(\vec{k})}{k}\hat{k} \tag{B.15}$$

The transverse part, however, mixes the information coming from the transverse electric field, and the magnetic field. So it is not so easy to extract a clear relationship with a particular aspect of the system.
This separation between longitudinal and transverse parts has been used widely in this thesis, and played an important role in the understanding of the dynamics of the primordial plasma.
To end the discussion of the lattice Maxwell equations, is important to say that although all previously said about the transverse and longitudinal parts is true for a general setting, in our case we have made use of the improved electromagnetic fields. As a consequence the Bianchi identities are only satisfied with an improved derivative, so it is natural to use this improved derivative in the Fourier form. We now define accordingly the longitudinal and transverse components of the fields. Transverse components, $\vec{E}_t$, of a vector $\vec{E}$ are defined such that $\vec{q}\cdot\vec{E}_t = 0$, where:

$$\vec{q} = \frac{1}{2}(\vec{v} - \vec{v}^*), \quad \text{with} \quad v_i = \frac{1}{a_s}(e^{-ik_i a_s} - 1)\,. \tag{B.16}$$

which is the vector associated with the Fourier transform of the improved derivative (see 5).

Appendix C

Thermal radiation

In the present appendix, we demonstrate that:

$$\langle |\vec{B}(\vec{x})|^{2n} \rangle = \langle : |\vec{B}(\vec{x})|^{2n} : \rangle_{Q(T)}, \tag{C.1}$$

where the left side of the equality is calculated using the Maxwellian classical distribution:

$$\langle |\vec{B}|^{2n} \rangle = \sqrt{\frac{2}{\pi}} \Big(\frac{3}{\langle B^2 \rangle} \Big)^{3/2} \int_0^\infty dB B^{2n+2} e^{-\frac{B^2}{\frac{2}{3}\langle B^2 \rangle}}, \tag{C.2}$$

whereas the right hand side is calculated using the thermal quantum distribution in the canonical formalism, so:

$$\langle : |\vec{B}(\vec{x})|^{2n} : \rangle = \frac{\mathrm{Tr}(: |\vec{B}(\vec{x})|^{2n} : \rho)}{\mathrm{Tr}(\rho)}. \tag{C.3}$$

where ρ is the usual canonical matrix density:

$$\rho = e^{-\frac{H}{T}}. \tag{C.4}$$

The calculation of all the classical terms can be performed at once using the Γ function definition, so:

$$\langle |\vec{B}(\vec{x})|^{2n} \rangle = \frac{(2n+1)!!}{3^n} (\langle |\vec{B}(\vec{x})|^2 \rangle)^n. \tag{C.5}$$

Let us compute

$$\langle : (\vec{B}(\vec{x}) \cdot \vec{B}(\vec{x}))^n : \rangle_{Q(T)}$$

where the subindex $Q(T)$ specifies that we are doing a quantum thermal average on the canonical distribution at temperature T. To do the calculation

we first realize that the only part of the normal-ordered operator that contributes to expectation must be diagonal in momentum space and has the form

$$:(\vec{B}(\vec{x})\cdot\vec{B}(\vec{x}))^n:=\prod_{i=1}^{n}\left(\sum_{a_i}\int d\vec{k_i}\mathbf{a}^\dagger_{a_i}(\vec{k_i})\mathbf{a}_{a_i}(\vec{k_i})\right)G_{a_1\ldots a_n}(\vec{k_1},\ldots\vec{k_n})+X \tag{C.6}$$

where X denotes the part that does not contribute to the expectation value and G is a a coefficient to be specified later.

Now we can evaluate the expectation value of the operator, which gives the product of $\overline{n}(k_i,a_i)$, the mean number of photons of momenta $\vec{k_i}$ and polarization a_i. Hence we arrive at

$$\prod_{i=1}^{n}\left(\sum_{a_i}\int d\vec{k_i}\,\overline{n}(k_i,a_i)\right)G_{a_1\ldots a_n}(\vec{k_1},\ldots\vec{k_n})$$

. Now we should unfold the form of the coefficient G. It is given by

$$\frac{1}{n!}\prod_i\left(v_{l_{2i-1}}(\vec{k_i},a_i)v_{l_{2i}}(\vec{k_i},a_i)\right)\sum_{\sigma\in S_{2n}}\delta_{l_{\sigma(1)}l_{\sigma(2)}}\cdots\delta_{l_{\sigma(2n-1)}l_{\sigma(2n)}}$$

where the sum is over all the permutations of the 2n indices and

$$v_i(\vec{k},a)=\frac{1}{(2\pi)^{3/2}\sqrt{2k}}(\vec{k}\times\vec{\epsilon}_a(\vec{k}))_i$$

. The sum over all permutations comes from taking all creation annihilation operators as distinguishable and assigning them to each of the $2n$ magnetic fields. Nonetheless, since we are integrating over all values of momenta one has to divide by $n!$ to eliminate double-counting.

Now we will introduce the matrix M given by

$$M_{ij}\equiv\sum_a\int d\vec{k}\,\overline{n}(k,a)v_i(\vec{k},a)v_j(\vec{k},a)=\lambda\delta_{ij} \tag{C.7}$$

The left-hand side is a consequence of rotational invariance. Substituting in the previous formulas we get

$$\frac{1}{n!}M_{l_1l_2}\cdots M_{l_{2n-1}l_{2n}}\sum_{\sigma\in S_{2n}}\delta_{l_{\sigma(1)}l_{\sigma(2)}}\cdots\delta_{l_{\sigma(2n-1)}l_{\sigma(2n)}}$$

The sum over permutations can be factored as follows

$$\sum_{\sigma\in S_{2n}}\delta_{l_{\sigma(1)}l_{\sigma(2)}}\cdots\delta_{l_{\sigma(2n-1)}l_{\sigma(2n)}}=2^n n!\sum_{\text{pairings}}\prod_{\text{pair}}\delta(\text{pair})$$

where a pairing is an arrangement of the $2n$ indices into pairs (equivalently a permutation made entirely of 2-cycles). The rest of the calculation is very much like a calculation to nth order in perturbation theory in a model with 2-leg vertexes given by the M matrix and a propagator given by the identity matrix. All diagrams are now characterised by n_l, the number of l-cycles (loops), where l runs from 1 to n. Applying the standard Feynman rules one arrives at

$$4^n n! \prod_i \left(\sum_{n_l} \frac{\mathrm{Tr} M^{n_l}}{(2l)^{n_l} n_l!} \right)$$

. The factors $2l$ and $n_l!$ provide the order of the symmetry group of the diagram. The $2l$ term is associated with cyclic permutations of the vertexes and to a change in orientation. In the previous formula, the sum over n_l runs over all possible integers subject to the constraint $\sum_l l n_l = n$. One can actually perform this sum. Setting $M = \lambda \mathbf{I}$ our expression becomes proportional to λ^n. Thus, we can eliminate the constraint on the n_l by summing over n. The constrained sum can be obtained from the unconstrained one by selecting the term proportional to λ^n. Hence,

$$4^n n! \prod_l \left(\sum_{n_l} \left(\frac{D\lambda^l}{2l} \right)^{n_l} \frac{1}{n_l!} \right) = 4^n n! \exp\{D/2 \sum_l \frac{\lambda^l}{l}\} = 4^n n! (1-\lambda)^{-D/2}$$

where D is the space dimension, which is 3 in our case. This quantity is the generating function of all the quantum averages. Differentiating n times with respect to λ we extract the n-th term that we were looking for:

$$\langle : (\vec{B}(\vec{x}) \cdot \vec{B}(\vec{x}))^n : \rangle_{Q(T)} = (2\lambda)^n (2n+1)!! \tag{C.8}$$

The result for $D = \lambda = 1$, given by $\frac{(2n)!}{n!}$, serves to crosscheck the result. From the previous equation (C.8) we get $\lambda = (1/6)\langle : |B|^2(v) : \rangle_{Q(T)}$ allowing to re-express eq. (C.8) in the form of eq. (C.5).
To conclude we give the expression of $\langle : |B(\vec{x})|^2 : \rangle_{Q(T)}$ in terms of the temperature. Taking the trace of eq. (C.7) we obtain:

$$\langle : |B|^2(x) : \rangle_{Q(T)} = \int d\vec{k} \frac{1}{(2\pi)^3} 2\, k\, \overline{n}(k,a)\,.$$

Taking into account $\overline{n}(k,a) = (e^{k/T} - 1)^{-1}$, we can perform the integration:

$$\frac{1}{\pi^2} \int dk k^3 \frac{1}{(e^{k/T} - 1)} = \frac{1}{\pi^2} \int dk k^3 \sum_{n=1}^{\infty} (e^{-k/T})^n = \frac{6}{\pi^2} T^4 \sum_{n=1}^{\infty} \frac{1}{n^4}.$$

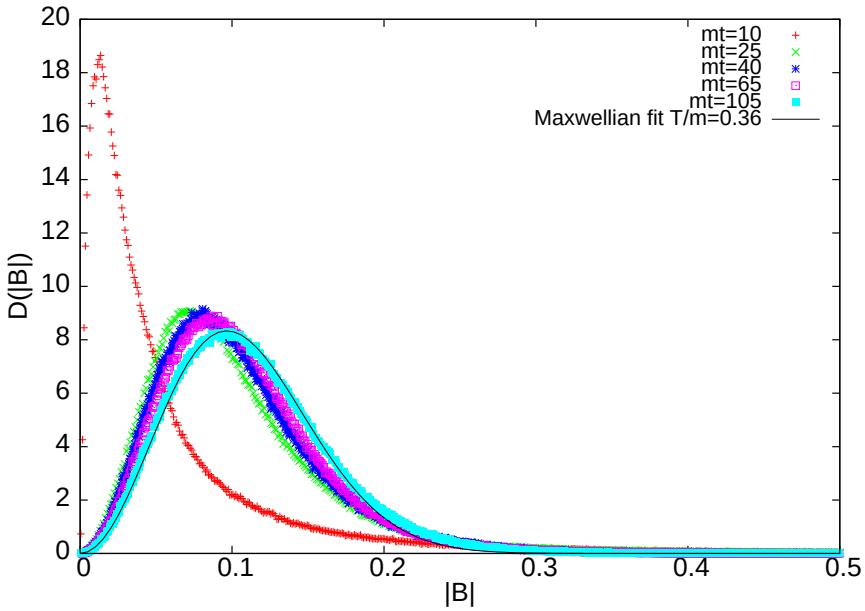

Figure C.1: Trent to Maxwellian of the magnetic norm distribution with time. A temperature is extracted from the fit.

The sum over n is the known $\zeta(4) = \pi^4/90$, leading to:

$$\frac{1}{2}\langle : |B|^2(x) : \rangle_{Q(T)} = \frac{\pi^2}{30} T^4$$

Figure C.1 exemplifies how the magnetic norm distribution of the system of the present study, nicely tends to the Maxwellian one with time.

Appendix D

Gaussian Random fields

In this appendix we revisit the predictions of the Gaussian random field model. As explained in chapter 6 of this thesis, the initial conditions produced by the quantum evolution shortly after inflation ends are of this type. Furthermore, this distribution seeds the generation of magnetic fields and Chern-Simons number. There is an extensive literature (see Refs. [127]-[130]) on Gaussian random fields and some of the analytic predictions are included in [111, 112]. However, here we are dealing with multicomponent fields and some of the predictions and methodology do not hold in this case. Besides, there are many more relevant observables directly related to the Physics issues addressed in this tesis. To explore these matters within this tesis, we have felt satisfied with its numerical study. Since gauge fields and non-linearities do not play a role at this stage, we have profited to increase statistics and test systematic errors at a low computational cost. These results can then be used as a reference to compare with our full-theoretical ones.

Our Gaussian random field is homogeneous and isotropic. The power spectrum was set to match the one produced by the quantum evolution of the Higgs field coupled to a linearly time-dependent Inflaton and neglecting the Higgs self-interaction. The details and nomenclature are explained in our previous tesis [111]. We recall that the Higgs field has 4 real components which are independent random variables with identical power spectrum which, for simplicity, is fitted to a simple form which reproduces nicely its shape:

$$P(k,t) = \frac{1}{2m^2\pi^2} k^2 (A(t) e^{-B(t)\,k^2/m^2} + 1)\Theta(\sqrt{2Vtm} - k) \qquad \text{(D.1)}$$

where V is the Inflaton velocity at the end of inflation, A and B are time-

dependent parameters and Θ is the Heaviside step function.

It is interesting to be able to trace the dependence of our results on the different parameters that enter our model. Fortunately, this dependence is greatly encoded in two scales that characterize the Gaussian random field. One scale fixes the magnitude of the Higgs field. We choose this scale to be the dispersion σ of the field at one spatial point. Notice that the physical scale v, giving the expectation value of the Higgs field in the true vacuum, has not yet entered the scene, since the Gaussian random field is generated before the self-interaction of the Higgs field affects the evolution. It is precisely the comparison between $\sigma(t)$ and v that must be taken into account in fixing the range of values of the initial times t_i for the subsequent non-linear classical evolution of the system.

In addition, the other scale of the problem is a length scale ξ_0 associated to the Gaussian random field as follows:

$$\frac{1}{\xi_0^2} \equiv \frac{\int \frac{dk}{k} P(k,t) k^2}{\int \frac{dk}{k} P(k,t)} \tag{D.2}$$

With our choice of velocity $V = 0.024$ at $mt_i = 5$ we obtain $\sigma = 0.139\, v$, for $m_{\rm H} = 3m_{\rm W}$. Thus, we are safely in the region where non-linearities are still small. On the other hand $m\xi_0 = 3.09$, which determines the adequate ranges of the ultraviolet and infrared cut-off of our numerical procedure. At $mt_i = 6.5$ these numbers have changed to $\sigma = 0.204\, v$ and $m\xi_0 = 2.95$ respectively. This observation allows us to give results in a way that are valid for all the values of initial times employed in this work.

In line with previous analysis, we will present our results for the density and distribution of local maxima of $|\phi|$. The density of maxima is given by $0.0140(4)\, \xi_0^{-3}$. The distribution of minimum distances among maxima can be studied directly and displays an approximate Gaussian distribution with mean $3.1(1)\, \xi_0$ and dispersion $0.62(2)\, \xi_0$. We have also studied the distribution of values of $|\phi|$ at the maxima, φ. The average height of a peak being $1.52(4)\sigma$. The histogram is much narrower than the one obtained for a single component Gaussian random field, and is well-fitted to the following expression

$$\varphi^a \exp\left\{-\frac{\varphi^2}{2\tilde{\sigma}^2}\right\}$$

with $a = 10.4(5)$ and $\tilde{\sigma} = 0.44(1)\, \sigma$. Nicely enough the results presented are robust as one changes the ultraviolet, infrared cut-offs and time within their safe windows (See Fig. D.1). Errors quoted are both statistical and systematic.

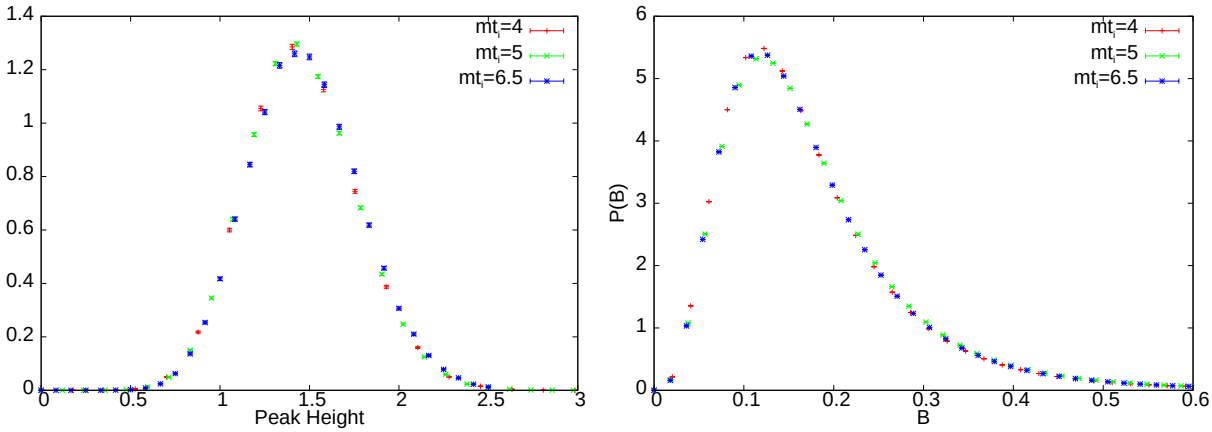

Figure D.1: Left: Histogram of peak (local maxima) heights, expressed in $\sigma(t_i)$ units. Right: Distribution of the local magnetic field intensity $B = |\vec{B}(x)|$ in $\xi_0(t_i)$ units.

Now we turn to observables which are characteristic of multi-component Gaussian random fields. A crucial role is played by the topological susceptibility χ which is obtained by dividing the mean value of the winding number square by the volume. We obtain $1.55(10) \times 10^{-3}\xi_0^{-3}$. We can also compute the initial magnetic field distribution. Notice that, as explained in the tesis, despite the fact that SU(2)×U(1) gauge fields are zero at this stage, our formulas induce a non-zero Z field and a non-zero magnetic field which is proportional to it. Computing this magnetic field at each point of space we obtain a distribution which is well fitted by a formula

$$P(B) = B^b \exp\left\{-\left(\frac{B}{d_1}\right)^{h_1}\right\} + A\,\exp\left\{-\left(\frac{B}{d_2}\right)^{h_2}\right\}\,,$$

with $B = |\vec{B}(x)|$, see Fig. 9.11. Our best fit values of the parameters are $b = 1.89(3)$, $d_1\,\xi_0^2 = 3.0(1)\,10^{-3}, h_1 = 0.368(3)$, $d_2\,\xi_0^2 = 2.61(2), h_2 = 1.34(3)$, $A = 1.0(5)\,10^{-7}$. The initial magnetic field distribution has a slower decrease at large values than the Maxwellian distribution obtained at later times. The aforementioned universality can be tested here. In particular, it follows that results obtained at different initial times t_i should fall in the same curve once normalised by the scales of σ and ξ_0. This is clearly seen in Fig. D.1.

We have also studied the spectrum of the magnetic field to compare it with the one obtained once non-linearities set in. In our case the high momentum profile differs from the thermal tail displayed at later times. Instead, the

high momentum tail is well fitted by a function

$$\exp\left\{-\left(\frac{k}{b}\right)^{c}\right\}$$

where $b\xi_0 = 0.01(1)$ and $c = 0.36(4)$.

List of Figures

4.1 Log-log schematic plot of the behavior of the energy density with the scale factor. The inflationary processes are plateaux in the figure. In the detail within the circle, we also show the short inflationary period at the EW scale, which is expected to last only a few e-folds. Also showed is a possible main inflationary process at the GUT scale, responsible of the CMB anisotropies. From "Signatures from preheating", J. García-Bellido, KITP Seminars (UCSB). 36

4.2 Higgs potential evolution during and after inflation. We show the initial narrow quadratic Higgs potential in the deeper stages of inflation, and the final "mexican hat" potential, where symmetry breaking has taken place. t_c stands for the time in which $\chi(t_c) = \chi_c$. 40

5.1 "Cubic space division" by M.C. Escher (1952). 45

5.2 Left: Link variable. Right: Plaquette definition. The arrows represent the corresponding links. The empty point in the middle is not a lattice point but the point where the continuum limit $\mathcal{F}_{\mu\nu}$ tensor field is placed. 51

5.3 Plaquettes averaged in the clover definition. The continuum limit $\mathcal{F}_{\mu\nu}$ tensor is placed in the central point n. 58

6.1 Schematic evolution line. On it the times relevant for the series of approximations are represented: τ_c: end of Inflation, τ_1: time where enough modes have been enhanced to be classical, in order to keep an accurate description of the system, τ_i: time where the quantum evolution is substituted by a classical one, τ_λ: time where the λ term of the Lagrangian can not be neglected anymore. 60

6.2 Representation of the Higgs-Inflaton system. Potential energy. From "Signatures from preheating", J. García-Bellido, KITP Seminars (UCSB). 61
6.3 Evolution of the energies for two different onsets of the initial time. Top left: Kinetic energy; Top right: Gradient energy. Bottom left: Potential Energy; Bottom right: SU(2) energy. . 68
6.4 Behavior of the energies with the g_Y coupling. Left: Kinetic energy. Right: Gradient energy. 69
6.5 Dependence of the energies on the g_W coupling. Top left: Kinetic energy; Top right: Gradient energy. Bottom left: Potential Energy; Bottom right: SU(2) energy. 72

7.1 Two linked lines with linking number 2. *Source: Wikipedia.* . 96
7.2 Two flux tubes with $L_{12} = 4$ and with both internal twist and writhe. *Source: Wikipedia.* 97
7.3 Schematic example of a turbulent dissipation process. The mean scale is represented as a red curve. The arrow represents the time evolution. 102
7.4 Representation of the decay of a two linked loops of Z-string (in black). The creation of a monopole anti-monopole pair, leads a magnetic flux remnant, represented in red. Adapted from [70]. 106

8.1 Evolution of the Higgs and Inflaton vevs, referred to v and χ_c respectively. From $mt = 5$ to $mt = 100$. For $ma = 0.42$ and $m_{\rm H}/m_{\rm W} = 2$. 108
8.2 Schematic picture of the evolution of the Higgs vev. The two differentiated behaviors of the vev translate into two regions where different processes of interest arise. Some of them are indicated within the boxes. Z-B hel. transf. stands for the process of helicity transfer between the Z and the magnetic fields. 109
8.3 Left, locus of Higgs norm maximum points. Right, locus of points with maximum Higgs-gradient norm. Both at initial time. 112
8.4 (Left) Locus of points where the value of the Higgs field norm is below $0.03m$. (Right) Locus of points where the magnetic energy density is above $0.03m^4$ (Right). Data correspond to $mt = 5$ and $m_{\rm H} = 2m_{\rm W}$. 114

8.5 Histogram of Higgs winding for the initial configuration $mt = 5$ for $p_{\min} = 0.15$. 115
8.6 Initial Z helicity density. Red: Locus of points with high positive helicity density. Blue: Locus of points with highly negative helicity density. 117
8.7 Left, locus of Higgs norm maxima. Right, locus of Inflaton norm minima. At two steps of evolution after initial time ($mt = 5.05$). 119
8.8 Evolution through the spontaneous symmetry breaking region of the histogram for the Higgs expectation value 120
8.9 Higgs norm histogram for models $m_{\rm H} = 2m_{\rm W}$ and $m_{\rm H} = 4.65m_{\rm W}$, for $mt = 5$ (left) and $mt = 15$ (right). 121
8.10 Evolution of the Higgs norm for all models. The symmetry breaking time ranges from $mt \sim 10$ to $mt \sim 12$. For $ma = 0.42$. 122
8.11 We show the time evolution of transverse and longitudinal electric and magnetic energy densities averaged over 150 configurations for $m_{\rm H} = 3m_{\rm W}$ and $ma = 0.42$. The vertical axis is in logarithmic scale. 122
8.12 Top: (Left) The location of the bubbles in the Higgs field norm (in red) with a lower cutoff set at $0.7\,v$ and the locus of points with twice the magnetic energy density ($|\vec{B}(\vec{x})|^2$) (in blue) higher than $0.01\,m^4$. (Right) Locus of points where the magnetic energy density is above $0.03\,m^4$. Bottom: (Left) Two-dimensional contour plots of the Higgs field norm. (Right) Two-dimensional contour plots of the magnetic energy density. Data correspond to $mt = 15$ and $m_{\rm H} = 2m_{\rm W}$. 123
8.13 Magnetic and Z-boson susceptibility evolution during the SSB epoch. The latter is rescaled by $\tan^4\theta_W$ to match the magnetic one at mt_i. 124
8.14 Top: (Left) Helicity of the magnetic field. (Right) Helicity of the Z-boson field. Bottom: (Left) Two dimensional contour plots of the helicity of the magnetic field. (Right) Two dimensional contour plots of the helicity of the Z-boson field. Data correspond to $mt = 15$, for $m_{\rm H} = 2m_{\rm W}$. 125
8.15 Averaged $l^2 H_l(r_0)$, Eq. (8.11), at $mt = 15$. We also show the l^2 asymptotic behaviour for the $m_{\rm H}/m_{\rm W} = 4.65$ model. The other data corresponds to $m_{\rm H}/m_{\rm W} = 2$. 126

8.16 Top Left: Locus of points with magnetic energy density $|\vec{B}(x)|^2$, above $0.01\,m^4$. Top Right: Locus of points with electric energy density $|\vec{E}(x)|^2$ above $0.01\,m^4$. Bottom: The distribution of $W^{\pm}$ charge density, tracking the magnetic field lines. Pink and blue areas represent negative and positive charge densities respectively. Data correspond to $mt = 15$, for $m_{\rm H} = 2m_{\rm W}$. . . 129
8.17 Left: Locus of points with magnetic field density $|\vec{B}(\vec{x})|^2$ above $0.01\,m^4$. Right: The 2-dimensional W-charge distribution localized in lumps of opposite sign facing each other. Note that the location of the charge lumps is strongly correlated with the magnetic field flux tubes. These figures correspond to early times, $mt = 10$, for $m_{\rm H} = 3m_{\rm W}$. 130
8.18 Evolution of the charge histogram across the SSB. The time period goes from $mt = 5$ to $mt = 45$. For $ma = 0.42$, $m_{\rm H} = 2m_{\rm W}$. 130
8.19 Charge spectrum evolution through the SSB. From the initial time to $mt = 30$. For $ma = 0.42$ and $m_{\rm H} = 2m_{\rm W}$. 131
8.20 Schematic idealization of the currents associated with the magnetic flux tubes. 133
8.21 Histogram for $\cos\alpha$ in the magnetic strings for one configuration. For $\alpha = \widehat{\vec{j}\vec{B}}$ and $\alpha = \widehat{\dot{\vec{E}}\vec{B}}$. $mt = 15$ and $m_{\rm H}/m_{\rm W} = 2$. . . 134
8.22 Evolution for σ, as defined in equation (8.14) averaged over 80 configurations. From the initial time ($mt = 5$) to $mt = 80$. Model $m_{\rm H}/m_{\rm W} = 3$. 135
8.23 Clusterization of W charges, at the same plane of fig. 8.17. Left $mt = 20$, right $mt = 25$. 135

9.1 We display the time evolution of the helical susceptibilities for the magnetic field (with fit t^{α}) and the Z-boson field (with fit t^{β}). The latter is rescaled by $\tan^4\theta_W$ to match the initial electromagnetic helicity. Top left is for $m_{\rm H}/m_{\rm W} = 2$, averaged over 80 configurations, with $\alpha = 0.7(1)$ and $\beta = -0.27(4)$. Top right is for $m_{\rm H}/m_{\rm W} = 4.65$, averaged over 80 configurations, with $\alpha = 0.3(1)$ and $\beta = -0.33(5)$. Bottom is for $m_{\rm H}/m_{\rm W} = 3$, averaged over 200 configurations, with $\alpha = 0.8(1)$ and $\beta = -0.82(4)$. All data correspond to $ma = 0.42$ and $p_{\rm min} = 0.15\,m$. The top left figure also shows the time evolution of the Higgs mean to illustrate the time when SSB takes place. 139

9.2 We display the log-log plot of the time evolution of the electric (transverse and longitudinal) and magnetic energy densities. The exponents of the power law fits are: Transverse electric field: 0.350(1); Magnetic field: 0.330(1) and Longitudinal electric field: $-0.234(2)$. For $m_{\rm H} = 3\,m_{\rm W}$, $ma = 0.42$ and $p_{\rm min} = 0.15\,m$, averaged over 200 configurations. 140

9.3 Late time evolution of the $\sigma_{T/L,B}$ averaged over 80 configurations. Model $m_{\rm H} = 3m_{\rm W}$. 141

9.4 Charge spectrum evolution from $mt = 105$ to $mt = 305$. For $ma = 0.42$ and $m_{\rm H} = 2m_{\rm W}$. 142

9.5 Turbulent behavior in the scalar sector of the model, for several lattice spacings. Model $m_{\rm H} = 3m_{\rm W}$. 143

9.6 Signal of turbulence in the $SU(2)$ magnetic spectra. From time $mt = 55$ to $mt = 235$. $ma = 0.65$ and $m_{\rm H} = 4.65m_{\rm W}$. . . 144

9.7 Evolution of the Higgs and Inflaton vevs from $mt = 100$ to $mt = 260$. The Inflaton vev is shifted by 1 for a better plot. For $ma = 0.42$ and $m_{\rm H} = 2m_{\rm W}$. 146

9.8 Evolution of the magnetic energy density normalized to the total energy density. With and without the Inflaton field. For $ma = 0.42$ and $m_{\rm H} = 3m_{\rm W}$. 147

9.9 We plot $\langle k^2|\vec{E}(k)|^2\rangle/\mathcal{V}$ vs k, averaged over 150 configurations. The lines represent fits to the radiation and seed field electromagnetic components according to Eqs. (9.5), (9.7) respectively. Results are presented at $mt = 105$, 145, 185 and 265. In all cases $m_{\rm H} = 3m_{\rm W}$, $ma = 0.42$ and $p_{\rm min} = 0.15\,m$. 148

9.10 The same as in Fig. 9.9 but for the magnetic component: $\langle k^2|\vec{B}(k)|^2\rangle/\mathcal{V}$. 149

9.11 We show the time evolution of the distribution of magnetic field norms. Left: For $m_{\rm H} = 3m_{\rm W}$ we display the log of $P(B)/B^2$ vs $B^2/B^2_{\rm max}$ (i.e. normalized to the value at the peak of the distribution) . Right: For $m_{\rm H} = 3m_{\rm W}$ we compare the initial distribution of the local magnitude of the magnetic field at $mt = 5$ with the one obtained at $mt = 265$, the latter fitted to a Maxwellian distribution. The fit to the $mt = 5$ data is described in Appendix D. 152

9.12 We show the time evolution of $\rho^B_{\rm seed}$ (left) and $m\xi_B$ (right), for $m_{\rm H} = 3m_{\rm W},\ ma = 0.42$. The results are obtained by averaging the values obtained for $p_{\rm min} = 0.15\,m$ and $p_{\rm min} = 0.125\,m$, with bands representing the dispersion in the errors. The fits are $\rho^B_{\rm seed}/\rho_0 = 0.0035(5) + 2.3(3) \times 10^{-5} mt$ and $m\xi_B = 20.1(4) + 0.033(2)mt$ respectively. 155

9.13 We show the dependence with ml of the three spatial averages (9.10)−(9.12), for $mt = 245$. The lines are extracted from our fits to the infrared and radiation parts of the spectrum. Note that the fall-off at large distances is just a volume effect. . . . 157

9.14 This figure shows the helical correlation length ξ_χ averaged over several configurations, for the magnetic field and the Z-boson. For $m_{\rm H} = 3m_{\rm W}$ and $ma = 0.42$. 159

10.1 Comparison of the fraction of total energy carried by electric (transverse and longitudinal) and magnetic fields. Top left: for two different values of the minimum momentum: $p_{\rm min} = 0.1$ and 0.15 for fixed $ma = 0.65$. Top Right and down: 3 different lattice spacings ma= 0.65, 0.52,0.42, for the longitudinal, transverse and magnetic components of the energy. The lines are the extrapolation of the results to the continuum $a \to 0$ limit. For $m_{\rm H} = 2m_{\rm W}$ which, from the point of view of lattice artifacts, is the worst case situation. 162

10.2 Left: Lattice spacing dependence of the magnetic susceptibility for $m_H = 2m_W, ma = 0.65,\ 0,52,\ 0.42$ and $N = 64,\ 80,\ 100$. Right: Temporal lattice spacing dependence of the magnetic susceptibility for $ma_t = 0.05, 0.025$. 163

10.3 Continuum extrapolation of the magnetic, transverse electric, longitudinal electric and Z-boson susceptibility. For $m_{\rm H} = 2m_{\rm W}$ and $mt = 95,\ 145,\ 190$, and $mt = 60,\ 190$ for the susceptibility. 164

10.4 We plot $\langle k^2 |B(k)|^2\rangle/\mathcal{V}$ vs k for the magnetic component of the electromagnetic energy. A comparison is made between results at $p_{\rm min} = 0.125\,m$ and $p_{\rm min} = 0.15\,m$. Results are presented at $mt = 105$ (Left) and 265 (Right). For $m_{\rm H} = 3m_{\rm W}$ and $ma = 0.52$. 165

10.5 Time evolution of the energy densities, in m^4 units, in the: Top Left: longitudinal electric field; Top Right: transverse electric field; Bottom Left: magnetic field. Bottom Right: χ_H in m^3 units. Energy densities are not normalized to the total energy density in order to emphasize λ independence in the initial stages of the evolution. 166

10.6 We show the time evolution of transverse and longitudinal electric and mag- netic elds averaged over 70 congurations for ma = 0.43. From top to bottom for $m_{\rm H} = 2$, 3 and 4.65 $m_{\rm W}$ The plot is Log-Log and the corresponding slopes are from left to right: Transverse electric field: 0.462(3), 0.350(1) and 0.230(7) ; Magnetic field: 0.444(3), 0.330(1) and 0.208(5); Longitudinal electric field: -0.31(2), -0.224(3) and -0.258(2). . 167

10.7 We plot $\langle k^2|\vec{B}(k)|^2\rangle/\mathcal{V}$ vs k, averaged over 70 configurations. The lines represent fits to the radiation and seed field electromagnetic components according to Eqs. (9.5), (9.7) respectively. Results are presented at $mt = 145$, 185, 225 and 245. In all cases $m_{\rm H} = 2m_{\rm W}$, $ma = 0.65$ and $p_{\rm min} = 0.1\,m$. 169

10.8 We show the time evolution of $\rho^B_{\rm seed}$ (left) and $m\xi_B$ (right), for $m_{\rm H} = 2m_{\rm W}$, $ma = 0.65$. The results are obtained by averaging the values obtained for $p_{\rm min} = 0.15\,m$ and $p_{\rm min} = 0.1\,m$, with bands representing the dispersion in the errors. The fits are $\rho^B_{\rm seed}/\rho_0 = 0.0040(3) + 3.7(2)\times 10^{-5} mt$ and $m\xi_B = 10.8(3) + 0.007(2)mt$ respectively. 170

B.1 Graphical interpretation for: Left, the magnetic field component in the i direction, $B_i(x)$. Right, the electric field component along the same direction $E_i(x + \hat{0}/2)$. 199

B.2 Graphical representation of the lattice Bianchi Identities in the formalism of the present thesis: B field improved by the clover, E field only spatial improved, and improved lattice derivative Δ^I. Some internal plaquettes are plotted in dot lines for a better view. 200

C.1 Trent to Maxwellian of the magnetic norm distribution with time. A temperature is extracted from the fit. 206

D.1 Left: Histogram of peak (local maxima) heights, expressed in $\sigma(t_i)$ units. Right: Distribution of the local magnetic field intensity $B = |\vec{B}(x)|$ in $\xi_0(t_i)$ units. 209

List of Tables

6.1 List of model parameters used in our analysis. We have taken the Inflaton velocity $V = 0.024$ and the Inflaton bare mass $\mu = 10^{-5} gv \approx 0$. The Hypercharge and SU(2) couplings are such that the W mass and the Z to W mass ratio reproduce the experimental values. 79

6.2 List of lattice parameters: a and a_t are respectively the spatial and temporal lattice spacings, N_s is the number of lattice points and $p_{\min} = 2\pi/(N_s a)$ is the minimal momentum. 80

6.3 List of lattice parameters: a and a_t are respectively the spatial and temporal lattice spacings, N_s is the number of lattice points and $p_{\min} = 2\pi/(N_s a)$ is the minimal momentum. 81

9.1 Parameters of the fit to the high momentum part of the transverse electric and magnetic spectra in Eq. (9.5), for $m_{\rm H} = 3m_{\rm W}$, $ma = 0.42$ and $p_{\min} = 0.15\, m$. Errors in parenthesis combine both systematic and statistical effects. 151

9.2 Parameters of the fit to the low momentum part of the transverse electric spectrum in Eq. (9.7), for $m_{\rm H} = 3m_{\rm W}$, $ma = 0.42$ and $p_{\min} = 0.15\, m$. 153

9.3 Parameters of the fit to the low momentum part of the magnetic spectrum in Eq. (9.7). For $m_{\rm H} = 3m_{\rm W}$, $ma = 0.42$ and $p_{\min} = 0.15\, m$. 154

9.4 Fraction of total energy and correlation length of the seed electromagnetic fields. They are both derived from the infrared spectrum as described in Eqs. (9.8) and (9.9). The results are obtained by averaging (over 150 configurations) the values obtained for $p_{\min} = 0.15\, m$ and $p_{\min} = 0.125\, m$, with errors reflecting the dispersion between them. Data correspond to $m_{\rm H} = 3m_{\rm W}$, $ma = 0.42$. 156

Bibliography

[1] E. W. Kolb and M.S. Turner, "The Early Universe," Addison Weasley 1990.

[2] A. A. Starobinsky, "A new type of isotropic cosmological models without singularity," Phys. Lett. **B91** (1980) 99-102.

[3] A. H. Guth, "The inflationary universe: A possible solution to the horizon and flatness problems," Phys. Rev. **D23** (1981) 347-356.

[4] A. D. Linde, "Lectures on inflationary cosmology," (1994)

[5] E. Komatsu et al. , "FIVE-YEAR WILKINSON MICROWAVE ANISOTROPY PROBE (WMAP1) OBSERVATIONS: COSMOLOGICAL INTERPRETATION", arXiv:0803.0547 [astro-ph]

[6] "WMAP 5 years data," http://lambda.gsfc.nasa.gov/product/map/dr3/parameters.cfm.

[7] A. Albrecht, P.J. Steindhardt, M. S. Turner, and F. Wilczek, "Reheating and inflationary universe," Phys. Rev. Lett. **48** (1982) 1437.

[8] L. Kofman, A. D. Linde, and A. A. Starobinsky, "Reheating after inflation," Phys. Rev. Lett. **73** (1994) 3195, [arXiv:hep-th/9405187].

[9] Y. Shtanov, J.H. Traschen, and R.H. Branderberger, "Universe Reheating after inflation," Phys. Rev. **D23** (1995) 5438-5455, [arXiv:hep-th/9407247].

[10] D. Boyanovsky, M. D'Attaniasio, H. J. de Vega, R. Holman, and D. S. Lee, "Reheating and thermalization: Linear versus non-linear relaxation," Phys. Rev. **D52** (1995) 6805-6827, [arXiv:hep-ph/9507414].

[11] D. I. Kaiser, "Post inflation reheating in an expanding universe", Phys. Rev. **D53** (1996) 1776-1783, [arXiv:astro-ph/9507108].

[12] L. Kofman, A. D. Linde, and A. A. Starobinsky, "Towards the theory of reheating after inflation," Phys. Rev. **D56** (1997) 3258-3295, [arXiv:hep-ph/9704452].

[13] D. Boyanovsky, H. J. de Vega, R. Holman, and J. F. J. Salgado, "Analytic an numerical study of preheating dynamics" Phys. Rev. **D54** (1996) 7570-7598, [arXiv:hep-ph/9608205].

[14] S.Y Khlebnikov and I. I. Tkachev, "Resonant decay of Bose condensates," Phys. Rev. Lett. **79** (1997) 1607-1610, [arXiv:hep-ph/9610477].

[15] J. Garcia-Bellido and A. D. Linde, "Preheating in hybrid inflation," Phys. Rev. D **57**, 6075 (1998) [arXiv:hep-ph/9711360].

[16] A. Rajantie, P.M. Saffin, and E. J. Copeland, "Electroweak preheating on a lattice," Phys. Rev. **D63** (2001) 123512, [arXiv:hep-ph/0012097].

[17] E. N. Parker, "Cosmological Magnetic Fields," Clarendon Press, Oxford (1979)

[18] Ya. B. Zeldovich, A. A. Ruzmaikin and D. D. Sokoloff, "Magnetic Fields in Astrophysics," Gordon and Breach, New York (1983)

[19] A. A. Ruzmaikin, A. M. Shukurov and D. D. Sokoloff, "Magnetic Fields of Galaxies," Kluwer Academic Publisher, Dordrecht (1988)

[20] D. Biskamp, "Non-linear magnetohydrodynamics," Cambridge U.P., Cambridge (1994)

[21] P. P. Kronberg, "Extragalactic magnetic fields," Rept. Prog. Phys. **57**, 325 (1994).

[22] R. Beck, A. Brandenburg, D. Moss, A. Shukurov and D. Sokoloff, "Galactic Magnetism: Recent developments and perspectives," Ann. Rev. Astron. Astrophys. **34**, 155 (1996).

[23] K. Enqvist, "Primordial magnetic fields," Int. J. Mod. Phys. D **7**, 331 (1998) [arXiv:astro-ph/9803196].

[24] R. M. Kulsrud, "A Critical Review Of Galactic Dynamos," Ann. Rev. Astron. Astrophys. **37**, 37 (1999).

[25] D. Grasso and H. R. Rubinstein, "Magnetic fields in the early universe," Phys. Rept. **348**, 163 (2001) [arXiv:astro-ph/0009061]

[26] C. L. Carilli and G. B. Taylor, "Cluster Magnetic Fields," Ann. Rev. Astron. Astrophys. **40**, 319 (2002) [arXiv:astro-ph/0110655]

[27] J. L. Han and R. Wielebinski, "Milestones in the Observations of Cosmic Magnetic Fields," Chin. J. Astron. Astrophys. **2**, 293 (2002) [arXiv:astro-ph/0209090]

[28] L. M. Widrow, "Origin of Galactic and Extragalactic Magnetic Fields," Rev. Mod. Phys. **74**, 775 (2003) [arXiv:astro-ph/0207240].

[29] M. Giovannini, "The magnetized universe," Int. J. Mod. Phys. D **13**, 391 (2004) [arXiv:astro-ph/0312614].

[30] B. M. Gaensler, R. Beck and L. Feretti, "The Origin and Evolution of Cosmic Magnetism," New Astron. Rev. **48**, 1003 (2004) [arXiv:astro-ph/0409100].

[31] M. Shaposhnikov, "Primordial magnetic fields," AIP Conf. Proc. **784** (2005) 423.

[32] R. Beck, "Magnetic fields in galaxies," Lecture Notes in Physics **664**, 41 (2005)

[33] R. Durrer, "Cosmic Magnetic Fields and the CMB," New Astron. Rev. **51**, 275 (2007) [arXiv:astro-ph/0609216]

[34] J. D. Barrow, R. Maartens and C. G. Tsagas, "Cosmology with inhomogeneous magnetic fields," Phys. Rept. **449**, 131 (2007) [arXiv:astro-ph/0611537]

[35] R. Durrer and C. Caprini, "Primordial Magnetic Fields and Causality," JCAP **0311**, 010 (2003) [arXiv:astro-ph/0305059]

[36] J. Vallée, "Observations of the Magnetic Fields Inside and Outside the Milky Way," Fund. Cosm. Phys. **19**, 1 (1997)

[37] A. Dar and A. De Rujula, "The Magnetic Field in Galaxies, Galaxy Clusters, and the InterGalactic Space," Phys. Rev. D **72**, 123002 (2005) [arXiv:astro-ph/0504480]

[38] J. M. Quashnock, A. Loeb and D. N. Spergel, Astrophys. J. 344 (1989) L49.

[39] C. J. Hogan, "Magnetohydrodynamic effects of a first-order cosmological phase transition," Phys. Rev. Lett. **51**, 1488 (1983).

[40] B. l. Cheng and A. V. Olinto, "Primordial magnetic fields generated in the quark - hadron transition," Phys. Rev. D **50**, 2421 (1994).

[41] G. Sigl, A. V. Olinto and K. Jedamzik, "Primordial magnetic fields from cosmological first order phase transitions," Phys. Rev. D **55**, 4582 (1997) [arXiv:astro-ph/9610201].

[42] J. Ahonen and K. Enqvist, "Magnetic field generation in first order phase transition bubble collisions," Phys. Rev. D **57**, 664 (1998) [arXiv:hep-ph/9704334]

[43] G. Baym, D. Bodeker and L. D. McLerran, "Magnetic fields produced by phase transition bubbles in the electroweak phase transition," Phys. Rev. D **53**, 662 (1996) [arXiv:hep-ph/9507429].

[44] M. Hindmarsh and A. Everett, "Magnetic fields from phase transitions," Phys. Rev. D **58**, 103505 (1998) [arXiv:astro-ph/9708004].

[45] A. Brandenburg, K. Enqvist and P. Olesen, "Large-scale magnetic fields from hydromagnetic turbulence in the very early universe," Phys. Rev. D **54**, 1291 (1996) [arXiv:astro-ph/9602031]

[46] Pierre Auger Collaboration 2007, Science **318** 938.

[47] O. Deligny, A. Letessier-Selvon and E. Parizot, "Magnetic horizons of UHECR sources and the GZK feature", J. Astropart. Phys. **21** (2004) 609-615.

[48] J. Smit, "Introduction to quantum fields on a lattice," Cambridge Lecture Notes in Physics (2002).

[49] H. J. Rothe, "Lattice gauge theories. An introduction," World Scientific Lecture Notes in Physics (1992).

[50] M. Creutz, "Quarks, gluons and lattices," Cambridge monographics on mathematical physics (1983).

[51] I. Montvay, G. Münster, "Quantum fields on a lattice," Cambridge monographics on mathematical physics (1997).

[52] K. Wilson, "Confinement of Quarks," Phys. Rev. **B**10, 2445 (1974);

[53] M. A. Berger, "Introduction to magnetic helicity," Plasma Phys. Control. Fusion **41** (1999) B167-B175.

[54] G. Hornig and L. Rastatter, " The role of the helicity in the reconnection process."

[55] J. Chae et al., "Magnetic helicity pumping by twisted flux tube expansion," Journal of the Korean Astronomical Society **35** 1 (2002).

[56] J.B. Taylor, "Relaxation of toroidal plasma and generation of reverse magnetic fields," Phys. Rev. Lett. **33** (1974) 1139

[57] M. Christensson, M. Hindmarsh and A. Brandenburg, "Inverse cascade in decaying 3D magnetohydrodynamic turbulence," Phys. Rev. E **64**, 056405 (2001) [arXiv:astro-ph/0011321].

[58] M. Christensson, M. Hindmarsh and A. Brandenburg, "Scaling laws in decaying helical 3D magnetohydrodynamic turbulence," Astron. Nachr. **326**, 393 (2005) [arXiv:astro-ph/0209119].

[59] D. T. Son, "Magnetohydrodynamics of the early universe and the evolution of primordial magnetic fields," Phys. Rev. D **59**, 063008 (1999) [arXiv:hep-ph/9803412]

[60] D. Biskmap and W. Müller, "Deacy laws for three-dimensional magnetohydrodynamic turbulence," Phys. Rev. Lett. **83** (1999) 2195

[61] L. Campanelli, "Scaling laws in magnetohydrodynamic turbulence," Phys. Rev. D **70**, (2004) 083009

[62] R. Banerjee and K. Jedamzik, "Are Cluster Magnetic Fields Primordial ?," Phys. Rev. Lett. **91** (2003) 251301; [Erratum-ibid. **93** (2004) 179901] [arXiv:astro-ph/0306211]. R. Banerjee and K. Jedamzik, "The Evolution of Cosmic Magnetic Fields: From the Very Early Universe, to Recombination, to the Present," Phys. Rev. D **70** (2004) 123003; [arXiv:astro-ph/0410032].

[63] D. Schnack, "Lectures on Magnetohydrodynamics", Universy of Wisconsin.

[64] A. N. Kolmogorov "On the degeneration of isotropic turbulence", Dokl. Akad. Nauk. SSSR, **31** (1941), 538541; "Dissipation of enery in isotropic turbulence", Dokl. Akad. Nauk. SSSR, **32** (1941), 1921; "Equations of turbulent motion", Izv. Akad. Nauk. SSSR ser. Fiz., **6** (1942), 5658

[65] S. Boldyrev and F. Cattaneo, "Magnetic-Field Generation in Kolmogorov Turbulence", Phys. Rev. Lett. **92** 144501 (2004)

[66] P. Olesen, "Inverse cascades and primordial magnetic fields ", Phys. Lett. B **398**, 321 (1997).

[67] T. Kahniashvili, T. Vachaspati, "On the Detection of Magnetic Helicity," Phys. Rev. D**73** (2006) 063507; [arXiv:astro-ph/0511373v3]

[68] T. Vachaspati, "Magnetic fields from cosmological phase transitions," Phys. Lett. B **265**, 258 (1991)

[69] T. Vachaspati, "Electroweak strings, sphalerons and magnetic fields," arXiv:hep-ph/9405286.

[70] T. Vachaspati, "Estimate of the primordial magnetic field helicity," Phys. Rev. Lett. **87**, 251302 (2001) [arXiv:astro-ph/0101261].

[71] T. W. B. Kibble and A. Vilenkin, Phys. Rev. D **52**, 679 (1995).

[72] J. M. Cornwall, "Speculations on primordial magnetic helicity," Phys. Rev. D **56**, 6146 (1997) [arXiv:hep-th/9704022].

[73] E. J. Copeland and P. M. Saffin, "Bubble collisions in Abelian gauge theories and the geodesic rule," Phys. Rev. D **54**, 6088 (1996) [arXiv:hep-ph/9604231].

[74] E. J. Copeland, P. M. Saffin and O. Tornkvist, "Phase equilibration and magnetic field generation in U(1) bubble collisions," Phys. Rev. D **61**, 105005 (2000) [arXiv:hep-ph/9907437].

[75] D. Grasso and A. Riotto, "On the nature of the magnetic fields generated during the electroweak phase transition," Phys. Lett. B **418**, 258 (1998) [arXiv:hep-ph/9707265].

[76] M. Joyce and M. E. Shaposhnikov, "Primordial magnetic fields, right electrons, and the Abelian anomaly," Phys. Rev. Lett. **79**, 1193 (1997) [arXiv:astro-ph/9703005].

[77] M. Giovannini and M. E. Shaposhnikov, "Primordial hypermagnetic fields and triangle anomaly," Phys. Rev. D **57**, 2186 (1998) [arXiv:hep-ph/9710234].

[78] M. S. Turner and L. M. Widrow, "Inflation Produced, Large Scale Magnetic Fields," Phys. Rev. D **37**, 2743 (1988)

[79] B. Ratra, "Cosmological 'seed' magnetic field from inflation," Astrophys. J. **391** (1992) L1

[80] W. D. Garretson, G. B. Field and S. M. Carroll, "Primordial magnetic fields from pseudoGoldstone bosons," Phys. Rev. D **46** (1992) 5346 [arXiv:hep-ph/9209238].

[81] A. Dolgov, "Breaking Of Conformal Invariance And Electromagnetic Field Generation In The Universe," Phys. Rev. D **48** (1993) 2499 [arXiv:hep-ph/9301280].

[82] F. D. Mazzitelli and F. M. Spedalieri, "Scalar electrodynamics and primordial magnetic fields," Phys. Rev. D **52** (1995) 6694 [arXiv:astro-ph/9505140].

[83] M. Novello, L. A. R. Oliveira and J. M. Salim, "Direct Electrogravitational Couplings And The Behavior Of Primordial Large Scale Magnetic Fields," Class. Quant. Grav. **13** (1996) 1089

[84] E. A. Calzetta, A. Kandus and F. D. Mazzitelli, "Primordial magnetic fields induced by cosmological particle creation," Phys. Rev. D **57** (1998) 7139 [arXiv:astro-ph/9707220].

[85] O. Bertolami and D. F. Mota, "Primordial magnetic fields via spontaneous breaking of Lorentz invariance," Phys. Lett. B **455** (1999) 96 [arXiv:gr-qc/9811087].

[86] M. Giovannini and M. E. Shaposhnikov, "Primordial magnetic fields from inflation?," Phys. Rev. D **62**, 103512 (2000) [arXiv:hep-ph/0004269].

[87] M. Giovannini, "Magnetogenesis and the dynamics of internal dimensions," Phys. Rev. D **62**, 123505 (2000) [arXiv:hep-ph/0007163].

[88] X. Chi and A. W. Wolfendale, Nature **362** (1993) 610.

[89] J. Han and G. J. Qiao, Astron. Astrophys. **288** (1994) 759.

[90] T. E. Clarke, P.P. Kronberg and H. Böhringer, Astrophys. J. **547** (2001) L111.

[91] H. Hebeling et al. , Mon. Not. Astron. Soc. **281** (1996) 799.

[92] A. C. Davis et al., "Primordial spectrum of gauge fields from inflation," Phys. Lett. B **501** (2001) 165 [arXiv:astro-ph/0007214]; K. Dimopoulos et al., "Natural magnetogenesis from inflation," Phys. Rev. D **65** (2002) 063505 [arXiv:astro-ph/0108093].

[93] T. Prokopec and E. Puchwein, "Photon mass generation during inflation: de Sitter invariant case," JCAP **0404** (2004) 007 [arXiv:astro-ph/0312274]; "Nearly minimal magnetogenesis," Phys. Rev. D **70** (2004) 043004 [arXiv:astro-ph/0403335].

[94] K. Enqvist, A. Jokinen and A. Mazumdar, "Seed perturbations for primordial magnetic fields from MSSM flat directions," JCAP **0411** (2004) 001 [arXiv:hep-ph/0404269].

[95] M. R. Garousi, M. Sami and S. Tsujikawa, "Generation of electromagnetic fields in string cosmology with a massive scalar field on the anti D-brane," Phys. Lett. B **606** (2005) 1 [arXiv:hep-th/0405012].

[96] A. Ashoorioon and R. B. Mann, "Generation of cosmological seed magnetic fields from inflation with cutoff," Phys. Rev. D **71** (2005) 103509 [arXiv:gr-qc/0410053].

[97] J. E. Madriz Aguilar and M. Bellini, "Stochastic gravitoelectromagnetic inflation," Phys. Lett. B **642** (2006) 302 [arXiv:gr-qc/0605043].

[98] L. Campanelli et al., "Inflation-Produced Magnetic Fields in Nonlinear Electrodynamics," Phys. Rev. D **77** (2008) 043001 [arXiv:0710.2993 [astro-ph]]; L. Campanelli, "Helical Magnetic Fields from Inflation," arXiv:0805.0575 [astro-ph].

[99] K. Ichiki, K. Takahashi, H. Ohno, H. Hanayama and N. Sugiyama, "Cosmological Magnetic Field: a fossil of density perturbations in the early universe," Science **311**, 827 (2006) [arXiv:astro-ph/0603631]

[100] K. Takahashi, K. Ichiki, H. Ohno and H. Hanayama, "Magnetic field generation from cosmological perturbations," Phys. Rev. Lett. **95**, 121301 (2005) [arXiv:astro-ph/0502283]

[101] R. Durrer "Is the mystery of cosmic magnetic fields solved?" Science **311**, 787 (2006)

[102] E. A. Calzetta and A. Kandus, "Self consistent estimates of magnetic fields from reheating," Phys. Rev. D **65**, 063004 (2002) [arXiv:astro-ph/0110341]

[103] D. Boyanovsky, M. Simionato and H. J. de Vega, "Magnetic field generation from non-equilibrium phase transitions," Phys. Rev. D **67** (2003) 023502 [arXiv:hep-ph/0208272].

[104] D. Boyanovsky, H. J. de Vega and M. Simionato, "Large scale magnetogenesis from a non-equilibrium phase transition in the radiation dominated era," Phys. Rev. D **67** (2003) 123505 [arXiv:hep-ph/0211022].

[105] D. Boyanovsky and H. J. de Vega, "Primordial magnetic fields from out of equilibrium cosmological phase transitions," AIP Conf. Proc. **784**, 434 (2005) [arXiv:astro-ph/0502212].

[106] D. H. Lyth and E. D. Stewart, "Cosmology With A Tev Mass GUT Higgs," Phys. Rev. Lett. **75** (1995) 201 [arXiv:hep-ph/9502417]; "Thermal Inflation And The Moduli Problem," Phys. Rev. D **53** (1996) 1784 [arXiv:hep-ph/9510204].

[107] R. Easther, J. T. Giblin, E. A. Lim, W. I. Park and E. D. Stewart, "Thermal Inflation and the Gravitational Wave Background," arXiv:0801.4197 [astro-ph].

[108] J. Garcia-Bellido, D. Y. Grigoriev, A. Kusenko and M. E. Shaposhnikov, "Non-equilibrium electroweak baryogenesis from preheating after inflation," Phys. Rev. D **60**, 123504 (1999) [arXiv:hep-ph/9902449]; L. M. Krauss and M. Trodden, "Baryogenesis below the electroweak scale," Phys. Rev. Lett. **83**, 1502 (1999) [arXiv:hep-ph/9902420]; J. Garcia-Bellido and D. Y. Grigoriev, "Inflaton-induced sphaleron transitions," JHEP **0001**, 017 (2000) [arXiv:hep-ph/9912515].

[109] G. N. Felder, J. Garcia-Bellido, P. B. Greene, L. Kofman, A. D. Linde and I. Tkachev, "Dynamics of symmetry breaking and tachyonic preheating," Phys. Rev. Lett. **87**, 011601 (2001) [arXiv:hep-ph/0012142]; G. N. Felder, L. Kofman and A. D. Linde, "Tachyonic instability and dynamics of spontaneous symmetry breaking," Phys. Rev. D **64**, 123517 (2001) [arXiv:hep-th/0106179].

[110] J. M. Cornwall, D. Grigoriev and A. Kusenko, "Resonant amplification of electroweak baryogenesis at preheating," Phys. Rev. D **64** (2001)

123518 [arXiv:hep-ph/0106127]; J. M. Cornwall and A. Kusenko, "Baryon number non-conservation and phase transitions at preheating," Phys. Rev. D **61** (2000) 103510 [arXiv:hep-ph/0001058].

[111] J. García-Bellido, M. García Perez and A. González-Arroyo, "Symmetry breaking and false vacuum decay after hybrid inflation," Phys. Rev. D **67**, 103501 (2003) [arXiv:hep-ph/0208228].

[112] J. García-Bellido, M. García Perez and A. González-Arroyo, "Chern-Simons production during preheating in hybrid inflation models," Phys. Rev. D **69**, 023504 (2004) [arXiv:hep-ph/0304285].

[113] J. Garcia-Bellido, E. Ruiz Morales, "Particle production from symmetry breaking after inflation and leptogenesis", Phys.Lett. B **536** 193-202 (2002), [arXiv:hep-ph/0109230].

[114] J. García-Bellido, S. Mollerach and E. Roulet, "Fermion production during preheating after hybrid inflation", *JHEP* **0002** (2000) 034.

[115] J.Smit, A.Tranberg, *JHEP* **12** (2002) 020; *JHEP* **0311** (2003) 016; *JHEP* **0608** (2006) 012; J. I. Skullerud, J. Smit and A. Tranberg, *JHEP* **0308** (2003) 045; M. van der Meulen, D. Sexty, J. Smit and A. Tranberg, *JHEP* **0602** (2006) 029;A. Tranberg, J. Smit and M. Hindmarsh, *JHEP* **0701** (2007) 034.

[116] J. Smit, *Simulations in Early-Universe Theory*, in proceedings of *Lattice 2005 conference*, PoS(LAT2005) 022, and references therein.

[117] J. Garcia-Bellido and D. G. Figueroa, "A stochastic background of gravitational waves from hybrid preheating," Phys. Rev. Lett. **98** (2007) 061302 [arXiv:astro-ph/0701014]; J. Garcia-Bellido, D. G. Figueroa and A. Sastre, "A Gravitational Wave Background from Reheating after Hybrid Inflation," Phys. Rev. D **77** (2008) 043517 [arXiv:0707.0839 hep-ph].

[118] A. Diaz-Gil, J. Garcia-Bellido, M. Garcia Perez and A. Gonzalez-Arroyo, "Magnetic field production during preheating at the electroweak scale," Phys. Rev. Lett. **100** (2008) 241301 [arXiv:0712.4263 hep-ph];

[119] A. Díaz-Gil, J. García-Bellido, M. García Pérez, A. González-Arroyo, in proceedings of *Lattice 2005 conference*, PoS(LAT2005) 242; ibid in proceedings of *Lattice 2007 conference*, PoS(LAT2007) 052.

[120] A. Díaz-Gil, "Preheating no perturbativo". Memory for the obtention of the "DEA" degree. Biblioteca Dpto. Física Teórica, Universidad Autónoma de Madrid.

[121] A. Diaz-Gil, J. Garcia-Bellido, M. Garcia Perez and A. Gonzalez-Arroyo, "Primordial magnetic fields from preheating at the electroweak scale," JHEP**0807**(2008)043 [arXiv:0805.4159 hep-ph];

[122] Particle Data Group, "Review of particle physics," Phys. Lett. B **667**, 1 (2008), `http://pdg.lbl.gov/`

[123] G. 't Hooft, "Magnetic monopoles in unified gauge theories," Nucl. Phys. B **79** (1974) 276.

[124] C. J. Copi, F. Ferrer, T. Vachaspati and A. Achucarro, "Helical Magnetic Fields from Sphaleron Decay and Baryogenesis," Phys.Rev.Lett. **101** (2008) 171302, arXiv:0801.3653 [astro-ph].

[125] F. R. Klinkhamer and N. S. Manton, "A Saddle Point Solution In The Weinberg-Salam Theory," Phys. Rev. D **30** (1984) 2212.

[126] R. Micha and I. I. Tkachev, "Relativistic turbulence: A long way from preheating to equilibrium," Phys. Rev. Lett. **90** (2003) 121301 [arXiv:hep-ph/0210202]; "Turbulent thermalization," Phys. Rev. D **70** (2004) 043538 [arXiv:hep-ph/0403101].

[127] J. M. Bardeen, J. R. Bond, N. Kaiser and A. S. Szalay, "The Statistics Of Peaks Of Gaussian Random Fields," Astrophys. J. **304**, 15 (1986).

[128] J. R. Bond, L. Kofman and D. Pogosian, "How Filaments are Woven into the Cosmic Web," Nature **380** (1996) 603 [arXiv:astro-ph/9512141].

[129] J. R. Bond, L. Kofman, D. Pogosian and J. Wadsley, "Theoretical tools for large scale structure," arXiv:astro-ph/9810093; Proceedings of 14th IAP Meeting on Wide Field Surveys in Cosmology (IAP 98), Paris, France, 26-30 May 1998

[130] D. Pogosian, J. R. Bond, L. Kofman and J. Wadsley, "Cosmic Web: Origin and Observables," arXiv:astro-ph/9810072.

[131] J. Berges, S. Scheffler, D. Sexty, "Turbulence in nonabelian gauge theory," arXiv:0811.4293v1 [hep-ph]

[132] J. Trier Frederiksen, C. B. Hededal, T. Haugboelle, A. Nordlund, "Magnetic Field Generation in Collisionless Shocks; Pattern Growth and Transport," Astrophys.J. **608** (2004) L13-L16, arXiv:astro-ph/0308104v3

[133] J. Dufaux et al., "Gravity Waves from Tachyonic Preheating afte Hybrid Infaltion", arXiv:0812.2917 [astro-ph].

[134] F. Bezrukov, D. Gorbunov and M. Shaposhnikov, "On initial conditions for the Hot Big Bang," arXiv:0812.3622 [hep-ph].